Magazine of Civil Engineering

ISSN 2712-8172

119(3), 2023

Magazine of Civil Engineering

ISSN 2712-8172

Online peer-reviewed open-access scientific journal in the field of Civil and Construction Engineering

Founder and Publisher: Peter the Great St. Petersburg Polytechnic University

This journal is registered by the Federal Service for Supervision of Communications, Information Technology, and Mass Media (ROSKOMNADZOR) in 2020. Certificate El No. FS77-77906 issued February 19, 2020.

Periodicity: 8 issues per year

Publication in the journal is open and free for all authors and readers.

Indexing: Scopus, Web of Sceince (ESCI, RSCI), DOAJ, Compendex, Google Academia, Index Copernicus, ProQuest, Ulrich's Serials Analysis System, CNKI

Corresponding address: 29 Polytechnicheskaya st., Saint Petersburg, 195251, Russia

Chief science editor: associate member of RAS, D.S. in Engineering, Vitaly V. Sergeev

Deputy chief science editors:
D.S. in Engineering, Galina L. Kozinetc

D.S. in Engineering, Sergey V. Korniyenko

Executive editor: Ekaterina A. Linnik

Translator, editor: Darya Yu. Alekseeva

DT publishing specialist:
Anastasiya A. Kononova

Contacts:
E-mail: mce@spbstu.ru
Web: http://www.engstroy.spbstu.ru

Date of issue: 15.05.2023

Contents

Magazine of Civil Engineering

ISSN 2712-8172

journal homepage: http://engstroy.spbstu.ru/

Research article

UDC 624

DOI: 10.34910/MCE.119.1

Sulfate corrosion resistance of foundation concrete with nano-particles

M. Zhang[1] ✉ ***, D. Ma***[1] ***, J. He***[2] ***, Y. Han***[1]

[1] *Northeast Forestry University, Harbin, China*

[2] *Harbin Institute of Petroleum, Harbin, China*

✉ *zmh7716@163.com*

Keywords: concrete, foundation, nanoparticles, sulfate, corrosion, dry-wet cycles

Abstract. With the rapid development of modern industry, the foundation soil and the underground water in some areas are severely polluted by the corrosive medium affecting the durability of foundation concrete. Sulfate corrosion is one of the major factors leading to the destruction of foundation concrete. The sulfate corrosion resistance of foundation concrete with nano-particles (nano-SiO_2 and nano-$CaCO_3$) under the action of dry-wet cycle is experimentally studied, and compared with that of plain foundation concrete. The test results indicate that, under the action of dry-wet cycle, the sulfate corrosion resistance of foundation concrete is significantly improved with the addition of nano-particles. With the increasing content of nano-particles, the sulfate corrosion resistance of foundation concrete gradually rises to its peak and then drops step by step. The sulfate corrosion resistance of foundation concrete with nano-SiO_2 is superior to that of foundation concrete with the same amount of nano-$CaCO_3$. When the content of nano-SiO_2 and nano-$CaCO_3$ is respectively 2.0 % and 1.0 % by weight of binder, the sulfate corrosion resistance of foundation concrete is the best. Because the pore structure of concrete is improved with the addition of nano-particles, as nano-SiO_2 can react with $Ca(OH)_2$ and nano-$CaCO_3$ can react with C_3A, nano-particles can significantly enhance the sulfate corrosion resistance of foundation concrete.

Funding: This study is financially supported by NSFC with Grant No. 52078109, the Heilongjiang Postdoctoral Science-Research Foundation (LBH-Q13001) and the Fundamental Research Funds for the Central Universities (2013CBQ02).

Citation: Zhang, M., Ma, D., He, J., Han, Y. Sulfate corrosion resistance of foundation concrete with nano-particles. Magazine of Civil Engineering. 2023. 119(3). Article no. 11901. DOI: 10.34910/MCE.119.1

1. Introduction

The natural environment is damaged with the rapid development of modern society because the industrial waste and household garbage are discharged randomly. The site soil and underground water in some areas are polluted seriously. The building foundation has close contact with the site soil and underground water, so the site soil and underground water contaminated by corrosive medium can affect the durability of foundation concrete. In addition, the sulfate corrosion is one of the key factors causing damage to foundation concrete. Because the building foundation is concealed, the corrosion phenomena are very difficult to discover, and are hard to control and repair. Except that the industrial and household waste can lead to the existence of corrosive ion in the site soil and underground water, the site soil in some areas contains corrosive ion in itself, such as SO_4^{2-}, which can give rise to the rapid failure of foundation concrete due to severe sulfate corrosion. Sulfate erosion of foundation concrete exists in many other countries, such as America, Germany, Canada and Japan. Consequently, it is essential to enhance the sulfate corrosion resistance of foundation concrete.

Nano-materials attract more and more attention due to their unique physical and chemical properties. With the reduction in manufacturing costs, the application field of nano-materials is more and more extensive. It has been proven that nano-materials can improve the mechanical properties and durability of concrete. Nano-materials gives lower heat of hydration, improved durability together with the responsiveness to hydrogen sulfate and hydrogen chloride attacks when equated to the standard concrete [1–10]. However, the research on the sulfate corrosion resistance of concrete with nano-materials is so limited at present.

Zhang et al. [11, 12] studied the sulfate corrosion resistance of foundation concrete with nano-particles in freeze-thaw environment, and the test results showed that the addition of nano-kaolin, nano-SiO_2 and nano-$CaCO_3$ can improve the sulfate corrosion resistance of foundation concrete to different extent. When the content of nano-kaolin, nano-SiO_2 and nano-$CaCO_3$ can is respectively 3 %, 2 % and 2 %, the life of sulfate corrosion resistance of foundation concrete is respectively increased by 99.33 %, 127.98 % and106.40 %. Li et al. [13] studied the effect of nano-$CaCO_3$ on the performance of concrete with fly ash in the dry-wet cycling environment, and the corrosion resistance of fly ash concrete is greatly enhanced when the content of nano-$CaCO_3$ is 1 %.

Nano-SiO2 has high pozzolanic activity, can quickly participate in cement hydration reaction, and can consume Ca(OH)2 in cement hydration products; Nano-CaCO3 can improve the pore structure of concrete, and the price is low, with reasonable economy. Therefore, in this paper, nano-SiO2 and nano-CaCO3 are mixed into the foundation concrete to study the change rules of physical properties (relative dynamic elastic modulus) and mechanical properties (compressive and flexural strength) of nanoparticle foundation concrete against sulphate corrosion and its modification mechanism of the sulfate corrosion resistance of foundation concrete with nano-particles under the action of dry-wet cycle. And the sulfate corrosion resistance is compared with that of plain foundation concrete.

2. Methods

2.1. Materials and mixture proportions

The cement used is Portland cement (P.O42.5). The fine aggregate is natural river sand with a fineness modulus of 2.43. The coarse aggregate used is crushed basalt with a diameter of 5–31.5 mm. The properties of nano-particles (SiO_2 and $CaCO_3$) are given in Table 1.

Table 1. Properties of nano-particles.

Item	Diameter (nm)	Purity (%)	Specific surface area (m^2/g)	pH value
nano-SiO_2	20	99.9	640 ± 60	6–8
nano-$CaCO_3$	30	99.0	–	9.3

The water-to-binder (the sum of cement and nano-particles) ratio used for all mixtures is 0.44, and the sand ratio is 34 %. The mixture proportions of concretes per cubic meter are shown in Table 2. The water-reducing agent (FDN, one kind of β-naphthalene sulfonic acid and formaldehyde condensates, 1.5 % by mass of binder) is adopted to ensure the good workability of fresh concrete, and act as a better dispersant to prevent the agglomeration of nano-particles in cement paste. Besides, the defoamer (tributyl phosphate) is employed with a mass ratio of 4 % to superplasticizer to eliminate air bubbles generated during the dispersion of nano-particles.

Table 2. Mix proportions of concretes (unit: kg/m^3).

Mixture type	Water	Cement	Sand	Coarse aggregate	Nano-SiO_2	Nano-$CaCO_3$	FDN	Defoamer
PC	165	375	645	1240	–	–	4.31	–
NS05	165	373.1	645	1240	1.9	–	4.31	0.172
NS10	165	371.2	645	1240	3.8	–	4.31	0.172
NS20	165	367.5	645	1240	7.5	–	4.31	0.172
NS30	165	363.7	645	1240	11.3	–	4.31	0.172
NC05	165	373.1	645	1240	–	1.9	4.31	0.172
NC10	165	371.2	645	1240	–	3.8	4.31	0.172
NC20	165	367.5	645	1240	–	7.5	4.31	0.172
NC30	165	363.7	645	1240	–	11.3	4.31	0.172

Here, PC denotes plain concrete. NS05, NS10, NS20 and NS30 denote the concrete with nano-SiO_2 in the amount of 0.5 %, 1.0 %, 2.0 % and 3.0 % by weight of binder, respectively. NC05, NC10, NC20 and NC30 denote the concrete with nano-$CaCO_3$ in the amount of 0.5 %, 1.0 %, 2.0 % and 3.0 % by weight of binder, respectively.

2.2. Specimen preparation and curing

To prepare the concrete with nano-particles, the water-reducing agent is firstly mixed into water in a mortar mixer, and then nano-particles are added in and stirred at a high speed for 5 min. Defoamer is added as stirring. Cement, sand and coarse aggregate are mixed at a low speed for 2 min in a concrete centrifugal blender, and then the mixture of water, water-reducing agent, nano-particles and defoamer is slowly poured in and stirred at a low speed for another 2 min to achieve good workability.

To prepare plain concrete, the water-reducing agent is firstly dissolved in water. After cement, sand and coarse aggregate are mixed uniformly in a concrete centrifugal blender, the mixture of water and water-reducing agent is poured in and stirred for several minutes.

Finally, the fresh concrete is poured into oiled molds to form cubes of size 100×100×100 mm to be used for compressive strength testing, and prisms of size 100×100×400 mm for sulfate corrosion resistance testing. After pouring, an external vibrator is used to facilitate compaction and reduce the amount of air bubbles. The specimens are de-molded at 24 h and then cured in a room at a temperature of 20±2 °C and a relative humidity of more than 95 % until the prescribed period.

2.3. Test methods

The workability of concrete includes three aspects, liquidity, cohesiveness and water holding capacity. The liquidity of fresh concrete is measured by slump test. The cohesiveness and water holding capacity is evaluated by visual range estimation and experience. Slump test is conducted in accordance with GB/T 50080-2016 (Standard for test method of performance on ordinary fresh concrete, China). Compressive strength test is performed according to GB/T 50081-2016 (Standard for test method of mechanical properties on ordinary concrete, China). The sulfate corrosion resistance test is conducted according to GB/T 50082-2009 (Standard for test methods of long-term performance and durability of ordinary concrete, China), and the dry-wet cycling pattern is used.

2.3.1. The dry-wet cycling mode

Concrete specimens are taken out of the curing room at 28 days and the specific dry-wet cycling mode is as follows. Firstly, concrete specimens are put into Na_2SO_4 solution with a concentration of 5 % and submerged for 16 h at room temperature. The solution surface should be at least 20 mm above the upper specimen surface, and the plastic box should be capped to prevent the solution from evaporating. Na_2SO_4 solution should be renewed every month to keep the pH value of the solution basically constant. Next, concrete specimens are taken out of Na_2SO_4 solution and dried in the air for 1 h. Then, concrete specimens are put in the drying oven at a temperature of 80 °C for 6 h. Finally, they are taken out of the drying oven and cooled for 1 h. This is one dry-wet cycle with the total time of 24 h.

2.3.2. The corrosion resistance coefficient of compressive strength

The corrosion resistance coefficient of compressive strength can be used to reflect the change of concrete strength, and thus to reflect the internal damage degree of concrete. Compressive strengths of concrete specimens are tested at 28 days, and then are measured per 20 times dry-wet cycles.

The corrosion resistance coefficient of compressive strength can be defined as

$$K_f = \frac{f_{cn}}{f_{c0}}, \tag{1}$$

where, K_f is the corrosion resistance coefficient of compressive strength (%); f_{cn} is the compressive strength of concrete specimen subjected to sulfate corrosion after N times dry-wet cycles (MPa); f_{c0} is the compressive strength of concrete specimen under the standard curing condition at the same curing age with corroded concrete specimen (MPa).

When the corrosion resistance coefficient of compressive strength is decreased to 75 %, the test can be stopped.

2.3.3. The relative dynamic elastic modulus

The relative dynamic elastic modulus can also reflect the internal damage degree of concrete. The nonmetal supersonic detecting instrument (RS-ST01C) shown in Fig. 1 is used to measure the relative dynamic elastic modulus of concrete specimen, because the propagation sonic time of supersonic wave in concrete can effectively reflect the internal structural change of corroded concrete.

Figure 1. The nonmetal supersonic detecting instrument and the probe.

The initial sonic time of supersonic wave through the concrete specimen is measured when the curing age is 28 days, and then the sonic time of supersonic wave through the concrete specimen is measured per 20 times dry-wet cycles. The sound velocity of supersonic wave in the concrete specimen can be calculated from the sonic time of supersonic wave. The relationship between dynamic elastic modulus of concrete and sound velocity of supersonic wave can be expressed by

$$E = \frac{(1+\mu)(1-2\mu)}{(1-\mu)}\rho V^2, \tag{2}$$

where, E is the dynamic elastic modulus of concrete; μ is the Poisson's ratio of concrete; ρ is the density of concrete; V is the sound velocity of supersonic wave through the concrete.

For the same material, the change of Poisson's ratio and density is very little, so the relative dynamic elastic modulus of concrete can be expressed by

$$E_d = \frac{E_n}{E_0} = \left(\frac{V_n}{V_0}\right)^2 = \left(\frac{t_0}{t_n}\right)^2, \tag{3}$$

where, E_d is the relative dynamic elastic modulus of concrete; E_0, V_0, t_0 are the initial dynamic elastic modulus of concrete, the initial sound velocity and sonic time of supersonic wave through the concrete, respectively; E_n, V_n, t_n are the dynamic elastic modulus of concrete, the sound velocity and sonic time of supersonic wave through the concrete, respectively, after N times dry-wet cycles.

When the relative dynamic elastic modulus of concrete is reduced to 60 %, the test can be terminated.

3. Results and Discussions

3.1. Compressive strength of foundation concrete

Fig. 2 shows the compressive strength of foundation concrete at 7d, 28d and 56d. It can be seen that the compressive strength of concrete with nano-particles at different curing ages can be increased compared with plain concrete. That is to say, the addition of nano-particles can improve the compressive strength of foundation concrete. However, if the variety or content of nano-particles is different, the improvement effect on the compressive strength of foundation concrete is diverse. At every testing age, the compressive strength of foundation concrete with nano-SiO_2 is larger than that with the same amount of nano-$CaCO_3$. When nano-SiO_2 in the amount of 2 % by weight of binder is added, the compressive strength of foundation concrete is increased most significantly at all ages.

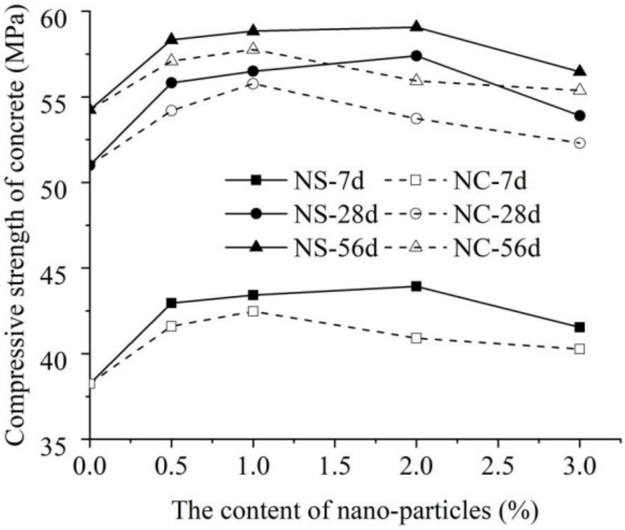

Figure 2. Relationship between the compressive strength of concrete and the content of nano-particles.

It also can be observed from Fig. 2 that, for the compressive strength of concrete at all ages, there is the same change trend with the addition of nano-SiO_2 and nano-$CaCO_3$. With the increased content of nano-particles, the compressive strength of concrete at all ages is firstly increased and then decreased, and this fully demonstrates that there is an optimum content range of nano-particles in concrete. From the view of compressive strength, the optimum content of nano-SiO_2 and nano-$CaCO_3$ in concrete is about 2 % and 1 %, respectively.

The effectiveness of nano-SiO_2 in enhancing compressive strength of concretes decreases in the order: NS20 > NS10 > NS05 > NS30, and the effectiveness of nano-$CaCO_3$ in enhancing compressive strength of concretes decreases in the order: NC10 > NC05 > NC20 > NC30. Obviously, when the content of nano-SiO_2 or nano-$CaCO_3$ is 3 %, the compressive strength of concrete is lower than that of concrete with nano-SiO_2 or nano-$CaCO_3$ in the amount of 0.5 % by weight of binder, and this indicates that it is unbeneficial when nano-particles are added in large amount.

Fig. 3 is the enhanced extent histogram of compressive strength of concrete with nano-particles at 7d, 28d and 56d. It can be seen that, when the content of nano-particles is the same, the enhanced extent of compressive strength of concrete is gradually decreased with the increase of curing age. This shows that the addition of nano-SiO_2 and nano-$CaCO_3$ can remarkably improve the early compressive strength of concrete. For the concrete with 2 % nano-SiO_2, the enhanced extent of compressive strength at 56d (8.88 %) is only 59.8 % compared with that of compressive strength at 7d (14.85 %). For the concrete with 1 % nano-$CaCO_3$, the enhanced extent of compressive strength at 56d (6.49 %) is only 58.8 % compared with that of compressive strength at 7d (11.03 %).

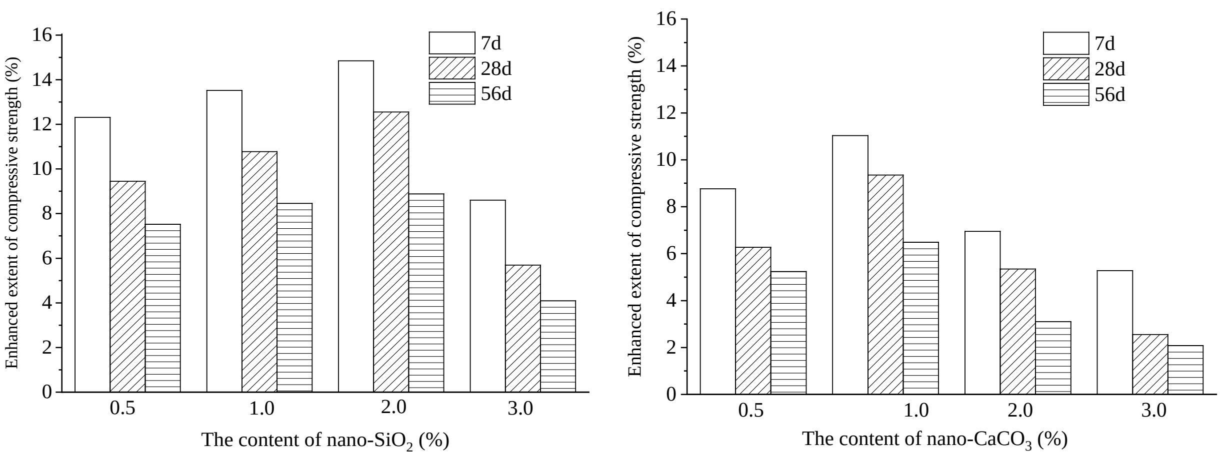

(a) Concrete with nano-SiO2 **(b) Concrete with nano-CaCO3**

Figure 3. Enhanced extent histogram of compressive strength of concrete with nano-particles.

3.2. Sulfate corrosion resistance of foundation concrete

3.2.1. Using corrosion resistance coefficient of compressive strength as evaluation index

The relationship between corrosion resistance coefficient of compressive strength of concrete with nano-particles and dry-wet cycling number is visually shown in Fig. 4. It can be seen that, with the increase number of dry-wet cycles, the corrosion resistance coefficient of compressive strength of concrete with nano-particles is also increased firstly and then decreased gradually. Furthermore, in the latter stage of sulfate corrosion resistance test, the decreasing rate of corrosion resistance coefficient of compressive strength of concrete with nano-particles is obviously slower than that of plain concrete.

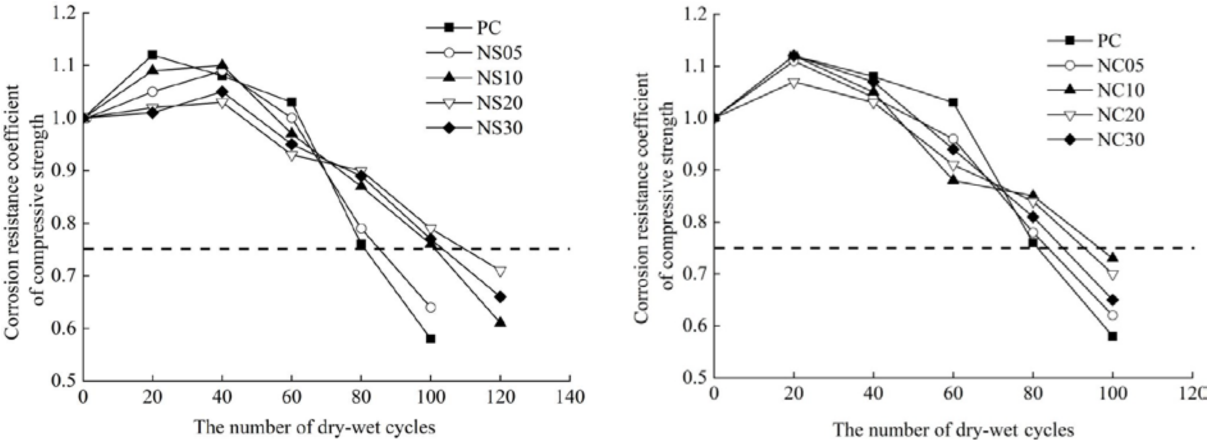

(a) Concrete with nano-SiO2 **(b) Concrete with nano-CaCO3**

Figure 4. Relationship between corrosion resistance coefficient of compressive strength and dry-wet cycling number.

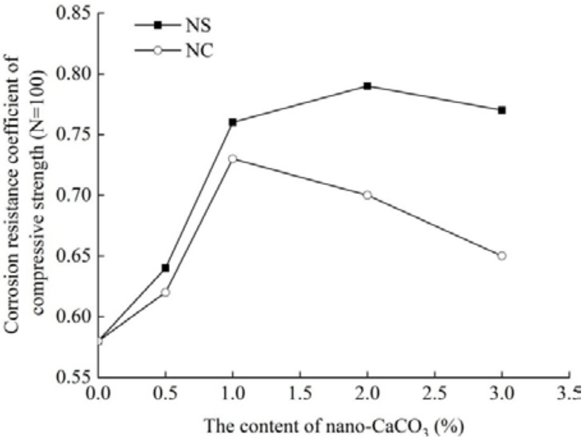

Figure 5. Relationship between corrosion resistance coefficient of compressive strength and the content of nano-particles (N = 100).

For the concrete with nano-SiO_2, when the dry-wet cycling number (N) is smaller than 40, the corrosion resistance coefficient of compressive strength $\left(K_f\right)$ is increased little by little; when N is larger than 40, K_f is decreased step by step. When N is larger than 60, K_f of PC and NS05 is decreased sharply. When N is equal to 100, K_f of PC and NS05 is reduced to less than 75 %, but K_f of NS05 is larger than that of PC. When N is equal to 120, K_f of concretes decreases in the order: NS20 > NS30 > NS10.

For the concrete with nano-$CaCO_3$, when the dry-wet cycling number (N) is equal to 120, the corrosion resistance coefficient of compressive strength $\left(K_f\right)$ is reaching the peak. When N is larger than 20, K_f is decreased gradually. When N is equal to 100, K_f of PC and all concretes with nano-$CaCO_3$ is decreased to less than 75 %, but K_f of NC is larger than that of PC. K_f of NC decreases in the order: NC10 > NC20 > NC30 > NC05.

Fig. 5 shows the relationship between corrosion resistance coefficient of compressive strength and the content of nano-particles when the dry-wet cycling number N is equal to 100. It can be observed that with the increasing content of nano-particles, the corrosion resistance coefficient of compressive strength increases firstly and then decreases, and this fully demonstrates again that there is an optimal content of nano-particles in concrete. When the content of nano-SiO_2 and nano-$CaCO_3$ in concrete is about 2 % and 1 %, respectively, the corrosion resistance coefficient of compressive strength is maximal, and the sulfate corrosion resistance of concrete is the best. In addition, the corrosion resistance coefficient of compressive strength of concrete with nano-SiO_2 is larger than that of concrete with the same amount of nano-$CaCO_3$.

Table 3 shows the dry-wet cycling number of concrete when the corrosion resistance coefficient of compressive strength is reduced to 75 %. Obviously, the sulfate corrosion resistance of various foundation concrete decreases in the order: NS20 > NS30 > NS10 > NC10 > NC20 > NC30 > NS05 > NC05 > PC.

Table 3. Dry-wet cycling number of concrete when corrosion resistance coefficient of compressive strength is reduced to 75 %.

Mixture type	PC	NS05	NS10	NS20	NS30	NC05	NC10	NC20	NC30
Dry-wet cycling number	81	85	101	110	104	84	97	93	87

3.2.2. Using relative dynamic elastic modulus as evaluation index

The attenuation curves of relative dynamic elastic moduli of concretes with nano-particles are given in Fig. 6. It can be seen that, the relative dynamic elastic modulus (E_d) is increased slightly when the dry-wet cycling number (N) is smaller than 20, and E_d is attenuated gradually when N is larger than 20. With the increase number of dry-wet cycles, the attenuation rate of E_d is speeded up in different degrees, and E_d of PC is attenuated most distinctly. When N is equal to 80, E_d of PC is already reduced to less than 60 %.

For the concrete with nano-SiO_2, E_d of NS05 is decreased to less than 60 % when N is equal to 100, and E_d of NS in other amounts will be reduced to less than 60 % when N is equal to 120. when N is equal to 120, E_d of NS decreases in the order: NS20 > NS30 > NS10, so the sulfate corrosion resistance of NS20 is the best.

For the concrete with nano-$CaCO_3$, E_d of NC05 is already decreased to less than 60 % when N is equal to 80, and E_d of NC in other amounts are all reduced to less than 60 % when N is equal to 100. When N is equal to 100, E_d of NC decreases in the order: NC10 > NC20 > NC30, so the sulfate corrosion resistance of NC10 is the best.

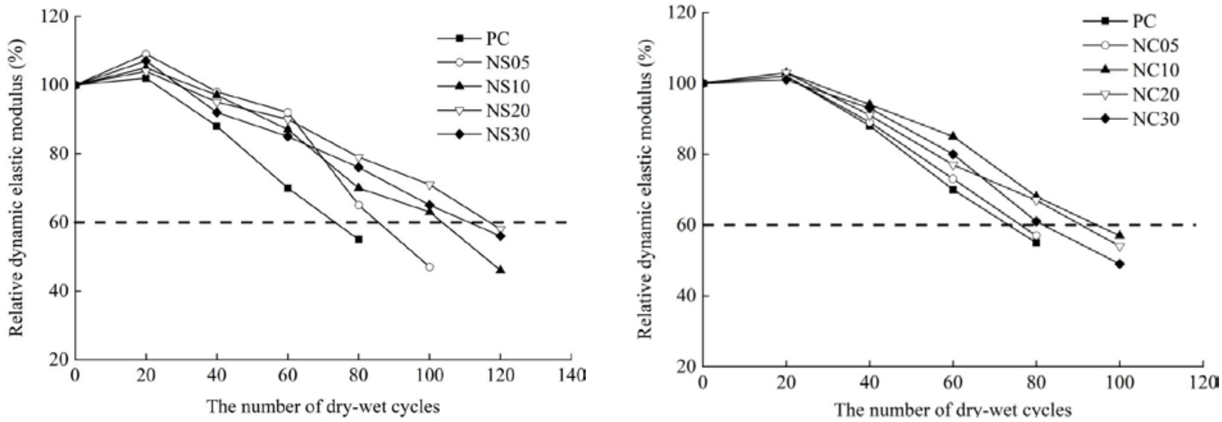

(a) Concretes with nano-SiO2 **(b) Concretes with nano-CaCO3**

Figure 6. Attenuation curves of relative dynamic elastic moduli of concretes with nano-particles.

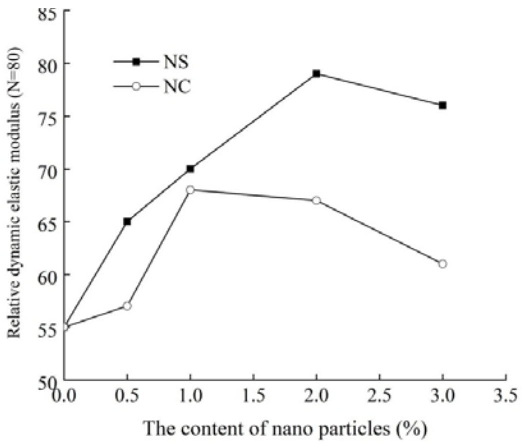

Figure 7. Relationship between relative dynamic elastic modulus and the content of nano-particles (N = 80).

Fig. 7 shows the relationship between relative dynamic elastic modulus of concrete and the content of nano-particles when the dry-wet cycling number N is equal to 80. It can be seen that, with the increase content of nano-particles, relative dynamic elastic modulus of concrete is also increased firstly and then decreased gradually, and there is an optimal amount of nano-particles in concrete. When the content of nano-SiO_2 and nano-$CaCO_3$ in concrete is about 2 % and 1 %, respectively, the relative dynamic elastic modulus of concrete is the largest, and the sulfate corrosion resistance of concrete is the best. Furthermore, the relative dynamic elastic modulus of concrete with nano-SiO_2 is larger than that of concrete with the same amount of nano-$CaCO_3$.

When the dry-wet cycling number N is equal to 80, the appearance of plain concrete, the concrete with 1 % nano-$CaCO_3$ and the concrete with 1 % nano-SiO_2 is presented in Fig. 8. It is obvious that, for the plain concrete, there is apparent spalling and cracks on the surface and at the corner, and part coarse aggregate is exposed. For the concrete with 1% nano-$CaCO_3$, there is only slight spalling on the surface. For the concrete with 1 % nano-SiO_2, there is not spalling and crack on the surface and at the corner. Consequently, after 80 times drying-wetting cycles, plain concrete is subjected to severer sulfate corrosion compared with the concrete with nano-particles.

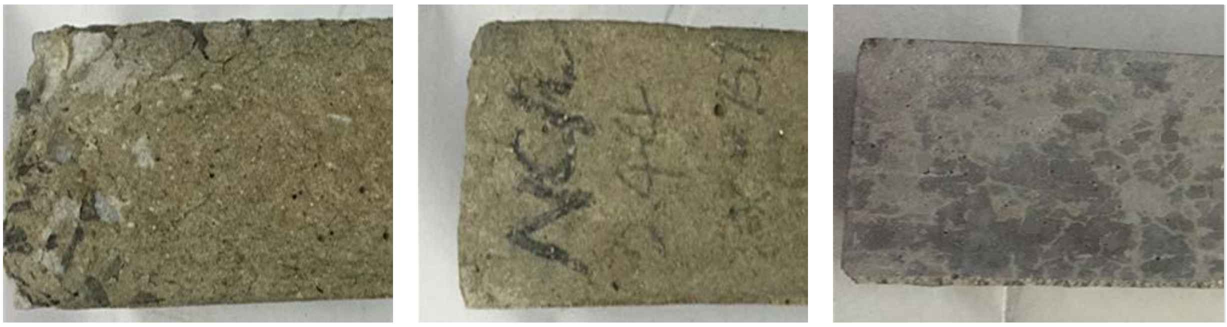

(a) PC **(b) NC10** **(c) NS20**

Figure 8. The appearance of PC, NC10 and NS20 (N = 80).

Table 4 shows the dry-wet cycling number of concrete when the relative dynamic elastic modulus is reduced to 60 %. It can be observed that, if the dry-wet cycling number of concrete is as the criterion when the relative dynamic elastic modulus is reduced to 60 %, the sulfate corrosion resistance of various foundation concrete decreases in the order: NS20 > NS30 > NS10 > NC10 > NC20 > NC30 > NS05 > NC05 > PC, and this is in accordance with the conclusion by using corrosion resistance coefficient of compressive strength as evaluation index.

Table 4. Dry-wet cycling number of concrete when the relative dynamic elastic modulus is reduced to 60 %.

Mixture type	PC	NS05	NS10	NS20	NS30	NC05	NC10	NC20	NC30
Dry-wet cycling number	73	86	103	117	111	76	95	91	81

3.3. Discussions

When the foundation concrete is subjected to sulfate corrosion under the action of dry-wet cycles, sodium sulfate (Na_2SO_4) in corrosive solution can react with cement hydration products, and then both ettringite and gypsum are generated. The process of producing ettringite and gypsum is crystallization process accompanied by volume expansion. The reaction equations forming ettringite and gypsum are as follows [14].

$$\begin{gathered} 4CaO\cdot Al_2O_3\cdot 12H_2O+3Na_2SO_4+2Ca\left(OH\right)_2+20H_2O\rightarrow \\ \rightarrow 3CaO\cdot Al_2O_3\cdot 3CaSO_4\cdot 31H_2O+6NaOH; \end{gathered} \tag{4}$$

$$Ca\left(OH\right)_2+Na_2SO_4+2H_2O\rightarrow CaSO_4\cdot 2H_2O+2Na\left(OH\right). \tag{5}$$

In the early stage of erosion, the ettringite and gypsum can fill the pore in concrete, and this makes the cement matrix denser. Consequently, the compressive strength of concrete is enhanced, and then both corrosion resistance coefficient of compressive strength and relative dynamic elastic modulus are increased. In the middle and later stage of erosion, with the increase number of dry-wet cycles, more and more ettringite and gypsum are generated [15]. After the pore in concrete is fully filled, subsequent ettringite and gypsum will produce great swelling stress. When the swelling stress is greater than the ultimate tensile strength of concrete, the cracks will be formed gradually in concrete. With the increase of swelling stress, the cracks will be extended rapidly, and the pore structure will be degraded. Moreover, corrosive solution will permeate more easily in concrete, and then the concrete will be subjected to more serious corrosion.

Furthermore, when foundation concrete is under the drying condition, the water in internal salt solution will be evaporated rapidly, and the quality fraction of Na_2SO_4 in pore solution is increased rapidly. If the quality fraction of Na_2SO_4 is larger than its solubility, the white crystal (Na_2SO_4. $10H_2O$) will be separated out, and the crystallization pressure will be formed in concrete [16]. With the increase number of dry-wet cycles, Na_2SO_4 will be dissolved during the water absorption and be crystallized during the dehydration again and again, which results in the internal damage of concrete accumulated gradually, and then the deterioration of concrete subjected to sulfate corrosion is accelerated.

To sum up, there are both physical and chemical damage during the dry-wet cycles of concrete. With the increase number of dry-wet cycles, foundation concrete is subjected to both the expansion pressure of ettringite and gypsum and the crystallization pressure of Na_2SO_4. $10H_2O$, and the cracks in concrete are increased gradually and the internal damage of concrete is aggravated step by step. So, the surface spalling of concrete is increasingly obvious, and then the corrosion resistance coefficient of compressive strength and the relative dynamic elastic modulus are decreased accordingly.

Both nano-SiO_2 and nano-$CaCO_3$ can improve the sulfate corrosion resistance of foundation concrete, and there are both common and different reasons.

3.3.1. Common reason of nano-particles improving the sulfate corrosion resistance of concrete

The common reason is that the addition of nano-particles refines the pore structure of concrete [1]. On the one hand, nano-particles can act as a filler to enhance the density of concrete, which causes the porosity of concrete to reduce significantly. On the other hand, nano-particles can not only act as an activator to accelerate cement hydration due to their high activity, but also act as a kernel in cement paste which makes the size of $Ca(OH)_2$ crystal smaller and the tropism of $Ca(OH)_2$ crystal more stochastic [3, 6]. Due to the refined pore structure, the permeability of concrete with nano-particles is reduced. So, the sulfate solution is difficult to penetrate in concrete with nano-particles, and then the sulfate corrosion resistance of concrete with nano-particles is enhanced.

3.3.2. Different reasons of nano-SiO_2 and nano-$CaCO_3$ improving the sulfate corrosion resistance of concrete

The sulfate corrosion resistance of concrete depends on the mineral composition and relative amount of cement clinker to a large extent, especially the amount of C_3A and C_3S [17]. Because C_3A is the precondition of forming ettringite, the possibility of forming ettringite will be decreased if the amount of C_3A is restricted. Abundant $Ca(OH)_2$ will be separated out with the hydration C_3S, and $Ca(OH)_2$ is the necessary part of forming ettringite and gypsum. So, the amount of forming ettringite and gypsum will be decreased if the amount of C_3S is restricted.

After ordinary Portland cement is completely hydrated, the content of calcium-silicate-hydrated (C-S-H) gel accounts for about 70 % of cement hydration products [18, 19]. The molecular number ratio of CaO to SiO_2 (CaO/SiO_2) is a continuously variable dynamic quantity, and its value is larger than 0.5 and smaller than 2.0 [20]. According to the difference of CaO/SiO_2, C-S-H gel can be divided into high-alkali C-

S-H gel and low-alkali C-S-H gel. CaO/SiO_2 of the former is larger than 1.5, and CaO/SiO_2 of the latter is smaller than 1.5. Compared to high-alkali C-S-H gel, low-alkali C-S-H gel has higher strength and better stability. In the hydration products of ordinary Portland cement, most C-S-H gel is high-alkali C-S-H gel [20]. Because the composition of C-S-H gel is very complicated, in general, the chemical expression of C-S-H gel is uniformly indicated by $3CaO\cdot 2SiO_2\cdot 3H_2O$ in the chemical equation of cement hydration reaction.

The content of $Ca(OH)_2$ accounts for about 20 % of cement hydration products, and its strength is very low and its stability is very poor [21, 22]. At the interface between hardened cement paste and aggregate, $Ca(OH)_2$ crystals are directionally separated out, and the bonding strength between hardened cement paste and aggregate is weakened. So, the existence of $Ca(OH)_2$ is unbeneficial to the mechanical properties and durability of concrete.

Due to its high pozzolanic activity, nano-SiO_2 can react with $Ca(OH)_2$, and C-S-H gel will be formed. Meanwhile, nano-SiO_2 can also react with high-alkali C-S-H gel, and low-alkali C-S-H gel will be formed [20, 23]. That is to say, nano-SiO_2 can transform high-alkali C-S-H gel into low-alkali C-S-H gel. The main chemical reaction process is as follows [20].

$$(0.8\sim 1.5)\mathrm{Ca}(\mathrm{OH})_2+\mathrm{SiO}_2+\left[n-(0.8\sim 1.5)\right]\mathrm{H_2O}\rightarrow(0.8\sim 1.5)\mathrm{CaO}\cdot\mathrm{SiO}_2\cdot n\mathrm{H_2O}; \quad (6)$$

$$(1.5\sim 2.0)\mathrm{CaO}\cdot\mathrm{SiO}_2\cdot n\mathrm{H_2O}+x\mathrm{SiO}_2+y\mathrm{H_2O}\rightarrow(0.8\sim 1.5)\mathrm{CaO}\cdot\mathrm{SiO}_2\cdot m\mathrm{H_2O}. \quad (7)$$

It can be seen from above equation that, C-S-H gel formed by reaction of nano-SiO_2 with $Ca(OH)_2$ belongs to low-alkali C-S-H gel, and the content of high-alkali C-S-H gel in concrete is reduced effectively. So, the compressive strength and the sulfate corrosion resistance of concrete is enhanced. In addition, because nano-SiO_2 can consume $Ca(OH)_2$, the amount of $Ca(OH)_2$ is decreased which results in the production of ettringite and gypsum be reduced. Then, the structure defect in concrete is lessened and the sulfate corrosion resistance of concrete is improved.

Nano-$CaCO_3$ also can participate in the hydration reaction of cement, although its activity is lower than that of nano-SiO_2. Nano-$CaCO_3$ can react with tricalcium aluminate (C_3A) in cement, and the calcium carboaluminate hydrate is formed which is more stable than ettringite [24]. The calcium carboaluminate hydrate can be divided into two kinds, that is low-calcium type ($3CaO\cdot Al_2O_3\cdot CaCO_3\cdot 12H_2O$) and high-calcium type ($3CaO\cdot Al_2O_3\cdot 3CaCO_3\cdot 31H_2O$). When nano-$CaCO_3$ reacts with C_3A in cement, the production of low-calcium calcium carboaluminate hydrate is higher than that of high-calcium calcium carboaluminate hydrate [14], and the specific reaction processes can be described as follows [25–27].

Because nano-$CaCO_3$ cannot consume $Ca(OH)_2$, $Ca(OH)_2$ in the liquid phase is very easy to reach saturation. When the concentration of $Ca(OH)_2$ in the liquid phase reaches saturation, C_3A reacts with $Ca(OH)_2$ and the tetracalcium aluminate hydrate is formed.

$$3\mathrm{CaO}\cdot\mathrm{Al_2O_3}+\mathrm{Ca}(\mathrm{OH})_2+12\mathrm{H_2O}\rightarrow 4\mathrm{CaO}\cdot\mathrm{Al_2O_3}\cdot 13\mathrm{H_2O}. \quad (8)$$

Because there is a small amount of gypsum in Portland cement, the tetracalcium aluminate hydrate can promptly react with gypsum, and the calcium sulfoaluminate hydrates, that is ettringite is produced.

$$\begin{gathered}4\mathrm{CaO}\cdot\mathrm{Al_2O_3}\cdot 13\mathrm{H_2O}+3\mathrm{CaSO_4}\cdot 2\mathrm{H_2O}+17\mathrm{H_2O}\rightarrow\\ \rightarrow 3\mathrm{CaO}\cdot\mathrm{Al_2O_3}\cdot 3\mathrm{CaSO_4}\cdot 31\mathrm{H_2O}+\mathrm{Ca}(\mathrm{OH})_2.\end{gathered} \quad (9)$$

After nano-$CaCO_3$ is added, nano-$CaCO_3$ can react with tetracalcium aluminate hydrate, and high-calcium calcium carboaluminate hydrate will be generated.

$$\begin{gathered}3\mathrm{CaCO_3}+4\mathrm{CaO}\cdot\mathrm{Al_2O_3}\cdot 13\mathrm{H_2O}+19\mathrm{H_2O}\rightarrow\\ \rightarrow 3\mathrm{CaO}\cdot\mathrm{Al_2O_3}\cdot 3\mathrm{CaCO_3}\cdot 31\mathrm{H_2O}+\mathrm{Ca}(\mathrm{OH})_2.\end{gathered} \quad (10)$$

Then, high-calcium calcium carboaluminate hydrate can further react with tetracalcium aluminate hydrate and low-calcium calcium carboaluminate hydrate is formed.

$$\begin{gathered}3\mathrm{CaO}\cdot\mathrm{Al_2O_3}\cdot 3\mathrm{CaCO_3}\cdot 13\mathrm{H_2O}+2\left(4\mathrm{CaO}\cdot\mathrm{Al_2O_3}\cdot 13\mathrm{H_2O}\right)\rightarrow\\ \rightarrow 3\left(3\mathrm{CaO}\cdot\mathrm{Al_2O_3}\cdot\mathrm{CaCO_3}\cdot 12\mathrm{H_2O}\right)+2\mathrm{Ca}(\mathrm{OH})_2+19\mathrm{H_2O}.\end{gathered} \quad (11)$$

If equation (8) is synthesized with equation (10) and equation (11), respectively, the following equations can be gotten.

$$3CaCO_3 + 31H_2O + 3CaO \cdot Al_2O_3 \rightarrow 3CaO \cdot Al_2O_3 \cdot 3CaCO_3 \cdot 31H_2O; \tag{12}$$

$$CaCO_3 + 12H_2O + 3CaO \cdot Al_2O_3 \rightarrow 3CaO \cdot Al_2O_3 \cdot CaCO_3 \cdot 12H_2O. \tag{13}$$

It can be seen from equation (9) and equation (10) that, nano-$CaCO_3$ can react with C_3A in cement and consume some C_3A, which makes the amount of C_3A reacting with gypsum be decreased. From equation (4), equation (12) and equation (13), we can see that, C_3A can react with both sulfate and nano-$CaCO_3$, the addition of nano-$CaCO_3$ makes the amount of C_3A reacting with sulfate be reduced.

To sum up, by the addition of nano-$CaCO_3$, the amount of ettringite is cut down from two aspects. On the one hand, nano-$CaCO_3$ makes the amount of C_3A reacting with gypsum be decreased, and then the production of ettringite is reduced. On the other hand, nano-$CaCO_3$ makes the amount of C_3A reacting with sulfate be decreased, and then the production of ettringite is also reduced. Consequently, the swelling stress in concrete is reduced accordingly. In addition, the carbon aluminate formed in the process of hydration can overlap with other hydration products, which makes the internal structure of concrete denser, so the resistance of sulfate solution permeating in concrete is enhanced, and the sulfate corrosion resistance of concrete is improved.

4. Conclusions

The following conclusions can be drawn from this study.

(1) The compressive strengths of foundation concretes with nano-particles at 7d, 28d and 56d are all higher than that of plain concrete, and the addition of nano-SiO_2 and nano-$CaCO_3$ can remarkably improve the early compressive strength of concrete. With the content increase of nano-particles, the compressive strengths of concretes with nano-particles at various ages is firstly increased and then decreased. As far as the compressive strength is concerned, the optimum content of nano-SiO_2 and nano-$CaCO_3$ in concrete is about 2 % and 1 %, respectively. The compressive strengths of concretes with nano-SiO_2 at all ages is larger than that of concretes with the same content of nano-$CaCO_3$.

(2) The sulfate corrosion resistance of foundation concretes with nano-particles is superior to plain foundation concrete. With the amount increase of nano-particles, the sulfate corrosion resistance of concretes with nano-particles is also firstly enhanced and then reduced. When the content of nano-SiO_2 and nano-$CaCO_3$ is about 2 % and 1 %, respectively, the sulfate corrosion resistance of concrete is improved significantly. When the content of nano-particles is the same, the sulfate corrosion resistance of concretes with nano-SiO_2 is better than that of concretes with nano-$CaCO_3$.

(3) For the concrete with nano-particles, the corrosion resistance coefficient of compressive strength and the relative dynamic elastic modulus are all firstly increased and then decreased with the increase number of dry-wet cycles. In the early stage of erosion, the pore in concrete is filled with ettringite and gypsum, and then the corrosion resistance coefficient of compressive strength and the relative dynamic elastic modulus are increased. In the middle and later stage of erosion, more and more ettringite and gypsum are formed. With the increase of swelling stress, the concrete is gradually cracked and broken, so the corrosion resistance coefficient of compressive strength and the relative dynamic elastic modulus are decreased.

(4) With the addition of nano-particles, the pore structure of foundation concrete is improved, thus the resistance of sulphate solution permeating into concrete is increased. Moreover, nano-SiO_2 can react with $Ca(OH)_2$, and high-strength low-alkali C-S-H gel is formed; Nano-$CaCO_3$ can react with C_3A in cement, and the calcium carboaluminate hydrate is formed which is more stable and has high strength. The addition of nano-particles can not only enhance the strength of concrete but also reduce the production of ettringite and gypsum, so the swelling stress in concrete is decreased and the structural defect in concrete is cut down. Consequently, nano-particles can improve the compressive strengths and the sulfate corrosion resistance of foundation concrete.

References

1. Zhang, M., Li, H. Pore structure and chloride permeability of concrete containing nano-particles for pavement. Construction and Building Materials. 2011. 25 (2). Pp. 608–616. DOI: 10.1016/j.conbuildmat.2010.07.032
2. Potapov, V., Efimenko, Y., Fediuk, R., Gorev, D., Kozin, A., Liseitsev, Y. Modification of cement composites with hydrothermal nano-SIO_2. Journal of Materials in Civil Engineering. 2021. 33 (12). Pp. 04021339. DOI: 10.1061/(ASCE)MT.1943-5533.0003964
3. Li, H., Zhang, M., Ou, J. Abrasion resistance of concrete containing nano-particles for pavement. Wear. 2006. 260 (11-12). Pp. 1262–1266. DOI: 10.1016/j.wear.2005.08.006
4. Saleem, H., Zaidi, S.J., Alnuaimi, N.A. Recent advancements in the nanomaterial application in concrete and its ecological impact. Materials. 2021. 14(21). Pp. 6387. DOI: 10.3390/ma14216387
5. Zhang, M., Zhang, W., Sun, Y. Durability of concrete with nano-particles under combined action of carbonation and alkali silica reaction. Journal of Asian Architecture and Building Engineering. 2019. 18(5). Pp. 421–429. DOI: 10.1080/134675-81.2019.1677470

6. Li, H., Zhang, M., Ou, J. Flexural fatigue performance of concrete containing nano-particles for pavement. International Journal of Fatigue. 2007. 29 (7). Pp. 1292–1301. DOI: 10.1016/j.ijfatigue.2006.10.004
7. Li, H., Ou, J., H., Guan, X., Han, B. Nanomaterials-Enabled Multifunctional Concrete and Structures. In: Gopalakrishnan, K., Birgisson, B., Taylor, P., Attoh-Okine, N.O. (eds) Nanotechnology in Civil infrastructure. Springer, Berlin, Heidelberg. 2011. Pp. 131-173. https://doi.org/10.1007/978-3-642-16657-0_5
8. Safaei, B., Davodian, E., Fattahi, A.M., Asmael, M. Calcium carbonate nanoparticles effects on cement Plast Properties. Microsystem Technologies. 2021. 27(8). Pp. 3059–3076. DOI: 10.1007/s00542-020-05136-6
9. Zhang, M., Zhang, W., Xie, F. Experimental study on ASR performance of concrete with nano-particles. Journal of Asian Architecture and Building Engineering. 2019. 18(1). Pp. 3–9. DOI: 10.1080/13467581.2019.1582420
10. Wani, A.Y., Bhandari, M. Effect of Ground Granulated Blast Furnace Slag, Silica Fume and Nano Silica on the Strength & Durability Properties of Concrete: A Contemporary Review. IOP Conference Series: Earth and Environmental Science. Mohali, 2021. 889 p. DOI: 10.1088/1755-1315/889/1/012007
11. Zhang, M., Li, X. Sulfate corrosion resistance of foundation concrete with nano-particles under freeze-thaw cycles. Journal of natural disasters. 2018. 27 (2). Pp. 94–99. DOI: 10.13577/j.jnd.2018.0211
12. Li, X. Sulfate corrocion resistance of foundation concrete with nano-particles in freeze-thaw environment. Harbin, 2018. 24 p.
13. Li, G., Gao, Bo. Effect of NM level $CaCO_3$ on performance of the concrete in drying-wetting in corrosive environments. Journal of Chongqing Jiaotong University. 2007. 26(02). Pp. 131–135.
14. Yan, H. Experimental Study on Concrete Sulfate Attack. Journal of Shenyang Jianzhu University (Natural Science). 2012. 28(6). Pp. 1083–1088.
15. Guo, J.J., Liu, P.Q., Wu, C.L., Wang, K. Effect of dry–wet cycle periods on properties of concrete under sulfate attack. Applied Sciences. 2021. 11 (2). Pp. 1–17. DOI: 10.3390/app11020888
16. Wang, H., Dong, Y., Sun, X., Jin, W. Damage mechanism of concrete deteriorated by sulfate attack in wet-dry environment. Journal of Zhejiang University (Engineering Science). 2012. 07. Pp. 1255–1261. DOI: 10.3785/j.issn.1008-973X.2012.07.016
17. Xiong, D., Wang, S. The production process of concrete subjected to sulfate corrosion. Concrete. 2002. 04. Pp. 35–38.
18. Zhang, X. Experimental study on anti-carbonation properties of high-volume fly ash concrete. Northwest A & F University, 2010. Pp. 21–26.
19. Reis, R., Malheiro, R., Camões, A., Ribeiro, M. Carbonation resistance of high volume fly Ash Concrete. Key Engineering Materials. 2014. 634. Pp. 288–299. DOI: 10.4028/www.scientific.net/KEM.634.288
20. Pu, X., Liu, F., Wang, C., Wu, J., Wan, C. Pozzolanic reaction and enhancement effect of active mineral admixtures in high-strength and high-performance concrete. Conference proceedings about the study and engineering application technology of high-performance concrete and active mineral admixtures. 2006. Pp. 149–152.
21. Liu, J. A review of carbonation in reinforced concrete (I): Mechanism of carbonation and evaluative methods. Concrete. 2005. (11). Pp. 10–13.
22. Jedidi, M. Carbonation of reinforced concrete structures. Current Trends in Civil & Structural Engineering.2020. 5 (2). DOI: 10.33552/CTCSE.2020.05.000609
23. Isaia, G.C., Gastaldini, A.L.G., Moraes, R. Physical and pozzolanic action of mineral additions on the mechanical strength of high-performance concrete. Cement and Concrete Composites. 2003. 25(1). Pp. 69–76.
24. Li, G., Gao, B. Effect of level SiO_2 and $CaCO_3$ on concrete performance. Journal of the China railway society. 2006. 01. Pp. 131–136.
25. Feng, C., Wang, X., Zhu, J., Feng, A., Li, D. Research progress of the application of nanometer materials in concrete. Bulletin of the Chinese ceramic society. 2013.08. Pp. 1557–1561. DOI: 10.16552/j.cnki.issn1001-1625.2013.08.006
26. Tailby, J., MacKenzie, K.J.D. Structure and mechanical properties of aluminosilicate geopolymer composites with Portland cement and its constituent minerals. Cement and Concrete Research. 2010. 40 (5). Pp. 787–794. DOI: 10.1016/j.cemconres.2009.12.003
27. Gismera-Diez, S., Manchobas-Pantoja, B., Carmona-Quiroga, P.M., Blanco-Varela, M.T. Effect of $BaCO_3$ on C3A hydration. Cement and Concrete Research. 2015. 73. Pp. 70–78. DOI: 10.1016/j.cemconres.2015.03.009

Information about authors:

Maohua Zhang,
ORCID: https://orcid.org/0000-0002-6586-530X
E-mail: zmh7716@163.com

Danan Ma,
ORCID: https://orcid.org/0000-0003-4814-070X
E-mail: mn2617@nefu.edu.cn

Jia He,
ORCID: https://orcid.org/0000-0002-9132-0039
E-mail: 461104630@qq.com

Yue Han,
ORCID: https://orcid.org/0000-0002-0017-2078
E-mail: 767147252@qq.com

Received 03.01.2022. Approved after reviewing 07.12.2022. Accepted 09.12.2022.

Magazine of Civil Engineering. 2023. 119(3). Article No. 11902

Magazine of Civil Engineering

ISSN
2712-8172

journal homepage: http://engstroy.spbstu.ru/

Research article

UDC 66.067.1

DOI: 10.34910/MCE.119.2

Numerical study of the process of unsteady flow in a three-layer porous medium

R. Ravshanov [1], Z.S. Abdullaev [2], E.V. Kotov [3] ✉, Sh.N. Turkmanova [2]

[1] Research Institute for the Development of Digital Technologies and Artificial Intelligence, Tashkent, Uzbekistan

[2] Tashkent Institute of Irrigation and Agricultural Mechanization Engineers, Tashkent, Uzbekistan

[3] Peter the Great St. Petersburg Polytechnic University, St. Petersburg, Russia

✉ *ekotov.cfd@gmail.com*

Keywords: mathematical model, groundwater, groundwater, filtration, analytical solution, numerical algorithm

Abstract. The unsteady fluid flow in a three-layer porous medium is numerically investigated and is an important and topical problem. An analytical solution of the equation for the pressure fluid layer is obtained on the basis of the theory of elastic regime, taking into account the overflow from the coating and the low-permeability layer into the low-permeability bulkhead and external sources that greatly affect the liquid level change. In the main bounded aquifer only horizontal liquid migrations prevail, and in the cover and low-conductive layers only vertical migrations prevail, allowing for horizontal components of the flow rate to be omitted here. Evaporation from the surface of a liquid in a porous medium is considered. Evaporation from the surface of a liquid in a porous medium significantly affects the distribution of overflows in the layers and the distribution of the liquid level in a porous medium. Therefore, when designing vertical drains for enhanced oil recovery in multilayer reservoirs and designing fluid flows in reservoirs, evaporation must be taken into account. The computational experiments have established that the dynamics of changes in the liquid level in a porous medium depends significantly on the evaporation parameter. With an increase in its value, the liquid level in a porous medium decreases proportionally over time. The accuracy of the numerical solution using the balance equation showed that the error does not exceed 1.3%.

Funding: This work is supported by the Russian Science Foundation under grant 21-79-10283, date 29 July 2021.

Citation: Ravshanov, R. Abdullaev, Z.S., Kotov, E.V., Turkmanova, Sh.N. Numerical study of the process of unsteady flow in a three-layer porous medium. Magazine of Civil Engineering. 2023. 119(3). Article no. 11902. DOI: 10.34910/MCE.119.2

1. Introduction

The pressureless flow of fluid through a multilayer porous medium is found in many technical applications. Historically, such flows were considered concerning hydraulic structures. Later, the obtained results and approaches were applied to filter technology, chemical processes and apparatuses, oil production, climate technology, and the analysis of fluid movement in the elements of buildings and structures.

In particular, the paper [1] proposes a mathematical model and a numerical algorithm for monitoring and forecasting groundwater and surface water migrations using geofiltration models.

The problem analytical solution aims to study the interaction of surface and subsurface water flows. The paper [2] considers two-dimensional steady subsurface water flow in the vertical plane. In that article, the aquifer is idealized as an infinite band, and the channel is modeled as a horizontal equipotential function.

The article [3] proposes a mathematical model and a numerical algorithm for solving the problem of unsteady free flow of groundwater filtration considering well galleries in heterogeneous porous media where the wells differ by their hydrogeological characteristics. The authors of article have compiled an analytical solution to the specified problem to get a linearized system describing groundwater free filtration using the Laplace transform with variable t. To create isolated areas preventing the spread of harmful liquids and to protect groundwater in the interlayers, ratios to support the water heads there have been derived, as well as formulas for determining interlayer water tables in the corresponding zones of the groundwater filtration area [4].

In the article [5], the authors have developed a general mass transfer model based on the infiltration model of shore intake considering water exchange between groundwater and surface water. The mass transfer model describes the salt transfer in groundwater and the kinetics of salt exchange in dry soil. Some attention in modeling the process is paid to developing a methodology for numerical modeling of the groundwater level regime in the zones of shore intake influence. This will ensure reliable calculations when forecasting the operation of wells and estimating groundwater reserves of water intakes in difficult hydrogeological conditions. Numerical algorithms and software are developed to perform calculations on computer systems to solve inverse problems of aquifers' hydrogeological parameters and identify water exchange parameters. The general mass transfer model proposed by the authors of the articles [6, 7] will make it possible to consider the main processes comprehensively and to assess the groundwater mineralization degree and the transfer of contaminants, including hydrocarbon ones, by interacting flows of surface water and groundwater.

The article [8] deals with filtration processes: with a stationary filtration mode on an interfluvial soil body with constant levels; with a nonstationary filtration mode at backwater on an interfluvial soil body; influenced by a rise in the water level on the right border. Depression curves are made for stationary and nonstationary modes, and the correctness of computer program calculations has been proved using the Dupuit formulation. As noted in the paper, the convergence of the actual level values and the model ones has been found unsatisfactory at levels of 0.40 m and 0.25 m and when applying the stationary mode. However, should the level increase to 0.35 m, there are almost no or small discrepancies. The numerical model demonstrates how the level change rate depends on the transmissivity level: the higher the transmissivity level, the faster the stationary filtration mode starts running.

The article [9] provides the results of mathematical modeling of the water table distribution in the underflow talik depending on the intensity of water intake from wells and pits. As concluded by the article's authors on the calculation results, the selected layout of wells along the talik zone of the river and the water intake regime will provide the water volumes required for the development of the mining and processing plant. it is necessary to operate five additional production wells To ensure the estimated demand for drinking water during 2013-2017. The hydrodynamic impact of the pit on the designed water intake wells is also insignificant. By the 31st (2044) year of development, an additional drop in the water level from 0.8 m (well 42) to 8.9 m (well 127) is forecasted, which does not exceed the permissible 65 m.

A mathematical model and a numerical algorithm are developed to forecast the groundwater table on the slope of the river valley [10] To provide hydrogeological forecasts. The article's authors note that it characterizes soils' geological structure, underground flow boundary conditions, and water-conductivity parameters. Hydrogeological parameters and boundary conditions intensity degree are identified by the multivariate numerical modeling. Using the results obtained from it, water flows to drainage structures, and their dependence on technogenic infiltration have been estimated. Parameters of shallow red-brown clays are determined at which the clays promote the local rise of the groundwater level. The article considers the hydrodynamic processes in the mouth of the Temernik River on the right bank of the Don River to give detailed data on the soil body's hydrogeological structure and assess the filtration parameters and boundary conditions. The authors used the results to determine the water flow to the in-situ drainage structures in the seepage zone. In the studies performed by the authors, the method used is based on numerical hydrogeological modeling that systematically includes the interrelated geofiltration parameters and makes it possible to cover the geoecological risk factors to develop effective solutions to combat flooding.

In the paper [11], the author modeled subsurface water filtration through a homogeneous earth dam with vertical slopes on a non-conductive base. The GEO-SLOPE GeoStudio hydrodynamic calculation software package has identified the main characteristics of the filtration flow and constructed the depression curves. To confirm the adequacy of the results of the numerical calculations, the author of the work has compared them with the results calculated using a proven method; the conclusion provides recommendations for using boundary conditions to make modeling more accurate.

The paper [12] considers steady plain filtration in a rectangular dam with a partially non-conductive vertical wall during evaporation from the water table. A mixed multiparameter boundary equation has been formulated for the analytical function theory to study the evaporation effect; it was solved using the method of P.Ya. Polubarinova-Cochina. The proposed model provides the basis for an algorithm for calculating the filtration characteristics of the flow. The results of a hydrodynamic analysis of the flow rate dependencies are presented, as well as the ordinate of the point where the depression curve starts concerning all physical parameters of the scheme. The exact values of the specified characteristics are compared with the known approximate values obtained by other authors out of evaporation process conditions. The results of the study give an idea (at least a qualitative one) on the possible dependence of the migration characteristics when considering the problem of filtration to an imperfect pump well.

The article [13–14] describes a numerical study of the problems of free nonlinear filtration in a trapezoidal and rectangular soil dam with the horizontal layers of different coefficients: filtration, partial saturation zone, vertical dam core, and horizontal drain canals. A generalization to the three-dimensional case is given as well. The proposed grid calculation method can be used to conduct multifactorial studies of the environmental aspects affecting water transfer in in-situ multilayer porous media.

The article [15] compares the solutions for two methods of calculating anisotropic dam filtration; numerical experiments have been performed for several profiles of soil dams, their elements, and antifiltration devices (downstream or upstream shell, screen, and core). Further, the following methods of solving anisotropic problems have been compared: through an imitated hydrodynamic filtration grid made by stretching an orthogonal hydrodynamic grid previously constructed by the EGDA method for a distorted isotropic model of the dam; and through a finite element numerical method supported by the local variation method.

The paper [16] considers the numerical solution of the anisotropic filtration problem for the soil dam. The results of computational experiments are given that were performed on a computer when solving the filtration problem and calculating the stability of the soil dam slope taking into account the anisotropy.

In the dissertation [17], the implementation methods are developed and compared concerning one-dimensional models of water runoff along river slopes and the channel network based on the finite difference methods and the finite element method; the behavior patterns are proposed, implemented, and studied for the difference schemes of numerical integration of two-dimensional models of water runoff along the surface of slopes with a topography of different complexity; the numerical integration method has been developed and verified for equations of vertical water transfer in soils based on a four-point implicit scheme; the model of water erosion during rainfall floods is proposed and implemented, which describes the processes of drip and plane erosion and the transfer of soil particles by water flow along the surface of river slopes and the channel network. The advantages of applying finite element schemes are also demonstrated concerning real catchments; effective algorithms for its application have been developed, various methods of combining models of rainwater runoff formation at various catchment schemes are proposed.

In the dissertation [18], a steam-assisted gravity drainage model is developed for the first time taking into account the law of filtration with the ultimate pressure gradient, which allows for describing the main development stages of the steam chamber, namely, its growth to the top of the stratum, horizontal expansion, and expansion of the steam chamber towards the stratum bottom; a method has been developed for determining the anisotropic stratum filtration parameters according to vertical interference test; a mathematical model has been developed for studying the stationary fluid flow to the radial system of horizontal wells in the anisotropic stratum taking into account the influence of hydraulic pressure losses on friction in wellbores; a semi-analytical model is created to describe the process of nonstationary fluid flow to a multisectional horizontal well equipped with inflow control valves and pressure sensors in isolated sections; short-time tests are designed for vertical wells with hydraulic fracture, imperfect wells, and horizontal wells; complex transfer functions are expressed, and amplitude-frequency and phase-frequency specifications are determined for the following systems: 'porous-fractured vertical well' and 'hydraulic fracture in layer of finite conductivity.'

According to the results obtained, many conceptual mathematical and computational models have been developed to forecast the process of groundwater filtration and migration of variable-saturated liquids in multilayer porous media. In contrast to the above works, in this research, the unsteady liquid flow in a three-layer porous media considers external sources that greatly affect the liquid level change.

2. Methods

For a numerical study, specific conditions have been considered. The unsteady flow to the vertical drain canals in a three-layer boundary stratum considers evaporation from the liquid stream's upper surface and the elastic regime in a low-conductive layer. The main bounded aquifer lies under a low-conductive cover stratum and has a low-conductive layer below, facilitating its connection with the bed rock. It is assumed that the A.N. Myatiyev-G.N. Girinskii theory is true for these conditions. It should be noted that in the main bounded aquifer only horizontal liquid migrations prevail, and in the cover and low-conductive layers only vertical migrations prevail, allowing for horizontal components of the flow rate to be omitted here.

Considering the above, the continuity equation for the cover layer has the following form:

$$\frac{\partial V}{\partial z} = 0. \tag{1}$$

For this purpose, V is the vertical component of the flowrate in the porous media.

Further, applying the Darcy Law and considering the condition of the continuity of the liquid heads on the cover layer bottom, gives the following:

$$\mu_{в} \frac{\partial H_1}{\partial t} = -K_{в} \frac{H - H_1}{H_1} + q + F; \tag{2}$$

and the following equation for the bounded aquifer based on the elastic regime theory including liquid migration from the cover and low-conductive layer

$$\mu \frac{\partial H}{\partial t} = \frac{\partial}{\partial x}\left(T \frac{\partial H}{\partial x} \right) + \frac{\partial}{\partial y}\left(T \frac{\partial H}{\partial y} \right) + K_{в} \frac{H_1 - H}{H_1} - K_n \frac{\partial H_2\left(x, y, -m, t \right)}{\partial z}; \tag{3}$$

with a low-conductive dam taking into account the elastic filtration mode will be written as follows:

$$a_n \frac{\partial H_2}{\partial t} = \frac{\partial^2 H_2}{\partial z^2}. \tag{4}$$

Here, H_1 is a liquid head in the top layer; $\mu_{б}$ is a free liquid loss or lack of saturation; $K_{б}$ is a filtration coefficient in the cover layer; H is a liquid head in the intralayer; q is the total infiltration characterizing the actual infiltration and evaporation from the liquid level in a porous medium; x and y are coordinates of the horizontal plane, μ is an elastic liquid loss coefficient; F is an external source; $T = mk$ is filtration conductivity; K is a filtration coefficient; m is the thickness of the middle aquifer layer; K_n is a filtration coefficient; $H_2(x,y,z,t)$ is a liquid head in the lower layer; z is a vertical coordinate; $a_n \frac{K_n m_n}{\mu_n}$ is a piezoelectric conductivity coefficient; μ_n is an elastic liquid loss coefficient; m_n is the thickness of the low-conductive layer (Fig. 1).

3. Results and Discussion

In contrast with the study performed by F.B. Abutaliyev [19] and other authors, the external *F* source on the cover layer of the porus media was considered.

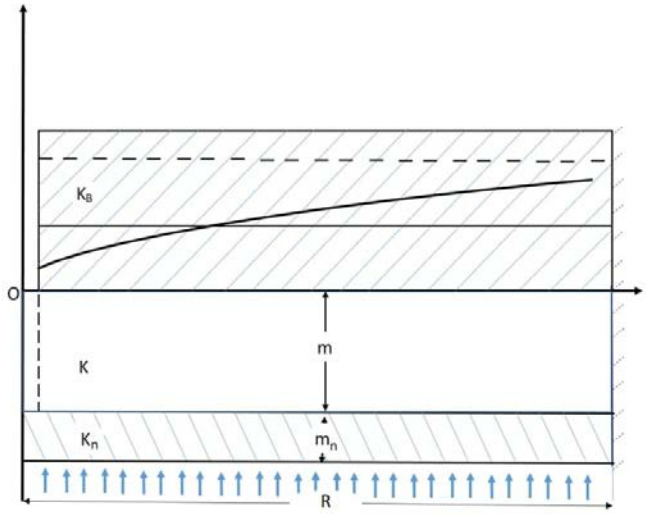

Figure 1. Schematic model of the flow in the three-layer porous medium.

Thus, the system of differential equations in partial derivatives (2)–(4) describes the flow process in a three-layer porous medium.

It should be noted that in the article [16], an analytical solution to the problem was given, with the linearization of equations (2) and (3) and condition $q = const$. However, it is necessary to emphasize that $q(x,y,H_1,t)$ is a function of coordinates x, y of the level (H_1) and time (t).

This function depends on H_1 as follows. If the liquid level in a porous medium is on the upper horizontal surface of a porous medium, then the function takes maximum values. If the liquid level in a porous medium drops below a critical depth, then the function equals zero.

This monotonically decreasing function reaches its maximum value when H_1 coincides with the upper horizontal surface of a porous medium and asymptotically tends to zero at $H_1 \rightarrow H_{kp}$, where H_{kp} is a critical value of the liquid level in a porous medium. Thus, $q \equiv 0$ below this critical depth. The value q in such assumptions denotes evaporation from the liquid level in a porous medium.

In the paper [20], the following relation is used to calculate the value q:

$$q = q_0 \left(1 - \frac{m_b - H_1}{m_b - H_{k\rho}} \right)^n . \quad (5)$$

Here, q_0 is the intensity of evaporation on the upper horizontal surface of a porous medium; H_{kp} is the critical subsurface liquid depth; n is an exponent that depends on external factors and the subsurface liquid depth.

It should be noted that, in the article [21], evaporation from the liquid level in a porous medium for a single-layer stratum model was considered at $n = 1$.

According to the study, the general case of the evaporation task in form (4) for the multilayer stratum model has no solution. It should be noted that, in general, it is difficult and rather impossible to formulate an analytical solution to the problem of unsteady filtration for the system (2)–(3). Therefore, it is advisable to apply the finite difference method to integrate the nonlinear system of equations (2)–(4), taking into account the evaporation in the form (5), and the external source F.

Let us consider the liquid flow to the vertical drainage well drilled into the main aquifer in a limited circular stratum with $r \leqslant R_k$, considering the evaporation in the form (5)

It is assumed that the well is located in the stratum center. Then, due to the flow symmetry in (2)–(4), the system of equations considering the liquid intake to the upper surface of the liquid flow:

$$F+q_0\left(1-\frac{m_b-H_1}{m_b-H_{k\rho}}\right)^n-\mu_b\frac{\partial H_1}{\partial t}=K_b\frac{H_1-H}{H_1}; \quad (6)$$

$$\frac{1}{a}\frac{\partial H}{\partial t}=\frac{1}{r}\frac{\partial}{\partial r}\left(r\frac{\partial H}{\partial r}\right)+\frac{K_b}{T}\frac{H_1-H}{H_1}-\frac{K_b}{T}\frac{\partial H_2\left(r,-m,t\right)}{\partial z}; \quad (7)$$

$$\frac{1}{a_n}\frac{\partial H_2}{\partial t}=\frac{\partial^2 H_2}{\partial z^2}. \quad (8)$$

With initial and boundary conditions based on the following:

$$H_1\left(r,0\right)=H\left(r,0\right)=H_2\left(r,z,0\right)=H_0; \quad (9)$$

$$\frac{\partial H\left(R_c,t\right)}{\partial r}=\frac{Q_c}{2\pi TR_c}; \quad (10)$$

$$\frac{\partial H\left(R_k,t\right)}{\partial r}=0; \quad (11)$$

$$H_2\left(r,-m,-m_n,t\right)=H_0; \quad (12)$$

$$H_2\left(r,-m,t\right)=H\left(z,t\right). \quad (13)$$

To integrate the system (6)–(8) numerically into the conditions (9)–(13), the nondimensional variables by the following formulas proceeded:

$$U=\frac{H_1}{H_{xa\rho}};\ V=\frac{H}{H_{xa\rho}};\ W=\frac{H_2}{H_{xa\rho}};\ s=\ell\,\mathrm{n}\frac{r}{R_k};\ z=m_b\zeta;$$

$$t=\frac{{R_k}^2}{a}\tau;\ Q=2\pi TH_{xa\rho}Q^*.$$

Together with the equations (6)–(13), the equations became as following:

$$F+P_0\left(1-\frac{1-\lambda U}{1-U_{k\rho}}\right)^n-\gamma\frac{\partial U}{\partial \tau}=\frac{U-V}{U}; \quad (14)$$

$$\frac{\partial V}{\partial \tau}=\ell^{-2s}\frac{\partial^2 V}{\partial s^2}+\alpha\frac{U-V}{U}-\beta\frac{\partial W\left(s,-\frac{m}{m_b},\tau\right)}{\partial \zeta}; \quad (15)$$

$$\delta\frac{\partial W}{\partial \tau}=\frac{\partial^2 W}{\partial \zeta}; \quad (16)$$

$$U\left(s,0\right)=V\left(s,0\right)=W\left(s,\zeta,0\right)=W_0; \quad (17)$$

$$\frac{\partial V\left(s_c,\tau\right)}{\partial s}=Q^*; \quad (18)$$

$$\frac{\partial V\left(0,\tau\right)}{\partial s}=0; \quad (19)$$

$$W\left(s,-\frac{m+m_n}{m_b},\tau\right)=W_0; \quad (20)$$

$$W\left(s,-\frac{m}{m_b},\tau\right)=V\left(s,\tau\right); \quad (21)$$

where

$$\alpha=\frac{K_bR_k{}^2}{TH_{ka\rho}};\ \ \beta=\frac{K_n}{T}\frac{R_k{}^2}{m_b};\ \gamma=\frac{a\mu_b}{K_bR_k{}^2}H_{kar};\ \delta=\frac{am_b{}^2}{a_nR_k{}^2};\ \ \lambda=\frac{H_{xa\rho}}{m_b};$$

$$\rho_0=\frac{q_0}{K_b};\ W_0=\frac{H_0}{H_{xa\rho}};\ s_c=\ell n\frac{R_c}{R_k};\ Q^*=\frac{Q}{2\pi TH_{xa\rho}}.$$

According to the analysis of material balance numerical solutions, it is found that the nondimensional spatial variable *s* must be taken in the form indicated above since only in this case, the solution outcomes in the vicinity of the well R_c are correctly considered. For example, if $s=\frac{r}{R_k}$, then the error in the balance ratio can be about 20 %.

An implicit finite difference scheme is applied to numerically solve the system of nonlinear equations (14)–(16) with additional conditions (16)–(21).

The segment (s_0, 0) was split into m equal parts with an increment of Δs. Then $s_i = s_0 + i\Delta s$, i = 0, 1, 2, …, m.

Due to condition (21), equation (16) must be solved $m-1$ time along the lines parallel to the *z*-axis passing through the points s_i, $I = 0, 1, 2, \ldots, m-1$. To solve this equation with the finite difference method, the segment

$$\left(-\frac{m}{m_b},-\frac{m+m_n}{m_b}\right)$$

is to be divided into ℓ equal segments with the points

$$\zeta_j=-\frac{m+m_n}{m_b}+j\Delta\zeta;\ j = 0, 1, 2, \ldots, l, \Delta\zeta = const.$$

The uniform time increment $\Delta\tau$ was introduced. As for the system of equations (14)–(16) with any of the spatial and temporal points $\{s_1,\zeta_j,k\Delta\tau\}$, $i = 0, 1, 2, \ldots, m-1, j = 0, 1, 2, \ldots, l-1, k = 1, 2, \ldots$, a stable implicit finite difference scheme with accuracy was compiled as follows

$$o\left[\left(\Delta s\right)^2+\left(\Delta\zeta\right)^2+\Delta\tau\right]$$

$$V_{i,k}-V_{i,k-1}=\theta\ell^{-2S_i}\left(V_{i+1,k}-2V_{i,k}+V_{i-1,k}\right)+\alpha\Delta\tau\frac{U_{i,k}-V_{i,k}}{U_{i,k}}+\frac{\beta\Delta\tau}{2\Delta\zeta}\left(-3W_{i,\ell,k}+4W_{i,\ell-1,k}-W_{i,\ell-2,k}\right); \quad (22)$$

$$W_{i,j,k}-W_{i,j,k-1}=\chi\left(W_{i,j+1,k}-2W_{i,j,k}+W_{i,j-1,k}\right); \quad (23)$$

$$\frac{\gamma}{\Delta\tau}\left(U_{i,k}-U_{i,k-1}\right)=\rho_0\left(1-\frac{1-\lambda U_{i,k}}{1-U_{k\rho}}\right)^n-\frac{U_{i,k}-V_{i,k}}{U_{i,k}}. \quad (24)$$

Here

$$\theta = \frac{\Delta\tau}{(\Delta s)^2};\ U_{i,k} = U(s_i, k\Delta\tau);\ \chi = \frac{\Delta\tau}{(\Delta\zeta)^2}$$

$$V_{i,k} = V(s_i, k\Delta\tau);\ W_{i,j,k} = W(s_i, \zeta_j, k\Delta\tau);$$

$$j = 1, 2, ..., \ell - 1,\ i = 1, 2, ..., m-1,\ k = 1, 2, ...$$

Considering (20), the equation (23) was written as follows

$$W_{i,j,k} = A_{i,j+1,k} W_{i,j+1,k} + B_{i,j+1,k}, \tag{25}$$

where the sweep coefficients are defined as follows:

$$A_{i,j+1,k} = \frac{\chi}{1 + (2 - A_{i,j,k})\chi};\ B_{i,j+1,k} = \frac{W_{i,j,k-1} + \chi B_{i,j,k}}{1 + (2 - A_{i,j,k})\chi};$$

$$A_{i,1,k} = 0;\ B_{i,1,k} = W_0;$$

$$j = 1, 2, ..., \ell - 1.$$

In the equation (22), W was substituted with its value from (25), taking into account the conditions (18) and (22), assuming $U_{i,k}$ known. The equation will be rewritten in the following form

$$V_{i,k} = C_{i+1,k} V_{i+1,k} + D_{i+1,k}. \tag{26}$$

Where

$$C_{i+1,k} = \frac{\theta \ell^{-2S_i}}{1 + (2 - C_{i,k})\theta \ell^{-2S_i} + \frac{\alpha\Delta\tau}{U_{i,k}} - \frac{\beta\Delta\tau}{2\Delta\zeta}\left[(4 - A_{i,\ell-1,k})A_{i,\ell,k} - 3\right]};$$

$$D_{i+1,k} = \frac{V_{i,k-1} + \alpha\Delta\tau + \frac{\beta\Delta\tau}{2\Delta\zeta}\left[(4 - A_{i,\ell-1,k})B_{i,\ell,k} - B_{i,\ell-1,k}\right] + \theta\ell^{-2S_i} D_{i,k}}{1 + (2 - C_{i,k})\theta \ell^{-2S_i} + \frac{\alpha\Delta\tau}{U_{i,k}} - \frac{\beta\Delta\tau}{2\Delta\zeta}\left[(4 - A_{i,\ell-1,k})A_{i,\ell,k} - 3\right]};$$

$$C_{i,k} = 1 - \frac{\ell^{2S_1}}{2\theta}\left\{1 + \frac{\alpha\Delta\tau}{U_1} - \frac{\beta\Delta\tau}{2\Delta\zeta}\left[(4 - A_{i,\ell-1,k})A_{i,\ell,k} - 3\right]\right\};$$

$$D_{1,k} = -\Delta s Q^* + \frac{\ell^{2S_1}}{2\theta}\left\{V_{i,k-1} + \alpha\Delta\tau + \frac{\beta\Delta\tau}{2\Delta\zeta}\left[(4 - A_{i,\ell-1,k})B_{i,\ell,k} - B_{i,\ell-1,k}\right]\right\};$$

$$i = 1, 2, ..., m-1.$$

Out of equation (26), considering condition (19), the formula got like this:

$$V_{m,k} = V_{m-1,k} = \frac{D_{m,k}}{1 - C_{m,k}}. \tag{27}$$

Thus, once $C_{i,k}$ and $D_{i,k}$ are calculated according to the recurrent ratios above and $V_{m-2,k}, \ldots, V_{0,k}$ is sequently determined, it will be possible to finally solve the following based on the formula (25)

$$W_{i,j,k} : W_{i,\ell,k}, ..., W_{i,1,k}.$$

It is assumed that $U_{i,k}$. Then, for example, assuming that $U_{i,k} = U_{i,k-1}$, the first approximation $V_{i,k}^{(I)} = W_{ijk}^{(I)}$ is known. The $U_{i,k}^{(I)}$ is found by substituting $V_{m,k}^{(I)}$ into equation (14) and integrating it, for example, by the Adams-Störmer method over $[(k-1)\Delta\tau,\ k\Delta\tau]$. The second approximation $V_{i,k}^{(2)}$ is determined by it substituted into (26).

The process will be finished when the following iterative process reproducibility condition is met

$$\max\left|V_{i,k}^{(p+1)}-V_{i,k}^{(p)}\right|<\varepsilon,$$

where $\varepsilon > 0$ is a small value of the calculation error.

Analysis of the numerical calculations performed according to the above algorithm demonstrates that it is advisable to apply damping according to the sequence $V_{i,k}^{(p)}$ with regard to the formula

$$V_{i,k}^{(\rho)}=\upsilon\overline{V}_{i,k}^{(\rho)}+\left(1-\upsilon\right)V_{i,k}^{(\rho-1)}, \tag{28}$$

where $\overline{V}_{i,k}^{(p)}$ is the solution of (2.33). That is, if the sequence $\overline{V}_{i,k}^{(p)}$ tends to be 'inconsistent,' the equation (28) stabilizes it.

To assess the accuracy of the numerical solution, the method of balance equations is used. This equation is deriveted as follows. The equation (7) can be written in nondimensional form

$$\xi\frac{\partial V}{\partial\tau}=\frac{\partial}{\partial\xi}\left(\xi\frac{\partial V}{\partial\xi}\right)+\alpha\rho_0\xi\left(1-\frac{1-\lambda U}{1-U_{k\rho}}\right)^n-\alpha\gamma\xi\frac{\partial U}{\partial\tau}-\beta\xi\frac{\partial W\left(\xi,-\frac{m}{m_b},\tau\right)}{\partial\xi}, \tag{29}$$

where $\xi=\dfrac{r}{R_k}$

The equation (29) is integrated throughout the pore space of the aquifer stratum. Then, due to *m* = *const*, the integrated form is as follows

$$\int_{\xi_c}^{1}\xi\frac{\partial V}{\partial\tau}d\xi=-Q^*+\alpha\rho_0\int_{\xi_c}^{1}\xi\left(1-\frac{1-\lambda U}{1-U_{k\rho}}\right)^n d\xi-\alpha\gamma\int_{\xi_c}^{1}\xi\frac{\partial W\left(\xi,-\frac{m}{m_b},\tau\right)}{\partial\xi}d\xi. \tag{30}$$

The notation was introduced:

$$V_{c\rho}\left(\tau\right)=\int_{\xi_c}^{1}\xi V\left(\xi,\tau\right)d\xi; \tag{31}$$

$$U_{c\rho}\left(\tau\right)=\int_{\xi_c}^{1}\xi U\left(\xi,\tau\right)d\xi; \tag{32}$$

Then equation (30) can be written as follows

$$\frac{dV_{c\rho}}{dt}=-Q^*+q_{ucn}\left(\tau\right)-\alpha\gamma\frac{dU_{c\rho}}{dt}-q_n. \tag{33}$$

For this purpose,

$$q_{ucn}\left(\tau\right)=\alpha\rho_0\int_{\xi_c}^{1}\xi\left(1-\frac{1-\lambda U}{1-U_{k\rho}}\right)^n d\xi; \tag{34}$$

$$q_n\left(\tau\right)=\beta\int_{\xi_c}^{1}\xi\frac{\partial W\left(\xi,-\frac{m}{m_b},\tau\right)}{\partial\xi}d\xi. \tag{35}$$

Integrating (33) by τ gives the follows

$$V_{c\rho}(\tau)=V_{c\rho}(0)-Q^{*}\tau+\int_{0}^{\tau}q_{ucn}(\tau)d\tau-\alpha\gamma\left[U_{c\rho}(\tau)-U_{c\rho}(0)\right]-\int_{0}^{\tau}q_{n}(\tau)d\tau. \qquad (36)$$

That the ratio is called the balance equation. The following is proceed to assess the accuracy of the numerical solution to this equation. The numerical solution corresponding to the moment of time (τ) is averaged by formulas (31) and (32). Then the evaporation and liquid migration is calculated by formulas (34) and (35) further substituting these values in (36). Then an approximate equation denoting the accuracy of the approximate solution averaged over the entire porous space is as follows

$$V_{c\rho}(\tau)+Q^{*}\tau+\alpha\gamma U_{c\rho}(\tau)-\int_{0}^{\tau}q_{ucn}(\tau)d\tau+\int_{0}^{\tau}q_{n}(\tau)d\tau\approx V_{c\rho}(0)-\alpha\gamma U_{c\rho}(0). \qquad (37)$$

The problem is considered with the following data to illustrate the abovementioned algorithm:

R_0 = 10 cm, R_K = 500 m, m_b = 40 m,	Q_c = 1,250 m^3/day,
m = 100 m, m_n = 10 m, H_0 = 39 m,	a = 10^6 m^2/day,
n = 0, 1, 2, 3;	a_n = 10^2 m^2/day,
q_0 = 0, 0.0036, 0.036 m/day	K = 0 m/day,
T = 10^3 m^2/day, μ_b = 0.1,	K_n = 0.01 m/day
H_{kp} = 37 m	K_b = 1 m/day

In this example, the vertical filtration coefficients vary greatly. The ratio of the filtration coefficients in the cover and high-conductive layers is $\frac{K}{K_6}=10$, while the ratio of these coefficients in the high-conductive layer and the low-conductive dam is $\frac{K}{K_6}=1,000$. Until recently, this fact suggested that low-conductive layers containing liquid are incompressible or, at best, have elastic reserves. However, it is assumed them to be completely negligible. Studies [22] have shown that layers can give a significant amount of liquid, even the low-conductive ones. The liquid saved against other reserves reduces the efficiency of vertical drain canals (wells), increasing the running time at the liquid level in a porous medium.

Figures 2–4 show the results of calculations regarding the liquid level in the cover layer for different parameters n and evaporation q_0 values. These figures illustrate how the parameter n and evaporation q_0 affect the distribution of the liquid level in a porous medium.

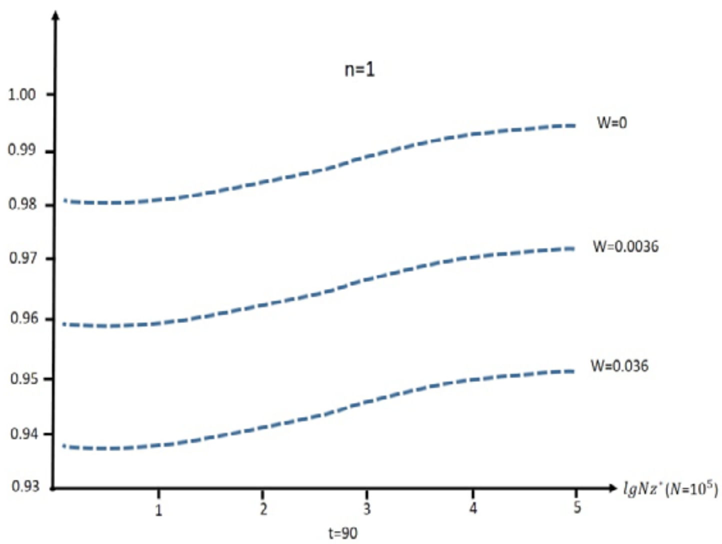

Figure 2. Change in the value of the liquid level in a porous medium at the cover layer at *n = 1* and different evaporation values *q_0*.

According to the curves in Fig. 2, the change in the liquid table value significantly depends on the evaporation value. As the evaporation value increases, the liquid level in a porous medium drops proportionally over time.

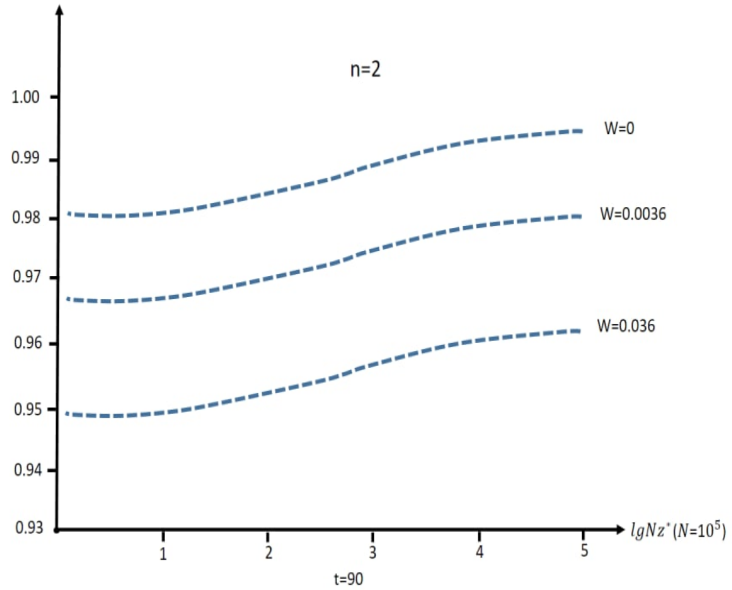

Figure 3. Change in the value of the liquid level in a porous medium in the cover layer at *n = 2* and different evaporation values *q_0*.

According to the numerical calculations obtained and the curves in Fig. 3 and 4, it can be seen that the change in the value of the liquid level in a porous medium also depends on the change in the parameter *n*. As it increases, the liquid level in a porous medium drop at different evaporation values [23].

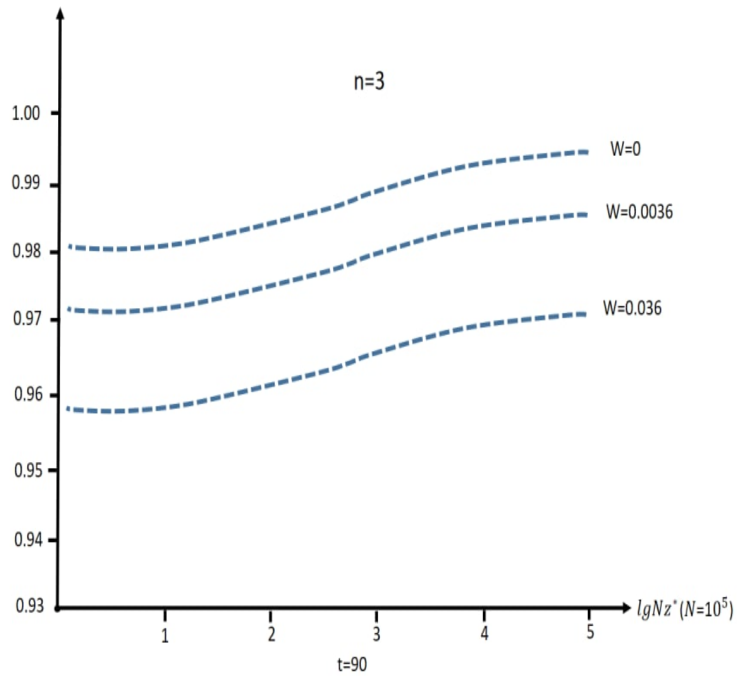

Figure 4. Change in the value of the liquid level in a porous medium in the cover layer at *n = 3* and different evaporation values *q_0*.

Fig. 5–7 represent flow curves reduced to an area unit with a cover layer and a low-conductive layer for different evaporation parameters q_0 and *n* values. Liquid migrations depend on evaporation parameters.

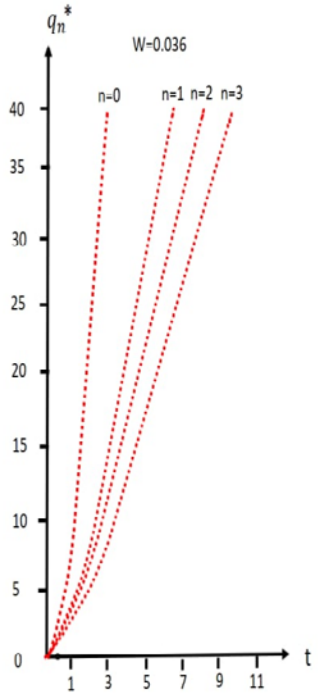

Figure 5. Flow curves reduced to an area unit with a cover and low-conductive layers at q_0 = 0.036.

Fig. 2–7 conclude that evaporation from the liquid level in a porous medium significantly affects the liquid migration distribution in the layers and the liquid level in a porous medium distribution. Thus, one must consider evaporation when designing pumped-well drain canals in multilayer medium to improve lands and study liquid flows in layers.

The paper verified the accuracy of the numerical solution according to the balance equation. It appears that the error margin is limited by 1.3 %.

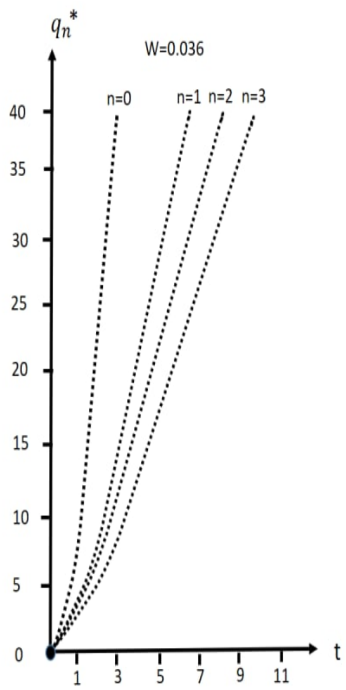

Figure 6. Flow curves reduced to an area unit with a cover and low-conductive layers at q_0 = 0.0036.

4. Conclusions

The computational experiments have established that the dynamics of changes in the liquid level in a porous medium depends significantly on the evaporation parameter. With an increase in its value, the liquid level in a porous medium decreases proportionally over time.

An analysis of the obtained numerical calculations showed that the change in the liquid level in a porous medium depends significantly on the parameter n. As its value increases, the liquid level in the porous medium decreases at different values of the evaporation parameter.

The analyzing results of numerical calculations show that evaporation from the surface of a liquid in a porous medium significantly affects the distribution of overflows in the layers and the distribution of the liquid level in a porous medium. Therefore, when designing vertical drains to improve fluid selection in multilayer reservoirs and designing liquid flows in layers, it is essential to take into account evaporation.

Checking the accuracy of the numerical solution using the balance equation showed that the error does not exceed 1.3 %.

References

1. Tskhay A.A., Koshelev, K.B., Kim, N.Yu. Model vzaimodeystviya podzemnykh i poverkhnostnykh vod dlya sistemy podderzhki prinyatiya resheniy [Model of interaction between ground and surface waters for a decision support system]. Informatsionnyye sistemy v ekonomike, ekologii i obrazovanii. Barnaul: Izd-vo AltGTU, 2002. Pp. 39–41. (rus)
2. Anderson E.I. An analytical solution representing groundwater–surface water interaction. Water Resource. Res. 2003. 39(3). P. 1071. DOI:10.1029/2002WR001536
3. Ravshanov, N., Kodirov, K. Modeling of the process of free water filtration of groundwater based on the availability of gallery of wells. Problems of Computational and Applied Mathematics. 2016. 2. Pp. 33–46
4. Ravshanov, N. Abdullaev, Z., Khafizov, O. Modeling the Filtration of Groundwater in Multilayer Porous Media. Construction of Unique Buildings and Structures. 2020. 92. Article No. 9206/ISSN 2304-6295. DOI: 10.18720/CUBS.92.6
5. Kashevarov, A.A. Matematicheskoye modelirovaniye kachestva podzemnykh vod v zonakh vliyaniya beregovykh infiltratsionnykh vodozaborov [Mathematical modeling of groundwater quality in the zones of influence of coastal infiltration water intakes] [Online]. URL: https://www.rfbr.ru/rffi/ru/project_search/o_238194 (date of application: 03.12.2022).
6. Ravshanov, N., Daliev, S., Abdullaev, Z., Khafizov, O. Ground and confined underground waters and their salt content. International Conference on Information Science and Communications Technologies, ICISCT 2020. 2020. 9351467. DOI: 10.1109/ICISCT50599.2020.9351467
7. Ravshanov, N., Daliev, Sh., Abdullaev, Z., Khafizov, O. Ground and confined underground waters and their salt content. IOP Conference Series: Materials Science and Engineering. 2020. 896(1). 012047. DOI 10.1088/1757-899X/896/1/012047
8. Belov, K.V., Lisenkov, A.B., Ponomarev, A.D., Gorbatenko, N.S. Study of fluid filtration in a porous medium using physical and numerical modeling. Bulletin of the Tomsk Polytechnic University. Geo Assets Engineering. 2017. 328(8). Pp. 64–74
9. Buyskikh, A.A., Basistyy, V.A. Evaluation by the method of mathematical modelinof the exploitation resources of underground waters of the gold ore deposit. Tekhnologii tekhnosfernoy bezopasnosti. 2010. 6(34). (rus)
10. Gridnevskiy, A.V. Numerical simulation of the filtration process in the right-bank of the river Don for protection the buildings against rise of groundwater in the city of Rostov-on-Don. Geology and Geophysics of Russian South. 2019. 9(1). Pp. 150–163. (rus)
11. Shalanin, V.A., Patlaĭ, K.I. Numerical simulation of the groundwater filtration process through a rectangular dam of homogeneous soil on a waterproof base. FEFU: School of engineering bulletin. 2019. 2/39. DOI: 10.24866/2227-6858/2019-2-13 (rus)
12. Bereslavskiy, E.N., Dudina, L.M. Problem of filtration in a rectangular web with a partially impenetrable vertical wall. Vestnik of Saint Petersburg University. Mathematics. Mechanics. Astronomy. 2019. 6(2). Pp. 288–297. DOI: 10.21638/11701/spbu01.2019.211 (rus)
13. Sheshukov, Ye.G., Kurtseva, K.P. Chislennoye issledovaniye krayevykh zadach nelineynoy filtratsii [Numerical investigation of boundary problems of nonlinear filtration]. Power engineering: research, equipment, technology. 2012. 9-10. Pp. 158–166. (rus)
14. Kurtseva, K.P., Lapin, A.V., Sheshukov, Ye.G. Resheniye setochnymi metodami zadachi filtratsii zhidkosti v plotine pri nelineynom zakone filtratsii [Solution by grid methods of the problem of fluid filtration in a dam with a nonlinear filtration law]. Izvestiya vuzov. Matematika. 1995. 2. Pp. 47–52. (rus)
15. Aniskin, A.N., Memarianfard, M.Ye. Chislennoye modelirovaniye anizotropnoy filtratsii v gruntovykh plotinakh [Numerical simulation of anisotropic filtration in ground dams]. Vestnik MGSU. 2009. 4. Pp. 219–224. (rus)
16. Aniskin, N.A., Memarianfard, M.Ye. Uchet anizotropii v filtratsionnykh raschetakh i raschetakh ustoychivosti otkosov gruntovykh plotin [Accounting for anisotropy in filtration calculations and calculations of slope stability of soil dams]. Vestnik MGSU. 2010. 4. Pp. 388–398. (rus)
17. Demidov V. N Chislennoye modelirovaniye protsessov formirovaniya dozhdevogo stoka [Numerical modeling of rain runoff formation processes]. Doctor thesis. Moscow, 2007. (rus)
18. Morozov P Ye Metody resheniya pryamykh i obratnykh zadach podzemnoy termogidrodinamiki [Methods for solving direct and inverse problems of underground thermohydrodynamics].Moscow, 2022. (rus)
19. Abutaliyev, F.B., Abutaliyev, E.B. Metody resheniya zadach podzemnoy gidromekhaniki na EVM [Methods for solving problems of underground hydromechanics on a computer]. Tashkent: Izd-vo “Fan”, 1968. 196 p.
20. Averyanov, S.F. Fil'tratsiya iz kanalov i yeye vliyaniye na rezhim gruntovykh vod [Filtration from canals and its impact on the groundwater regime]. Moscow: Kolos, 1956. 237 p.
21. Porubarinova-Kochinav, P.Ya. Teoriya dvizheniya gruntovykh vod [Theory of groundwater movement]. Moscow: Nauka, 1977. 664 p. (rus)
22. Khantush, M.S. Novoye o teorii peretikaniya [New about the theory of poking]. Voprosy gidrogeologicheskikh raschetov. Moscow: Mir, 1964. Pp. 43–60. (rus)

23. Ravshanov, N., Abdullaev, Z., Aminov, S., Khafizov, O. Numerical study of fluid filtration in three-layer interacting pressure porous formations. E3S Web of Conferences. 2021. 264. 01018. DOI: 10.1051/e3sconf/202126401018

Information about authors:

Normahmad Ravshanov,
E-mail: ravshanxade-09@mail.ru

Zafar Abdullaev, *PhD in Physics and Mathematics,*
ORCID: https://orcid.org/0000-0003-1351-7861
E-mail: abdullaevv.zafar@gmail.com

Evgeny Kotov,
E-mail: ekotov.cfd@gmail.com

Shodiya Turkmanova,
ORCID: https://orcid.org/0000-0003-0521-6882
E-mail: turkmanovashodiya@gmail.com

Received 04.12.2022. Approved after reviewing 26.12.2022. Accepted 26.02.2023.

Magazine of Civil Engineering. 2023. 119(3). Article No. 11903

ок

Magazine of Civil Engineering

ISSN 2712-8172

journal homepage: http://engstroy.spbstu.ru/

Research article

UDC 624.35:531.391.3

DOI: 10.34910/MCE.119.3

Hexagonal rod pyramid: deformations and natural oscillation frequency

M.N. Kirsanov ✉

National Research University "Moscow Power Engineering Institute", Moscow, Russia

✉ *c216@ya.ru*

Keywords: spatial truss, hexagonal dome, natural vibrations, lower frequency bound, upper frequency bound, Dunkerley method, Rayleigh method, Maple, induction

Abstract. A new scheme of a statically determinate dome truss is proposed. The purpose of the study is to obtain exact formulas for structural deflections under a uniform load and to find upper and lower analytical estimates of the first frequency of natural oscillations depending on the number of panels, sizes, and masses concentrated in the truss nodes. Calculation of forces in the truss rods is performed by cutting nodes. The system of equations in projections on the coordinate axes, compiled in the Maple software, includes the forces in the rods and the reactions of vertical supports located along two contours of the structure at the base. The amount of deflection and stiffness of the entire truss is calculated using the Mohr integral. To determine the lower estimate of the first frequency an approximate Dunkerley method is used. The formula for the upper limit of the first frequency is derived by the Rayleigh energy method. In the Rayleigh method, the shape of the deflection from the action of a uniformly distributed load is taken as the deflection of the truss. Displacements of loads are assumed to be only vertical. The overall dependence of the solution on the number of panels is obtained by induction on a series of solutions for trusses with a successively increasing number of panels. The operators of the Maple system of symbolic mathematics are used. Based on the calculation results, it was concluded that the distribution of forces over the structure rods does not depend on the number of panels. Asymptotes were found on the graphs of the obtained analytical dependences of the deflection on the number of panels for different truss heights. The estimates of the first natural frequency are compared with the numerical solution obtained from the analysis of the natural frequency spectrum. The coefficients of the frequency equation are found using the eigenvalue search operators in the Maple system. It is shown that the lower analytical estimate based on the calculation of partial frequencies differs from the numerical solution by no more than 54 %, and the upper estimate by the Rayleigh method has an error of about 2 %. The formula for the lower Dunkerley frequency estimate is simpler than the Rayleigh estimate.

Funding: This work was financially supported by the Russian Science Foundation 22-21-00473.

Citation: Kirsanov, M.N. Hexagonal rod pyramid: deformations and natural oscillation frequency. Magazine of Civil Engineering. 2023. 119(3). Article no. 11903. DOI: 10.34910/MCE.119.3

1. Introduction

The study of the stress state, deformations, and stability of spatial multifaceted dome structures are of both practical and theoretical interest [1, 2]. In the calculations of building structures of this type, as a rule, the finite element method is used [3, 4]. Regular (with periodic structure elements) statically determinate truss schemes are quite rare. The search for such schemes was even called "hunting" by R.G. Hutchinson and N.A. Fleck [3, 4]. One of the advantages of regular schemes [5] is that for them it is possible to analytically derive the dependences of the characteristics of the stress-strain state on their order (the number of periodicity elements, for example, the number of panels). To search for analytical solutions in the form of compact formulas, operators of symbolic mathematics, such as Maple, Mathematica [6], and others, are applicable. To obtain analytical solutions in the form of closed formulas, when modeling structures, it is necessary to make some simplifications. The construction must be statically determined. If at the same time it is regular, then for such a design it is possible to obtain calculation formulas for an arbitrary number of repeating elements. Regular trusses are, for example, planar or spatial trusses with identical panels or groups of panels. In this case, the analytical solution has a great advantage over the numerical one, not only due to the saving of computation time but also due to the fundamental possibility to calculate the truss with a very large number of panels without a loss of accuracy. A larger number of elements causes the inevitable effect of accumulation of rounding errors in the numerical calculation. Analytical solutions are especially effective for preliminary draft calculations, for assessing the accuracy of numerical solutions, and in truss optimization problems.

Analytical solutions for building structures do not always lead to the final compact design formula. In such works, an algorithm for calculations in the system of symbolic mathematics is given [7, 8]. The purpose of this work is to obtain formulas for calculating deflections and estimates of the first natural frequency of a three-dimensional truss. Most often, to solve such problems for planar [9–13], and three-dimensional [14] trusses, the induction method is used. Solutions of problems on the deformation of some planar arch trusses [15] with an arbitrary number of panels are obtained inductively and some problems on natural frequencies of regular structures are solved [16–19]. Calculation formulas for deflections and oscillation frequencies of spatial regular trusses were obtained in [20].

In the analytical form, it is impossible to obtain a solution directly from the analysis of the entire frequency spectrum in the general case.

Therefore, to estimate its lower limit of the first (lowest) frequency of natural oscillations, we will use the Dunkerley method [21–23], and for the upper one, the Rayleigh method [24, 25]. These approximate methods are based on the calculation of partial frequencies, for which it is not necessary to compose high-order characteristic polynomials (in terms of the number of degrees of freedom).

Pyramidal trusses are studied in connection with the design of structural panels (composite) in which the trusses act as a kind of reinforcement. Hexagonal trusses are also used in mesh coatings [26, 27]. Eccentrically braced frames and beam-type spatial trusses were studied numerically and experimentally in [28]. An overview of analytical solutions for planar statically determinate regular trusses is given in [29].

In this paper, we propose a new scheme of a statically determinate dome-type hexagonal spatial truss. The truss has architectural expressiveness and can be used in public buildings (circus, airport building, railway station, etc.).

The construction can be used as a basis for complicated statically indeterminate systems of this type.

2. Methods

2.1. The truss scheme

The truss in the form of a regular pyramid $2h_1 + h_2$ high with a hexagonal base side na contains $n_s = 36n - 15$ rods, including $6n$ vertical support posts h_1 high located along the outer contour of the structure and $6(n-2)$ posts $2h_1$ high supporting the upper contour (Fig. 1, 2). There are no posts in the corner nodes D of the upper contour. A similar hexagonal cover, but with a dome attached to the corner points of the outer (upper) contour, is considered in [30].

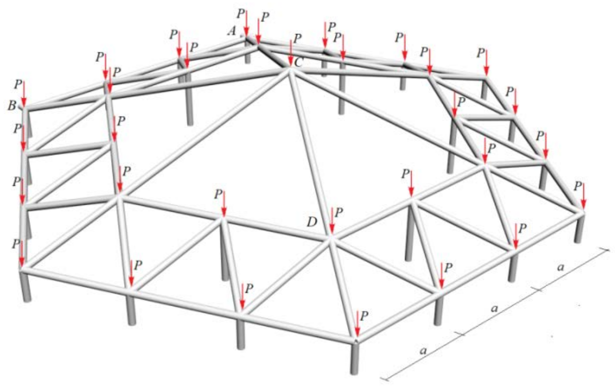

Figure 1. Truss scheme, *n* = 3, vertical load.

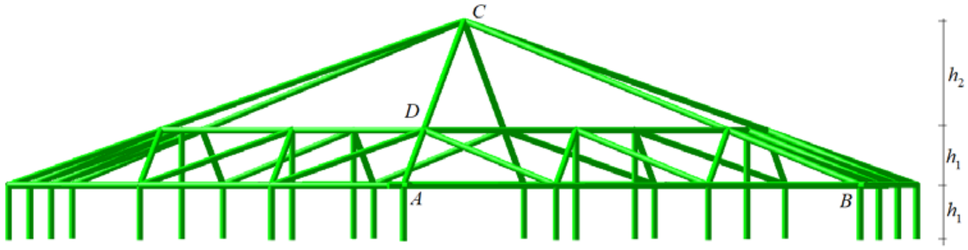

Figure 2. The truss dimensions, *n* = 3.

The lower horizontal rod contour consists of $6n$ rods of length a, the upper one consists of $6(n-1)$ similar rods. The braces connecting the contours have a length of $c=\sqrt{a^2+h^2}$. The lengths of six identical braces emanating from vertex C depend on the number of panels: $(n-1)c.$ Corner node A rests on a spherical support hinge, modeled by three mutually perpendicular rods, one of which is a vertical post. Node B is a cylindrical hinge corresponding to two support bars. The following ratios of sizes are chosen: $h_1=h,\ \ h_2=(n-1)h.$ All connections of the truss rods are hinged. An analytical calculation of the deformations of a spatial coating with a similar structure was performed in [20]. In [31] an optimization problem is solved for an irregular spatial truss of 25 rods.

Calculation of forces in rods in symbolic form is performed based on a program written in the language of computer mathematics Maple [32]. To do this, we introduce the coordinates of the nodes (Fig. 3), using the annular periodic structure of the truss:

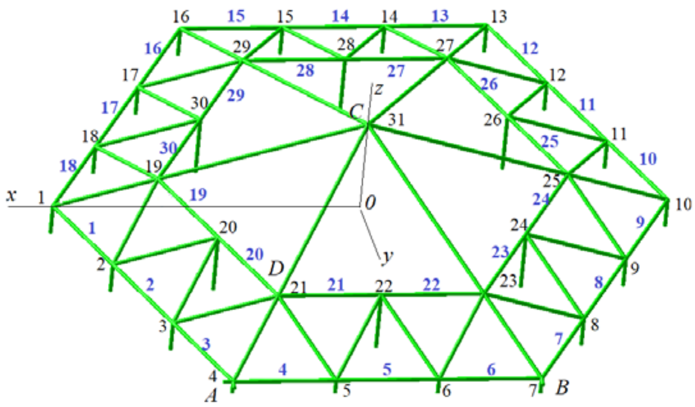

Figure 3. Numbers of nodes and rods of contours *n* = 3.

The coordinates of the nodes of the lower contour look like this:

$$x_{i+jn}=L\cos\phi-a(i-1)\cos\beta,$$
$$y_{i+jn}=L\sin\phi+a(i-1)\sin\beta,$$
$$z_{i+jn}=0,\ i=1,..,n,\ j=0,..,5,$$

where $L=na,\ \ \phi=j\pi/3,\ \ \beta=\pi/3-\phi.$

The coordinates of the nodes of the smaller (upper) contour:

$$x_{i+j(n-1)+6n}=(L-a)\cos\phi-a(i-1)\cos\beta,$$
$$y_{i+j(n-1)+6n}=(L-a)\sin\phi+a(i-1)\sin\beta,$$
$$z_{i+j(n-1)+6n}=h,\ \ i=1,...,n-1,\ \ j=0,...,5.$$

Vertex C coordinates: $x_{12n-5}=y_{12n-5}=0,\ z_{12n-5}=h_1+h_2.$

The order of connecting the bars of the lattice is entered into the program using ordered lists Φ_i, $i=1,..,n_s$. of numbers of the ends of the corresponding bars, similar to how graphs are given in discrete mathematics. For example, the bars of the lower chord are encoded with the following vertex lists $\Phi_i=[i,\ i+1],\ i=1,..,6n-1, \Phi_{3n}=[6n,1]$.

Upper chord bar code:
$\Phi_{i+6n}=[i+6n,\ i+6n+1],\ i=1,\ ...,\ 6n-7,\ \ \Phi_{12n-6}=[12n-6,\ 6n+1]$.

The numbers of ends and other rods are set similarly.

2.2. Calculation of forces in bars

Let us represent the system of equilibrium equations of nodes in the projection on the coordinate axes in matrix form $\mathbf{GS}=\mathbf{\Psi}$, where $\mathbf{S}$ is the vector of unknown forces, including the reactions of the supports, $\mathbf{G}$ is the matrix of coefficients (projections of unit forces in the rods), $\mathbf{\Psi}$ is the vector of loads on the nodes. For each node in the matrix, three rows are assigned, corresponding to projections onto three coordinate axes. Similarly, in the elements of the load vector of the form Ψ_{3i-2}, where i is the number of the node, the loads on node i in the projection on the x-axis are written. Elements Ψ_{3i-1} contain projections of external forces in projection onto the y-axis. Vertical loads on nodes are recorded in elements Ψ_{3i}.

Matrix $\mathbf{G}$ elements are calculated according to the data on the structure of the connection of the bars and the coordinates of the nodes

$$g_{x,i}=\left(x_{\Phi_{i,1}}-x_{\Phi_{i,2}}\right)/l_i,\quad g_{y,i}=\left(y_{\Phi_{i,1}}-y_{\Phi_{i,2}}\right)/l_i,$$
$$g_{z,i}=\left(z_{\Phi_{i,1}}-z_{\Phi_{i,2}}\right)/l_i,\quad i=1,...,n_s+3,$$

where $l_i=\sqrt{l_{x,i}^2+l_{y,i}^2+l_{z,i}^2}$ is the length of the rod *i*. The number of rods also includes three horizontal support rods at angles A and B. The matrix of coefficients of equilibrium equations in projections is filled in rows. Every three lines correspond to the projection equations on the x, y, and z axes, respectively:

$$G_{3\Phi_{i,1}-2,i}=g_{x,i},\ G_{3\Phi_{i,1}-1,i}=g_{y,i},\ \ G_{3\Phi_{i,1},i}=g_{z,i},$$
$$G_{3\Phi_{i,2}-2,i}=-g_{x,i},\ G_{3\Phi_{i,2}-1,i}=-g_{y,i},\ G_{3\Phi_{i,2},i}=-g_{z,i}.$$

If a uniform vertical load is applied to the truss nodes (Fig. 1), then the non-zero elements of the load vector have the form: $\Psi_{3i}=P,\quad i=1,...,12n-5$. Numerical calculation of forces for a structure with $n=3,\ a=5.0\,\text{m},\ h=1.0\,\text{m}$ gives a picture of the distribution of forces shown in Fig. 4. Compressed rods are highlighted in blue, tension rods are highlighted in red. The thickness of the line is greater, the greater the modulus of force in the corresponding rod. The force value is related to the value of the nodal load P with an accuracy of two significant digits.

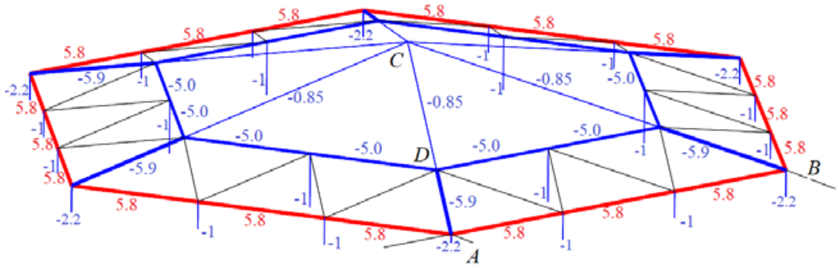

Figure 4. Distribution of forces in the rods, n = 3, a = 5.0 m, h = 1.0 m.

The upper contour of the truss under such a load is compressed, the lower one is stretched. The braces connecting the contours have zero forces. An interesting feature of the stressed state of the truss was noticed. The patterns of distribution of forces in the rods from a uniform load for trusses of different orders are similar. The order of the truss is equal to the number of rods in the side edge of the lower contour. The compressive forces in the rods of the upper contour for any n are equal to

$$S_i = -aP/h,\ i = 6n+1,...,12n-6. \tag{1}$$

The greatest tensile forces are observed in the lower belt

$$S_i = 7aP/(6h),\ i = 1,...,6n. \tag{2}$$

The six lower corner ribs are most compressed

$$S_i = -7Pc/(6h),\ \ i = 12n-5,...,17n-5. \tag{3}$$

The forces in the six upper rods of the dome, connected at the top $C,$ are equal to $-Pc/(6h).$ The forces in the six corner support posts do not depend on the dimensions of the structure: $-13P/6.$ The reactions of the supports of the intermediate posts along the outer (lower) and inner (upper) contours are equal to $P.$

2.3. Deflection

The formula for the dependence of the deflection of the top C on the dimensions of the structure, the load, and the number of panels will be obtained by induction. Under the deflection Δ_n we mean the vertical displacement of the node C of the truss of order $n.$ To calculate the deflection value, we use the Mohr integral

$$\Delta_n = \sum_{j=1}^{n_S} \frac{S_j s_j l_j}{EF}, \tag{4}$$

where l_j is the length of the rod, S_j is the force in the *j*th rod from the action of the load, s_j is the force in the rod from the action of a single vertical force applied to the vertex $C,$ E is the modulus of elasticity of the rods, F is the cross-sectional area. The summation is carried out over all the bars of the structure. The elastic moduli and cross-sectional areas are the same for all rods. Sequential calculation of the deflection of a series of trusses with an increasing number of panels gives the following results

$$\Delta_2 = P\left(14a^3 + 8c^3 + 13h^3\right)/\left(6h^2EF\right),$$
$$\Delta_3 = P\left(21a^3 + 9c^3 + 13h^3\right)/\left(6h^2EF\right),$$
$$\Delta_4 = P\left(28a^3 + 10c^3 + 13h^3\right)/\left(6h^2EF\right),$$
$$\Delta_5 = P\left(35a^3 + 11c^3 + 13h^3\right)/\left(6h^2EF\right),$$
$$\Delta_6 = P\left(42a^3 + 12c^3 + 13h^3\right)/\left(6h^2EF\right).$$

In the general case, we have the form of a formula for the deflection:

$$\Delta_n = P\left(C_1a^3 + C_2c^3 + C_3h^3\right)/\left(h^2EF\right). \tag{5}$$

The coefficients in this expression are functions of the number of panels $n.$ The common members of the sequences they form can be found using the special operators *rsolve* and *rgf_findrecur* from the Maple system. Equally effective in finding common members of sequences are the operators of the Mathematica computer mathematics system. The common terms of the sequences of coefficients at $n = 2,3,...,7$ are linear concerning n

$$C_1 = 7n/6,\ \ C_2 = (n+6)/6,\ \ C_3 = 13/3. \tag{6}$$

Compared to similar well-known solutions for planar trusses, which have a shape that is non-linear in terms of the number of panels, the solution turned out to be much more compact. In part, this can be explained by the observed feature of the stress state of the structure, which does not depend on the number of panels. The same simple solution is obtained in the problem of the deflection of node D at the corner (not supported) point of the upper contour. The coefficients in (5) in this case have the form

$$C_1=(13n-6)/27, \quad C_2=7/6, \quad C_3=13/6. \tag{7}$$

Let us plot the solution graphs (5), (6). Let us denote the total load on the truss $P_{sum}=P(12n-5)$ and the length of the outer side of the cover $L=na$. Let us introduce the designation for the dimensionless deflection: $\Delta'=\Delta_n EF/(P_{sum}L)$. The graphs of the curves of solutions (6) and (7) at $L=50$ m show that in this setting the dimensionless deflection at points C and D decreases monotonically with an increase in the number of panels (Fig. 5).

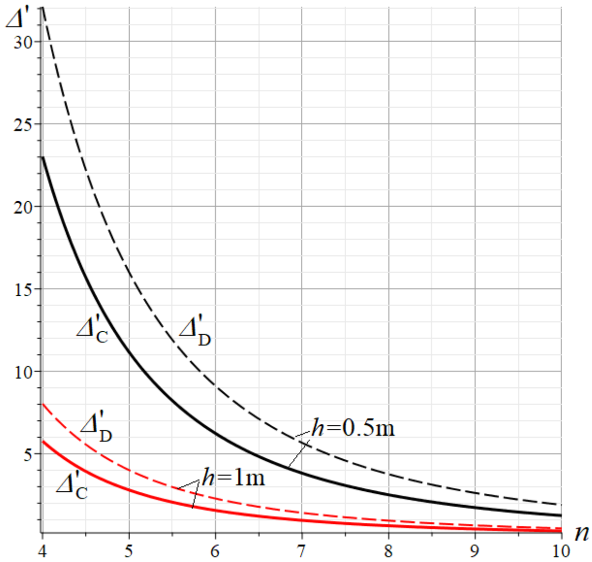

Figure 5. Dependence of dimensionless deflection of top C and node D on the number of panels.

For small n, the deflection of the non-supported node D is one and a half times greater than the deflection of the vertex C. Horizontal asymptotes of the solutions (ultimate deflection) are noted. Using the analytical form of the solution, using the operators of the Maple system, we obtain the lower limits of the relative deflections: $\lim\limits_{n\to\infty}\Delta'_C=h/(72L)$, $\lim\limits_{n\to\infty}\Delta'_D=0$. It follows that curves Δ'_D and Δ'_C must intersect. Calculations show that the intersection of the curves for the height $h=1.0$ m occurs at $n=76$ and for $h=0.5$m at $n=151$.

In practice, there are problems about the deflection of a structure under the action of a load on only part of its surface. This corresponds, for example, to a snow load applied to one half of the roof (Fig. 6). The derivation of the formula in this case is no different from the previous tasks. The form of the solution obtained by induction on eight girders with a successively increasing number of panels on one edge coincides with solution (5). The coefficients look like:

$$C_1=5n/6, \quad C_2=(4+n)/6, \quad C_3=3/2.$$

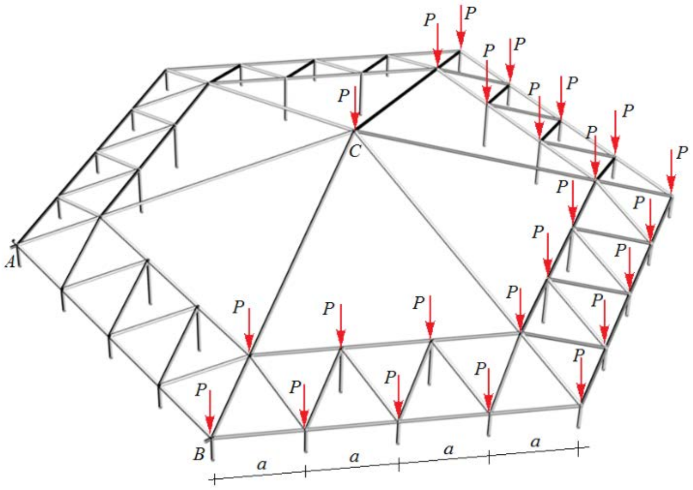

Figure 6. Vertical load on half of the truss surface, *n* = 4.

2.4. Natural oscillation frequency

The calculation of the first (lowest) frequency of natural oscillations is included in most dynamic calculations of the structure and is of independent interest. In addition to the direct calculation of the spectrum of natural frequencies, which is performed numerically [33–35], there are also known approximate methods for obtaining its upper and lower estimates of the first natural oscillation frequency [21–25]. These methods are based on the calculation of partial frequencies, the values of which can be found analytically. For regular constructions, analytical estimates can be generalized to an arbitrary number of panels using the [16] induction method.

The inertial properties of the truss are modeled by concentrated masses in the nodes. In the simplest setting, the masses of loads m are the same. Only vertical vibrations of nodes are considered. The number of degrees of freedom of the truss weight system of order n is equal to the number of nodes $K = 12n - 5.$

The dynamics of the system is described by a system of differential equations for the movement of goods in matrix form:

$$\mathbf{M}_K \ddot{\mathbf{Z}} + \mathbf{D}_K \mathbf{Z} = 0, \tag{8}$$

where $\mathbf{D}_K$ is the structural stiffness matrix, $\mathbf{Z}$ is the vector of vertical displacements of masses 1,..., K, $\mathbf{M}_K$ is the inertia matrix of size $K \times K,$ $\ddot{\mathbf{Z}}$ is the acceleration vector. The inertia matrix is proportional to the identity matrix $\mathbf{M}_K = m\mathbf{I}_K$ if the masses are the same. The elements of the compliance matrix $\mathbf{B}_K,$ which is the inverse of the stiffness matrix $\mathbf{D}_K,$ can be found using the Mohr integral

$$b_{i,j} = \sum_{\alpha=1}^{n_S} S_\alpha^{(i)} S_\alpha^{(j)} l_\alpha \Big/ (EF), \tag{9}$$

where $S_\alpha^{(i)}$ is the force in the rod α from the action of a unit vertical force at node $i.$ The problem can be reduced to the problem of matrix eigenvalues $\mathbf{B}_K.$ To do this, we multiply (8) from the left by $\mathbf{B}_K$ and, taking into account the replacement $\ddot{\mathbf{Z}} = -\omega^2 \mathbf{Z},$ which is valid for harmonic oscillations of the form

$$z_i = u_i \sin(\omega t + \varphi_0) \tag{10}$$

we obtain $\mathbf{B}_K \mathbf{Z} = \lambda \mathbf{Z},$ where $\lambda = 1/(m\omega^2)$ is the eigenvalue of the matrix $\mathbf{B}_K,$ ω is the natural frequency of oscillations.

From here we obtain the calculation formula for the frequency $\omega = \sqrt{1/(m\lambda)}.$

The forces $S_\alpha^{(i)}$ in the truss rods included in the elements of the matrix $\mathbf{B}_K$ are determined by solving the system of equations of the truss nodes, which also includes the reactions of the supports.

Consider approximate methods that give upper and lower estimates of the first frequency.

2.5. Energy method. Top rating

The Rayleigh formula, which follows from the equality of the maximum values of the kinetic and potential energies, has the form:

$$T_{\max} = \Pi_{\max}. \tag{11}$$

The kinetic energy of a system consisting of K identical masses m located at the nodes of the structure has the form: $T = \sum_{i=1}^{K} m v_i^2 \Big/ 2.$

The vertical velocity v_i of the mass *i* according to (7) has the form: $v_i = \dot{z}_i = \omega u_i \sin\left(\omega t + \varphi_0\right).$

The maximum kinetic energy corresponds to equality $\max\left(\sin\left(\omega t + \varphi_0\right)\right) = 1.$ From here we get:

$$T_{\max} = \omega^2 m \sum_{i=1}^{K} u_i^2 \Big/ 2, \tag{12}$$

where the amplitude of the vertical displacement is calculated using the Mohr integral:

$$u_i = \sum_{\alpha=1}^{n_s} S_\alpha^{(P)} \tilde{S}_\alpha^{(i)} l_\alpha / (EF) = P \sum_{\alpha=1}^{n_s} \tilde{S}_\alpha^{(P)} \tilde{S}_\alpha^{(i)} l_\alpha / (EF) = P\tilde{u}_i \ .$$

The previous designations are used: $S_\alpha^{(P)}$ is force in the rod $\alpha = 1, ..., n_s$ from the action of the load $P,$ uniformly distributed over the nodes, $\tilde{S}_\alpha^{(i)}$ is force in the same rod from a single (dimensionless) load applied to the mass with number $i,$ $\tilde{S}_\alpha^{(P)} = S_\alpha^{(P)} \big/ P.$ The choice of a uniformly distributed load is determined by the proximity of the shape corresponding deflection to the form of vibrations of the system of weights with the first frequency. Thus, (12) takes the form:

$$T_{\max} = P^2 \omega^2 \sum_{i=1}^{K} m \tilde{u}_i^2 / 2, \tag{13}$$

where $\tilde{u}_i = u_i / P = \sum_{\alpha=1}^{n_S} \tilde{S}_\alpha^{(P)} \tilde{S}_\alpha^{(i)} l_\alpha \Big/ \left(EF\right)$ is amplitude of displacements of the mass with number i under the action of a distributed load, referred to the value of $P.$ The potential energy of deformation of the truss rods has the form:

$$\Pi_{\max} = \sum_{\alpha=1}^{n_S} S_\alpha^{(P)} \Delta l_\alpha \Big/ 2 = \sum_{\alpha=1}^{n_S} \left(S_\alpha^{(P)}\right)^2 l_\alpha \Big/ \left(2EF\right).$$

Due to the linearity of the problem concerning loads, we have $S_\alpha^{(P)} = P \sum_{i=1}^{N} \tilde{S}_\alpha^{(i)}.$ From here we get:

$$\begin{aligned} \Pi_{\max} &= P^2 \sum_{\alpha=1}^{n_S} \tilde{S}_\alpha^{(P)} \sum_{i=1}^{K} \tilde{S}_\alpha^{(i)} l_\alpha \Big/ \left(2EF\right) = \\ &= P^2 \sum_{i=1}^{K} \sum_{\alpha}^{n_S} \tilde{S}_\alpha^{(P)} \tilde{S}_\alpha^{(i)} l_\alpha \Big/ \left(2EF\right) = P^2 \sum_{i=1}^{N} \tilde{u}_i \Big/ 2. \end{aligned} \tag{14}$$

From (11), (13), (14) we obtain a formula for the upper estimate of the first oscillation frequency of the truss (the Rayleigh formula):

$$\omega_R^2 = \sum_{i=1}^{K} \tilde{u}_i \Bigg/ \sum_{i=1}^{K} m\tilde{u}_i^2. \tag{15}$$

We find the displacements $\tilde{u}_i$ as functions of n. We generalize the solution obtained for a different number of panels concerning n. Consider the sums $\sum\limits_{i=1}^{K} \tilde{u}_i$ and $\sum\limits_{i=1}^{K} \tilde{u}_i^2$ separately.

The calculation of displacement for trusses with the different number of panels shows that the form of the solution $\sum\limits_{i=1}^{K} \tilde{u}_i$ does not depend on n. Note that irregular trusses do not have this property. The numerator in (15) can be represented as:

$$\sum_{i=1}^{K} \tilde{u}_i = \left(C_a a^3 + C_c c^3 + C_h h^3\right) \Big/ \left(h^2 EF\right),$$

or in a more compact form

$$\sum_{i=1}^{K} \tilde{u}_i = \sum_{\alpha=[a,c,h]} mC_\alpha \alpha^3 \Big/ \left(h^2 EF\right), \tag{16}$$

where the coefficients C_a, C_c, C_h are obtained by induction, generalizing a series of solutions for different n:

$$n = 2, \quad \sum_{i=1}^{K} \tilde{u}_i = \left(134a^3 + 50c^3 + 205h^3\right) \Big/ \left(6h^2 EF\right),$$
$$n = 3, \quad \sum_{i=1}^{K} \tilde{u}_i = \left(219a^3 + 51c^3 + 313h^3\right) \Big/ \left(6h^2 EF\right),$$
$$n = 4, \quad \sum_{i=1}^{K} \tilde{u}_i = \left(304a^3 + 52c^3 + 421h^3\right) \Big/ \left(6h^2 EF\right),$$
$$n = 5, \quad \sum_{i=1}^{K} \tilde{u}_i = \left(389a^3 + 53c^3 + 529h^3\right) \Big/ \left(6h^2 EF\right),$$
$$n = 6, \quad \sum_{i=1}^{K} \tilde{u}_i = \left(474a^3 + 54c^3 + 637h^3\right) \Big/ \left(6h^2 EF\right), \ldots$$

As a result, we have the coefficients

$$C_a = \left(85n - 36\right), \quad C_c = \left(n + 48\right)/6, \quad C_h = \left(108n - 11\right)/6. \tag{17}$$

The denominator (15) has a more complex form:

$$\sum_{k=1}^{N} m\tilde{u}_k^2 = \sum_{\alpha,\beta=[a,c,h]} mC_{\alpha\beta} \alpha^3 \beta^3 \Big/ \left(h^4 E^2 F^2\right), \tag{18}$$

where

$$C_{aa} = (1063n^2 - 936n + 216)/36,$$
$$C_{cc} = \left(n^2 + 12n + 330\right)\Big/36,$$
$$C_{hh} = \left(1080n + 253\right)\Big/36,$$
$$C_{ac} = \left(7n^2 + 588n - 252\right)\Big/36, \tag{19}$$
$$C_{ah} = \left(1105n - 468\right)\Big/36,$$
$$C_{\mathrm{ch}} = \left(13n + 624\right)\Big/36.$$

Thus, the upper estimate of the first frequency of the truss, depending on the number of panels, can be obtained by the formula:

$$\omega_R = h\sqrt{\frac{EF \sum\limits_{\alpha=[a,c,h]} C_\alpha \alpha^3}{m \sum\limits_{\alpha,\beta=[a,c,h]} C_{\alpha\beta}\alpha^3\beta^3}} \tag{20}$$

with coefficients (17), (19) depending only on the construction order n.

2.6. Dunkerley score

We obtain a lower estimate of the first frequency of oscillations using the Dunkerley formula:

$$\omega_D^{-2} = \sum_{i=1}^{K} \omega_i^{-2}, \tag{21}$$

where ω_i is the oscillation frequency of one mass m located at node i. To calculate the partial frequencies ω_i, we compose equation (8) in the scalar form:

$$m\ddot{z}_i + D_i z_i = 0,$$

where D_i is the scalar stiffness coefficient (i is the mass number). The frequency of vibrations of the load is $\omega_i = \sqrt{D_i/m}$. The stiffness coefficient, the reciprocal of the compliance coefficient, is determined by the Mohr integral (4):

$$\delta_i = 1/D_i = \sum_{\alpha=1}^{n_S}\left(\tilde{S}_\alpha^{(i)}\right)^2 l_\alpha \Big/ \left(EF\right).$$

Arguing in the same way as when calculating the frequencies of a system with many degrees of freedom, we obtain

$$\omega_D^{-2} = \sum_{i=1}^{K}\omega_i^{-2} = m\sum_{i=1}^{K}\frac{1}{D_i} = m\sum_{i=1}^{K}\delta_i =$$
$$= m\sum_{i=1}^{K}\sum_{\alpha=1}^{n_S}\left(\tilde{S}_\alpha^{(i)}\right)^2 l_\alpha \Big/ \left(EF\right) = m\Sigma_n \Big/ \left(h^2 EF\right). \tag{22}$$

Let us successively calculate the sums $\Sigma_n = h^2\sum_{i=1}^{K}\sum_{\alpha=1}^{n_S}\left(\tilde{S}_\alpha^{(i)}\right)^2 l_\alpha$ for n = 2, 3, 4, ...

$$\sum_2 = \frac{94a^3 + 154c^3 + 173h^3}{12},$$
$$\sum_3 = \frac{279a^3 + 231c^3 + 601h^3}{18},$$
$$\sum_4 = \frac{1124a^3 + 584c^3 + 2495h^3}{48},$$
$$\sum_5 = \frac{4715a^3 + 1739c^3 + 10555h^3}{150},...$$

Let us calculate the common terms of the sequences of coefficients in these expressions.

We get $\sum_n = \sum_{\alpha=[a,c,h]} r_\alpha \alpha^3$, where

$$r_a = \left(49n^2 - 60n + 18\right) / (6n),$$
$$r_c = \left(n^3 + 36n^2 + 186n - 216\right) / \left(6n^2\right), \tag{23}$$
$$r_h = \left(108n^3 - 107n^2 - 60n + 30\right) / \left(6n^2\right).$$

When deriving expressions for the coefficients (23), the operators for compiling and solving the recursive equations of the Maple system were used. Some complication was the dependence on n not only of the numerators of the sequence members but also of their denominators. Maple system operators are adapted to define common members of such sequences. The result in the form of expressions (23) was obtained only because it was possible to guess the form of the denominators.

Thus, we obtain the lower estimate for the first frequency according to Dunkerley:

$$\omega_D = h\sqrt{\frac{EF}{m \sum_{\alpha=[a,c,h]} r_\alpha \alpha^3}}. \tag{24}$$

The form of the Dunkerley estimate (24) almost coincides with formula (20) obtained by the Rayleigh method, but formula (24) is much simpler. The desired coefficients are contained here only in the denominator.

3. Results and Discussion

To estimate the error of the estimates found, consider an example of a truss with n panels for $a = 6.0$ m and $h = 1.0$ m. The stiffness of the steel rods of the truss will be taken $EF = 1.8 \cdot 10^5$ kN. Fig. 7 plots the dependences of the upper estimate of the first frequency ω_R of natural oscillations of the truss (20), obtained by the Rayleigh energy method, ω_D the Dunkerley estimate (24), and the numerical solution ω_1, found as the minimum frequency of the entire frequency spectrum.

The numerical value of the lowest natural frequency ω_1 of a system with $K = 12n - 5$ degrees of freedom is so close to the Rayleigh estimate that for $n > 3$ the curves merge. To refine the error estimates, we introduce the relative values $\varepsilon_D = |\omega_D - \omega_1| / \omega_1$, $\varepsilon_R = |\omega_R - \omega_1| / \omega_1$.

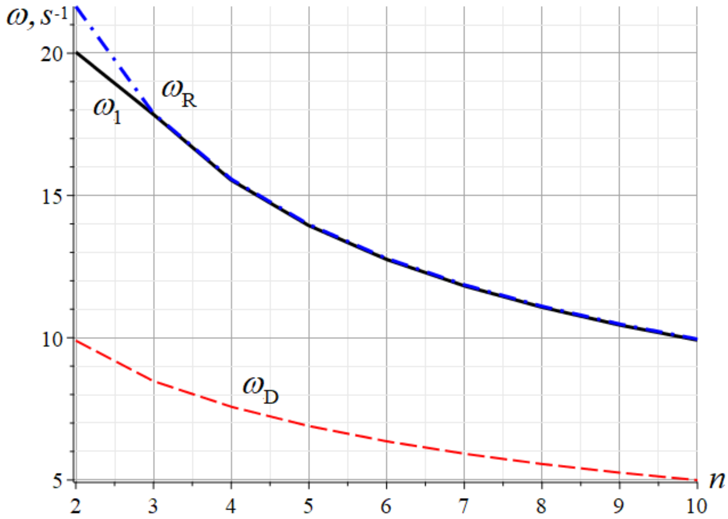

Figure. 7. The first oscillation frequency obtained in three ways.

Depending on the number of panels, the error of the Dunkerley solution is relatively large (Fig. 8), but it changes little, increasing sharply only at $n=3$. The Rayleigh estimate error (Fig. 9) is very small and, in principle, it can be neglected, considering the analytical solution (20) to be exact.

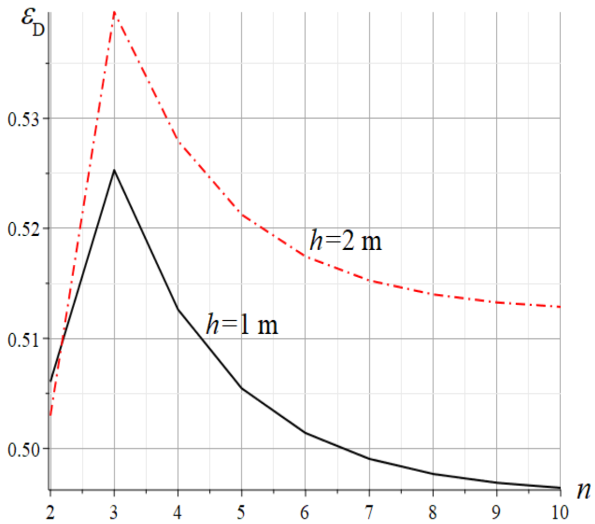

Figure 8. Dunkerley's estimation.

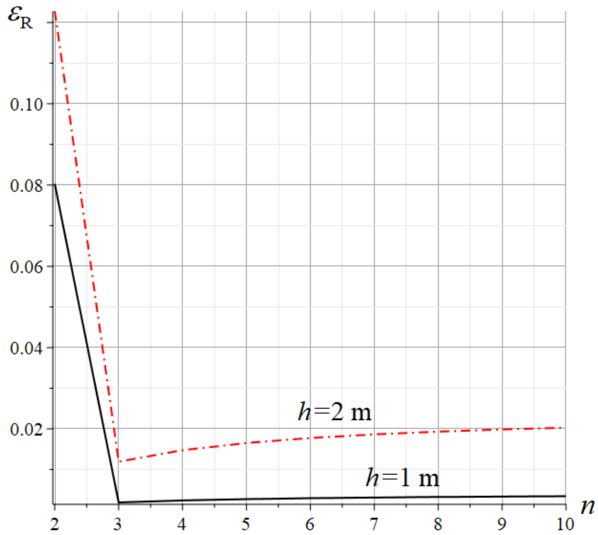

Figure 9. Rayleigh estimation.

With an increase in the number of panels up to a certain number *n*, the Dunkerley estimate error slightly decreases, and then, starting from $n=12$ at $h=2\,\mathrm{m}$, it grows a little.

The error in the Rayleigh estimate increases slightly while remaining very small. The error of both methods increases with the height of the truss.

3.1. Discussion

A new scheme of a statically determined truss of a three-dimensional hexagonal cover is proposed. The truss can only partly be considered regular. It has only a regular base with two hexagonal horizontal contours, while the upper part has the shape of a regular hexagonal pyramid of rods connected at the vertex C. Despite this, the inductive method using a computer mathematics system made it possible to obtain analytical exact solutions for the deflections of its characteristic peaks and a two-sided estimate of the first frequency.

The design under consideration can be used in coverings of public buildings and structures of a large span, for example, arenas, buildings of stations and airports, circuses.

The external static indeterminacy, which means that the reactions of the supports can only be found from the solution of the joint system of equilibrium equations for all nodes simultaneously with the forces in the rods, did not complicate the solution. On the contrary, some obtained formulas turned out to be linear in the number of panels, which distinguishes this solution from similar formulas even for planar trusses. This is largely due to the property of the truss itself. An important property of similarity of the stressed states of trusses of various orders is noticed. The calculation showed that the pattern of force distribution over the structure rods does not depend on the number of panels. When n changes, the forces in the chords do not change, the formulas for the forces (1) – (3) and the reactions of the supports do not contain the number of panels n.

Comparison with the numerical solution of the complete problem of oscillations of a mass system with many degrees of freedom confirmed the well-known fact [16] that the Rayleigh formula for the upper estimate gives much greater accuracy than the Dunkerley method for the lower estimate of the first frequency.

4. Conclusion

Main results of the work:

1. A scheme of a spatial statically determinate rod structure of the dome type has been developed. Analytical solutions for deflection are obtained for both symmetrical and asymmetric loads. The truss design does not contain a central support post and can be used in large-span structures without central supports.

2. The calculation showed that the pattern of force distribution over the structure rods does not depend on the number of panels.

3. Formulas are derived both for the deflections of the truss and the boundaries of its first frequency of natural oscillations for an arbitrary number of panels. The obtained estimate of the first frequency from above has very high accuracy. Formulas can be used to evaluate numerical solutions for a very large number of panels, that is, precisely in those cases where the accumulation of calculation errors in numerical form is most likely.

4. The closed analytical form of the obtained formulas allows the use of mathematical analysis tools to identify their features and to search for combinations of design parameters that are optimal in terms of strength, rigidity, or stability.

References

1. Kobielak, S., Zamiar, Z. Oval concrete domes. Archives of Civil and Mechanical Engineering. 2017. 17 (3). Pp. 486–501. DOI: 10.1016/J.ACME.2016.11.009
2. Rezaiee-Pajand, M., Rajabzadeh-Safaei, N. Exact post-buckling analysis of planar and space trusses. Engineering Structures. 2020. 223. Pp. 111146. DOI: 10.1016/J.ENGSTRUCT.2020.111146
3. Hutchinson, R.G., Fleck, N.A. Microarchitectured cellular solids – The hunt for statically determinate periodic trusses. ZAMM Zeitschrift fur Angewandte Mathematik und Mechanik. 2005. 85 (9). Pp. 607–617. DOI: 10.1002/zamm.200410208
4. Hutchinson, R.G., Fleck, N.A. The structural performance of the periodic truss. Journal of the Mechanics and Physics of Solids. 2006. 54 (4). Pp. 756–782. DOI: 10.1016/j.jmps.2005.10.008
5. Zok, F.W., Latture, R.M., Begley, M.R. Periodic truss structures. Journal of the Mechanics and Physics of Solids. 2016. 96. Pp. 184–203. DOI: 10.1016/j.jmps.2016.07.007.
6. Zotos, K. Performance comparison of Maple and Mathematica. Applied Mathematics and Computation. 2007. 188 (2). Pp. 1426–1429. DOI: 10.1016/j.amc.2006.11.008
7. Goloskokov, D.P., Matrosov, A.V. A Superposition Method in the Analysis of an Isotropic Rectangle. Applied Mathematical Sciences. 2016. 10 (54). DOI: 10.12988/ams.2016.67211. (date of application: 17.06.2020).
8. Goloskokov, D.P., Matrosov, A.V. Comparison of two analytical approaches to the analysis of grillages. 2015 International Conference on “Stability and Control Processes” in Memory of V.I. Zubov, SCP 2015 – Proceedings. 2015. Pp. 382–385. DOI: 10.1109/SCP.2015.7342169
9. Rakhmatulina, A.R., Smirnova, A.A. The dependence of the deflection of the arched truss loaded on the upper belt, on the number of panels. Science Almanace. 2017. 28 (2–3). Pp. 268–271. DOI: 10.17117/na.2017.02.03.268. (date of application: 9.05.2021).
10. Kitaev, S.S. Derivation of the formula for the deflection of a cantilevered truss with a rectangular diagonal grid in the computer mathematics system Maple. Postulat. 2018. 5–1. Pp. 43. URL: http://e-postulat.ru/index.php/Postulat/article/view/1477 (date of application: 3.03.2021).
11. Ilyushin, A. The formula for calculating the deflection of a compound externally statically indeterminate frame. Structural mechanics and structures. 2019. 3 (22). Pp. 29–38. URL: https://www.elibrary.ru/download/elibrary_41201106_54181191.pdf
12. Arutyunyan, V.B. Calculation of the deflection of a statically indeterminate beam truss. Postulat. 2018. 6(6). URL: http://vuz.exponenta.ru/1/ar18.pdf (date of application: 26.02.2021).
13. Dai, Q. Analytical Dependence of Planar Truss Deformations on the Number of Panels. AlfaBuild. 2021. 17. Pp. 1701. DOI: 10.34910/ALF.17.1
14. Kirsanov, M.N., Zaborskaya, N. Deformations of the periodic truss with diagonal lattice. Magazine of Civil Engineering. 2017. 71(3). DOI: 10.18720/MCE.71.7
15. Voropay, R., Domanov, E. Analytical solution of the problem of shifting a movable support of a truss of arch type in the Maple system. Postulat. 2019. 1. URL: http://vuz.exponenta.ru/1/vd.pdf (date of application: 27.02.2021).

16. Vorobev, O.V. Bilateral Analytical Estimation of the First Frequency of a Plane Truss. Construction of Unique Buildings and Structures. 2020. 92 (7). Pp. 9204–9204. DOI: 10.18720/CUBS.92.4. URL: https://unistroy.spbstu.ru/article/2020.92.4 (date of application: 27.02.2021).
17. Petrenko, V.F. The natural frequency of a two-span truss. AlfaBuild. 2021. (20). Pp. 2001. DOI: 10.34910/ALF.20.1
18. Vorobyev, O. About methods of obtaining analytical solution for eigenfrequencies problem of trusses. Structural mechanics and structures. 2020. 1 (24). Pp. 25–38. URL: http://vuz.exponenta.ru/PDF/NAUKA/elibrary_42591122_21834695.pdf
19. Kirsanov, M., Safronov, V. Analytical estimation of the first natural frequency and analysis of a planar regular truss oscillation spectrum. Magazine of Civil Engineering. 2022. 111 (3). DOI: 10.34910/MCE.111.14
20. Kirsanov, M. Deformations And Spatial Structure Vibrations Frequency of The Rectangular Contour Type Cover: Analytical Solutions. AlfaBuild. 2021. 98. Pp. 9805. DOI: 10.4123/CUBS.98.5
21. Low, K.H. A modified Dunkerley formula for eigenfrequencies of beams carrying concentrated masses. International Journal of Mechanical Sciences. 2000. 42(7). Pp. 1287–1305. DOI: 10.1016/S0020-7403(99)00049-1
22. Trainor, P.G.S., Shah, A.H., Popplewell, N. Estimating the fundamental natural frequency of towers by Dunkerley's method. Journal of Sound and Vibration. 1986. 109(2). Pp. 285–292. DOI: 10.1016/S0022-460X(86)80009-8
23. Levy, C. An iterative technique based on the Dunkerley method for determining the natural frequencies of vibrating systems. Journal of Sound and Vibration. 1991. 150(1). Pp. 111–118. DOI: 10.1016/0022-460X(91)90405-9
24. Mochida, Y., Ilanko, S. On the Rayleigh-Ritz Method, Gorman's Superposition Method and the exact Dynamic Stiffness Method for vibration and stability analysis of continuous systems. Thin-Walled Structures. 2021. 161. Pp. 107470. DOI: 10.1016/j.tws.2021.107470
25. Low, K.H. Natural frequencies of a beam-mass system in transverse vibration: Rayleigh estimation versus eigenanalysis solutions. International Journal of Mechanical Sciences. 2003. 45 (6–7). Pp. 981–993. DOI: 10.1016/j.ijmecsci.2003.09.009
26. Clough, E.C., Ensberg, J., Eckel, Z.C., Ro, C.J., Schaedler, T.A. Mechanical performance of hollow tetrahedral truss cores. International Journal of Solids and Structures. 2016. 91. Pp. 115–126. DOI: 10.1016/J.IJSOLSTR.2016.04.006
27. Kang, K.J. Wire-woven cellular metals: The present and future. Progress in Materials Science. 2015. 69. Pp. 213–307. DOI: 10.1016/J.PMATSCI.2014.11.003
28. Haji, M., Azarhomayun, F., Azad, A.R.G. Numerical investigation of truss-shaped braces in eccentrically braced steel frames. Magazine of Civil Engineering. 2021. 102(2). DOI: 10.34910/MCE.102.8
29. Tinkov, D.V. The optimum geometry of the flat diagonal truss taking into account the linear creep. Magazine of Civil Engineering. 2016. 61(1). Pp. 25–32. DOI: 10.5862/MCE.61.3
30. Kirsanov, M. Model of a spatial dome cover. Deformations and oscillation frequency. Construction of Unique Buildings and Structures. 2022. 99 Article No 9904. DOI: 10.4123/CUBS.99.4
31. Bekdaş, G., Yucel, M., Nigdeli, S.M. Evaluation of metaheuristic-based methods for optimization of truss structures via various algorithms and lèvy flight modification. Buildings. 2021. 11(2). Pp. 1–25. DOI: 10.3390/BUILDINGS11020049
32. Buka-Vaivade, K., Kirsanov, M.N., Serdjuks, D.O. Calculation of deformations of a cantilever-frame planar truss model with an arbitrary number of panels. Vestnik MGSU. 2020. (4). Pp. 510–517. DOI: 10.22227/1997-0935.2020.4.510-517
33. Siriguleng, B., Zhang, W., Liu, T., Liu, Y.Z. Vibration modal experiments and modal interactions of a large space deployable antenna with carbon fiber material and ring-truss structure. Engineering Structures. 2020. 207. Pp. 109932. DOI: 10.1016/J.ENGSTRUCT.2019.109932
34. Liang, L., Li, X., Sun, Y., Gong, Z., Bi, R. Measurement research on vibro-acoustic characteristics of large-span plate-truss composite bridge in urban rail transit. Applied Acoustics. 2022. 187. Pp. 108518. DOI: 10.1016/J.APACOUST.2021.108518
35. Vo, N.H., Pham, T.M., Bi, K., Hao, H. Model for analytical investigation on meta-lattice truss for low-frequency spatial wave manipulation. Wave Motion. 2021. 103. Pp. 102735. DOI: 10.1016/J.WAVEMOTI.2021.102735

Information about author:

Mikhail Kirsanov, *Doctor of Physics and Mathematics*
ORCID: https://orcid.org/0000-0002-8588-3871
E-mail: c216@ya.ru

Received 18.02.2022. Approved after reviewing 07.12.2022. Accepted 07.12.2022.

Magazine of Civil Engineering

ISSN 2712-8172

journal homepage: http://engstroy.spbstu.ru/

Research article

UDC 624.046.3

DOI: 10.34910/MCE.119.4

Numerical buckling calculation method for composite rods with semi-rigid ties

E.V. Popov ✉, ***B.V. Labudin***, ***A.Y. Konovalov***, ***A.V. Karelskiy***, ***V.V. Sopilov***, ***A.V. Bobyleva***, ***D.A. Stolypin***

Northern (Arctic) Federal University named after M.V. Lomonosov, Arkhangelsk, Russia

✉ *EPV1989@yandex.ru*

Keywords: composite structures, semi-rigid connections, buckling, numerical methods, nonlinear analysis, experimental study, shear stiffness

Abstract. Research object: composite centrally-compressed structures with semi-rigid nonlinearly deformable connections, which are put into operation at the very beginning of loading the element. Research goal: development of a numerical method for calculating the strength and stability of compressed composite rods, which takes into account the nonlinear deformation of shear bonds, the shear stiffness coefficient of which has the form of a functional dependence and is equal to the angle of inclination of the tangent drawn to the experimental load–strain curve (T–δ) at the point with a given shear force T. Methods: the method of solving the problem consists in dividing the component element into separate sections, compiling a system of equations describing the increment of contiguous fibers in the shear seams. The load is applied in steps, after the next step the total shear forces in the bonds are determined and the stiffness coefficients for the next calculation step are clarified; at each step, the system is “probing” for the possibility of loss of stability. The resulting value of the critical force is compared with the sum of all load steps applied at this stage of the calculation, the calculation stops when the specified calculation accuracy is reached. If necessary, to obtain the resulting values, the received forces in the bonds and the normal stresses in the branches of the component structure are summed up. Results: the calculation of a three-layer timber pillar is presented. The pillar is reinforced with side overlays fastened using nonlinear-compliant shear bonds. The results of linear and nonlinear calculations are compared for different values of the stiffness coefficient of the bonds. The possible calculation error with the normative value of the stiffness coefficient is established.

Funding: This research work was supported by the Northern (Arctic) Federal University named after M.V. Lomonosov, Arkhangelsk, Russian Federation.

Citation: Popov, E.V., Labudin, B.V., Konovalov, A.Y., Karelskiy, A.V., Sopilov, V.V., Bobyleva, A.V., Stolypin, D.A. Numerical buckling calculation method for composite rods with semi-rigid ties. Magazine of Civil Engineering. 2023. 119(3). Article no. 11904. DOI: 10.34910/MCE.119.4

1. *Introduction*

Timber and timber-composite products serve as the starting material for the manufacture of various building structures. This is because such structures have high architectural merit, are reliable, strong, durable and virtually light. They are economical, resistant to aggressive environments. In many countries of the world, there is a huge renewable raw material base for the manufacture of such structures. The use of timber in the construction of public, industrial, agricultural, and multi-storey residential and warehouse frame buildings is becoming increasingly popular. The main load-bearing elements of such buildings are, as a rule, timber or timber composite columns, the calculation and design of which are discussed in a number of works by domestic and foreign scientists.

Paper [1] presents the results of a monitoring case study on a tall timber–hybrid building in Switzerland, a 15 storey, and 60 m high office building completed in 2019. A fibre–optic measuring system showed an increase of the deformation with increasing load during the construction phase of highly stressed spruce–GLT and beech–LVL columns. However, the highest strain values were not reported in the columns themselves but at the ceiling transitions and in the area near their supports.

In [2, 3] the strength and stability of timber columns with steel cores of various configurations under central compression is studied. In studies [4, 5] are considered columns with a timber core, covered with a steel shell of round and square cross-section. Article [6] steel-wood-concrete columns with a double steel shell and various configurations of the location of the placeholder relative to the cross section of the element are investigated.

A steel–timber axial compressed composite (STC) column made of H-shaped steel and glulam is proposed in paper [7].

A novel L-shaped steel-timber composites column, fabricated using STC (L-STC), which are used in the construction of large-span structures and multistory buildings under concentric loading, was proposed in paper [8].

The objective of study [9] is to establish a theoretical calculation model for this type of retrofitted splice columns. Firstly, a theoretical model for the axial compressive strength of splice columns retrofitted with a steel jacket is proposed considering the contact stresses at a splice joint and the relevant stability theory. Secondly, the buckling modes of splice columns and the actual stress distributions at the splice joints are thoroughly investigated. Finally, the theoretical model is confirmed by the experimental data and the results of finite element analysis with different splice parameters.

In [10] various performance improvement techniques have been used for enhancing the strength parameters in long columns made from a timber specie (Poplar) found in abundance in the Kashmir region of India. Poplar used in the cross-laminated form with different binding/wrapping techniques viz. bolted, wrapped cold steel, single helix carbon fiber reinforced polymer (FRP), and double helix carbon FRP wrapping, have been fabricated and tested.

The work [11] investigated the different axial compression behaviors of cross–laminated timber columns (CLTCs) and control glued–laminated timber columns (GLTCs). The average compression modulus of elasticity (MOE) and strength values of the CLTCs were lower than those of the control GLTCs and appeared to be dependent on the area ratio in the axial direction. The column length had different effects on the compression behaviors of CLTCs and GLTCs, and compared with the GLTCs, the CLTCs exhibited enhanced ductility and energy absorption properties due to the cross–lamination.

A number of new design developments [12, 13] made it possible to design columns with a rigid joint in the reference section.

Despite extensive research in the field of calculations, design and testing of component timber and timber composite columns, all of them apply only to such structures with rigid shear bonds between the constituent layers. There are no studies on the assessment of the sustainability of such structures in the presence of nonlinear compliance of discrete bonds. In some cases, for example, in centrally compressed two-layer component columns, shear bonds are put into operation only at the moment of loss of stability, which is due to the appearance of a bending moment from the action of a longitudinal compressive force during creep. For such elements, the stability calculation can be carried out taking into account the initial stiffness modulus of compliant joints. For the three-layer component elements presented in Fig. 1, a characteristic feature will be the occurrence of forces in shear bonds already at the very beginning of loading, since due to the work of shear bonds, the load is redistributed between the central and peripheral layers.

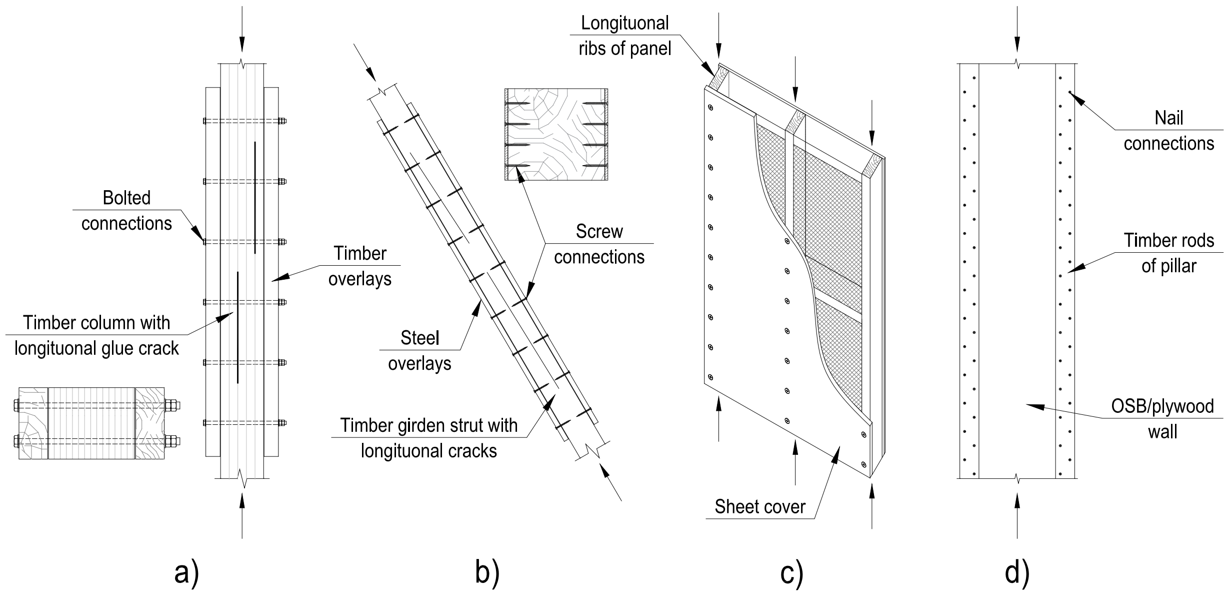

Figure 1. Component timber composite elements: *a* – glued timber column with longitudinal cracks reinforced timber overlays with bolted connections; *b* – timber girder strut reinforced steel overlays with screw connections; *c* – wall panel with sheet cover included in the joint work with ribs; *d* – I-section pillar with timber chords and sheet material wall (plywood, OSB, etc.).

At the moment of loss of stability, the shear bonds from the concave side of the element will experience additional loading, the stiffness modulus of the bonds will be determined by the slope of the tangent to the “load-strain” dependence (Fig. 2). Shear bonds located on the curved side of the element will experience unloading according to the linear law $(c = \mathrm{tg}\beta)$, as a result of which their actual stiffness modulus will be equal to their initial stiffness modulus $(c = \mathrm{tg}\alpha)$. The more significant the characteristic of nonlinearity for compliant joints, the more this factor will affect the stability of the component element. The method given in [14] for calculating component rod elements on compliant bonds involves the use of a linear stiffness coefficient k_u, which does not allow taking into account the real nature of the deformation of the joints, and, as a result, adequately assessing the stability reserves of such structures.

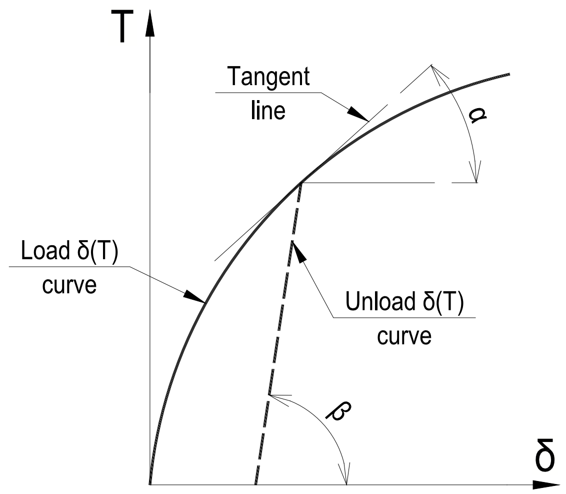

Figure 2. Scheme for determining the joint stiffness modulus for a given force during additional loading and unloading: α – angle of inclination of the tangent line at a point at actual stress values; β – is the same, at the beginning of loading.

The research object is build–up centric–compressed timber pillars. The subject of research is nonlinear dependence “load–shear” of ties and stability of such structures. The purpose of the article is to design the mathematical step method for stability estimation, which considers nonlinear deformability of shear ties. The task of researches is to calculate a three–layer build–up timber rod critical force according to the developed mathematical model, and to compare the exact and approximate critical force calculations of such structure with the assumption of different approaches in determining of elastic modulus of the ties.

2. Methods

For most types of shear bonds: nogs [15], bolts [16], MTP [17], claw connectors [18], screws [19], brackets [20] and others are characterized by nonlinear dependence between the load and the deformation of the joint. Thus, for component columns with nonlinearly deformable compliant joints, it is necessary to take into account the change in the stiffness of shear bonds depending on the forces acting in them, that is, the stiffness coefficient of each bond should be considered as a function [21]:

$$c = c\left(T_c\right), \tag{1}$$

where c is shear stiffness of a single joint; T_c is force applied to the joint.

The common chain for the such task numerical solution is presented in the form of a block scheme in Fig. 3.

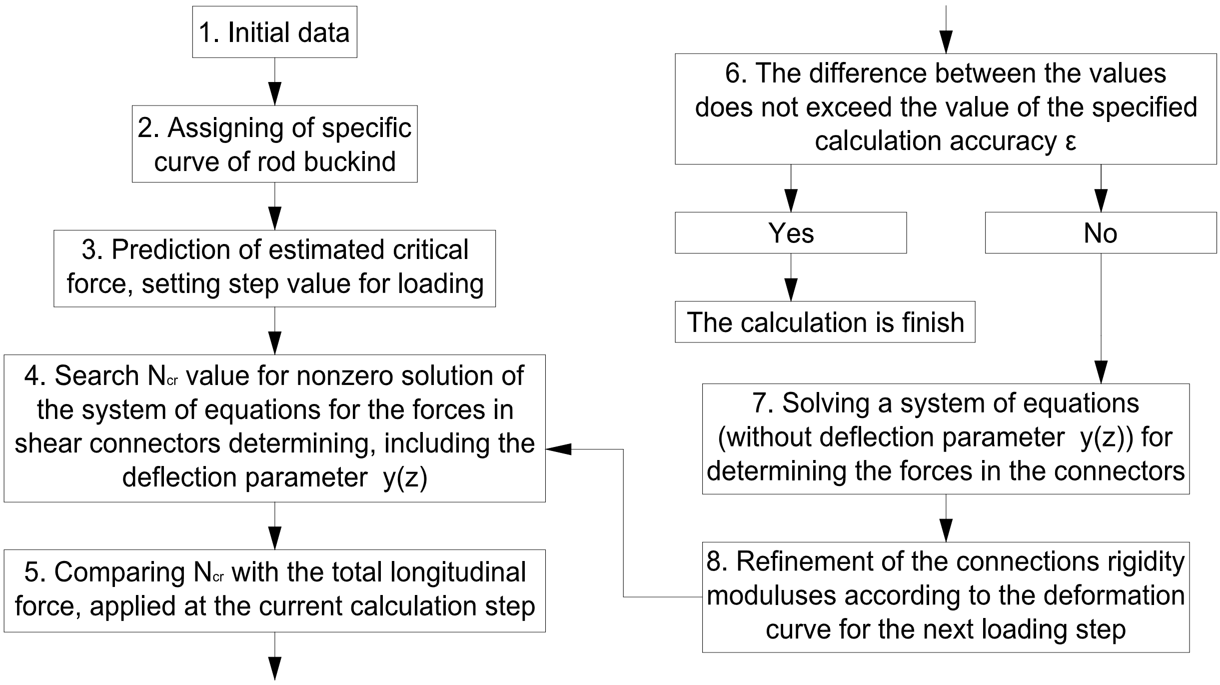

Figure 3. Block scheme of numerical solution.

The composite element, which is shown in Fig. 4, can be considered. Under the action of a longitudinal force applied to the central element, shear forces arise in shear bonds $T_{1,i}$ and $T_{2,i}$, where the first index means the seam number, and the second – the number of the discrete bond. To construct an algorithm, we consider a symmetrical case with respect to the middle of the height for a three-layer component element, the outer layers of which are not obstructed by mutual displacements along the ends. The interconnection of the layers is carried out due to flexible shear bonds, located, in general, with a variable step, but symmetrically with respect to the section with zero shear deformations and the center of gravity of the section of the middle element.

The i-th section of the element can be considered, limited by i-th and $i+1$-th connectors. The increment of the concentrated shear along the length of the allocated site will be equal to the difference in shears i-th and $i+1$-th bonds on a section of length l_i and is described by the system of equations:

$$\begin{cases} \Gamma_{1,i+1} - \Gamma_{1,i} = \dfrac{T_{1,i+1}}{c_{1,i+1}} - \dfrac{T_{1,i}}{c_{1,i}} = \\ = \Delta_{11,i} l_i \sum\limits_{k=1}^{i} T_{1,k} + \Delta_{12,i} l_i \sum\limits_{k=1}^{i} T_{2,k} + \int\limits_0^{l_i} \Delta_{10,i}\left(z_i\right) dz_i; \\ \Gamma_{2,i+1} - \Gamma_{2,i} = \dfrac{T_{2,i+1}}{c_{2,i+1}} - \dfrac{T_{2,i}}{c_{2,i}} = \\ = \Delta_{21,i} l_i \sum\limits_{k=1}^{i} T_{1,k} + \Delta_{22,i} l_i \sum\limits_{k=1}^{i} T_{2,k} + \int\limits_0^{l_i} \Delta_{20,i}\left(z_i\right) dz_i, \end{cases} \tag{2}$$

where $\Gamma_{1,i}$, $\Gamma_{2,i}$ are concentrated shifts of i-th bond of 1st and 2nd seams, respectively; $c_{1,i}$, $c_{2,i}$ are stiffness coefficient of i-th bond of 1st and 2nd seams; z_i is the coordinate measured by length i-th section; $\Delta_{11,i}$, $\Delta_{12,i}$, $\Delta_{22,i}$ are coefficients of equations that take into account the amount of shear from unknown shear forces $T_{1,i}$, $T_{2,i}$; $\Delta_{10,i}$, $\Delta_{20,i}$ are load functions that take into account the impact on shear of external loads applied to the structure.

$$\begin{gathered} \Delta_{11} = \frac{1}{E_1^z F_1} + \frac{1}{E_2^z F_2} + \frac{w_1^2}{\sum E^z I^y}; \\ \Delta_{12} = \Delta_{21} = \frac{w_1 w_2}{\sum E^z I^y} - \frac{1}{E_2^z F_2}; \\ \Delta_{22} = \frac{1}{E_2^z F_2} + \frac{1}{E_3^z F_3} + \frac{w_2^2}{\sum E^z I^y}; \end{gathered} \tag{3}$$

$$\begin{gathered} \Delta_{10,i} = \frac{N_2}{E_2^z F_2} - \frac{N_1}{E_1^z F_1} - \frac{M_{0,i}\left(z_i\right) \cdot w_1}{\sum E^z I^y}; \\ \Delta_{20,i} = \frac{N_3}{E_3^z F_3} - \frac{N_2}{E_2^z F_2} - \frac{M_{0,i}\left(z_i\right) \cdot w_2}{\sum E^z I^y}, \end{gathered} \tag{4}$$

where F_1, F_2, F_3, E_1, E_2, E_3 are cross-sectional areas and elastic modulus of the branch material of a component column; N_1, N_2, N_3 are longitudinal forces in the branches; w_i are distances between centers of gravity of branches; $\sum El$ is the sum of the stiffness of the layers: $\sum E^z I^y = E_1^z I_1 + +E_2^z I_2 + E_3^z I_3$; $M_{0,i}\left(z_i\right)$ is distribution function of the bending moment within the i-th section.

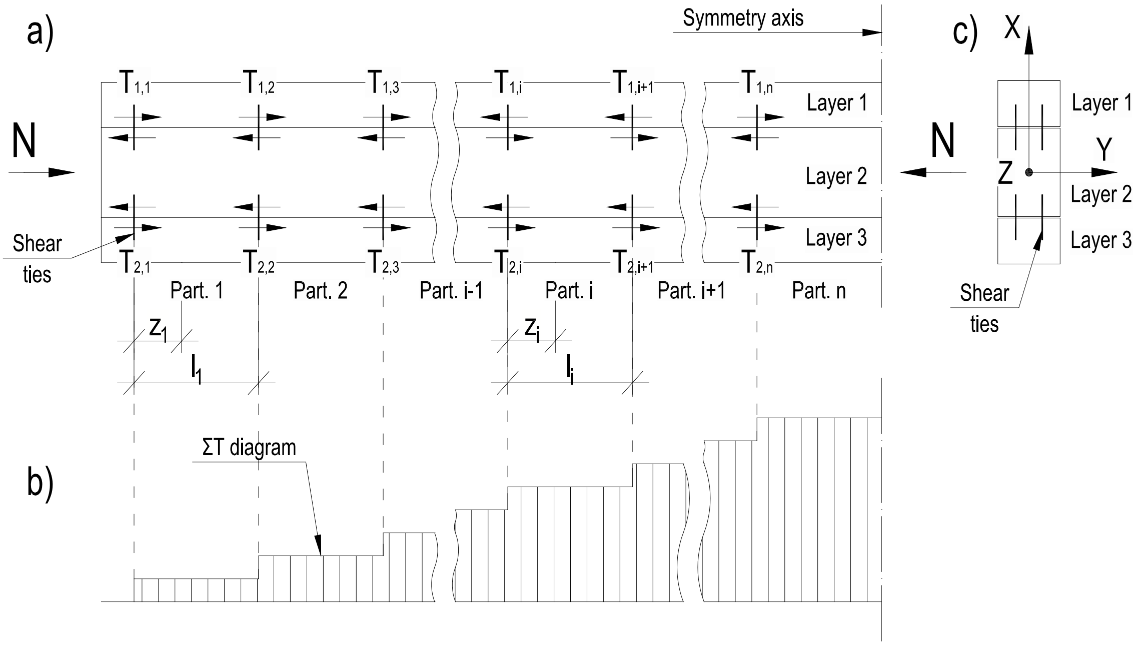

Figure 4. Scheme of a compressed composite pressed rod with discrete shear connections: a – numeration of bonds and sections; b – scheme of resulting shear forces in discrete connections diagram; c – composite rod cross-section; N – compressive force; T – shear forces in discrete connectors; X, Y, Z – coordinate axes.

Composing expressions (2) for each section of length $l_i,$ a system of equations can be obtained to determine the shear forces in each connector:

$$\begin{cases} \dfrac{T_{j,2}}{c_{j,2}} - \dfrac{T_{j,1}}{c_{j,1}} = \Delta_{j1,1} \cdot l_1 \cdot T_{1,1} + \Delta_{j2,1} \cdot l_1 \cdot T_{2,1} + \int\limits_0^{l_1} \Delta_{j0,1}\left(z_1\right) dz_1 \\ \quad\quad\quad\quad \ldots \\ \dfrac{T_{j,i+1}}{c_{j,i+1}} - \dfrac{T_{j,i}}{c_{j,i}} = \Delta_{j1,i} \cdot l_i \cdot \sum\limits_{k=1}^{i} T_{1,k} + \Delta_{j2,i} \cdot l_i \cdot \sum\limits_{k=1}^{i} T_{2,k} + \int\limits_0^{l_i} \Delta_{j0,i}\left(z_1\right) dz_i \\ \quad\quad\quad\quad \ldots \\ 0 - \dfrac{T_{j,n}}{c_{j,n}} = \Delta_{j2,n} \cdot l_n \cdot \sum\limits_{k=1}^{n} T_{1,k} + \Delta_{22,i} \cdot l_n \cdot \sum\limits_{k=1}^{i} T_{2,k} + \int\limits_0^{l_i} \Delta_{j0,n}\left(z_1\right) dz_n \end{cases}, \quad (5)$$

where j is seam number $\left(j = 1,\ 2\right).$

The index after the comma of the coefficients at unknown and free members means that in some cases they can be variable in the length of the element and be determined for each section (for example, in the case of a variable cross section or the presence of local defects in the reinforced structure).

A system with nonlinear elastic shear bonds is characterized by an uneven decrease in the modulus of stiffness [21, 22]; as a result, the calculation must be carried out by the step method. The total number of steps of the nonlinear calculation is denoted as $\sum m,$ where m is step number $\left(m = 1,\ 2,\ 3 \ldots \sum m\right).$ We denote by ΔN_m the value of the step of application of the external load at the m-th calculation step.

The system of equations (5) for determining the forces at the m-th calculation step in shear bonds can be represented in matrix form:

$$X_m = A_m^{-1} \cdot B_m, \quad (6)$$

where X_m is the desired matrix of unknown shear forces $T_{1,i}$, $T_{2,i}$, A_m is matrix composed of coefficients at unknown shear forces (formulas (3)); B_m is matrix composed of free members, obtained by integrating expressions (4).

The index "m" in the designations given in formula (6) means that the elastic characteristics of materials at each calculation step can also be refined (when calculating taking into account the physical nonlinearity of materials).

$$A_m=\begin{bmatrix} \frac{1}{c_{1,1}}+\Delta_{11,1}l_1 & -\frac{1}{c_{1,2}} & \cdots & 0 & \cdots & 0 & \Delta_{1,2}l_1 & 0 & \cdots & 0 & \cdots & 0 \\ \Delta_{11,1}l_2 & \frac{1}{c_{1,2}}+\Delta_{11,1}l_2 & \cdots & 0 & \cdots & 0 & \Delta_{12,2}l_2 & \Delta_{12,2}l_2 & \cdots & 0 & \cdots & 0 \\ & & & & & \cdots & \cdots & & & & & \\ \Delta_{11,i}l_i & \Delta_{11,i}l_i & \cdots & \frac{1}{c_{1i}}+\Delta_{11,i}l_i & \cdots & 0 & \Delta_{12,i}l_i & \Delta_{12,i}l_i & \cdots & \Delta_{12,i}l_i & \cdots & 0 \\ & & & & & \cdots & \cdots & & & & & \\ \Delta_{11,n}l_n & \Delta_{11,n}l_n & \cdots & \Delta_{11,n}l_n & \cdots & \frac{1}{c_{1,n}}+\Delta_{11,n}l_n & \Delta_{12,n}l_n & \Delta_{12,n}l_n & \cdots & \Delta_{12,n}l_n & \cdots & \Delta_{12,n}l_n \\ \Delta_{21,1}l_1 & 0 & \cdots & 0 & \cdots & 0 & \frac{1}{c_{2,1}}+\Delta_{22,2}l_1 & -\frac{1}{c_{2,2}} & \cdots & 0 & \cdots & 0 \\ \Delta_{21,1}l_2 & \Delta_{2,1}l_2 & \cdots & 0 & \cdots & 0 & 0 & \frac{1}{c_{2,2}}+\Delta_{22,2}l_2 & \cdots & 0 & \cdots & 0 \\ & & & & & \cdots & \cdots & & & & & 0 \\ \Delta_{21,i}l_i & \Delta_{21,i}l_i & \cdots & 0 & \cdots & 0 & \Delta_{22,i}l_i & \Delta_{22,i}l_i & \cdots & \frac{1}{c_{2,i}}+\Delta_{22,i}l_i & \cdots & 0 \\ & & & & & \cdots & \cdots & & & & & \\ \Delta_{21,1}l_n & \Delta_{21,1}l_n & \cdots & \Delta_{21,1}l_n & \cdots & 0 & \Delta_{22,n}l_2 & \Delta_{22,n}l_2 & \cdots & \Delta_{22,n}l_2 & \cdots & \frac{1}{c_{2,n}}+\Delta_{22,n}l_n \end{bmatrix}; \quad (7)$$

$$B_m=\begin{bmatrix} \cdots \\ \cdots \\ \cdots \\ -\int_0^{l_i}\left(\frac{N_2}{E_2F_2}-\frac{N_1}{E_1F_1}-\frac{M_{0,i}w_1}{\sum EI}\right)dz_i \\ \cdots \\ -\int_0^{l_n}\left(\frac{N_2}{E_2F_2}-\frac{N_1}{E_1F_1}-\frac{M_{0,n}w_1}{\sum EI}\right)dz_n \\ \cdots \\ \cdots \\ \cdots \\ -\int_0^{l_i}\left(\frac{N_3}{E_3F_3}-\frac{N_2}{E_2F_2}-\frac{M_{0,i}w_2}{\sum EI}\right)dz_i \\ \cdots \\ -\int_0^{l_n}\left(\frac{N_3}{E_3F_3}-\frac{N_2}{E_2F_2}-\frac{M_{0,n}w_2}{\sum EI}\right)dz_n \end{bmatrix}; \quad X_m=\begin{bmatrix} T_{1,1} \\ \cdots \\ T_{1,2} \\ \cdots \\ T_{1,i} \\ \cdots \\ T_{1,n} \\ T_{2,1} \\ T_{2,2} \\ \cdots \\ T_{2,i} \\ \cdots \\ T_{2,n} \end{bmatrix}. \quad (8)$$

At the calculation stage m the resulting force vector in the bonds can be represented as the sum of the required shear force vectors X_m at all previous and current calculation steps:

$$\vec{T}_{i,j} = \sum_{k=1}^{m} \vec{X}_k .$$

As the column is loaded, the forces in the bonds will increase, in the general case (with a decrease in the degree of loading of the derivative of the function describing the deformation of the bonds from the shear force T_c) the stiffness modulus of the bonds, which will cause to less in the stiffness of the component element as a whole. Therefore, it is impossible to determine in advance which stiffness value for each bond will correspond to the moment when the compressive load reaches a critical value.

At the moment of buckling, the centrally compressed rod will deviate from the initial rectilinear position, in addition to the longitudinal force, a bending moment will appear due to eccentricity:

$$M_0\left(z_i\right) = \sum N \cdot y\left(z_i\right), \tag{9}$$

whose meaning is unknown. Thus, one more equation will be added to the system of equations for determining shear deformations in the seams, for determining the deflection:

$$\sum EI \cdot y'' = \sum N \cdot y - w_1 \sum T_{1,\ldots} - w_2 \sum T_{2,\ldots}, \tag{10}$$

Under the action of an external load only on the middle element $\left(N_1 = N_3 = 0\right)$, the system of equations (5), with consideration of the moment from deflection during buckling, will take the form:

$$\begin{cases} \dfrac{T_{j,2}}{c_{j,2}} - \dfrac{T_{j,1}}{c_{j,1}} = \Delta_{1j,1} \cdot l_1 \cdot T_{1,1} + \\ + \Delta_{2j,1} \cdot l_1 \cdot T_{2,1} \pm \dfrac{N_2}{E_2 \cdot F_2} - \displaystyle\int_0^{l_1} \dfrac{N_2 \cdot y\left(z_1\right) \cdot w_j}{\sum EI} dz_1; \\ \qquad \ldots \\ \dfrac{T_{j,i+1}}{c_{j,i+1}} - \dfrac{T_{j,i}}{c_{j,i}} = \Delta_{1j,i} \cdot l_i \cdot \displaystyle\sum_{k=1}^{i} T_{1,k} + \\ + \Delta_{j2,i} \cdot l_i \cdot \displaystyle\sum_{k=1}^{i} T_{2,k} \pm \dfrac{N_2}{E_2 \cdot F_2} - \displaystyle\int_0^{l_i} \dfrac{N_2 \cdot y\left(\sum_{k=1}^{i-1} l_k + z_i\right) \cdot w_j}{\sum EI} dz_i; \\ \qquad \ldots \\ 0 - \dfrac{T_{j,n}}{c_{j,n}} = \Delta_{1j,n} \cdot l_n \cdot \displaystyle\sum_{k=1}^{n} T_{1,k} + \\ + \Delta_{2j,n} \cdot l_n \cdot \displaystyle\sum_{k=1}^{n} T_{2,k} \pm \dfrac{N_2}{E_2 \cdot F_2} - \displaystyle\int_0^{l_n} \dfrac{N_2 \cdot y\left(\sum_{k=1}^{n-1} l_k + z_i\right) \cdot w_j}{\sum EI} dz_n; \\ \qquad \left(j = 1, 2\right) \\ y''\left(z_1\right) \cdot \sum EI = \sum N \cdot y\left(z_1\right) - w_1 T_{1,1} - w_2 T_{2,1}; \\ \qquad \ldots \\ y''\left(\displaystyle\sum_{k=1}^{n-1} l_k + z_n\right) \cdot \sum EI = \\ = N_2 \cdot y\left(\displaystyle\sum_{k=1}^{n-1} l_k + z_n\right) - w_1 \displaystyle\sum_{k=1}^{n-1} T_{1,k} - w_2 \displaystyle\sum_{k=1}^{n-1} T_{2,k} \end{cases} \tag{11}$$

For some values of the longitudinal force $N_{cr} = N_2$ homogeneous system of equations obtained from (5) will have nonzero solutions. These values will correspond to the critical forces for many different forms of loss of stability. To determine N_{cr}, it is necessary to solve the equation:

$$\det|A| = 0. \tag{12}$$

where A is matrix consisting of the coefficients at unknowns of the homogeneous system of equations obtained from (11).

The calculation should be carried out by the method of successive approximations, in the following order (the order is considered for the m-th calculation step):

– given the value of the longitudinal force, the total shear forces in the bonds at the m-th step are determined. Based on these values, the tangent-modulus stiffness coefficients of joints located on the concave side of a compressed rod that loses stability are calculated by the formula:

$$c_i\left(T_i\right) = \frac{dT_i}{d\delta_i}, \tag{13}$$

where T_i is shear force attributable to the i-th bond; δ_i is the value of deformation of the i-th bond at a given load T_i, determined by the approximating function of the experimental curve of the deformation of the joint.

The stiffness coefficients of the bonds located in the opposite seam of the component rod are taken equal to the initial stiffness modulus, because they are experiencing unloading:

– the critical force is determined by solving the transcendental equation (12), the obtained value of the critical longitudinal force is compared with the total longitudinal force applied at the m-th calculation step:

$$\Delta = \frac{\left|\sum\limits_{k=1}^{m} \Delta N_k - N_{cr}\right|}{N_{cr}} \le \varepsilon. \tag{14}$$

If the difference between the values does not exceed the value of the specified calculation accuracy ε, then the calculation is terminated, the value of the critical force is taken to be the value that is the solution of equation (12). If (14) is not fulfilled, the calculation continues in the same way for the step m+1, m+2, etc. until condition (14) is met.

As an example, consider a component timber pillar reinforced on both sides with timber overlays (Fig. 5,a). There are no obstacles to mutual shear at the end faces of the column. The column and overlays are made of pine wood of strength class C22 with an elastic modulus $E_{0.05}$ = 6.7 GPa. The branches of the component column are interconnected by steel bolted joints and toothed connectors. To obtain characteristics of the stiffness of the joints tests of samples of joints for intermediate shear were performed. The deformation of the joints occurs according to a nonlinear law, i.e. the stiffness parameter of the joints is expressed by the dependence $c = c\left(T_c\right)$ (Fig. 5, c). The behavior of timber is assumed linearly elastic. The following parameters are accepted as initial data: column height: H = 5 m, column cross-sectional dimensions 200×150 mm, overlays – 50×150 mm. Shear bonds spacing is $S_1 = S_2 = S_3 = S_4 = S_5 = 0.5\ \mathrm{m}$. Column loaded with longitudinal force N, transmitted to the column central middle element. It is necessary to define the value of the critical force.

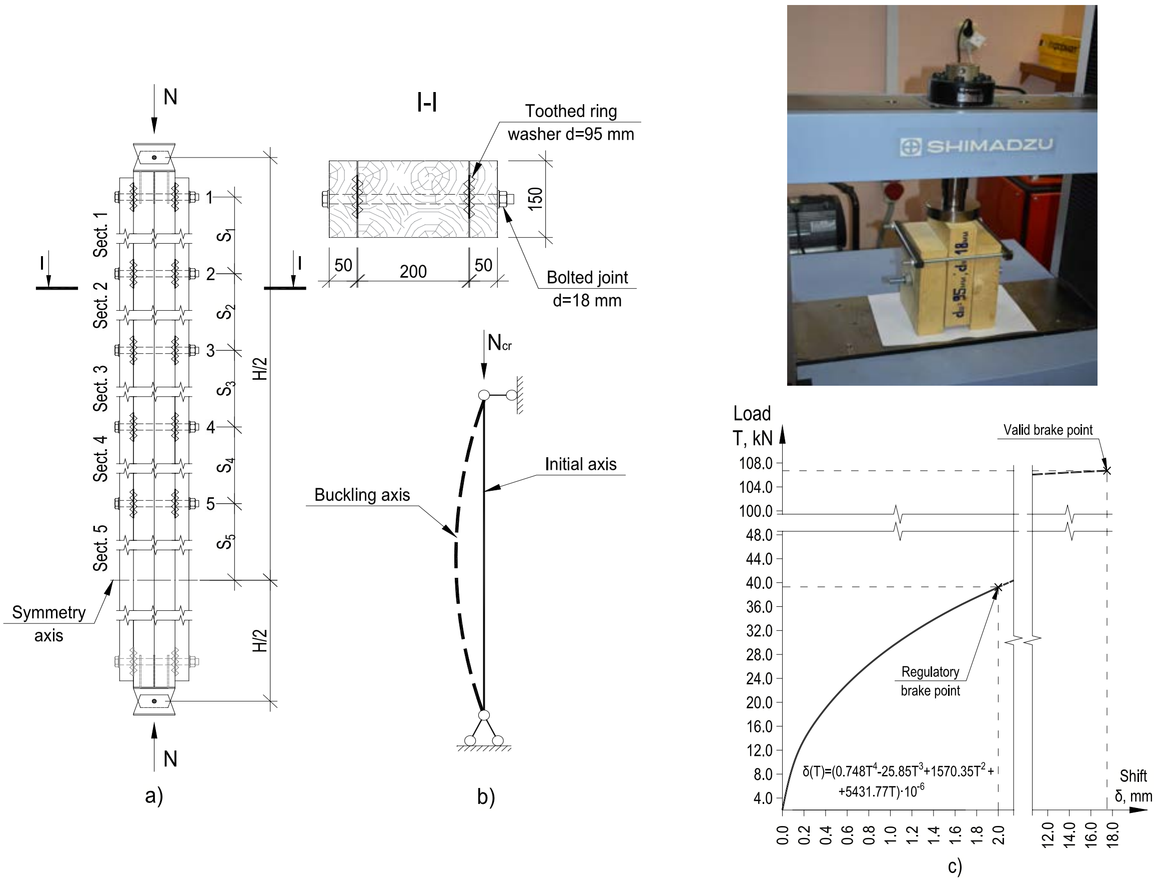

Figure 5. The component column on compliant bonds: *a* – column scheme; *b* – form of loss of stability with hinged fixing of ends; *c* – testing of samples on a hydraulic press Shimadzu and load-shift diagram (*T*–δ) for a single bond with longitudinal shift (for 1 seam).

Loading is performed by the step method, the value of the loading step is taken equal to ΔN = 50 kN. Determination of forces in shear bonds at each calculation step is made by solving the equation (6). According to the resulting forces in the shear bonds obtained at the previous step, according to expression (13), the stiffness coefficients of the bonds are assigned for the next calculation step. In addition, at each step, the system is “probing” for the possibility of loss of stability, for which equation (12) is solved and the results are compared according to expression (14). Taking into account the conditions of fixing, the buckling deflection function for the considered pillar can be represented by an affine curve:

$$y = \alpha \cdot \sin \frac{n\pi z}{H}, \tag{15}$$

where α is dimensionless parameter that determines the maximum deflection amplitude; n is number of pillar bending half-waves (in the considered case, the smallest critical force corresponds to n = 1); z is element height coordinate; H is full pillar height.

Since the shape of the pillar bend depends only on a single parameter – α, then in the case under consideration, the number of equations of system (11) can be reduced from 15 to 11 pcs. (as unknown parameters, the forces in the shear bonds $T_{j,i}$ and the parameter α). The matrix of coefficients for unknowns, compiled for a homogeneous system of equations, will have the form:

$$A=\begin{bmatrix} \frac{1}{c_{1,1}}+\Delta_{1,1}l_1 & \frac{-1}{c_{1,2}} & 0 & 0 & 0 & \Delta_{2,1}l_1 & 0 & 0 & 0 & 0 & \Delta_{1,1y} \\ \Delta_{1,1}l_2 & \frac{1}{c_{1,2}}+\Delta_{1,1}l_2 & \frac{1}{c_{1,3}} & 0 & 0 & \Delta_{2,1}l_2 & \Delta_{2,1}l_2 & 0 & 0 & 0 & \Delta_{1,2y} \\ \Delta_{1,1}l_3 & \Delta_{1,1}l_3 & \frac{1}{c_{1,3}}+\Delta_{1,1}l_3 & \frac{1}{c_{1,4}} & 0 & \Delta_{2,1}l_3 & \Delta_{2,1}l_3 & \Delta_{2,1}l_3 & 0 & 0 & \Delta_{1,3y} \\ \Delta_{1,1}l_4 & \Delta_{1,1}l_4 & \Delta_{1,1}l_4 & \frac{1}{c_{1,4}}+\Delta_{1,1}l_4 & \frac{1}{c_{1,5}} & \Delta_{2,1}l_4 & \Delta_{2,1}l_4 & \Delta_{2,1}l_4 & \Delta_{2,1}l_4 & 0 & \Delta_{1,4y} \\ \Delta_{1,1}l_5 & \Delta_{1,1}l_5 & \Delta_{1,1}l_5 & \Delta_{1,1}l_5 & \frac{1}{c_{1,5}}+\Delta_{1,1}l_5 & \Delta_{2,1}l_5 & \Delta_{2,1}l_5 & \Delta_{2,1}l_5 & \Delta_{2,1}l_5 & \Delta_{2,1}l_5 & \Delta_{1,5y} \\ \Delta_{2,1}l_1 & 0 & 0 & 0 & 0 & \frac{1}{c_{2,1}}+\Delta_{2,1}l_1 & \frac{-1}{c_{2,1}} & 0 & 0 & 0 & \Delta_{2,1y} \\ \Delta_{2,1}l_2 & \Delta_{2,1}l_2 & 0 & 0 & 0 & \Delta_{2,2}l_2 & \frac{1}{c_{2,2}}+\Delta_{2,2}l_2 & \frac{-1}{c_{2,2}} & 0 & 0 & \Delta_{2,2y} \\ \Delta_{2,1}l_3 & \Delta_{2,1}l_3 & \Delta_{2,1}l_3 & 0 & 0 & \Delta_{2,2}l_3 & \Delta_{2,2}l_3 & \frac{1}{c_{2,3}}+\Delta_{2,3}l_3 & \frac{-1}{c_{2,4}} & 0 & \Delta_{2,3y} \\ \Delta_{2,1}l_4 & \Delta_{2,1}l_4 & \Delta_{2,1}l_4 & \Delta_{2,1}l_4 & 0 & \Delta_{2,2}l_3 & \Delta_{2,2}l_3 & \Delta_{2,2}l_3 & \frac{1}{c_{2,4}}+\Delta_{2,4}l_4 & \frac{-1}{c_{2,5}} & \Delta_{2,4y} \\ \Delta_{2,1}l_5 & \Delta_{2,1}l_5 & \Delta_{2,1}l_5 & \Delta_{2,1}l_5 & \Delta_{2,1}l_5 & \Delta_{2,2}l_3 & \Delta_{2,2}l_3 & \Delta_{2,2}l_3 & \Delta_{2,2}l_3 & \frac{1}{c_{2,5}}+\Delta_{2,5}l_5 & \Delta_{2,5y} \\ -w_1 & -w_1 & -w_1 & -w_1 & -w_1 & -w_2 & -w_2 & -w_2 & -w_2 & -w_2 & \Delta_{yy} \end{bmatrix} \quad (16)$$

where Δ_{iy}, $\Delta_{i'y}$ are coefficients that considering the impact of the moment from the longitudinal force on the value of the shear forces in the seams, determined by the formulas (17); Δ_{yy} is multiplier at unknown parameter α, obtained from expression (10) subject to the accepted deformation curve (15), determined by the formula (18).

$$\Delta_{1,iy}=\frac{1}{\sum EI}\int_0^{l_i} N_2 w_1 \sin\left(\frac{\sum_{k=1}^{i-1} l_k + z_i}{H}\right) dz_i;$$
$$\Delta_{2,iy}=\frac{1}{\sum EI}\int_0^{l_i} N_2 w_2 \sin\left(\frac{\sum_{k=1}^{i-1} l_k + z_i}{H}\right) dz_i; \quad (17)$$

$$\Delta_{yy}=\frac{1}{H^2}\pi^2\sum EI\sin\left(\frac{\pi}{2}\right)+N_2\sin\left(\frac{\pi}{2}\right). \quad (18)$$

To compare the results, the calculation is carried out at a constant value of the stiffness coefficient of the joint k_u. According to [14] for bolted joints with toothed connectors, this coefficient is determined by the formula:

$$k_u=\frac{2}{3}k_{ser}, \quad (19)$$

where k_{ser} is normative coefficient of connectors stiffness, defined as a secant modulus at a load equal to 40 % of the maximum allowable value.

3. Results and Discussion

Forces in shear bonds at all loading stages, total applied values of longitudinal forces and predicted values of critical force are presented in Tables 1–3. At the 14th step of the calculation, the accuracy indicator for determining the critical force was less than 1 %, so the pillar was not loaded further.

Table 1. Calculation progress (stages 1-5).

Bond number	Calculation stage number, m														
	1			2			3			4			5		
	c, kN/m	ΔT, kN	$\sum T$, kN	c, kN/m	ΔT, kN	$\sum T$, kN	c, kN/m	ΔT, kN	$\sum T$, kN	c, kN/m	ΔT, kN	$\sum T$, kN	c, kN/m	ΔT, kN	$\sum T$, kN
1,1 (2,1)	56016	4.89	4.89	49807	4.67	9.57	39529	4.22	13.79	28976	3.63	17.42	20554	3.01	20.43
1,2 (2,2)	56016	2.02	2.02	54227	2.12	4.14	51148	2.33	6.47	46672	2.57	9.03	40823	2.74	11.77
1,3 (2,3)	56016	0.83	0.83	55431	0.90	1.72	54563	1.03	2.75	53285	1.23	3.98	51419	1.46	5.44
1,4 (2,4)	56016	0.33	0.33	55807	0.36	0.70	55538	0.42	1.12	55174	0.51	1.63	54662	0.63	2.26
1,5 (2,5)	56016	0.12	0.12	55947	0.13	0.25	55865	0.15	0.40	55764	0.18	0.58	55630	0.23	0.81
ΔN, kN	50			50			50			50			50		
$\sum N$, kN	50			100			150			200			250		
$\sum N_{cr}$, kN	863.23			862.16			860.49			857.95			854.05		
Δ, %	–			–			–			–			–		

Table 2. Calculation progress (stages 6–10).

Bond number	Calculation stage number, m														
	6			7			8			9			10		
	c, kN/m	ΔT, kN	$\sum T$, kN	c, kN/m	ΔT, kN	$\sum T$, kN	c, kN/m	ΔT, kN	$\sum T$, kN	c, kN/m	ΔT, kN	$\sum T$, kN	c, kN/m	ΔT, kN	$\sum T$, kN
1,1 (2,1)	14971	2.51	22.94	11800	2.20	25.14	10325	2.08	27.22	9989	2.12	29.34	10264	2.25	31.58
1,2 (2,2)	34038	2.75	14.51	27197	2.58	17.10	21236	2.30	19.40	16687	1.99	21.39	13574	1.74	23.12
1,3 (2,3)	48771	1.70	7.14	45224	1.90	9.03	40826	2.02	11.05	35852	2.02	13.07	30763	1.93	15.00
1,4 (2,4)	53930	0.77	3.03	52889	0.91	3.94	51487	1.05	4.99	49626	1.18	6.17	47304	1.27	7.43
1,5 (2,5)	55451	0.28	1.08	55208	0.34	1.42	54884	0.40	1.82	54458	0.46	2.28	53913	0.51	2.79
ΔN, kN	50			50			50			50			50		
$\sum N$, kN	300			350			400			450			500		
$\sum N_{cr}$, kN	848.26			840.02			829.05			815.23			798.95		
Δ, %	–			–			–			–			–		

Table 3. Calculation progress (stages 11–14).

Bond number	Calculation stage number, m											
	11			12			13			14		
	c, kN/m	ΔT, kN	$\sum T$, kN	c, kN/m	ΔT, kN	$\sum T$, kN	c, kN/m	ΔT, kN	$\sum T$, kN	c, kN/m	ΔT, kN	$\sum T$, kN
1,1 (2,1)	10001	2.27	33.85	6424	1.66	35.52	1188	0.38	35.89	1081	0.35	36.24
1,2 (2,2)	11624	1.59	24.71	10513	1.67	26.39	10017	1.99	28.37	10112	2.08	30.46
1,3 (2,3)	26016	1.82	16.82	21830	1.84	18.67	18031	1.97	20.64	14643	1.72	22.36
1,4 (2,4)	44561	1.35	8.78	41423	1.55	10.33	37639	1.87	12.20	32942	1.82	14.03
1,5 (2,5)	53236	0.58	3.37	52395	0.70	4.07	51264	0.92	4.99	49623	1.00	6.00
ΔN, kN	50			50			50			50		
$\sum N$, kN	550			600			650			700		
$\sum N_{cr}$, kN	779.95			755.22			719.12			704.27		
Δ, %	–			25.87			10.64			0.61		

Fig. 6, a shows graphs of the increase in shear forces in shear bonds as the considered pillar is loaded with load steps ΔN. Graphs of force changes in bonds T_1 and T_2 are concave inward, and T_3, T_4 and T_5 are outward. From which it follows that from stage to stage of loading, the forces are redistributed between the bonds located closer to the end sections of the element and located closer to the axis of symmetry (cross section with zero shear). As whole, it can judge that the stiffness coefficient of more loaded bonds near the end sections decreases faster than that of bonds in the middle section, which negatively affects the operation of the entire structure with each stage of loading, reducing the predicted value of the critical force by an increasing value.

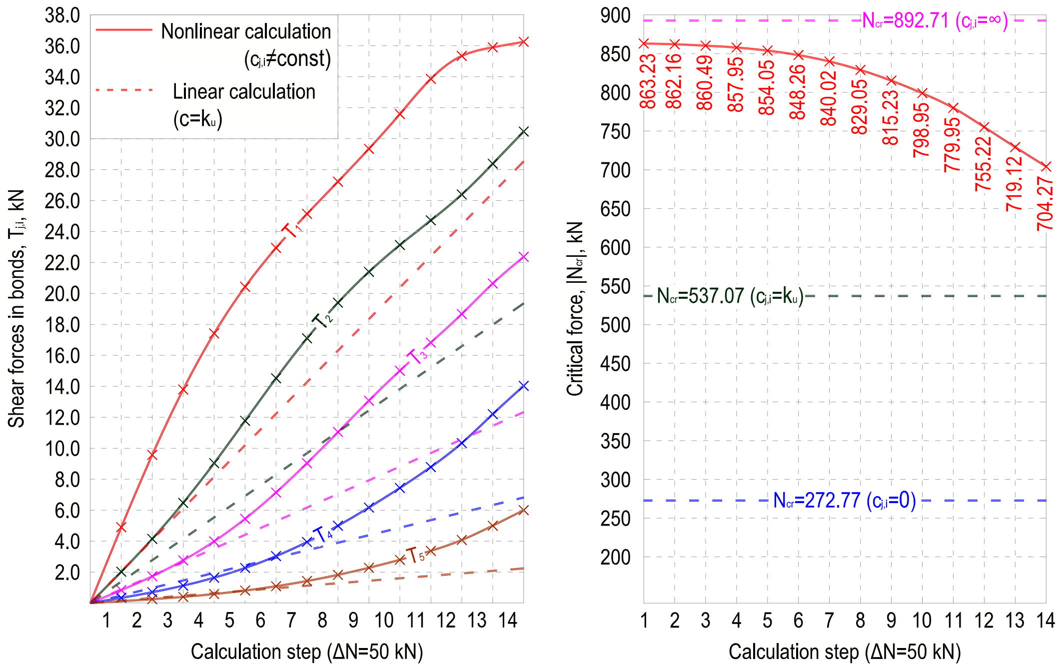

a) b)

Figure 6. Dependency graphs: *a* – forces in shear bonds T_i at each stage of the calculation; *b* – critical force values in nonlinear calculation (predicted value at each step) and linear calculation for various values of the stiffness coefficient of the connectors c; N_{cr} ($c = \infty$) is the critical force for solid section rod; N_{cr} ($c = k_u$) is the same, for composite rod with normative coefficient of connectors stiffness k_u (19); N_{cr} ($c = 0$) is the same, for composite rod without shear connectors.

The paper [23] presents the results of the study of the stress–strain state of square concrete-filled double-skin steel tubular columns under axial compression taking into account the physical nonlinearity of deformation of materials. A new design equation is suggested based on stress distribution over the concrete cross-section. It is shown that material properties and dimensions of composite columns can highly affect their performance. Also, the thickness of the inner tube must be controlled to prevent its premature failure. In the article [24], the supercritical forms of buckling loss of hyperelastic columns under axial compression are investigated. As its width-to-length ratio increases, the column can undergo transitions from continuous buckling, like the Euler buckling, to snapping-through buckling, and eventually to snapping-back buckling. The results of these studies give reason to believe that taking into account the physical and geometric nonlinearity makes it possible to identify a noticeable error in the assessment of buckling compared to the calculation according to an undeformed scheme under the assumption of linear work of materials.

In the process of searching for sources, it was not possible to find works related to the buckling of composite structures with nonlinear deformable connections, however, the results of this study gives grounds to judge that the actual reserves of the bearing capacity and stability of such structures can be adequately obtained only with a nonlinear calculation and a sufficient number of iterations. In the linear calculation of such a pillar, an erroneous decision can be adopted about the need to increase the number of bonds near the end sections, or reduce their spacing, although in reality such a need does not arise. When taking into account the “normative” stiffness coefficient of the bonds, the forces in them do not exceed 80 % of the maximum permissible value, however, in this case, a significantly underestimated (in the case under consideration by 24 %) value of the critical load is obtained. Depending on the character of the deformation curve of the shear connectors and the bending stiffnes flexibility of the element layers, the calculation using the normative linear stiffness coefficient (19) may also leads to overestimated values of the critical force N_{cr}, since the actual stiffness of the connectors depends on the shear forces level in the moment of buckling, which are significantly different for rods with high and low flexibility of layers.

The actual reserve of the bearing capacity of centrally compressed component columns with nonlinearly deformable shear bonds is almost impossible to predict in advance, but it will be between two values of the critical load: calculated for a solid element (at $c_{j,i} \to \infty$) and for a composite element, taking into account zero stiffness seams $\left(c_{j,i} \to 0\right)$. These values can be used when assigning the value of the load step, on which the number of iterations will depend. To obtain adequate values, the number of iterations should be 10...15 [25].

The use of the presented calculation algorithm can be extended to component elements with defects, the nature of which causes the variability of the geometric characteristics of the rod sections along the length (for example, a wooden pillar with longitudinal cracks); component structures with disconnected bonds (when calculating according to the idealized Prandtl diagram); as well as structures, the material of which creates the need to calculate them taking into account the physical nonlinearity. The introduction of an additional variable, the time factor, allows to consider the influence of creep deformations of joints in the calculation.

4. Conclusions

1. A mathematical model has been devised that makes it possible to calculate the strength and stability of three-layer compressed component rods, taking into account the nonlinear operation of shear bonds; with an uneven arrangement of bonds; when using idealized bond deformation diagrams, described, for example, according to the Prandtl diagram.

2. When taking into account the “normative” stiffness coefficient of the bonds, the forces in them do not exceed 80 % of the maximum permissible value, however, in this case, a significantly underestimated (in the case under consideration by 24 %) value of the critical load is obtained.

3. The introduction of the normative coefficient of connections stiffness into the calculation may give an invalid value of the critical force and does not allow obtaining reliable values of shear forces in the bonds, taking into account redistribution. A correct bucking estimation of the such structures should be produced taking into account the uneven stiffness coefficient changes of shear connections according to actual deformation curves.

References

1. Jockwer, R., Grönquist, P., Frangi, A. Long-term deformation behaviour of timber columns: Monitoring of a tall timber building in Switzerland. Engineering Structures. 2021. 234. 111855. DOI: 10.1016/j.engstruct.2021.111855

2. Kia, L., Valipour, H.R. Composite timber-steel encased columns subjected to concentric loading. Engineering Structures. 2012. 232. 111825. DOI: 10.1016/j.engstruct.2020.111825
3. Qiao, Q., Yang, Z., Mou, B. Experimental study on axial compressive behavior of CFRP confined square timber filled steel tube stub columns. Structures, 2020. 24. Pp. 823–834. DOI: 10.1016/j.istruc.2020.02.007
4. Navaratnam, S., Thamboo, J., Poologanathan, K., Roy, K., Gatheeshgar, P. Finite element modelling of timber infilled steel tubular short columns under axial compression. Structures. 2021. 30. Pp. 910–924. DOI: 10.1016/j.istruc.2020.12.087
5. Karampour, H., Bourges, M., Gilbert, B.P., Bismire, A., Bailleres, H., Guan, H. Compressive behaviour of novel timber-filled steel tubular (TFST) columns. Construction and Building Materials. 2020. 238. 117734. DOI: 10.1016/j.conbuildmat.2019.117734
6. Ghanbari-Ghazijahani, T., Magsi, G.A., Gu, D., Nabati, A., Ng, C.T. Double-skin concrete-timber-filled steel columns under compression. Engineering Structures. 2019. 200. 109537. DOI: 10.1016/j.engstruct.2019.109537
7. Hu, Q., Gao, Y., Meng, X., Diao, Y. Axial compression of steel–timber composite column consisting of H-shaped steel and glulam. Engineering Structures. 2020. 216. 110561. DOI: 10.1016/j.engstruct.2020.110561
8. Xu, F., Xuan, S., Li, W., Meng, X., Gao, Y. Compressive performance of steel-timber composite L-shaped columns under concentric loading. Journal of Building Engineering. 2022. 48. 103967. DOI: 10.1016/j.jobe.2021.103967
9. Li, H., Qiu, H., Lu, Y. An analytical model for the loading capacity of splice-retrofitted slender timber columns. Engineering Structures. 2020. 225. 111274. DOI: 10.1016/j.engstruct.2020.111274
10. Bhat, J.A. Buckling behavior of cross laminated poplar timber columns using various performance improvement techniques. Materials Today: Proceedings. 2021. 44. Pp. 2792–2796. DOI: 10.1016/j.matpr.2020.12.785
11. Wei, P., Wang, B.J., Li, H., Wang, L., Peng, S., Zhang, L. A comparative study of compression behaviors of cross-laminated timber and glued-laminated timber columns. Construction and Building Materials. 2019. 222. Pp. 86–95. DOI: 10.1016/j.conbuildmat.2019.06.139
12. Rimshin, V.I., Labudin, B.V., Melekhov, V.I., Orlov, A.O., Kurbatov, V.L. Improvement of strength and stiffness of components of main struts with foundation in wooden frame buildings. ARPN Journal of Engineering and Applied Sciences. 2018. 13(11). Pp. 3851–3856.
13. Rimshin, V., Labudin, B., Morozov, V., Orlov, A., Kazarian, A., Kazaryan, V. Calculation of Shear Stability of Conjugation of the Main Pillars with the Foundation in Wooden Frame Buildings. International Scientific Conference Energy Management of Municipal Facilities and Sustainable Energy Technologies EMMFT 2018. 2019. Pp. 867–876. Springer International Publishing.
14. CEN EN 1995−1−1:2004/A2−2014 Eurocode 5: Design of timber structures − Part 1−1: General − Common rules and rules for buildings.
15. Šmak, M., Straka, B. Development of new types of timber structures based on theoretical analysis and their real behaviour. Wood Research. 2014. 59(3). Pp. 459–470.
16. Lokaj, A., Klajmonová, K. Round timber bolted joints exposed to static and dynamic loading. Wood Research. 2014. 59(3). Pp. 439–448.
17. Karelskiy, A.V., Zhuravleva, T.P., Labudin, B.V. Load-to-failure bending test of wood composite beams connected by gang nail. Magazine of Civil Engineering. 2015. 54(2). Pp. 77–85. DOI: 10.5862/MCE.54.9
18. Chernykh, A., Danilov, E., Koval, P. Stiffness Analysis of Connections of LVL Structures with Claw Washers. Lesnoy Zhurnal (Forestry Journal). 2020. 4. Pp. 157–167. DOI: 10.37482/0536-1036-2020-4-157-167
19. Baszeń, M. Semi-rigid Behavior of Joints in Wood Light-frame Structures. Procedia Engineering. 2017. 172. Pp. 88–95. DOI: 10.1016/j.proeng.2017.02.022
20. Hassanieh, A., Valipour, H. Experimental and numerical study of OSB sheathed-LVL stud wall with stapled connections. Construction and Building Materials. 2020. 233. 117373. DOI: 10.1016/j.conbuildmat.2019.117373
21. Labudin, B.V., Popov, E.V., Vladimirova, O.A., Sopilov, V.V., Bobyleva, A.V. Wood-Composite Structures with Non-Linear Behavior of Semi-Rigid Shear Ties. Construction of Unique Buildings and Structures. 2021. 97. 9702. DOI: 10.4123/CUBS.97.2
22. Popov, E.V., Sopilov, V.V., Bardin, I.N., Lyapin, D.M. (2021). Calculation of Vertical Deformations of Composite Bending Wooden Structures with Non-linear Behavior of Shear Bonds. Environmental and Construction Engineering: Reality and the Future. Pp. 109–116. Springer International Publishing.
23. Ayough, P., Ramli Sulong, N.H., Ibrahim, Z., Hsiao, P.C. Nonlinear analysis of square concrete-filled double-skin steel tubular columns under axial compression. Engineering Structures. 2020. 216. 110678. DOI: 10.1016/j.engstruct.2020.110678
24. Chen, Y., Jin, L. From continuous to snapping-back buckling: A post-buckling analysis for hyperelastic columns under axial compression. International Journal of Non-Linear Mechanics. 2020. 125. 103532. DOI: 10.1016/j.ijnonlinmec.2020.103532
25. Popov, E.V., Karelsky, A.V., Sopilov, V.V., Labudin, B.V., Cherednichenko, V.V. Calculation features of compressed-bent build-up timber columns with nonlinear-deformable shear bracings. IOP Conference Series: Materials Science and Engineering. 2022. 1211(1). 012007. DOI: 10.1088/1757-899x/1211/1/012007

Information about author:

Egor Popov, *PhD in Technical Sciences*
ORCID: https://orcid.org/0000-0002-8950-7558
E-mail: EPV1989@yandex.ru

Boris Labudin, *Doctor of Technical Sciences*
ORCID: https://orcid.org/0000-0002-2547-3096
E-mail: sevned@mail.ru

Anatolij Konovalov, *PhD in Technical Sciences*

ORCID: https://orcid.org/0000-0003-2810-6336
E-mail: a.konovalov@narfu.ru

Alexander Karelskiy,
E-mail: kaw_79@mail.ru

Valerii Sopilov,
ORCID: https://orcid.org/0000-0002-1236-5950
E-mail: sopilov.v@edu.narfu.ru

Aleksandra Bobyleva,
ORCID: https://orcid.org/0000-0002-1216-7567
E-mail: aleksandra-bobyleva@mail.ru

Denis Stolypin,
ORCID: https://orcid.org/0000-0003-0153-8729
E-mail: Stolypin.Denis.A@yandex.ru

Received 12.05.2022. Approved after reviewing 17.01.2023. Accepted 17.01.2023.

Magazine of Civil Engineering

ISSN 2712-8172

journal homepage: http://engstroy.spbstu.ru/

Research article

UDC 691

DOI: 10.34910/MCE.119.5

Dynamic response characteristics of CFRP/steel-cylinder confined rubber cement mortar based on cyclic impact loading

R.-Z. Yang[1] ✉, ***Y. Xu***[1], ***P.-Y. Chen***[2]

[1] State Key Laboratory of Mining Response and Disaster Prevention and Control in Deep Coal Mines, Anhui University of Science and Technology, Huainan, China

[2] School of Civil Engineering and Architecture, Anhui University of Science and Technology, Huainan, China

✉ *Rongzhouy@outlook.com*

Keywords: cyclic loads, rubber, mechanical properties, stress-strain curves, strain rate, energy absorption, cracks

Abstract. Rubber cement-based material is one of the important ways of utilizing waste rubber. Fatigue failure and impact failure are the most common failure forms of concrete structures, but the low stiffness and low strength of rubber cement-based materials do no allow them to be used in the main bearing structure. Therefore, the use of appropriate reinforcement materials and technical methods to effectively improve the yield stiffness, bearing capacity, ductility, and energy dissipation capacity of rubber cement-based materials can not be ignored. To explore the dynamic response characteristics of rubber cement mortar (RCM) with different confine conditions, the split Hopkinson pressure bar (SHPB) cyclic impact tests of four kinds of confined RCM were carried out. Firstly, the four different confine modes of RCM were designed by using the carbon fiber reinforced polymer (CFRP) sheet and steel cylinder. Then, the SHPB test system was used to carry out the amplitude-enhanced cyclic impact tests of RCM with different confine modes. Lastly, the dynamic mechanical behavior, energy behavior, dynamic damage, and failure modes of RCM with different confine modes were compared and analysed. The results show that the end faces and side of RCM were confined effectively by using the CFRP sheet and steel cylinder, which strengthened the structural resistance of RCM. However, with the simultaneous increase in impact load and impact times, stiffness degradation still occurred due to the cumulative effect of fatigue damage. The end friction constraint of the CFRP sheet and the passive confining pressure constraint of the CFRP sheet/steel cylinder significantly improved the energy dissipation capacity and impact resistance of RCM, controlled and delayed the transverse expansion deformation and crack development of RCM, and ensured the minimum damage of RCM structure. The purpose of this paper is to provide a reference for further promoting the resource utilization of waste rubber and the practical engineering application of rubber cement-based materials.

Funding: Scientific Research Foundation for High-level Talents of Anhui University of Science and Technology (2022yjrc84)

Citation: Yang, R.-Z., Xu, Y., Chen, P.-Y. Dynamic response characteristics of CFRP/steel-cylinder confined rubber cement mortar based on cyclic impact loading. Magazine of Civil Engineering. 2023. 119(3). Article no. 11905. DOI: 10.34910/MCE.119.5

1. Introduction

Concrete material is commonly used in civil engineering and national defense engineering [1]. Fatigue failure and impact failure are the most common failure forms of concrete structures [1–3]. Under the action of vehicle load, wind load, seismic load, frequent explosion and impact loads, and other fatigue loads, due to the evolution of internal microcracks and the development of damage, once the damage value exceeds the critical threshold, concrete will lose its bearing capacity, resulting in serious property losses and casualties [2]. Up to now, the problems of fatigue failure and dynamic damage of concrete materials are still prominent, especially in the aspect of dynamic fatigue failure. For this reason, many researchers have carried out a large number of experimental studies on the development of anti-fatigue concrete materials [4–5], the strengthening methods of concrete [6–7], and the impact resistance of concrete materials [8–9].

In the aspect of anti-fatigue concrete materials, a series of concrete materials such as fiber-reinforced concrete [5, 10], plastic concrete [11–12], and rubber concrete [13–14] have been developed, which improve the mechanical properties of ordinary concrete to some extent. However, some studies [13–18] have shown that rubber concrete materials have more outstanding properties in fatigue resistance [13–14], impact resistance [15–16], and explosion resistance [17–18]. As a result, rubber cement-based materials have attracted the attention of researchers, which makes them become the focus of the current research. Lv et al. [14] studied the fatigue behavior of self-compacting rubber lightweight aggregate concrete (SCRLC) under uniaxial compression. The results [14] show that the fatigue life and fatigue strain of SCRLC generally increases with the increase of rubber particle substitution rate, and the fatigue strain increases with the increase of cycle times. The fatigue performance of SCRLC is better than that of normal concrete. Yang et al. [15] carried out SHPB dynamic mechanical tests of rubber concrete under four loading modes. The results [15] show that rubber concrete shows ideal crack resistance and fatigue impact resistance. Yang et al. [17] carried out a field blasting test on the reinforced rubber concrete slab and proved that the reinforced rubber concrete slab is a practical explosion-proof structure, especially under the action of high energy explosion. Although rubber cement-based materials have a wide application prospect in earthquake resistance [19–20], roads [4, 21], and protective engineering [17–18], the low stiffness and strength of rubber cement-based materials are the key factors that it is difficult to be used as the main bearing structure.

In terms of strengthening methods of concrete, the use of appropriate reinforcement materials and techniques can significantly improve the yield stiffness, bearing capacity, ductility, and energy dissipation capacity of concrete materials. Carbon fiber reinforced polymer (CFRP) is a kind of composite material widely used in the field of civil engineering [22]. Because CFRP has superior mechanical properties to traditional materials, its application in the reinforcement and repair of concrete structures has been developed rapidly [22–32]. To comprehensively evaluate the strengthening effect of CFRP on concrete, researchers studied in detail the mechanical properties of CFRP-confined concrete from single to structure and from test to simulation. Wang et al. [29] carried out the SHPB cyclic impact compression test of CFRP-confined cement mortar, and the results showed that CFRP reduced the generation of cracks inside specimens, improved the ductility of specimens, and CFRP-confined cement mortar showed better impact resistance and energy absorption capacity. Xiong et al. [30] carried out an experimental study on the compressive performance of CFRP-confined concrete under a high strain rate. The results [30] show that CFRP can improve the strength and ductility of concrete. Li et al. [31] to clarify the bond-slip behavior of CFRP at the high loading rate (more than 800 mm/s), a new method for high loading rate impact test using an improved SHPB device was proposed, and the constitutive equation of dynamic bond-slip behavior of CFRP-concrete interface was established. Zhai et al. [32] proposed a method of using CFRP external bonding to repair prestressed concrete cylindrical tubes.

In addition to strengthening concrete with CFRP sheets, strengthening concrete with steel cylinder/tube with high stiffness is also a common reinforcement method in the field of stability of concrete structures, such as concrete-filled steel tubes [33–34]. However, there is little research on the dynamic fatigue impact of concrete strengthened with the steel cylinder. Tam et al. [33] studied the effect of the expansive agent on the axial compression behavior of recycled concrete-filled steel tubular short columns. It is found that due to the improvement of constraint conditions, the strength of expansive concrete-filled steel tubular columns is slightly higher than that of its benchmark concrete-filled steel tubular columns. Yang et al. [34] conducted an experimental study on the impact force, deformation, and energy absorption performance of a square steel tubular high-strength concrete column under transverse impact load by using a drop weight testing machine. The results [34] show that the square steel tubular high-strength concrete column has a strong impact resistance, which shows a higher impact platform value and a smaller deflection.

Based on the above research results, it can be known that although researchers have done a large number of experimental studies on rubber concrete and CFRP/steel cylinder confined concrete, they have never combined rubber concrete material with CFRP/steel cylinder reasonably and effectively. If the rubber concrete material can be effectively strengthened by using CFRP/steel cylinder, and the mode of "complementary advantages" between different materials can be formed, it plays a key role in fully improving the bearing capacity and fatigue performance of rubber concrete material. To solve this problem, this paper took RCM as the research object, used CFRP/steel cylinder to strengthen it in different confine methods, and the amplitude-enhanced cyclic impact tests with the help of the SHPB test system were carried out. The dynamic response characteristics of CFRP/steel cylinder confined RCM were deeply explored and analysed from the aspects of dynamic mechanical behavior, energy characteristics, damage evolution, and failure states.

2. Methods

2.1. Test materials and specimen preparation

2.1.1. Test raw materials

Cementitious material: 42.5 grade ordinary Portland cement (P.O 42.5); Mixed water: laboratory tap water; Fine aggregates: natural river sand with a density of 2600 kg/m^3 and a fineness modulus of 2.60 [35]; Rubber fine aggregates: waste tire rubber particles with a mesh of 20 and a density of 1120 kg/m^3 [35]; Confine materials: CFRP sheet and steel cylinder; CFRP sheet impregnated adhesive: epoxy resin and curing agent.

2.1.2. Specimen preparation

The detailed process of specimen preparation with four different confine conditions in this experiment is shown in Fig. 1. In the first stage of specimen preparation: According to the standard JGJ/T 70-2009 [36], the specimens were removed after 24 hours of casting and molding, and the specimens after demoulding were placed in an environment with a temperature of (20 ± 2) °C and humidity greater than 90 % for 28 days. In the second stage of specimen preparation: Firstly, the unconfined impact specimen with a size of Φ 50 mm × h 25 mm was obtained after a series of the processing; Secondly, two kinds of impact specimens with different CFRP confines were prepared by using CFRP sheet impregnated adhesive to paste single-layer CFRP sheet on the upper, lower round end and side of the unconfined impact specimen; Finally, the passive confining pressure confine was carried out on the unconfined impact specimen with the help of high modulus steel cylinder. Combined with the preparation method, the impact specimens with four different confine conditions were obtained. In addition, the static uniaxial compression test of unconfined RCM specimens with a size of Φ 50 mm × h 100 mm was carried out by using WAW-2000 electro-hydraulic servo universal testing machine, and the static compression strength was about 15.45 MPa.

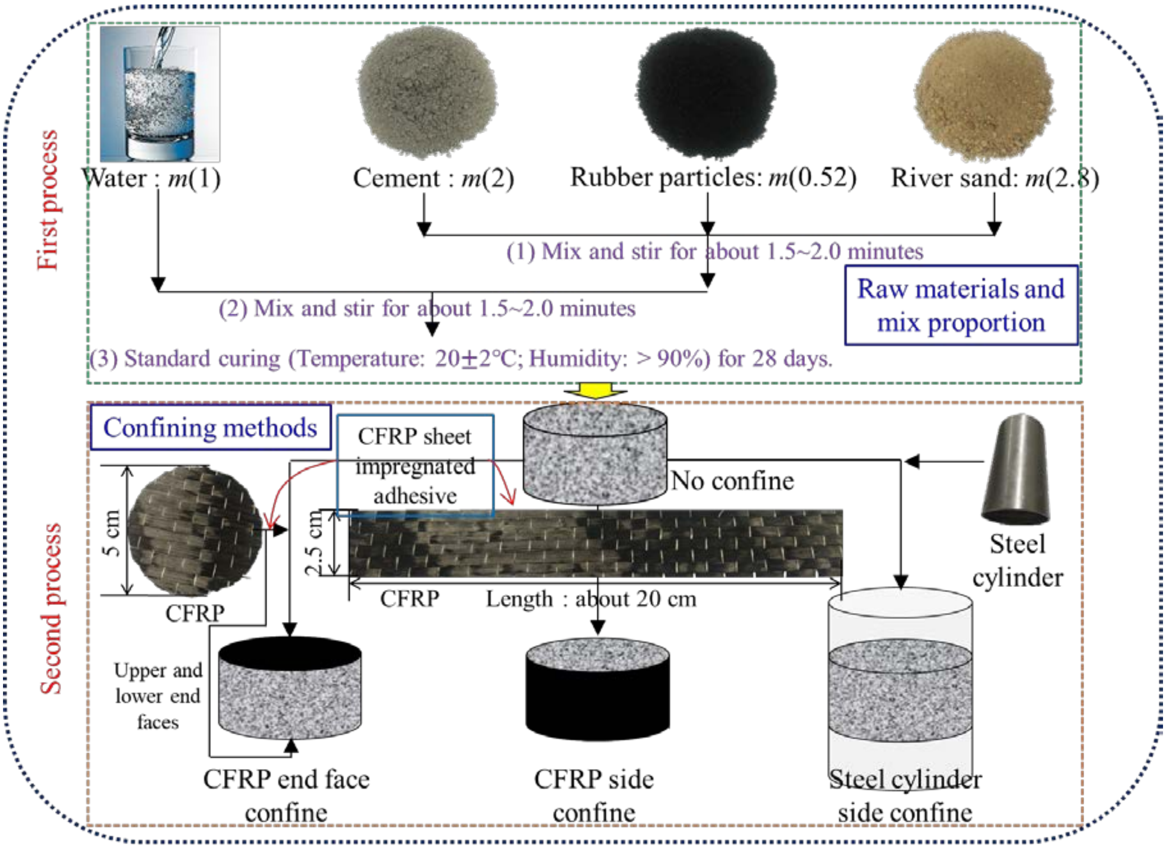

Figure 1. The preparation process of the specimens with four different confine conditions.

In this test, the physical and technical parameters of the CFRP sheet, CFRP sheet impregnated adhesive, and steel cylinder are shown in Table 1.

Table 1. Physical and technical parameters of CFRP sheet, CFRP sheet impregnated adhesive, and steel cylinder.

CFRP sheet		CFRP sheet impregnated adhesive		Steel cylinder	
Strength grading	High strength level-2			Material	High-alloy steel
Gram weight (g/m^2)	200				
Theoretical thickness (mm)	0.111	Composition	① Epoxy resin, ②curing agent	Height (mm)	100.50
Tensile strength (MPa)	3325				
Elastic modulus (MPa)	2.40 × 10^5	Mixed proportion	2(①) : 1(②)	Thickness (mm)	1.96
Elongation (%)	1.74				
General component-Design value of tensile strength (MPa)	2000			Inner diameter (mm)	51.67
General component-Design value of elastic modulus (MPa)	2.0 × 10^5	Design value of shear strength (MPa)	18	Density (g/cm^3)	7.85
General component-Design value of strain resistant (%)	1	Solid content (%)	99.6		

2.2. SHPB system and test principle

SHPB system: this test used a variable cross-section SHPB test system with a diameter of 50 mm in the Impact Dynamics Laboratory of Anhui University of Science and Technology, as shown in Fig. 2. The bar material in the SHPB test system is alloy steel with a density of 7.8 g/cm^3 and an elastic modulus of 210 GPa. The power system consists of high-pressure nitrogen, gas valve, launch chamber, impact bars, and automatic launcher. The data acquisition and processing system consisting of the resistance strain gauge, KD6009 strain amplifier, MDO3024 oscilloscope, and computer.

Test principle: the SHPB testing principle is based on the one-dimensional elastic stress wave hypothesis and the stress/strain uniformity hypothesis (two basic hypotheses) [37]. According to the strain signals collected by strain gauges on the incident bar and transmission bar, combined with one-dimensional stress wave theory [37] and cyclic impact deformation effect [15, 37–38], the equations for calculating strain rate, strain, and stress of cyclic impact specimens under the three-wave method can be derived:

$$\begin{cases} \varepsilon_{i+1} = \dfrac{C\int_0^t \left(\varepsilon_{I(i+1)} - \varepsilon_{R(i+1)} - \varepsilon_{T(i+1)}\right)\mathrm{d}t}{L_{\mathrm{S}(i-1)} - \varepsilon_i L_{\mathrm{S}(i-1)}} \\ \dot{\varepsilon}_{i+1} = \dfrac{C\left(\varepsilon_{I(i+1)} - \varepsilon_{R(i+1)} - \varepsilon_{T(i+1)}\right)}{L_{\mathrm{S}(i-1)} - \varepsilon_i L_{\mathrm{S}(i-1)}} \\ \sigma_{i+1} = \dfrac{2AE}{\pi D_{\mathrm{S}i}^2}\left(\varepsilon_{I(i+1)} + \varepsilon_{R(i+1)} + \varepsilon_{T(i+1)}\right) \end{cases} \tag{1}$$

where, ε_{i+1}, $\dot{\varepsilon}_{i+1}$, and σ_{i+1} are the compressive strain, the compressive strain rate, and the compressive stress of the specimen under the (i+1)-th cycle impact, respectively; E, A, and C are the elastic modulus, the cross-sectional area, and the wave velocity of the compression bars, respectively; $\varepsilon_{I(i+1)}$, $\varepsilon_{R(i+1)}$, and $\varepsilon_{T(i+1)}$ are the incident strain, the reflection strain, and the transmission strain of the compression bars under the (i+1)-th cycle impact, respectively; $L_{\mathrm{S}i}$ is the length of the specimen under the i-th cycle impact; $D_{\mathrm{S}i}$ is the diameter of specimen under the i-th cycle impact.

The equations of the three-wave method were further simplified to that of the two-wave method:

$$\begin{cases} \varepsilon_{i+1} = \dfrac{2C\int_0^t \left(\varepsilon_{I(i+1)} - \varepsilon_{T(i+1)}\right)\mathrm{d}t}{L_{\mathrm{S}(i-1)} - \varepsilon_i L_{\mathrm{S}(i-1)}} \\ \dot{\varepsilon}_{i+1} = \dfrac{2C\left(\varepsilon_{I(i+1)} - \varepsilon_{T(i+1)}\right)}{L_{\mathrm{S}(i-1)} - \varepsilon_i L_{\mathrm{S}(i-1)}} \\ \sigma_{i+1} = \dfrac{4AE}{\pi D_{\mathrm{S}i}^2}\varepsilon_{T(i+1)} \end{cases} \tag{2}$$

It should be noted that the diameter of the circular end face of the specimen changes very little in the process of cyclic impact. To facilitate the calculation of the stress of the specimen under the cyclic impact, it can be assumed that the diameter of the circular end face of the specimen remains unchanged in the process of cyclic impact, that is, the area of the circular end face is approximately constant [15]:

$$A_{\mathrm{S}0} = \frac{\pi D_{\mathrm{S}0}^2}{4} \approx A_{\mathrm{S}i} = \frac{\pi D_{\mathrm{S}i}^2}{4} \tag{3}$$

Therefore, Eq. (4) can be obtained from Eqs. (2)-(3):

$$\sigma_{i+1} = \frac{4AE}{\pi D_{\mathrm{S}i}^2}\varepsilon_{T(i+1)} \approx \frac{4AE}{\pi D_{\mathrm{S}0}^2}\varepsilon_{T(i+1)} \tag{4}$$

where, $A_{\mathrm{S}0}$ and $D_{\mathrm{S}0}$ are the initial cross-sectional area and the initial diameter of the specimen; $A_{\mathrm{S}i}$ is the cross-sectional area of the specimen under the *i*-th cycle impact.

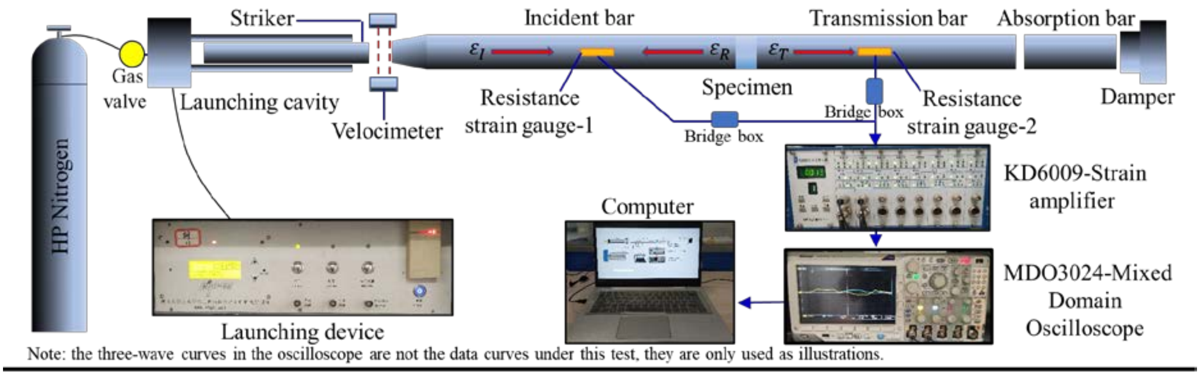

Figure 2. Schematic diagram of SHPB dynamic test system.

2.3. Test types and results

In the experiment, gradually increasing cyclic impact pressure was used to carry out cyclic impact tests on the specimens with four different confine conditions. The test types and test results are listed in Table 2.

Table 2. Test types and test results of the specimens.

Test types		Sample type	Impact pressure (MPa)	Number of cyclic impacts
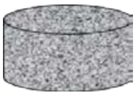	No confine	No-C-1	0.2	3
		No-C-2	0.3	
		No-C-3	0.4	
	CFRP end face confine	CFRP-E-C-1	0.2	4
		CFRP-E-C-2	0.3	
		CFRP-E-C-3	0.4	
		CFRP-E-C-4	0.5	
	CFRP side confine	CFRP-S-C-1	0.2	4
		CFRP-S-C-2	0.3	
		CFRP-S-C-3	0.4	
		CFRP-S-C-4	0.5	
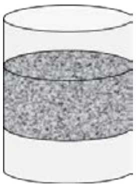	Steel cylinder side confine	SC-S-C-1	0.2	7
		SC-S-C-2	0.3	
		SC-S-C-3	0.4	
		SC-S-C-4	0.5	
		SC-S-C-5	0.6	
		SC-S-C-6	0.7	
		SC-S-C-7	0.8	

3. Results and Discussion

3.1. Stress-strain curves

The stress-strain curves of specimens with four different confines during the cyclic impact test are shown in Fig. 3. It can be seen from Fig. 3 that the stress-strain curves of specimens with four different confines showed similar behavior evolution characteristics to some extent, but there were also some obvious differences.

Similarly, the peak stress of specimens increased at first and then decreases with the increase of cyclic impact times, which reflected the evolution characteristic of "first cyclic hardening and then cyclic softening". The peak strain and ultimate strain of specimens increased with the synchronous increase of impact times and impact load, which showed obvious cyclic deformation ductility. The difference is that, compared with the specimen No-C, the impact resistance times of the specimens CFRP-E-C, CFRP-S-C, and SC-S-C were increased, especially the specimen SC-S-C showed better impact resistance, which showed that the end faces and side of the confined RCM specimen can improve its impact resistance. When the strength and stiffness of the confining material were larger, the specimen can withstand greater impact times and impact force. Many studies [3, 39–40] have shown that compared with normal cement-based materials, rubber cement-based materials have better impact resistance, but because of their low strength, rubber cement-based materials are effectively limited to a wider range of engineering applications. More importantly, under high-energy impact load, rubber cement-based materials will also lose structural resistance due to lower strength and then lose impact resistance. In other words, rubber cement-based materials will be seriously damaged due to low structural resistance under high-energy impact load, so that they are vulnerable to a single blow. As can be seen from Fig. 3, compared with specimen No-C, the maximum cyclic peak stress of specimens CFRP-E-C, CFRP-S-C, and SC-S-C increased by 28.34 %, 105.94 %, and 201.37 %, respectively. Thus it can be seen that the effective confinement on the end face and side of the RCM specimen can obviously improve the structural resistance of the material itself.

On the whole, it can be seen that the stress-strain curves of specimens under four different confines mainly showed two evolution types in the process of cyclic impact test. That is, stress-strain curve type-1 and stress-strain curve type-2 (Fig. 4). The main difference between stress-strain curve type-1 and stress-strain curve type-2 was that stress-strain curve type-1 mainly occurred in the first few impacts in the whole process of cyclic impact, while stress-strain curve type-1 mainly occurred in the last few impacts in the whole process of cyclic impact. The specific results are as follows: (1) at the initial stage of loading (*OA*), stress-strain curve type-1 had an obvious elastic stage, while stress-strain curve type-2 showed an obvious compaction stage; (2) in the later stage of loading (*BC*), stress-strain curve type-1 mainly occurred post-peak stress unloading or partial damage fracture, while stress-strain curve type-2 mainly occurred post-peak fracture damage; (3) in the elastic-plastic deformation stage (*AB*) of the stress-strain curves, it can be seen that the deformation modulus of the stress-strain curves decreased continuously with the synchronous increase of impact times and impact load, especially reflected in the stress-strain curves of specimens CFRP-E-C and CFRP-S-C in the fourth impact (Fig. 3(b)-(c) and Fig. 4). According to fatigue damage mechanics, the essential reason leading to the behavior evolution characteristics of the above stress-strain curves and the difference between stress-strain curves is mainly due to the increase of structural damage and the degradation of stiffness due to the existence of damage cumulative effect or fatigue damage effect, which is mainly reflected in the generation of cracks, the development of cracks, and the formation of the fracture surface [2, 15, 41].

From the point of view of energy, the specimen mainly goes through three processes: energy accumulation, energy dissipation, and energy release in the process of cyclic impact, which is accompanied by four kinds of energy: compaction plastic energy, elastic energy, elastic-plastic energy, and post-peak fracture energy (see Fig. 4) [15]. Different energy densities of specimens during cyclic impact were defined, as shown in Fig. 4. The evolution characteristics of the energy density of the stress-strain curves are as follows: (1) In the *OA* stage, the elastic energy density was mainly reflected in the stress-strain curve type-1, and the compaction plastic energy density was mainly reflected in the stress-strain curve type-2, and the compaction plastic strain was significantly greater than the elastic strain. On this point, the specimen CFRP-E-C was more obvious than the specimen CFRP-S-C, which showed that the compaction hardening effect of the specimen CFRP-S-C was greater than that of the specimen CFRP-E-C. (2) In the *AB* stage, the elastic-plastic energy density of stress-strain curve type-1 was higher than that of stress-strain curve type-2, which indicated that the cyclic cumulative damage seriously weakened the structural bearing capacity of the specimen. Compared with specimen No-C, the elastic-plastic energy densities of specimens CFRP-E-C, CFRP-S-C, and SC-S-C were significantly increased, especially the elastic-plastic energy densities of specimens CFRP-S-C and SC-S-C were significantly increased under the side confine. (3) In the *BC* stage, the post-peak fracture energy density of stress-strain curve type-1 was higher than that of stress-strain curve type-2, and the post-peak residual bearing capacity of the specimens decreased significantly after the previous cyclic impacts. However, compared with the specimens with other confines, the post-peak fracture energy of the specimen SC-S-C decreased slightly in the last cycle, and still had larger post-peak fracture energy. To sum up, reasonable confine and reinforcement of RCM with effective confine materials can improve the structural fracture energy of RCM, which required higher external impact energy to cause structural damage to RCM after confine reinforcement, and then improved the impact resistance of RCM.

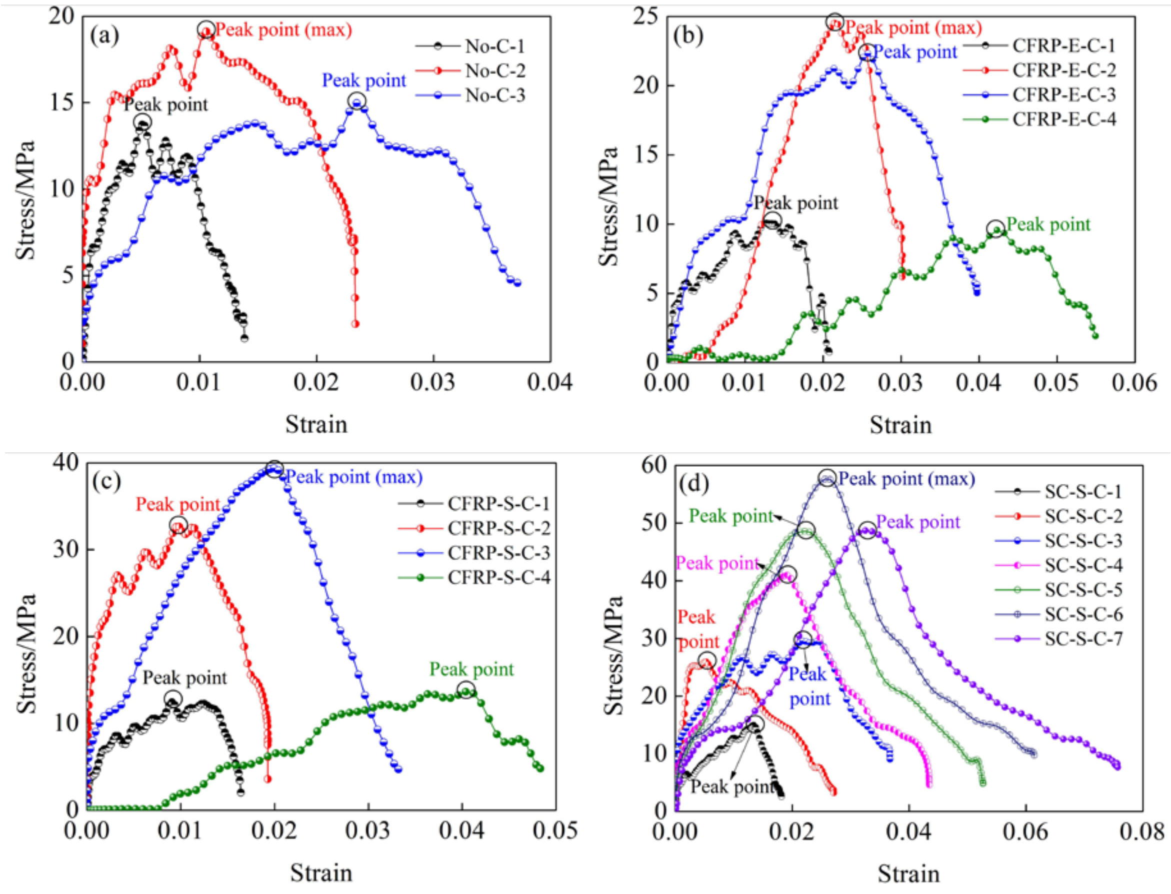

Figure 3. Cyclic impact stress-strain curves of the specimens with four different confine conditions: (a) No-C; (b) CFRP-E-C; (c) CFRP-S-C; and (d) SC-S-C.

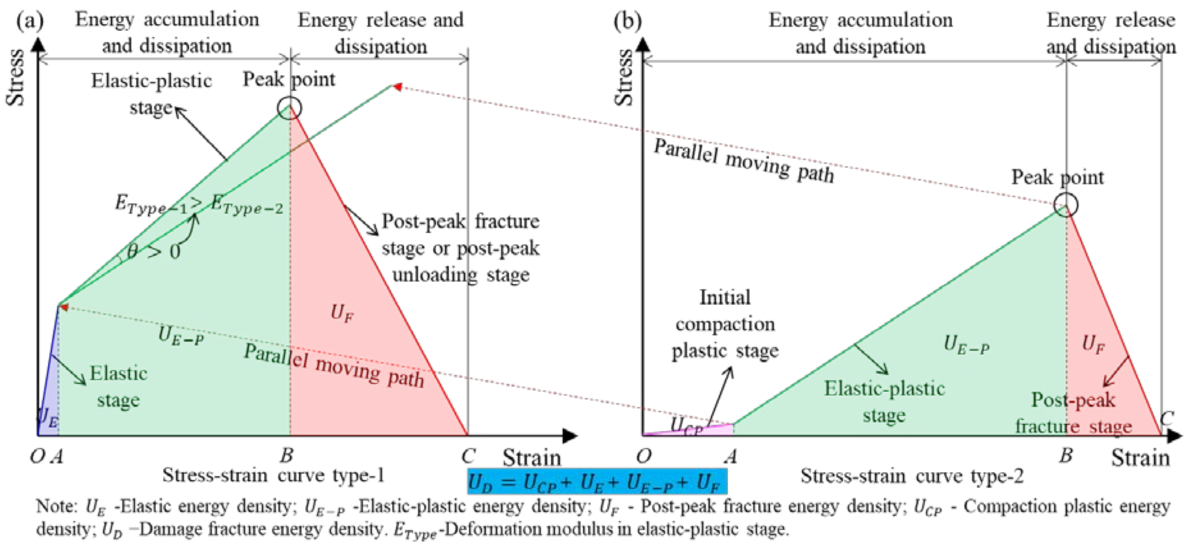

Figure 4. Simplified types cyclic impact stress-strain curves of the specimens with four different confine conditions: (a) stress-strain curve type-1; and (b) stress-strain curve type-2.

3.2. Strain rate-time curves and stress rate-time curves

The strain rate-time curves and stress rate-time curves of specimens with four different confine conditions during cyclic impact tests are shown in Fig. 5-6. It can be seen from Fig. 5-6 that the strain rate-time curves and stress rate-time curves of specimens with four different confines showed similar behavior evolution characteristics to some extent, but the behavior evolution characteristics of strain rate-time curves and stress rate-time curves were quite different.

3.2.1. Strain rate-time curves

The observation and analysis of the evolution characteristics of the strain rate-time curves showed that the strain rate-time curves were approximately longitudinal axisymmetric, and its evolution characteristics became more obvious with the synchronous increase of impact times and impact load. The strain rate-time curves can be divided into three evolution stages: Strain rate growth stage, strain rate fluctuation stage, and strain rate attenuation stage [Fig. 5, Fig. 7 (a)]. The evolution characteristics of the strain rate-time curves are as follows: (1) In the strain rate growth stage (0 ~ 50 μs), the strain rate increased linearly at the initial stage of impact load, and the strain rate increased obviously with the synchronous increase of impact times and impact load, which led to a certain strain of the specimen. (2) In the strain rate fluctuation stage (50 ~ 250 μs), the strain rates of the specimens mainly showed the development trend of horizontal fluctuation, and the horizontal fluctuation of strain rate lasted for a relatively long time, reaching about 200 μs, resulting in a larger strain of the specimen, so that it exceeded the peak strain. Therefore, the loading process of approximately constant strain rate was the main stage leading to the damage of the specimen. (3) In the strain rate attenuation stage (250 ~ 300 μs), the strain rates of the specimens under the impact load in the later period decreased rapidly in a linear form mainly due to the unloading of the impact load, and the strain rate attenuation rate increased obviously with the synchronous increase of the impact times and the impact load. In the process of strain rate attenuation to 0, the strain continues to increase to the maximum.

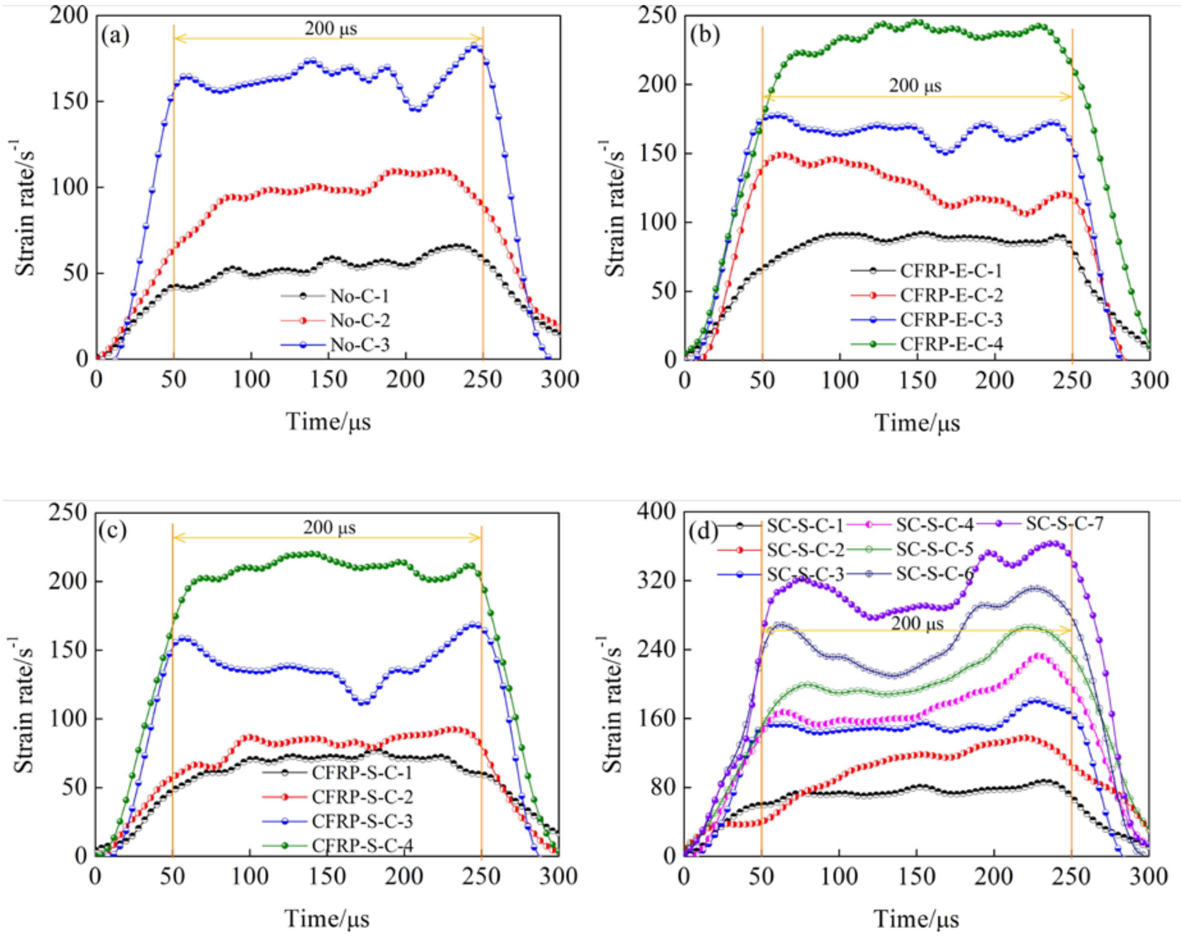

Figure 5. Cyclic impact strain rate-time curves of the specimens with four different confine conditions: (a) No-C; (b) CFRP-E-C; (c) CFRP-S-C; and (d) SC-S-C.

3.2.2. Stress rate-time curves

For the stress rate-time curve, the evolution characteristics of its behavior are more complex, but on the whole, there are certain rules to follow. The stress rate-time curves as a whole showed five stages: initial fluctuation stability (*a*-*b*), positive abrupt change (*b*-*c*-*d*), medium-term fluctuation stability attenuation (*d*-*e*-*f*), negative abrupt change (*f*-*g*-*h*), and later fluctuation stability (*h*-*i*). The shapes of the stress rate-time curves were approximately central-symmetric, while the corresponding stress-time curves were approximately axisymmetric [Fig. 6, Fig. 7 (b)]. In general, the evolution characteristics of the above stress rate-time curves became more obvious with the synchronous increase of impact times and impact load, but the fluctuation amplitude and peak value of stress rate under the last impact decreased to some extent. Even zero value continued to appear in the initial stage, reflecting the obvious strain-softening phenomenon. According to the simplified stress rate-time curve, the specific evolution characteristics of the stress rate with time are as follows: (1) In the pre-peak stage (*OA*), the stress rate of the specimen was greater than zero, and the strain-softening effect was less than the strain-hardening effect, so the stress increased, and the stress rate reached the maximum at the positive abrupt change point *c*. As can be seen from Fig. 7 (b), when the stress increased to the point after *c*, the stress rate showed a downward trend of first fast and then slow under the strain rate fluctuates steadily, indicating that the specimen had slight structural damage in the *c*-*d*-*e* stage. In the *c*-*d*-*e* stage, as the stress rate decreased to 0, the corresponding stress increased to the maximum and reached the peak stress. (2) In the post-peak stage (*AB*), the stress rate of the specimen was less than zero, and the strain-softening effect was greater than the strain-hardening effect, so the stress decreased, and the stress rate reached the minimum at the negative abrupt change point *g*. As can be seen from Fig. 7 (b), when the stress decreased to the point before *g*, the stress rate showed a downward trend of first slow and then fast under the strain rate fluctuates steadily, indicating that the specimen had large structural damage in the *e*-*f*-*g* stage. Subsequently, the stress rate increased rapidly in the *g*-*h* stage, and then entered a fluctuating and stable state, which indicated that the specimen still had a certain residual bearing capacity after large damage in the post-peak *e*-*f*-*g* stage.

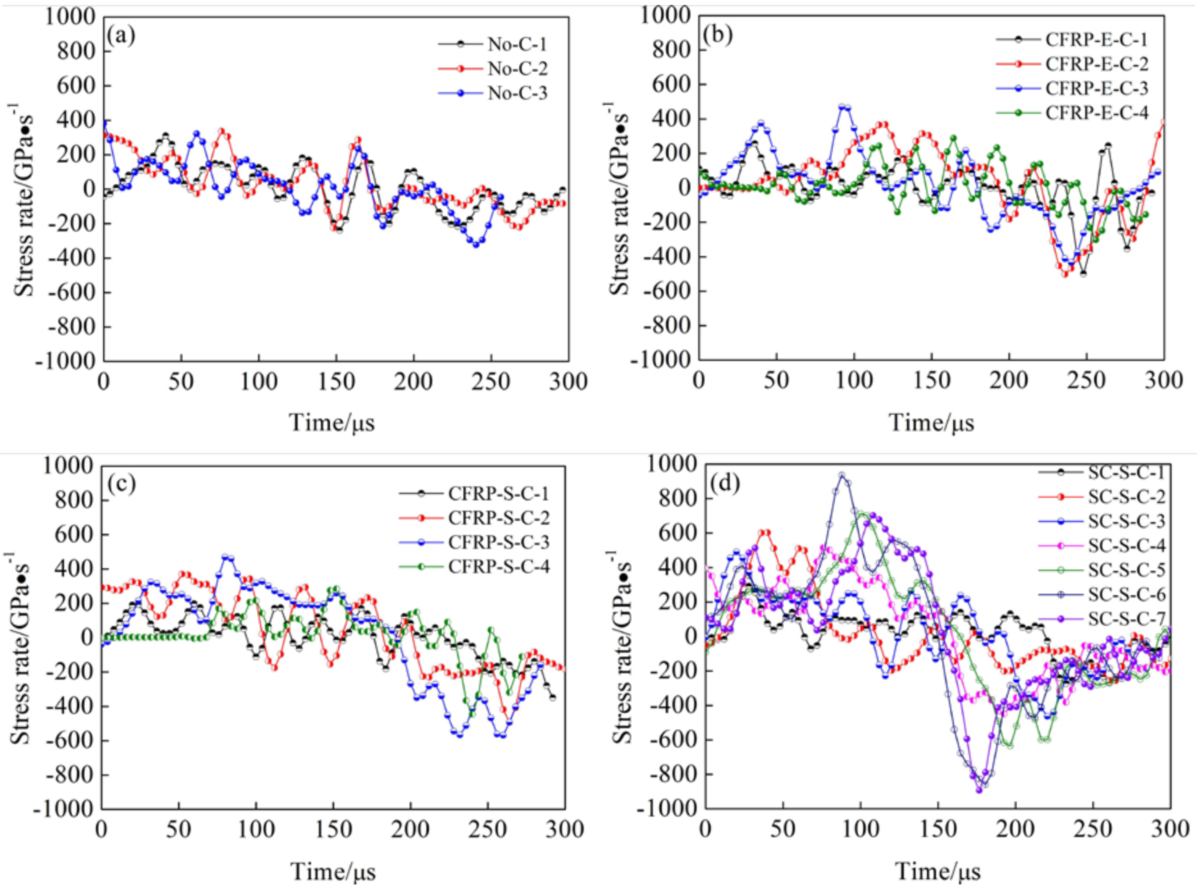

Figure 6. Cyclic impact stress rate-time curves of rubber cement mortar specimens with four different confine conditions: (a) No-C; (b) CFRP-E-C; (c) CFRP-S-C; and (d) SC-S-C.

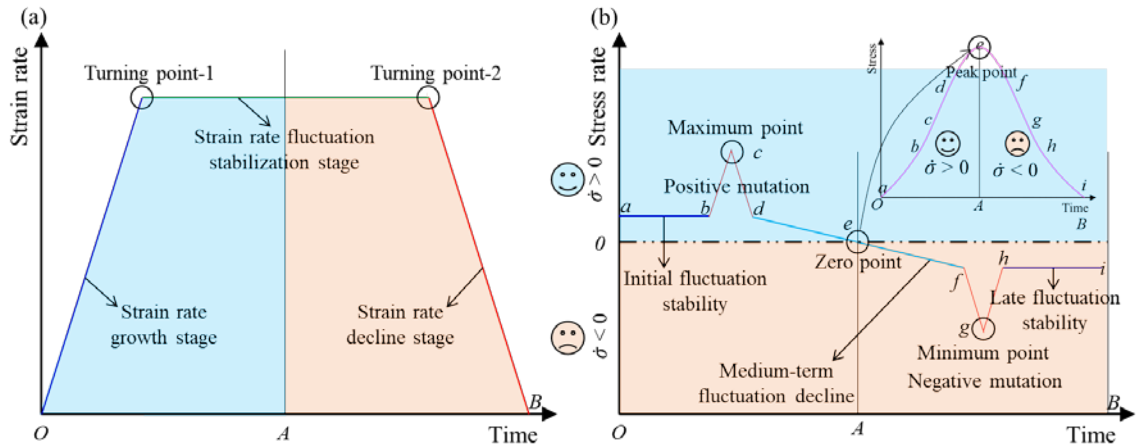

Figure 7. Simplified behavior characteristics of (a) strain rate-time curve and (b) stress rate-time curve of the specimens with four different confine conditions under cyclic impact test.

3.3. Energy evolution characteristics

3.3.1. Energy in test and its calculation principle

Based on the one-dimensional stress wave theory, the incident energy, reflected energy, and transmitted energy in the SHPB cyclic impact testing process can be obtained from the incident strain, reflected strain, and transmitted strain in the bars, respectively. The specific calculation equations are as follows [42–43]:

$$W_{I,\mathrm{Total}} = \sum_{i}^{n} W_{Ii} \rightarrow W_{Ii} = AEC\int_0^t \varepsilon_{Ii}^2 \mathrm{d}t \qquad (5)$$

$$W_{R,\text{Total}} = \sum_{i}^{n} W_{Ri} \rightarrow W_{Ri} = AEC\int_0^t \varepsilon_{Ri}^2 \mathrm{d}t \tag{6}$$

$$W_{T,\text{Total}} = \sum_{i}^{n} W_{Ti} \rightarrow W_{Ti} = AEC\int_0^t \varepsilon_{Ti}^2 \mathrm{d}t \tag{7}$$

$$W_{D,\text{Total}} = \sum_{i}^{n} W_{Di} \rightarrow W_{Di} = -2AEC\int_0^t \varepsilon_{Ri}\varepsilon_{Ti} \mathrm{d}t \tag{8}$$

where, $W_{I,\text{Total}}$, $W_{R,\text{Total}}$, $W_{T,\text{Total}}$, and $W_{D,\text{Total}}$ are the total incident energy, total reflection energy, total transmission energy, and total damage energy during the whole SHPB cycle impact test, respectively; W_{Ii}, W_{Ri}, W_{Ti}, and W_{Di} are the incident energy, reflection energy, transmission energy , and damage energy under the i-th cycle impact, respectively.

The energy ratio can directly reflect the specific distribution and transformation of energy. To explore the evolution characteristics of energy under cyclic impact from the point of view of energy ratio, according to the above energy calculation method, the corresponding calculation equations of energy ratios are[43]:

$$\begin{cases} \eta_{R,\text{Total}} = \dfrac{W_{R,\text{Total}}}{W_{I,\text{Total}}}; \quad \eta_{Ri} = \dfrac{W_{Ri}}{W_{Ii}} \\ \eta_{T,\text{Total}} = \dfrac{W_{T,\text{Total}}}{W_{I,\text{Total}}}; \quad \eta_{Ti} = \dfrac{W_{Ti}}{W_{Ii}} \\ \eta_{D,\text{Total}} = \dfrac{W_{D,\text{Total}}}{W_{I,\text{Total}}}; \quad \eta_{Di} = \dfrac{W_{Di}}{W_{Ii}} \end{cases} \tag{9}$$

where, $\eta_{R,\text{Total}}$, $\eta_{T,\text{Total}}$, and $\eta_{D,\text{Total}}$ are the total reflection energy ratio, total transmission energy ratio, and total damage energy ratio during the whole SHPB cycle impact tests, respectively; η_{Ri}, η_{Ti}, and η_{Di} are the reflection energy ratio, transmission energy ratio, and damage energy ratio under the i-th cyclic impact, respectively.

3.3.2. Energy and energy ratio

The relationship between the energy, energy ratio and confining conditions, impact times of the specimen under cyclic impact is shown in Fig. 8-9. Among them, Fig. 8 shows the relationship between the total energy, the total energy ratio and the confine conditions in the whole cyclic impact process, and Fig. 9 shows the relationship between the energy ratio and the impact times in the i-th impact process.

In terms of total energy, Fig. 8 (a) shows that the total reflection energy and total incident energy showed the same change with the change of confine conditions, and the total transmission energy and total damage energy showed the same change with the change of confine conditions. The details are as follows: ① Compared with specimen No-C, the total incident energies of specimens CFRP-E-C, CFRP-S-C, and SC-S-C can withstand complete failure under cyclic impact were significantly increased by 123.18 %, 99.60 %, and 535.84 %, respectively. ② Compared with specimen No-C, the total reflected energies dissipated by specimens CFRP-E-C, CFRP-S-C, and SC-S-C in complete failure under cyclic impact were increased by 162.68 %, 90.50 %, and 431.92 % respectively. ③ Compared with specimen No-C, the total transmission energies dissipated by specimens CFRP-E-C, CFRP-S-C, and SC-S-C during complete failure under cyclic impact were significantly increased by 26.95 %, 225.35 %, and 887.23 %, respectively. ④ Compared with specimen No-C, the total damage energies of specimens CFRP-E-C, CFRP-S-C, and SC-S-C can resist complete failure under cyclic impact were significantly increased by 56.07 %, 105.57 %, and 752.65 %, respectively. The above results confirm without a doubt that the CFRP and steel cylinder can significantly improve the energy dissipation capacity and impact resistance of RCM.

In terms of total energy ratio, Fig. 8 (b) shows that total reflection energy ratio > total damage energy ratio > total transmission energy ratio (0.02 ~ 0.06), which showed that total reflection energy and total damage energy were the main conversion objects of total incident energy, but it was undeniable that total reflection energy was the most important dissipation mode of total incident energy. At the same time, as can be seen from Fig. 8 (b), with the change of confine conditions, the total reflection energy ratio, total damage energy ratio, and total transmission energy ratio showed a trend of "first increase then decrease", "first decrease then increase", and "first decrease then increase", respectively, and the total reflection energy ratio and total damage energy ratio were transversely axisymmetric to each other. The details are as follows: ① Total reflection energy ratio: CFRP-E-C > No-C > CFRP-S-C > SC-S-C; ② Total transmission energy ratio: CFRP-E-C < No-C < SC-S-C < CFRP-S-C; ③ Total damage energy ratio: CFRP-E-C < No-C < CFRP-S-C < SC-S-C. The above phenomena show that: ① The end-face restraint reinforcement of RCM with CFRP sheet leads to the increase of the total reflection energy ratio and then leads to the decrease of both the total transmission energy ratio and the total damage energy ratio. The main reason for this phenomenon is that the wave impedance of the CFRP sheet is lower than that of RCM, which further leads to a more mismatch between the wave impedance of CFRP-E-C and SHPB. ② The side restraint reinforcement of RCM with CFRP sheet and steel cylinder leads to the decrease of the total reflection energy ratio, which leads to the increase of the total transmission energy ratio and the total damage energy ratio. The main reason for this phenomenon is that the restrained reinforcement of CFRP sheet and steel cylinder effectively delays the development of cracks in RCM and ensures the minimization of structural damage.

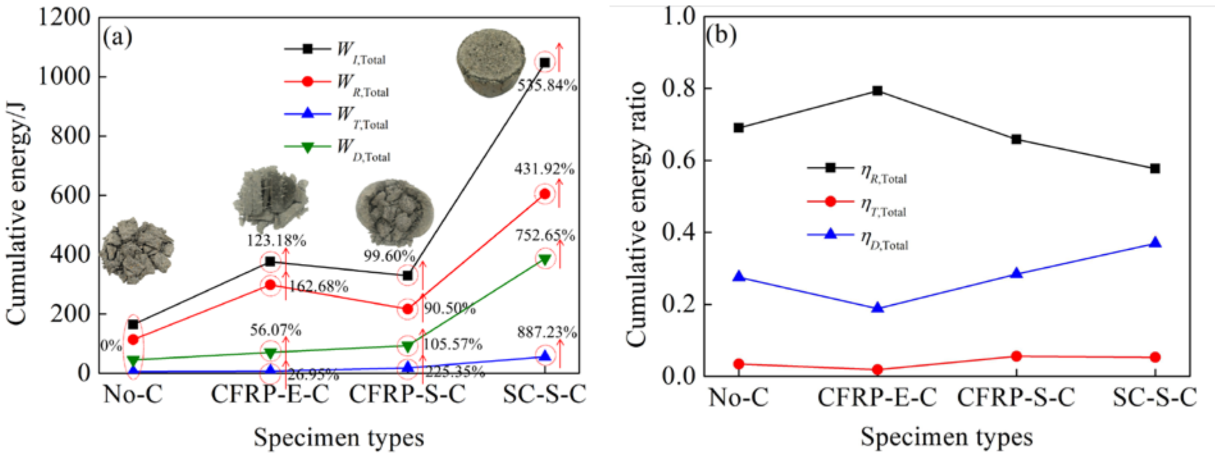

Figure 8. Relationship between (a) cumulative total energy,
(b) cumulative total energy ratio and the confine conditions.

Similarly, in terms of energy ratio, Fig. 9 shows that reflection energy ratio > damage energy ratio > transmission energy ratio, which showed that reflection energy and damage energy were the main conversion objects of incident energy. But it was undeniable that reflection energy was the most important way to dissipate incident energy. At the same time, as can be seen from Fig. 9, on the whole, with the increase of impact times, the reflection energy ratio, damage energy ratio, and transmission energy ratio showed the trend of "first decreasing and then increasing", "first increasing then decreasing", and "first increasing then decreasing", respectively, and the reflection energy ratio and damage energy ratio were transversely axisymmetric to each other. The details are as follows: ① The reason for the larger reflection energy ratio/lower damage energy ratio/lower transmission energy ratio under the first impact is that the initial specimen structure is in a compactible state, and the incomplete dense structure promotes the reflection of stress waves. ② The reason why the reflection energy ratio is larger/the damage energy ratio is smaller/the transmission energy ratio is smaller under the last impact is that the specimen structure is in a loose state due to the damage accumulation effect under the cyclic impact, and the loose structure also promotes the reflection of stress waves. ③ In addition to the first and last impact, in the whole intermediate impact process of cyclic impact, the reason for the smaller reflection energy ratio/larger damage energy ratio/larger transmission energy ratio is that the specimen structure promotes the compaction of the structure due to the first impact or the compaction effect of the previous times, suppresses the reflection of the stress wave and promotes the transmission of the stress wave. For the above results, CFRP-E-C, CFRP-S-C, and SC-S-C are more significant than No-C.

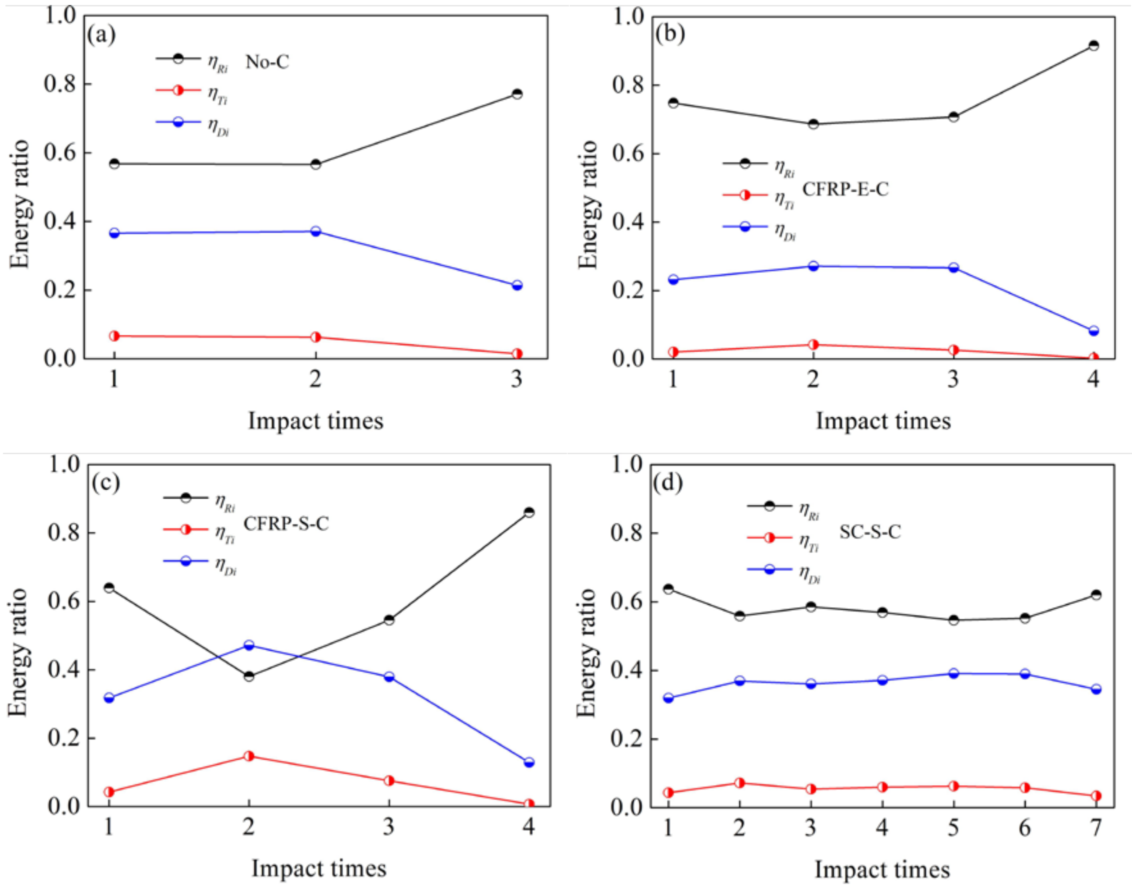

Figure 9. Relationship between energy ratio and impact times:
(a) No-C; (b) CFRP-E-C; (c) CFRP-S-C; and (d) SC-S-C.

3.4. Definition of damage variable and characteristics of damage evolution

3.4.1. Definition of damage variable

To effectively evaluate the effects of four confine conditions on the impact fatigue damage of RCM, and to explore the evolution characteristics of impact fatigue damage of RCM. In this paper, the damage variables were defined from three aspects: peak stress, ultimate strain, and damage energy. The specific calculation equations are as follows:

$$D_{C-\text{peak stress}} = \sum_{i}^{n} \frac{\sigma_{\text{peak},i}}{\sigma_{\text{peak,Total}}} \tag{10}$$

$$D_{C-\text{ulimate strain}} = \sum_{i}^{n} \frac{\varepsilon_{\text{ult},i}}{\varepsilon_{\text{ult,Total}}} \tag{11}$$

$$D_{C-\text{damage energy}} = \sum_{i}^{n} \frac{W_{Di}}{W_{D,\text{Total}}} = \sum_{i}^{n} \frac{U_{Di}}{U_{D,\text{Total}}} \tag{12}$$

where, $D_{C-\text{peak stress}}$, $D_{C-\text{ulimate strain}}$, and $D_{C-\text{damage energy}}$ are the damage variables defined by the specimen in terms of peak stress, ultimate strain, and damage energy, respectively; $\sigma_{\text{peak},i}$ and $\sigma_{\text{peak,Total}}$ are the peak stress of the specimen in the *i*-th cycle impact and the cumulative peak stress of the specimen in the whole cycle impact process, respectively; U_{Di} and $U_{D,\text{Total}}$ are the damage energy density of the specimen under the *i*-th cycle impact and the damage energy density of the specimen in the whole SHPB cycle impact test process, respectively.

3.4.2. Evolution characteristics of impact damage

It can be seen from Fig. 10 that the damage evolution characteristics of peak stress, ultimate strain, and damage energy were basically the same, that was, the values of damage variables increased with the increase of impact times, which showed that peak stress, ultimate strain, and damage energy can effectively characterize the fatigue damage characteristics of specimens in the process of cyclic impact. Fig. 10 shows that the characteristics of damage evolution were different with different confine conditions, and the damage growth rates of specimens CFRP-E-C, CFRP-S-C, and SC-S-C were lower than that of specimen No-C, which confirmed the fact that the restraint and reinforcement of CFRP sheet and steel cylinder can significantly reduce the damage growth rate. Especially with the confine of steel cylinder, the damage growth rate of RCM was the slowest, which stabilized the structure of RCM to a large extent and significantly weakened the cyclic impact fatigue damage effect. It can also be found that there was little difference in damage growth rate between CFRP-E-C and CFRP-S-C, which indicated that the restraining and strengthening effect of CFRP sheet on the end and side of RCM had a similar effect on the damage evolution characteristics of RCM under incremental cyclic impact.

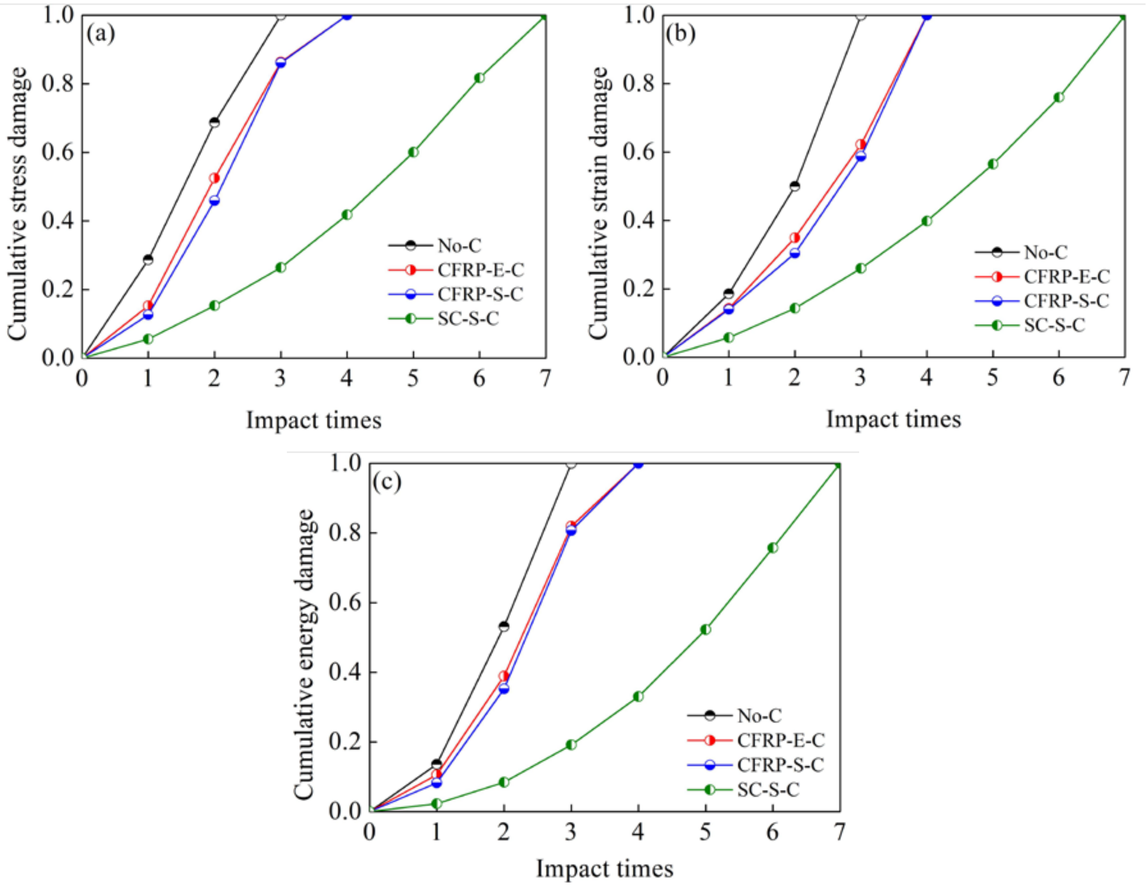

Figure 10. Relationship between (a) stress damage, (b) strain damage, and (c) energy damage and impact times.

Fig. 11 shows the differences among the three damage variables established in terms of peak stress, ultimate strain, and damage energy. It can be seen from Fig. 11 that there was a great difference among the three damage variables of specimens No-C, CFRP-E-C, and CFRP-S-C, while the difference among the three damage variables of specimen SC-S-C was small, and it is not difficult to see that the difference between the three damage variables was relatively stable. Specifically, there were some similarities and differences among stress damage, strain damage, and energy damage of RCM with four confine conditions: ① The stress damage was basically above the strain damage and energy damage, which indicated that the stress damage was larger than the strain damage and energy damage in the evolution process. ② There was an intersection point *I* between strain damage and energy damage. In the stage before the intersection point *I*, the strain damage was above the energy damage, while in the stage after the intersection point *I*, the strain damage was below the energy damage or the strain damage basically coincides with the energy damage. Interestingly, for this phenomenon, there was a high similarity between specimens CFRP-E-C and CFRP-S-C, which fully showed that the restraint and strengthening effect of CFRP sheet on the end and side of RCM had a similar effect on the damage evolution of RCM under incremental cyclic impact.

To sum up, the three damage variables established from the three aspects of peak stress, ultimate strain, and damage energy can effectively characterize the impact fatigue damage evolution of RCM under the four confine conditions. However, from the difference among stress damage, strain damage, and energy damage, it is recommended to use stress damage to characterize the impact fatigue damage evolution of materials. The reason is that in the same cyclic impact state, the stress damage value is higher than strain damage and energy damage, so stress damage can play an effective role in warning the structural damage of RCM.

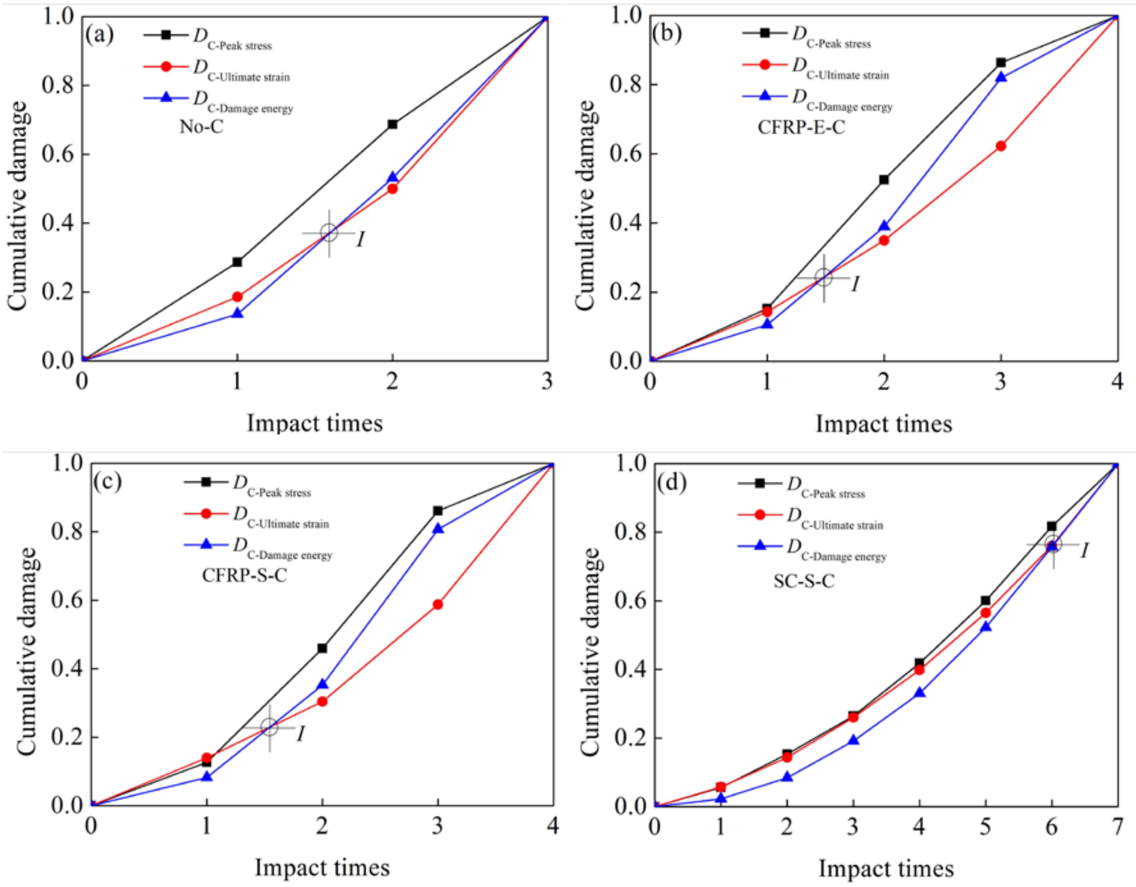

Figure 11. Comparison of stress damage, strain damage, and energy damage of specimens with four different confine conditions: (a) No-C; (b) CFRP-E-C; (c) CFRP-S-C; and (d) SC-S-C.

3.5. Failure states

The failure states of material specimens of different structures under impact load can reflect the dynamic damage modes, the mechanisms of fracture damage, and the mechanisms of structural crack resistance to a certain extent. As can be seen from Fig. 12, it is obvious that the cyclic impact damage process and failure states of RCM with four kinds of confines were quite different.

Fig. 12 (a) shows that a single fine crack clearly visible to the naked eye appeared in the side local area of the specimen No-C under the first cycle impact, and under the subsequent second cycle impact, the fine crack in this side area expanded into a coarse crack with larger crack width, and at the same time, the number of cracks increased. Under the third cycle impact, specimen No-C was completely damaged due to the excessive damage of the structural skeleton, which showed the compression failure of a transverse/radial free expansion. From this analysis, it can be seen that the mechanism of fracture damage is mainly due to the radial expansion deformation effect of specimen No-C under axial impact compression, and tensile cracks will appear in specimen No-C when the radial expansion deformation is greater than the ultimate tensile strain of specimen No-C. With the synchronous increase of impact times and impact pressure, the number and width of tensile cracks in specimen No-C must increase significantly. Finally, the specimen No-C is completely damaged under the combined action of axial compression and transverse tension.

Fig. 12 (b) shows that the specimen CFRP-E-C was seriously damaged under the third cycle impact, which was mainly reflected in the transverse tensile fracture of the end face and the expansion and spalling of the side. Under the fourth cyclic impact, the specimen CFRP-E-C mainly occurred along the fiber direction until it is completely damaged, which generally showed the transverse fracture released by the friction confine of the end faces. Different from the specimen No-C, the structural crack resistance mechanism of specimen CFRP-E-C mainly lies in the synergistic effect of CFRP sheet and RCM, that was, the CFRP sheet of the end faces can play a certain role of buffer and radial restraint reinforcement of the end faces, and the transverse expansion deformation of the RCM matrix is restrained by the friction resistance effect of the end faces, which effectively improves the dynamic fatigue performance of the RCM.

Fig. 12 (c) shows that the specimen CFRP-S-C was also seriously damaged under the third cycle impact, which was mainly reflected in the damage behavior of the expansion and fracture of the CFRP sheet and the edge matrix. Under the fourth cyclic impact, the CFRP sheet of the specimen CFRP-S-C was broken into two halves and the intermediate matrix was completely damaged, which showed the transverse explosion fracture under the instantaneous release of confining pressure. The same as specimen CFRP-E-C, the crack resistance mechanism of specimen CFRP-S-C was mainly due to the synergistic effect of CFRP sheet and RCM. But the difference is that the side CFRP sheet can only play a certain role in radial restraint reinforcement, and the passive confining pressure effect restricts the transverse expansion deformation of the RCM matrix and effectively improves the dynamic fatigue performance of RCM.

Fig. 12 (d) and Fig. 13 show that the damage states of specimen SC-S-C under the first and second cyclic impacts were the same as that of specimen No-C. However, in the process of subsequent impact load, the passive confining pressure effect occurs due to the interaction between the RCM and the steel cylinder due to the transverse expansion deformation of RCM. The passive confining pressure exerted by the steel cylinder makes the development of the crack further controlled. With the synchronous increase of impact times and impact pressure, there were still more fine cracks in other parts of the specimen SC-S-C due to structural deformation. Finally, the specimen SC-S-C was damaged in the compound form of the matrix covered with fine cracks, side coarse cracks, and edge circumferential fracture, which generally showed the internal circumferential fracture which can not be released by the confining pressure. In terms of fracture damage and structural crack resistance mechanism, the fracture damage mechanism of specimen SC-S-C before the interaction between RCM and steel cylinder was the same as that of specimen No-C, and the structural crack resistance mechanism of specimen SC-S-C after the interaction between RCM and steel cylinder was the same as that of specimen CFRP-S-C. It is worth mentioning that the damage degree of RCM with the confine of the steel cylinder was obviously less than that of RCM with the confine of the CFRP sheet, and the specimen SC-S-C maintained a relatively complete shape, showing better dynamic fatigue resistance.

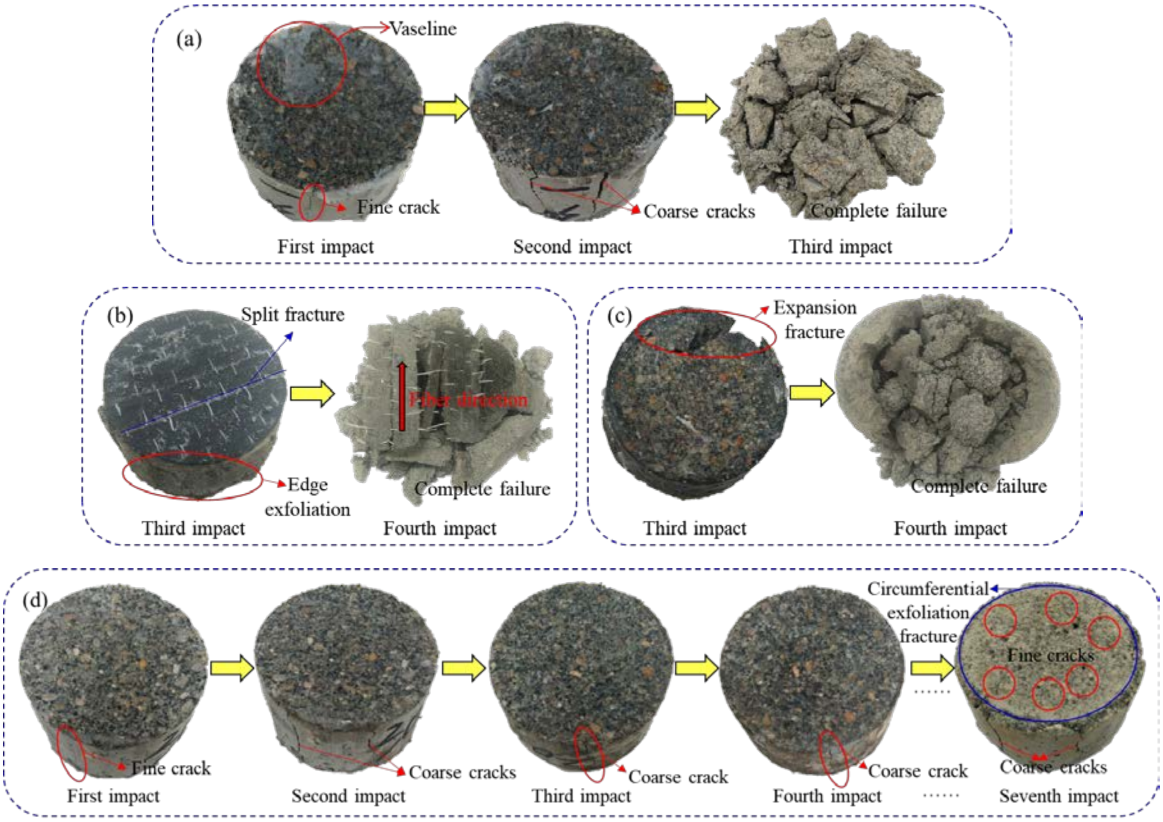

Note: To facilitate the observation of the fine cracks on the end face of the specimen, the picture of the specimen under the seventh impact was taken after the Vaseline on the surface of the specimen was dried, so the color of the specimen under the seventh impact is different from that of the previous impact specimens.

Figure 12. Cyclic impact failure states of specimens with four different confine conditions: (a) No-C; (b) CFRP-E-C; (c) CFRP-S-C; and (d) SC-S-C.

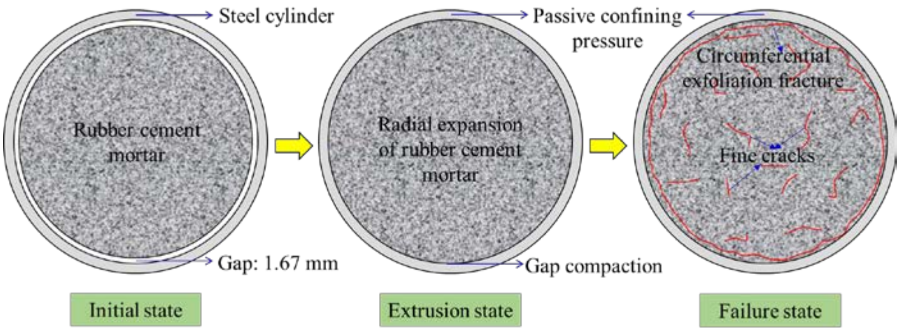

Figure 13. Mechanism of dynamic fatigue fracture failure of specimen SC-S-C.

To sum up, the structural crack resistance mechanism of confined RCM under cyclic impact load can be analysed from two aspects of material performance and confined structure mode. The details are as follows: (1) Compared with normal cement mortar, RCM itself has better impact resistance because of cushioning energy dissipation and plastic deformation [16]. (2) A "rigid-flexible combination" structure mode was formed under the rigid confines of the CFRP sheet and steel cylinder. The structure mode can play the role of "internal flexible energy consumption + external rigid confine = work along both lines" under cyclic impact load, and the effect of rigid-flexible joint crack resistance was formed.

4. Conclusions

In this paper, the amplitude-enhanced SHPB cyclic impact tests of four kinds of confined RCM were carried out, and the dynamic mechanical behavior, energy behavior, dynamic fatigue damage, and failure modes of RCM with the four confine conditions were compared and analysed. The following conclusions were drawn:

1. Compared with specimen No-C, the maximum cyclic peak stresses of specimens CFRP-E-C, CFRP-S-C, and SC-S-C were increased by 28.34 %, 105.94 %, and 201.37 %, respectively. It can be seen that the effective restraint on the end face and side of the RCM specimen obviously improved the structural resistance and structural damage fracture energy of the material itself. However, with the synchronous increase of impact load and impact times, stiffness degradation still occurred due to the cumulative effect of fatigue damage.

2. The shape of the strain rate-time curve was approximately longitudinal axial symmetry, showing three stages of growth, fluctuation stability, and attenuation, while the shape of the stress rate-time curve was approximately central symmetry, showing five stages of initial fluctuation stability, positive abrupt change, medium-term fluctuation stability attenuation, negative abrupt change, and late fluctuation stability. The above evolution characteristics became more obvious with the synchronous increase of impact times and impact load, but the fluctuation amplitude of the stress rate under the last impact decreased, which reflected the obvious strain-softening phenomenon.

3. Compared with specimen No-C, the total damage energies of specimens CFRP-E-C, CFRP-S-C, and SC-S-C increased by 56.07 %, 105.57 %, and 752.65 %, respectively, when the specimens were completely damaged in the process of cyclic impact, which fully proved that the confinement of CFRP and steel cylinder significantly improved the energy dissipation ability of RCM. The restrained reinforcement of CFRP sheet and steel cylinder effectively delays the development of cracks in RCM and ensures the minimization of structural damage.

4. With the increase of impact times, the reflected energy ratio, damage energy ratio, and transmission energy ratio showed a changing trend of "decreasing first and then increasing", "increasing first and then decreasing", and "increasing first and then decreasing", respectively. The reflected energy ratio and damage energy ratio showed a transverse axisymmetry state among each other. The three damage variables established from the three aspects of peak stress, ultimate strain, and damage energy can effectively characterize the impact fatigue damage evolution of RCM under the four confine conditions.

5. The failure modes of RCM with different confine modes were different. It was undeniable that RCM formed a "rigid-flexible combination" structure mode under the rigid confines of the CFRP sheet and steel cylinder. This structure mode can play the role of "internal flexible energy consumption + external rigid confine = work along both lines" under cyclic impact load, and the effect of rigid-flexible joint crack resistance was formed, which effectively improved the anti-fatigue impact performance of RCM.

References

1. Zhang, S., Kong, X., Fang, Q., Chen, L., Wang, Y. Numerical prediction of dynamic failure in concrete targets subjected to projectile impact by a modified Kong-Fang material model. International Journal of Impact Engineering. 2020. 144. 103633. DOI: 10.1016/j.ijimpeng.2020.103633
2. Zhang, Q., Wang, L. Investigation of stress level on fatigue performance of plain concrete based on energy dissipation method. Construction and Building Materials. 2021. 269. 121287. DOI: 10.1016/j.conbuildmat.2020.121287
3. Assaggaf, R.A., Ali, M.R., Al-Dulaijan, S.U., Maslehuddin, M. Properties of concrete with untreated and treated crumb rubber-A review. Journal of Materials Research and Technology. 2021. 11. Pp. 1753–1798. DOI: 10.1016/j.jmrt.2021.02.019
4. Alsaif, A., Garcia, R., Figueiredo, F.P., Neocleous, K., Christofe, A., Guadagnini, M., Pilakoutas, K. Fatigue performance of flexible steel fibre reinforced rubberised concrete pavements. Engineering Structures. 2019. 193. Pp. 170–183. DOI: 10.1016/j.engstruct.2019.05.040
5. Ríos, J.D., Cifuentes, H., Blasón, S., López-Aenlle, M., Martínez-De La Concha, A. Flexural fatigue behaviour of a heated ultra-high-performance fibre-reinforced concrete. Construction and Building Materials. 2021. 276. 122209. DOI: 10.1016/j.conbuildmat.2020.122209
6. Al-Rousan, R.Z. Integration of CFRP strips as an internal shear reinforcement in reinforced concrete beams exposed to elevated temperature. Case Studies in Construction Materials. 2021. 14. e00508. DOI: 10.1016/j.cscm.2021.e00508
7. Zaiter, A., Lau, T.L. Experimental study of jacket height and reinforcement effects on seismic retrofitting of concrete columns. Structures. 2021. 31. Pp. 1084–1095. DOI: 10.1016/j.istruc.2021.02.020
8. Kheyroddin, A., Arshadi, H., Ahadi, M.R., Taban, G., Kioumarsi, M. The impact resistance of Fiber-Reinforced concrete with polypropylene fibers and GFRP wrapping. Materials Today: Proceedings. 2021. 45(6). Pp. 5433–5438. DOI: 10.1016/j.matpr.2021.02.116
9. Mezzal, S.K., Al-Azzawi, Z., Najim, K.B. Effect of discarded steel fibers on impact resistance, flexural toughness and fracture energy of high-strength self-compacting concrete exposed to elevated temperatures. Fire Safety Journal. 2021. 121. 103271. DOI: 10.1016/j.firesaf.2020.103271
10. Gao, D., Gu, Z., Zhu, H., Huang, Y. Fatigue behavior assessment for steel fiber reinforced concrete beams through experiment and Fatigue Prediction Model. Structures. 2020. 27. Pp. 1105–1117. DOI: 10.1016/j.istruc.2020.07.028
11. Adnan, H.M., Dawood, A.O. Recycling of plastic box waste in the concrete mixture as a percentage of fine aggregate, Construction and Building Materials. 2021. 284. 122666. DOI: 10.1016/j.conbuildmat.2021.122666
12. Carlesso, D.M., Cavalaro, S., de la Fuente, A. Flexural fatigue of pre-cracked plastic fibre reinforced concrete: Experimental study and numerical modeling. Cement and Concrete Composites. 2021. 115. 103850. DOI: 10.1016/j.cemconcomp.2020.103850
13. Hernández-Olivares, F., Barluenga, G., Parga-Landa, B., Bollati, M., Witoszek, B. Fatigue behaviour of recycled tyre rubber-filled concrete and its implications in the design of rigid pavements. Construction and Building Materials. 2007. 21 (10). Pp. 1918–1927. DOI: 10.1016/j.conbuildmat.2006.06.030
14. Lv, J., Zhou, T., Du, Q., Li, K. Experimental and analytical study on uniaxial compressive fatigue behavior of self-compacting rubber lightweight aggregate concrete. Construction and Building Materials. 2020. 237. 117623. DOI: 10.1016/j.conbuildmat.2019.117623
15. Yang, R., Xu, Y., Chen, P., Wang, J. Experimental study on dynamic mechanics and energy evolution of rubber concrete under cyclic impact loading and dynamic splitting tension. Construction and Building Materials. 2020. 262. 120071. DOI: 10.1016/j.conbuildmat.2020.120071
16. Pham, T.M., Chen, W., Khan, A.M., Hao, H., Elchalakani, M., Tran, T.M. Dynamic compressive properties of lightweight rubberized concrete. Construction and Building Materials. 2020. 238. 117705. DOI: 10.1016/j.conbuildmat.2019.117705
17. Yang, F., Feng, W., Liu, F., Jing, L., Yuan, B., Chen, D. Experimental and numerical study of rubber concrete slabs with steel reinforcement under close-in blast loading. Construction and Building Materials. 2019. 198. Pp. 423–436. DOI: 10.1016/j.conbuildmat.2018.11.248
18. Feng, W., Chen, B., Yang, F., Liu, F., Li, L., Jing, L., Li, H. Numerical study on blast responses of rubberized concrete slabs using the Karagozian and Case concrete model. Journal of Building Engineering. 2021. 33. 101610. DOI: 10.1016/j.jobe.2020.101610
19. Khan, I., Shahzada, K., Bibi, T., Ahmed, A., Ullah, H. Seismic performance evaluation of crumb rubber concrete frame structure using shake table test. Structures. 2021. 30. Pp. 41–49. DOI: 10.1016/j.istruc.2021.01.003
20. Youssf, O., ElGawady, M.A., Mills, J.E. Experimental investigation of crumb rubber concrete columns under seismic loading. Structures. 2015. 3. Pp. 13–27. DOI: 10.1016/j.istruc.2015.02.005
21. Pacheco-Torres, R., Cerro-Prada, E., Escolano, F., Varela, F. Fatigue performance of waste rubber concrete for rigid road pavements. Construction and Building Materials. 2018. 176. Pp. 539–548. DOI: 10.1016/j.conbuildmat.2018.05.030
22. Yazdani, S., Asadollahi, S., Shoaei, P., Dehestani, M. Failure stages in post-tensioned reinforced self-consolidating concrete slab strengthened with CFRP layers. Engineering Failure Analysis. 2021. 122. 105219. DOI: 10.1016/j.engfailanal.2021.105219
23. Al-Rousan, R. Impact of elevated temperature on the shear behavior of strengthened RC beams. Magazine of Civil Engineering. 2022. 110 (2). Article No. 11002. DOI: 10.34910/MCE.110.2
24. Jahami, A., Temsah, Y., Khatib, J., Baalbaki, O., Kenai, S. The behavior of CFRP strengthened RC beams subjected to blast loading. Magazine of Civil Engineering. 2021. 103 (3). Article No. 10309. DOI: 10.34910/MCE.103.9
25. Al-Rousan, R. Impact of elevated temperature on the behavior of strengthened RC beams with CFRP. Magazine of Civil Engineering. 2021. 106 (6). Article No. 10612. DOI: 10.34910/MCE.106.12
26. Al-Rousan, R. Behavior of CFRP strengthened columns damaged by thermal shock. Magazine of Civil Engineering. 2020. 97(5). Article No. 9708. DOI: 10.18720/MCE.97.8
27. Barham, W.S., Obaidat, Y.t., Alkhatatbeh, H.A. Behavior of heat damaged reinforced recycled aggregate concrete beams repaired with NSM-CFRP strips. Magazine of Civil Engineering. 2022. 111 (3). Article No. 11106. DOI: 10.34910/MCE.111.6
28. Zhang, X., Shi, Y., Li, Z.-X. Experimental study on the tensile behavior of unidirectional and plain weave CFRP laminates under different strain rates. Composites Part B: Engineering. 2019. 164. Pp. 524–536. DOI: 10.1016/j.compositesb.2019.01.067
29. Wang, J., Xu, Y., Yang, R., Zheng, Q., Ni, X. Dynamic mechanic and energy properties of cement mortar with CFRP confines. Journal of Building Materials. 2022. 25 (04). Pp. 344–352. DOI: 10.3969/j.issn.1007-9629.2022.04.003

30. Xiong, B., Demartino, C., Xiao, Y. High-strain rate compressive behavior of CFRP confined concrete: Large diameter SHPB tests. Construction and Building Materials. 2019. 201. Pp. 484–501. DOI: 10.1016/j.conbuildmat.2018.12.144
31. Li, G., Tan, K.H., Fung, T.C. Experimental study on CFRP-concrete dynamic debonding behaviour. Engineering Structures. 2020. 206. 110055. DOI: 10.1016/j.engstruct.2019.110055
32. Zhai, K., Fang, H., Guo, C., Fu, B., Ni, P., Ma, H., He, H., Wang, F. Mechanical properties of CFRP-strengthened prestressed concrete cylinder pipe based on multi-field coupling. Thin-Walled Structures. 2021. 162. 107629. DOI: 10.1016/j.tws.2021.107629
33. Tam, V.W.Y., Tao, Z., Evangelista, A. Performance of recycled aggregate concrete filled steel tubular (RACFST) stub columns with expansive agent. Construction and Building Materials. 2021. 272. 121627. DOI: 10.1016/j.conbuildmat.2020.121627
34. Yang, X., Yang, H., Zhang, S. Transverse impact behavior of high-strength concrete filled normal-/high-strength square steel tube columns. International Journal of Impact Engineering. 2020. 139. 103512. DOI: 10.1016/j.ijimpeng.2020.103512
35. Xu, Y., Yang, R. Dynamic mechanics and damage evolution characteristics of rubber cement mortar under different curing humidity levels. Journal of Materials in Civil Engineering. 2020. 32 (10). DOI: 10.1061/(ASCE)MT.1943-5533.0003351
36. JGJ/T 70-2009, Standard for test method of basic properties of construction mortar, China Architecture & Building Press, Beijing China. 2009.
37. Lu, F.Y., Chen, R., Lin, Y.L., Zhao, P.D., Zhang, D. Hopkinson bar techniques, Beijing: Science Press. 2013. ISBN: 978-7-03-038434-8.
38. Dai, B., Shan, Q.W., Chen, Y., Luo, X.Y. Mechanical and energy dissipation characteristics of granite under cyclic impact loading. Journal of Central South University. 2022. 29(01). Pp. 116–128. DOI: 10.1007/s11771-022-4897-9
39. He, L., Cai, H., Huang, Y., Ma, Y., Van Den Bergh, W., Gaspar, L., Valentin, J., Vasiliev, Y.E., Kowalski, K.J., Zhang, J. Research on the properties of rubber concrete containing surface-modified rubber powders. Journal of Building Engineering. 2021. 35. DOI: 10.1016/j.jobe.2020.101991
40. Feng, W., Liu, F., Yang, F., Jing, L., Li, L., Li, H., Chen, L. Compressive behaviour and fragment size distribution model for failure mode prediction of rubber concrete under impact loads. Construction and Building Materials. 2021. 273. 101991. DOI: 10.1016/j.conbuildmat.2020.121767
41. Feng, L., Chen, X., Zhang, J., Yuan, J., Dong, W. Fatigue behavior and prediction model of self-compacting concrete under constant amplitude load and incremental amplitude load. International Journal of Fatigue. 2021. 145. 106107. DOI: 10.1016/j.ijfatigue.2020.106107
42. Gong, F.Q., Zhong, W.H., Gao, M.Z., Si, X.F., Wu, W.X. Dynamic characteristics of high stressed red sandstone subjected to unloading and impact loads. Journal of Central South University. 2022. 29 (02). Pp. 596–610. DOI: 10.1007/s11771-022-4944-6
43. Shu, R., Yin, T., Li, X., Yin, Z., Tang, L. Effect of thermal treatment on energy dissipation of granite under cyclic impact loading. Transactions of Nonferrous Metals Society of China. 2019. 29 (2). Pp. 385–396. DOI: 10.1016/S1003-6326(19)64948-4

Information about authors:

Rong-Zhou Yang, *PhD*
ORCID: https://orcid.org/0000-0002-0126-2446
E-mail: Rongzhouy@outlook.com

Ying Xu, *PhD*
ORCID: https://orcid.org/0000-0001-8438-3130
E-mail: yxu@aust.edu.cn

Pei-Yuan Chen, *PhD*
ORCID: https://orcid.org/0000-0002-5538-617X
E-mail: peiyuan29@126.com

Received 02.06.2022. Approved after reviewing 13.01.2023. Accepted 01.03.2023.

Magazine of Civil Engineering. 2023. 119(3). Article No. 11906

Magazine of Civil Engineering

ISSN 2712-8172

journal homepage: http://engstroy.spbstu.ru/

Research article

UDC 624.042.41:624.95

DOI: 10.34910/MCE.119.6

Tank shell stability: refined design schemes

M. N. Tcepliaev ✉ **, *V.F. Mushchanov, A.V. Zubenko, A.V. Mushchanov, A.N. Orzhehovsky***

Donbas National Academy of Civil Engineering and Architecture, Makeevka

✉ *m.n.cepliaev@donnasa.ru*

Keywords: structural stability, storage tank, stress-strain state, finite element method, cylindrical shell, wind, aerodynamic coefficients, staircase

Abstract. In many ways, the reliability of vertical cylindrical tanks is determined by the resistance to buckling of the wall. In the current work, a variant of a detailed design scheme is considered, taking into account the presence of a spiral technological staircase for servicing the tank roof. The possibility of using the specified structural element as an external reinforcement to increase stability is analyzed. Finite element models of tanks with volumes of 10..30 thousand m^3 were developed. The models took into account the actual distribution of the wind flow for tanks with a circular staircase. Using a multifactorial experiment, an analysis of the stability and stress state of the tank wall was carried out. The variable parameters were: the design solution of the stairs, the dimensions of the tanks and the load. Corresponding graphs and diagrams were constructed. As a result, the design solution and the recommended angle of inclination of the spiral staircase in the range of 30–40° were substantiated. The application of the obtained solutions improved the stability in the annular direction by up to 13 % compared to standard solutions. Wall displacements from wind load are reduced by 14 %, in turn, local stresses in the ladder attachment areas increased by no more than 5 %. In general, the inclusion of spiral staircases significantly increases the stability of the tank wall and can be considered as a good alternative to standard reinforcement methods.

Citation: Tcepliaev, M.N., Mushchanov, V.F., Zubenko, A.V., Mushchanov, A.V., Orzhehovsky, A.N. Tank shell stability: refined design schemes. Magazine of Civil Engineering. 2023. 119(3). Article no. 11906. DOI: 10.34910/MCE.119.6

1. Introduction

1.1. Relevance of the study

Modern trends towards more efficient use of natural resources are also reflected in the construction of buildings and structures. Scroll tanks (ST) are high-risk facilities, so any design choices, especially those that lead to steel economy, should be studied extensively. The relevance of studying new approaches to tank designing is beyond any doubt. There's a case for the increasing demand for such constructions due to the development of petrochemical and other industries [1–4]. Another important factor is the demand for regular renovation of the tank battery, due to the relatively short life span of such constructions.

The shell of variable thickness is basic in steel intensity and the most important element of ST. The durability and rigidity of the shell to a large extent determines the reliability of the whole construction of the tank. Despite significant progress in the field of tank designing and construction, accidents associated with the loss of rigidity of the cylindrical shell still occur. A lot of authors, among which we can note the works of J. I. Chang and C.-C. Lin [5], L. A. Godoy and F.G Flores [6], H.M. Hanukhov and A.V. Alipov [7] studied the causes of tank failures and analysed their consequences. According to the results of their researches, damage from wind and vacuum can account for up to 10 % of the total number of structural failures. At the same time, it is stated in the research of the Melnikov Central Research Institute of Scientific and Technical Problems [8] that no more than 40 % of total number of failures that are happening to facilities of the tank park are registered. The same is confirmed by the data given in the work of V.V. Filippov [9], where upon inspection results of several tank parks, significant violations of geometric shape were found in 30 % of all inspected constructions. Over half of geometry kiks were dents and bulges, caused by the influence of wind and vacuum as well.

There is a great variety of constructive and computational methods to ensure the operational reliability of tank shells. For example, the recommendations for keeping a sufficient filling level of a product to resist the loss of wind rigidity were developed in the work [10]. The contributors [11] suggest using composite materials in the form of a garland of plastic bottles filled with carbonate rock powder. And yet, the modern practice of tank design offers only two principled approaches to ensure the reliability of the tank shell from the condition of rigidity:

- structural analysis of appropriate shell thickness;
- installation of additional shell rigidness of elements.

The second approach is technologically more complicated, but it reduces the weight of the construction. By additional elements of rigidness we mean vertical and stiffening rings, banders and similar constructions. Banding can be made either by sheet-iron plates or composite materials [12, 13]. Various peculiarities of usage of stiffening rings are considered in many scientists' works [14–22]. As a rule, stiffening rings are used to increase rigidity, and banding is used to restore the load-carrying ability of apron rings of the shell. The possibility and effectiveness of external force is also confirmed in the specification documents of the USA (API 650), Europe (Eurocode 3, part 4-2) and Russia (SP 16.13330.2011, STO-SA-03-002-2009).

At the same time there are elements of tanks, consideration of the impact of which is not detailed in the engineering methods of calculation of the shell, the staircases, in particular. Technological staircases are used for maintenance of the roof and peep-holes and belong to the list of required equipment of tanks. There are two principal varieties of staircases: with attachment to the shell (spiral) and freestanding (shaft) – Fig. 1a, 1b, respectively. The variant shown in Fig. 1a doesn't work on the stress-strain state (SSS) of the tank because it has its own understructure. The variant shown in Fig. 1b transmits all the load directly to the shell and changes the stress-strain state of the construction. First of all, the presence of the staircase affects the overall rigidity of the shell. Thus, proper consideration of the combined action of the shell and staircases can allow us to design a more streamlined construction without reducing its design reliability.

Figure 1a. Tank stair tower.

Figure 1b. Spiral tank staircase.

1.2. Overview of the state of the issue

The effectiveness of external reinforcement of cylindrical tank shells is confirmed by many researchers and does not require additional justification. However, searching optimal methods of designing such reinforcement and taking into account their design features is still a relevant objective.

Using experimental and numerical research methods in their works, the authors J.G. Teng and J.M. Rotter 2003 [20] and M. Jaharanjiri et al [21] came to the conclusion in 2012 that installing even one stiffening ring increases the resistance to rigidity loss by 1.5 times. Authors D. Lemak in his paper in 2005 [18], F. Bu and C. Qian [19] in his paper in 2015 [20] based on the results of numerical calculations determine the recommended ring pitch and number of rings for a limited range of constructions. The result of the work cycle by the authors V. F. Mushchanov and M.N. Tsepliaev [14, 15] is a universal methodology of rational stiffening rings location. The range of tank constructions is limited to a volume of 30 thousand m3 in the works of these authors. The authors note that stiffening rings do not increase rigidity in axial direction. The main strengthening effect arises due to increasing amounts of annular critical stresses of rigidity loss.

The authors in their works [23] compare the performance of a spiral staircase with an element in the form of an inclined stiffening rib on the tank shell. The conclusions note that the spiral staircase under wind pressure significantly improves the bending resistance of the tank shell. The authors determined the orientation of the hoop staircase toward the wind flow, at which the ultimate crippling load of rigidity loss increases by 20 %. The research is of significant scientific importance, however, it covers only one size of a tank and cannot be considered to be a complex value.

Cases of tank shell rigidity loss due to storm wind are considered in the work [24] – Fig. 2a, b. It is noted that the tank shell at the location of the spiral staircase has not lost its rigidity. Differences in the buckling mode due to the presence closely spaced objects and the magnitude of the vacuum. Taking into account the combined actions of the shell and the hoop staircase, the authors got the following results:

- motions of the shell from the wind load are reduced by 5 %;
- the weight of the cylindrical shell can be reduced to 15 %.

a) b)

Figure 2. Buckling under the influence of wind.

The specification documents of the Russian Federation, Europe and the USA do not specify the question of taking into account the combined actions of the shell and the hoop staircase in the design of tanks. Design requirements for spiral staircases coincide in most parameters.

According to the reviewed publications the possibility of increasing the rigidity of the tank shell using the hoop staircase raises no doubts. The consideration of the calculations of spiral staircases can be an excellent alternative to the established shell reinforcement. However, many variations in the location and design of spiral staircases opens up a wide range of scientific and practical issues that require more detailed study.

The article aimed to determine the rational, in terms of ensuring maximum rigidity of the cylindrical tank shell, parameters of a hoop staircase.

The objectives were:

- computer modeling of wind flow distribution for the tank with the hoop staircase in SolidWorks;
- a redetermined finite element model of ST for SSS analysis in the complex LIRA-SAPR 2019 R1 was developed;
- calculation of general shell rigidity at different parameters of hoop staircases was done;
- local stresses in the shell at the attaching points of the staircases were determined;
- the recommendation on the best positioning of the staircases were formed.

2. Materials and methods

2.1. Formation of the experiment matrix

A review of existing designs allowed us to identify two principal variants for attaching spiral staircases:

– with attachment of each step to the tank shell – Fig. 3a;

– with attachment of platforms to the shell – Fig. 3b.

Figure 3a. Spiral staircases – variant 1

Figure 3b. Spiral staircases – variant 2.

The variant in Fig. 3b is more steel-intensive due to the presence of strings, and also has higher stiffness. However, a small number of points of attachment to the tank shell does not allow unambiguously determining the most preferred variant without performing calculations.

The general requirements of regulatory documents indicate the maximum slope of the staircase (up to 50°), the minimum width of the flight is 700 mm; the minimum width of the step is 200 mm. The lower limit of the investigated slope angle of staircases (30°) is justified by analysis of existing structures. Russian and USA documents require installation of half paces with a step of not more than 7.5 meters along the shell height. EU regulations do not stipulate the requirements for the location of half paces. By analyzing existing designs in this paper, the tank models with two variants of spiral staircases will be made. Schematic view of staircases is given in Fig. 4 a,b.

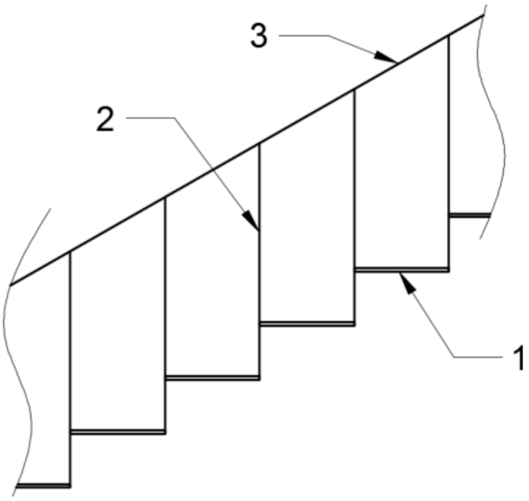

Figure 4a. Spiral staircase diagram – variant 1.

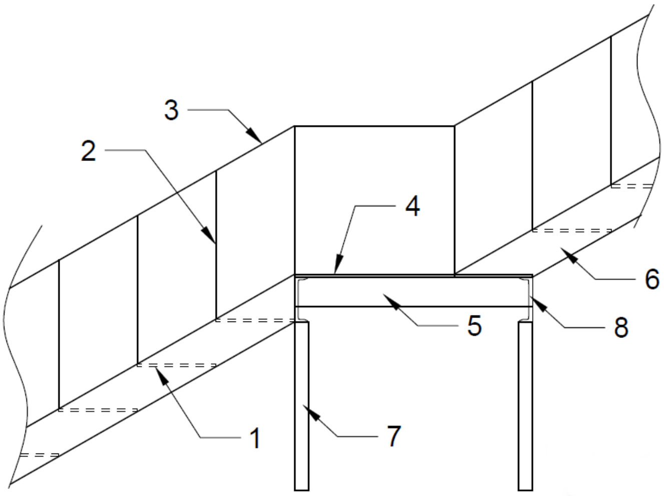

Figure 4b. – Spiral staircase diagram – variant 2.

Based on the experience of existing projects, the cross sections of elements for two variants of spiral staircases have been determined – Table 1.

Table 1. Sections of elements of described staircase types.

Staircase type	The number of the element in the diagram	Section type	Element length, mm
Variant 1 (V1)	1	Sheet 250×6	800
	2	Angle 45×45×3	800...1000
	3	Angle 45×45×3	Depends on the slope
Variant 2 (V2)	1	Sheet 250×6	700
	2	Angle 45×45×3	Depends on the slope 800...1000
	3	Angle 45×45×3	Depends on the slope
	4	Sheet 900×6	700
	5	Channel120×60×4	900
	6	Channel 180×50×4	Depends on the slope
	7	Angle 63×6	1100
	8	Channel 120×60×4	900

The performed analysis of publications as well as the results of the current study allowed to limit the considered range of tanks. As the diameter of the tank increases, the influence of the presence of stairs decreases. The most representative values are noted for tanks with a diameter of up to 50 meters, the volume of which does not exceed 30 thousand m^3. Taking into account the existing tank farm, several typical variants were selected. Different stair locations were considered for each tank size. For the second structural variant of staircases, the number of platforms was 5 pcs. Parameters and a complete list of variants under consideration for numerical studies are given in Table 2.

Table 2. Variants of tank models for numerical studies

No	Volume, m^3	Tank diagram	Dimensions, m	Variants of staircases	Slope angels of staircases, α◦
1	10000	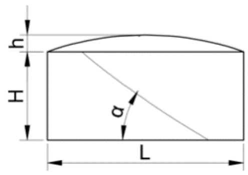	H=18, h=3.5, L=28.5	V1, V2	30, 35, 40, 45, 49
2	20000		H=18, h=3.4, L=40 H=18, h=3.4, L=40		
3	30000		H=18, h=4, L=45.6		

Thus, the formed numerical experiment matrix includes 33 variants (including 3 models without stairs). Account of the actual distribution of wind flow for a tank with a staircase has been implemented by an additional calculation of 3 models. The total number of variants under consideration was 36 pcs.

2.2. Development of a numerical model to determine the refined distribution of wind flow

For a comprehensive study the actual distribution of wind flow should be taken into account in the case of a spiral staircase. The complex allows obtaining wind pressure values on the surface of the object in question without physical modeling of the process. The parameters of the design model are substantiated in detail in the works [25–27] and recommendations on the main dimensions of the design area are proposed. Thus, for isolated structures, the vertical size of the design area for isolated structures should be at least 5H, the distance along the flow should be at least 5H, and the distance behind the structure should be more than 15H (H is the height of the structure).

The variant of placing the staircase in the zone of maximum wind pressure on the shell was considered. All considered tank volumes are modeled with the following ratio of height (H) to diameter (D): 0.63, 0.45 and 0.4. The general view and top view of the three-dimensional model for calculating the wind pressure taking into account the presence of a spiral staircase is shown in Fig. 5a and b, respectively.

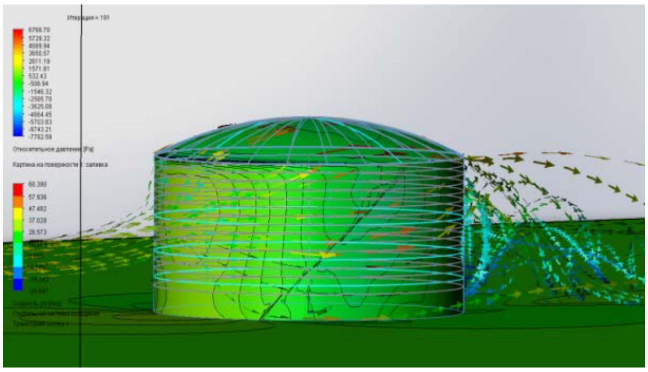

a) general view

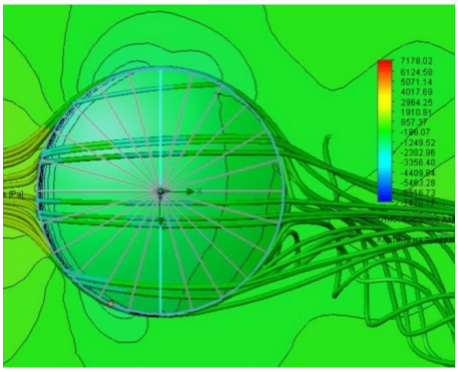

b) top view

Figure 5. Model in SolidWorks for wind pressure calculation.

Based on the obtained data the wind pressure values for the calculation of VAT and stability in LIRA-SAPR 2019 R1 have been determined.

2.3. Development of a numerical model for tank calculation

Based on the experience of previous studies [16, 17, 30, 31], the parameters of the finite element model of the tank for calculating stability and VAT have been determined. To perform calculations the LIRA-SAPR 2019 R1 software package was used. Element sampling was carried out on the basis of ensuring the convergence of analytical and numerical stresses from hydrostatic load. The main structural components of the finite element model are given in Table 3.

Table 3. Experimental matrix for numerical studies

Model element	Graphic image	Types of a finite element used
Plate coating FE No44	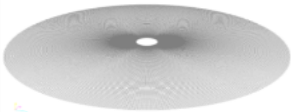	Plate finite element No44
Ribbed-ring dome	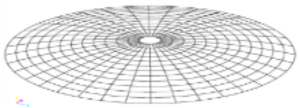	Rob finite elements No10 The joint of the bearing dome rib with the supporting ring was simulated by combining movements.
Stiffening support ring	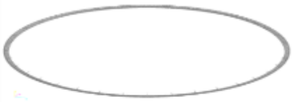	Plate finite elements No42 and 44
Variable thickness wall plate FE No44	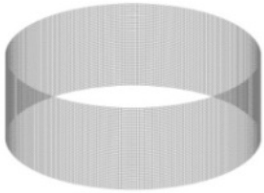	Plate No44 (width up to 1/480 of the circle, height up to 1/82 of the wall height)
Spiral staircase	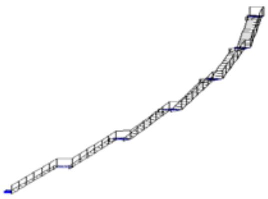	Platforms – plate finite elements No44, the rest of the elements are rod.
Bottom		Plates No44 and 42 (flashing places of the bottom to the wall)

Formed finite element model of one of the tank variants (without displaying loads) is shown in Fig. 6.

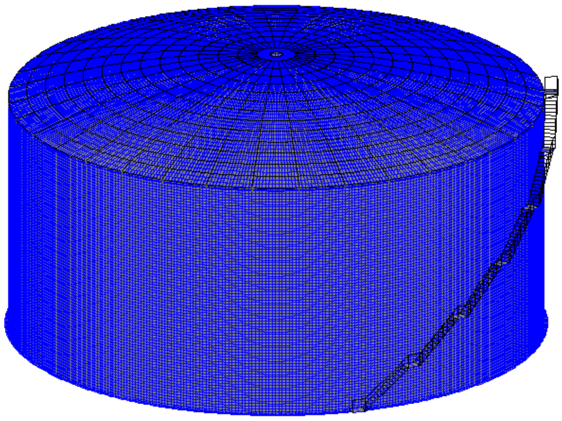

Figure 6 Tank model LIRA-SAPR 2019 R1.

According to the objectives of the study, two characteristic design cases of loading were considered - an empty and filled reservoir. Design load combinations used in this study are given in Table 4.

Table 4. Design load combinations.

No	Method of calculation	Combination of load
1	VAT	dead load + hydrostatic pressure (oil 0.9 t/m^3) + overpressure (2 kPa)
2	Rigidity	wind (0.5 kPa) + vacuum (0.25 kPa)

The mounting points of the stairs are stress concentrators. The maximum stresses in the tank shell result from hydrostatic stress action (combination #1 in Table 5). Both grid clustering was made and stress jumps were determined in the specified areas of the finite-element model.

The design load for structural rigidity design is to be presented as a combination of wind and vacuum (combination No2 in Table 5). The form of wind flow distribution was considered in two variants:

- according to the Eurocode;
- specified wind flow distribution for a tank with staircase (based on the results of structural analysis in SolidWorks Flow Simulation).

The exact shape of the wind load was modeled in LIRA-SAPR 2019 R1 by means of a text file. The detailed methodology of this way of setting the load is described in the paper [28]. The type of both the basic wind load and the load on the model for the characteristic cross section of the cylindrical shell is given in Fig. 7a, 7b respectively.

a) basic wind flow distribution **b) wind load simulated by LIRA-SAPR 2019 R1 system**

Figure 7. Wind load on the tank wall.

2.4. Methods for evaluating the results

For the present study, the main comparative parameter will be the value of critical stresses of instability in the cylindrical shell of the tank. This parameter is manifested by the rigidity factor (SF) of the cylindrical shell. It allows us to define the theoretical value of the critical pressure corresponding to the moment of rigidity loss (formula 1).

$$SF = \frac{P_{cr}}{P}, \tag{1}$$

where P_{cr} is the critical pressure of the cylindrical shell rigidity loss, P is the operating pressure.

The value of the SF was determined by means of LIRA-SAPR 2019 R1 software system (in case of load combination No. 2 from Table 5). Since the design combination does not include axial loads, the SF is directly related to the circular critical stress of rigidity loss.

The stress state analysis was made for a limited list of options and it includes two criteria, such as:

- the value of tank shell deformations for different structural variants of the staircase (load combination 1 – Table 5);
- the value of stress concentration in the mounting points of the staircase (load combination 2 – Table 5).

The general procedure for determining the recommended parameters of the staircases is as follows:

1. structural rigidity designing for determining the SF for each variant of tanks under consideration;
2. constructing dependency graphs of the SF and the dimensions and design solution of the tank staircases;
3. local stresses analysis in the attachment zones of the staircases to the tank shell under the hydrostatic load;
4. determination of the most preferable structural variant of the staircases on the basis of the rigidity design and strain-stress state;
5. determination of the recommended slope of the selected structural variant of the staircases on the basis of the rigidity design;
6. conclusion on the applicability of the obtained results for the case of the specified wind pressure diagram (obtained by SolidWorks Flow Simulation).

The resulting array of data has allowed us to give recommendations for choosing parameters of staircases for the considered types of structures.

3. Results and Discussion

3.1. Results of rigidity design

According to the research algorithm (Sec. 2.4) the structural design for 36 tank models in the design variations listed in Table 2 has been made. As a result, values of critical stresses of rigidity loss and a picture of the stress-strain state have been obtained. Since the graphical representation of the deformed models does not give a qualitative assessment of the results obtained, only a few typical variants for a tank in the volume of 20 thousand m^3 will be given in the paper.

Fig. 8 a and b shows the first forms of rigidity loss of the tank shell fragment for two structural variants of the staircases. The first variant of the staircase deforms by repeating the form of the shell, unlike the second structural variant. It is explained by the fact that the attachment points of the second variant transmit the stiffness of the staircase to the shell to a lesser extent. The location of the buckling waves corresponds to the case of the prevailing action of circumferential stresses.

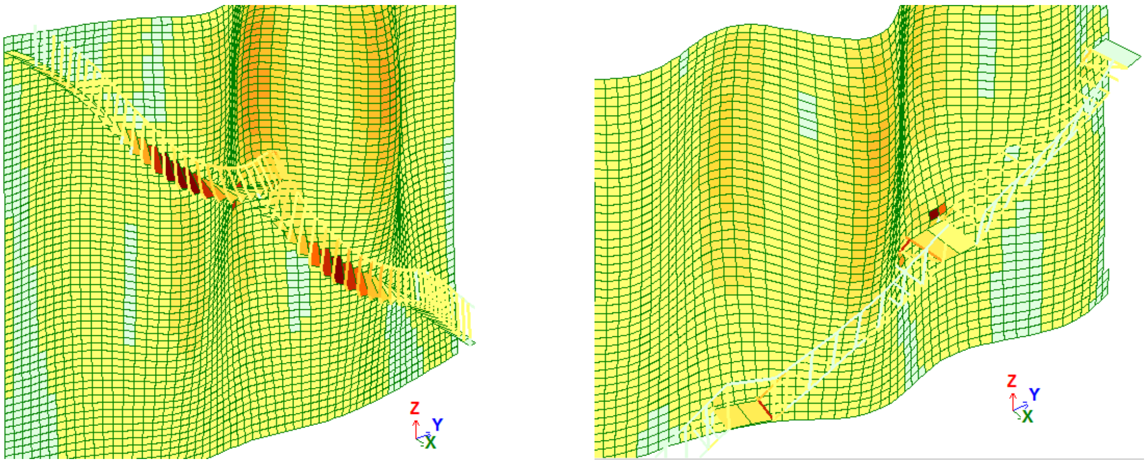

a) B1 – 40° slope **b) B2 – 40° slope**

Figure 8. General view of the loss of rigidity of the shell fragment of the tank with a volume of 20 thous. m^3.

Rigidity loss occurs from the windward side of the tank shell. This is clearly seen in the characteristic section of the cylindrical shell at the height of 9 meters – Fig. 9. The cases without modeling staircases and with staircases in the two considered design variants are given – Fig. 9 a, b, c, respectively. The forms of rigidity loss for the model without staircase (Fig. 9a) and with structural variant No. 2 (Fig. 9c) are similar. For the structural variant of staircase No. 1 (Fig. 9b) the number of waves is greater while their amplitude is smaller.

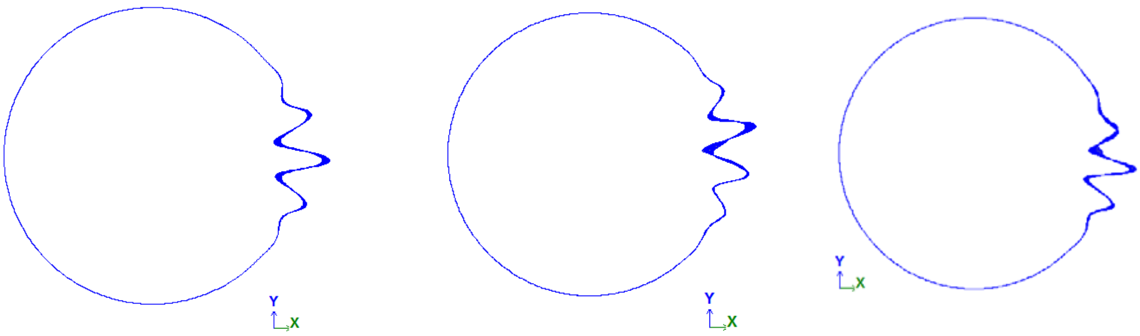

a) without staircase modelling **b) B1 – 40° slope** **c) B2 – 40° slope**

Figure 9. The shape of the loss of rigidity of the shell of the tank with a volume of 20 thousand m^3 at the level of +9.000 m.

The resulting data for the other studied volumes of the tanks confirms the conclusion. The shapes of the tank shell rigidity loss coincide with the results of other authors [6, 19, 21, 29]. However, when analyzing the buckling of a real structure (Fig. 2), some differences were noted. In particular, a significant dispersal of buckling waves along the length and height of the tank wall. The change in geometry in a real design occurs mainly in the upper part of the tank wall on the windward side, and not along the entire height. The differences are due to the lack of accounting for supercritical work. In addition, for research purposes, the stability calculation does not take into account the weight of the roof, which changes the type of wall buckling.

Graphs of SF changes depending on the slope of the staircase α (Table 3) and the volume of the tank are shown in Fig. 10 a-c. The structural variants of the stairs are described in item 2.1 (B1 – option 1, B2 – option 2). Each graph additionally shows the SF value for the model without staircase.

The values of the maximum effective circular stresses do not change in case of staircase modeling which is also typical of other types of shell reinforcement [15, 17]. Taking into account the absence of axial loads, the dependence between the SF and the circular critical stresses of rigidity loss can be considered directly proportional.

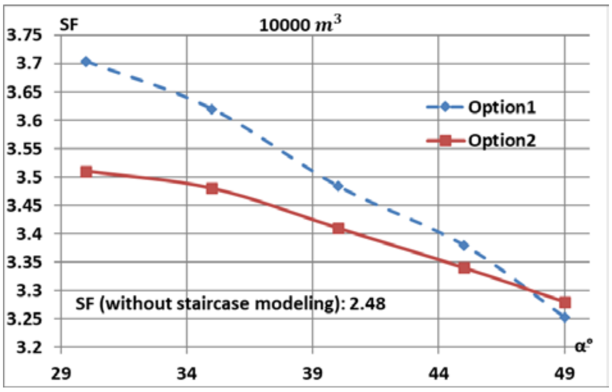

a) VCT of 10 thousand m^3 volume

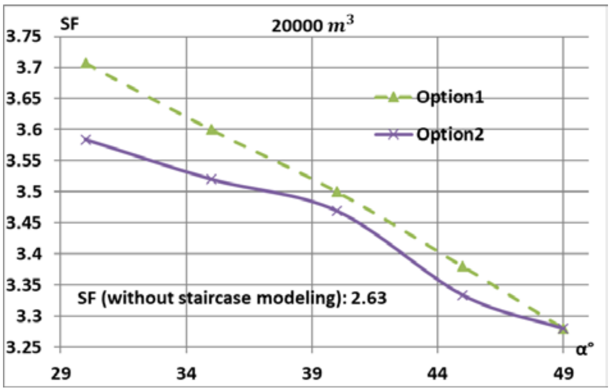

b) VCT of 10 thousand m^3 volume

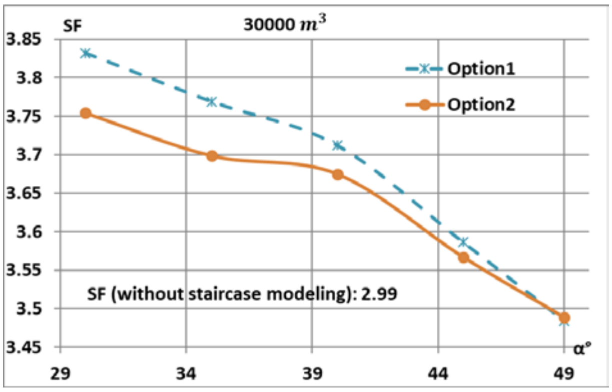

c) VCT of 10 thousand m^3 volume

Figure 10. Rigidity of the tank shell for different staircase parameters.

The foregoing graphs made it possible to determine the most typical features for all the considered volumes of tanks:

- the range of SF values depending on the slope of the staircase changes by up to 13 %;
- availability of a circular staircase increases the critical stresses of shell rigidity losses (under active wind pressure) by 20...50 % depending on its slope and design;
- the structural variant of staircase No.1 provides greater rigidity in comparison to the structural variant No. 2 (SF is 6 % greater);
- the α angle increasing, the difference between the values of SF for the considered structural variants of staircases is reduced;
- dependences of SF on α angle are close to the linear ones in the ranges of α angle = 30...40°;
- SF sharp decrease is noted for the tanks of 20 and 30 thousand m^3 volume for α angles > 40°.

The value of critical buckling stresses increases by up to 42 %, which generally correlates with the results obtained in the current work [23]. It was noted in the work [24] that a decrease in the acting stresses for a vertical cylindrical tank with a staircase by up to 5 % under the action of a wind load, which could not be confirmed in the current study. The difference may be due to the parameters of the reservoir and wind load.

Based on the results presented in paragraph 3.1, the constructive version of staircase No. 1 was chosen for further research as more preferable in terms of increasing the rigidity of the tank shell. The recommended staircase inclination angle α is 30..40°.

3.2. Results of calculating the adjusted wind pressure

Using the method given in paragraph 2.3, wind flow distributions were obtained, taking into account the presence of a spiral staircase on the tank shell. Using the built-in capabilities of the SolidWorks program, an array of data was formed to establish the dependences of the change in the aerodynamic coefficient for the tanks of the considered volumes – Fig. 11a-c.

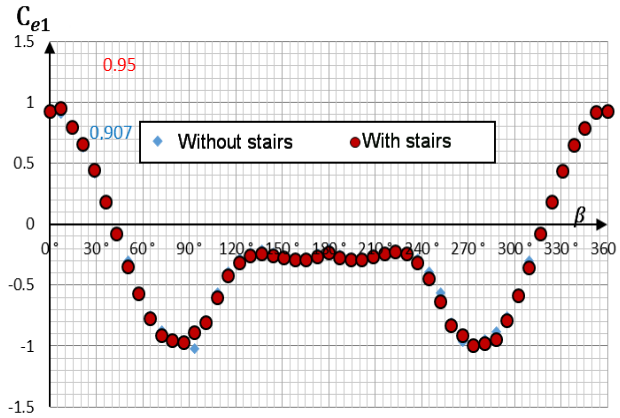

a) vertical cylindrical tank with a volume of 10 thousand m^3 with H/D = 0.63

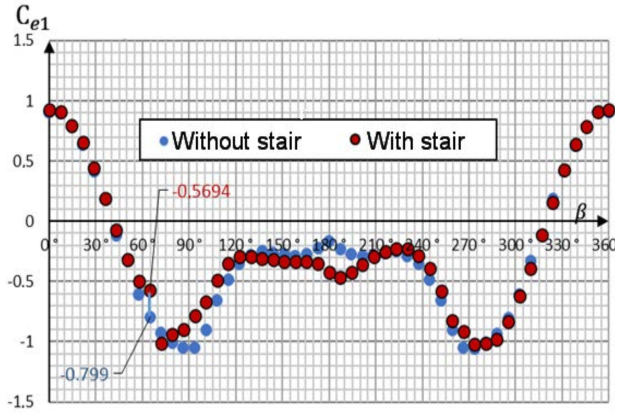

b) vertical cylindrical tank with a volume of 10 thousand m^3 with H/D = 0.45

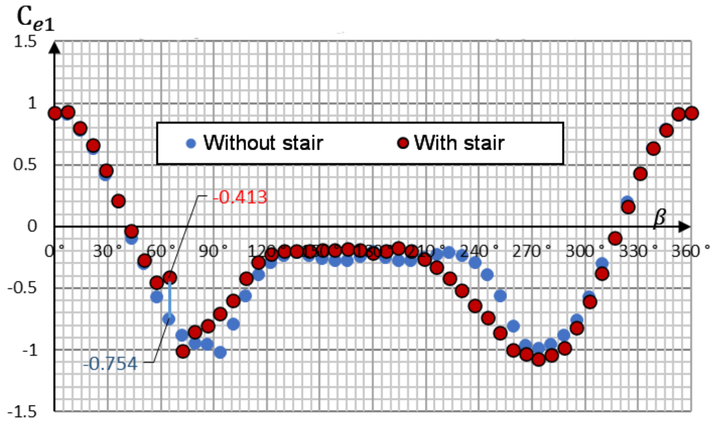

c) vertical cylindrical tank with a volume of 10 thousand m^3 with H/D = 0.4

Figure 11. Improved aerodynamic coefficients for a tank with a spiral staircase.

The obtained data on changes in the aerodynamic coefficient made it possible to determine the following features for the structures under consideration:

– with an increase in the volume of the tank, a change in wind pressure is observed in the area of adjacency of the staircase, in contrast to a tank without a staircase;

– the maximum discrepancy up to 20 % is noted in the zones of negative pressure (tearing effect on the tank shell);

– in the zone of active pressure, there is a decrease in the vacuum pressure, depending on the size, up to 6 %.

Since the data obtained show a difference from the normative approaches, the calculation of the stress-strain state and rigidity for the reservoirs under consideration was carried out, taking into account the specified parameters.

3.3. The results of the tank shell rigidity calculation for the refined distribution of the wind flow

The impact on the rigidity of the adjusted values of wind pressure is determined for the constructive version of staircase No. 1 (angle of inclination 30°). The methodology for setting the load and the parameters of the finite element model are given in clause 2.3. The obtained results are presented in the form of a diagram showing the change in the factor of rigidity y for various options in Fig. 12. The values of the factor of rigidity of the tank shell obtained earlier (in clause 3.1) for the standard wind load, for greater information content, are repeated in the current diagram.

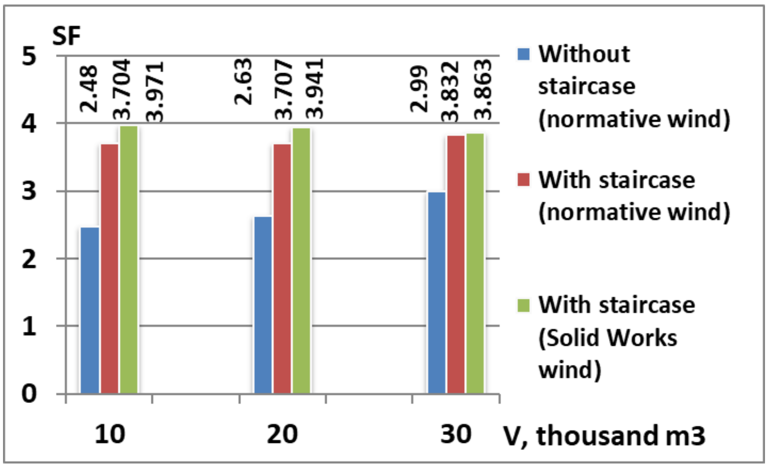

Figure 12. The tank shell rigidity for various variants of the finite element model.

From the diagram in Fig. 12 it follows that the adjusted wind load causes an increase in the ultimate buckling load by up to 7 % compared to the normative distribution. With an increase in the volume of vertical cylindrical tank, the difference in the factor of rigidity between the standard and specified wind pressure becomes less pronounced. In general, taking into account the staircase and the refined wind pressure in the model makes it possible to increase the ring critical buckling stresses by up to 50 %.

3.4. Results of stress-strain state analysis

According to the research algorithm (clause 2.4), the analysis of the stress-strain state includes:

– calculation of the tank shell deformations from the action of wind load for two versions of staircase;

– calculation of local stresses in the area of staircase fastening from the effect of hydrostatic load.

Fig. 13 a-c shows the deformed schemes of the tank shell with a volume of 20 thousand m^3 at a level of +9.000 meters from the impact of load combination No. 2.

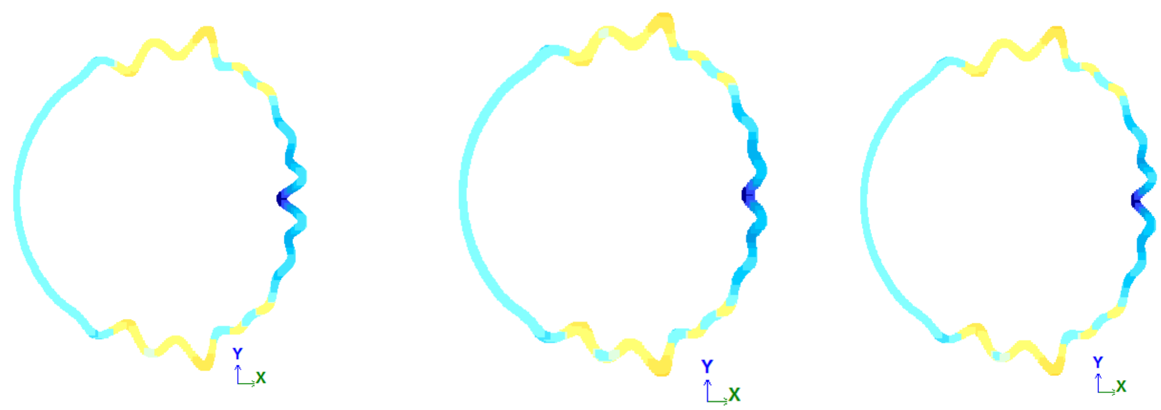

a) without staircase modeling **b) V1 – 40° inclination** **c) V2 –40° inclination**

Figure 13. Deformation of the tank shell with a volume of 20 thousand m^3 at a level of +9.000 meters.

The maximum tank shell displacements compared to the model without a staircase (Fig. 13a) are reduced by:

– 9 % for the case of the constructive version of staircases No. 2 (Fig. 13b);

– 14 % for the case of the constructive version of staircases No. 1 (Fig. 13c).

Fig. 13 a-b allow us to conclude that the constructive version of staircases No. 1 provides a greater total stiffness of the tank shell compared to option No. 2.

The results of the study [24] show a reduction in displacement by 5 % for a constructive type of staircases close to type No. 2. It is not possible to perform a direct comparison of the results, since the parameters of the staircase and the studied reservoir are not specified. In this case, the form of displacement is similar.

For the options under consideration, the circumferential (σx, MPa) and axis (σy, MPa) stresses from the action of a hydrostatic load (combination 2 from Table 5) were studied. The main controlled parameter was the concentration of stresses arising at the points of attachment of staircases to the tank shell. The stresses arising in the area of the two lower (most loaded) tank courses (the height of the considered section of the tank shell is up to +4.000 m) were considered. Several typical cases of distributions for a vertical cylindrical tank with a volume of 30 thousand m^3 are shown in Fig. 14–16. The results are presented in the form of images and graphs of changes in circumferential (σx, MPa) and axis (σy, MPa) stresses along the tank shell height. The fragments of the structural design (Fig. 14a, 15a) show the color distribution of stresses, and also show the position of the Z axis along which the stress change diagrams are plotted (Fig. 14b, 15b). The Z axis passes in the plane of the cylindrical tank course, perpendicular to the base. Fragments of structural design in Fig. 14a and 15a are models of real structures shown in Fig. 3a and 3b, respectively.

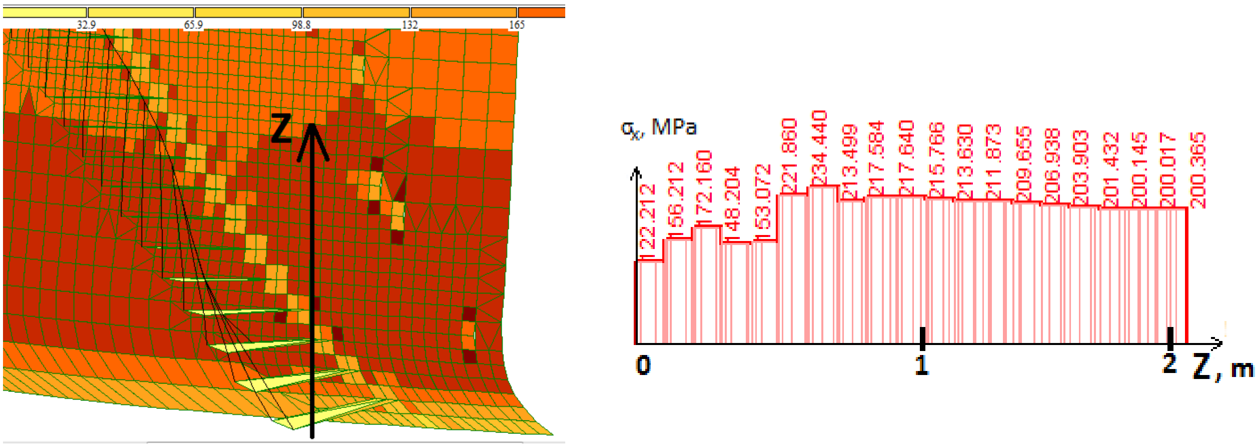

a) fragment of the deformed scheme **b) graph with tank shell height distribution**

Figure 14. Distribution of σ_x (MPa) for vertical cylindrical tank of 30 thousand m^3 in the area of staircase presence (V1).

For the constructive version of staircases No. 1 (V1), the presence of the staircase slightly changes the deformed scheme (Fig. 14a), while the values of hoop stresses increase. Thus on the graph presented in Fig. 14b, the maximum stress value is 234 MPa, which is 5 % higher than the value in areas remote from the staircase (Fig. 16a).

The concentration of meridional stresses is most prominent for the constructive version of staircase No. 2 – Fig. 15a. At the same time, due to the low rigidity of the attachment points of option 2, the value of the hoop stresses changes slightly.

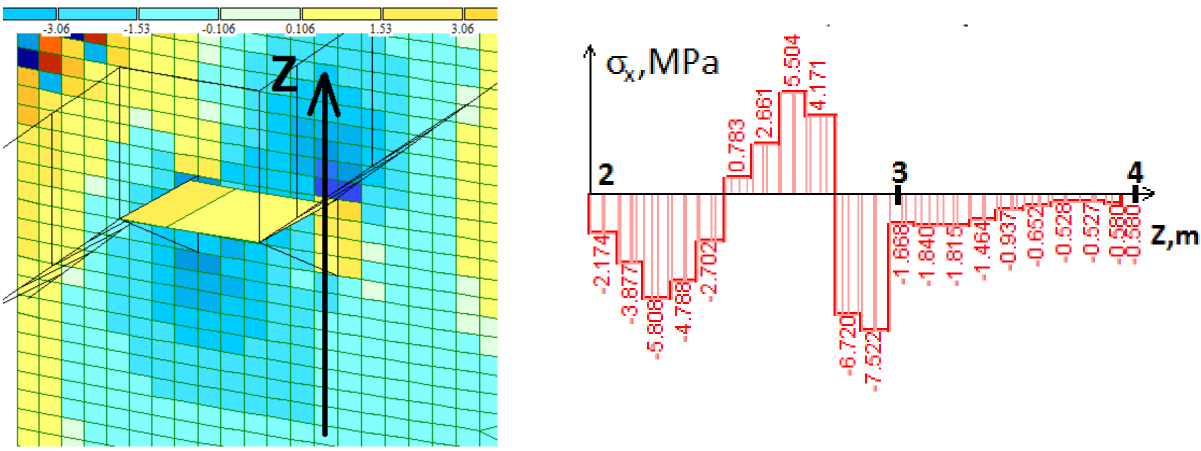

a) fragment of the structural design **b) graph with shell height distribution**

Figure 15 Distribution σ_y (MPa) for a vertical cylindrical tank of 30 thousand m^3 in the area of the presence of a staircase (V2).

It is important to note that the values of the meridional stresses are significantly less than the hoop stresses (up to 5 MPa) and are not a determining factor for this study – Fig. 15b. The graph of the distribution of circumferential (σ_x, MPa) and axis (σ_y, MPa) stresses along the tank shell height in the zone of the lower two tank rings is shown in Fig. 16 a and b, respectively.

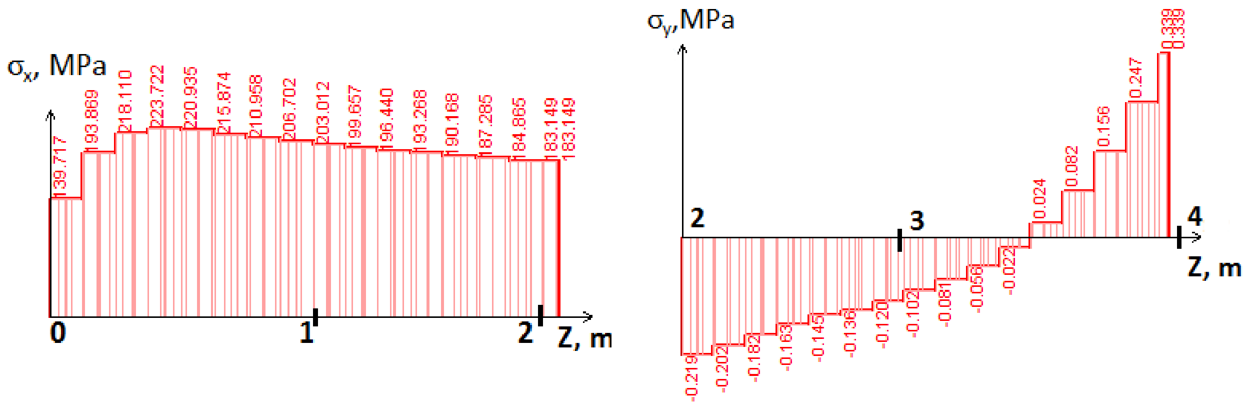

a) belt stresses, MPa **б) meridian stresses, MPa**

Figure 16. Stress distribution for VCT 30 thous. m^3 without staircase modeling.

Table 5 represents a piece of detailed information about the states of stress in the staircase fastening zones. The maximum of the belt stresses in the two lower chords are determined for two cases. Comparison of meridian stresses is not informative due to their small value and variances in it.

Table 5. Maximum belt stresses of the tank shell

Tank capacity, thous. m^3	Stresses, MPa (design 1)			Stresses, MPa (design 2)		
	For the loose part	For the staircase fastening zone	%	For the loose part	For the staircase fastening zone	%
10	206	210	1.9	208	211	1.44
20	212	218	2.8	216	217	0.46
30	223.22	234	4.9	196	198	1.02

The first design of the staircase leads to a higher concentration of belt stresses in comparison with the second one. There is a tendency to increase the stresses concentration with an increasing in the tank capacity. The maximum stress excess in the staircase fastening zone does not exceed 5 %. It is a case that does not lead to significant overspending of steel.

The subject of stress concentration in the places of staircase fastening is discussed in detail in this paper [30]. The results obtained by the author show an increase in stress by 8 %. The maximum is observed in the zone of the lower chord of the shell.

Steel consumption is chosen as an additional criterion for evaluating the choice of the recommended range. The mass of the spiral staircase (B1) is calculated depending on the slope to solve the problem. The corresponding graph is represented in Fig. 17.

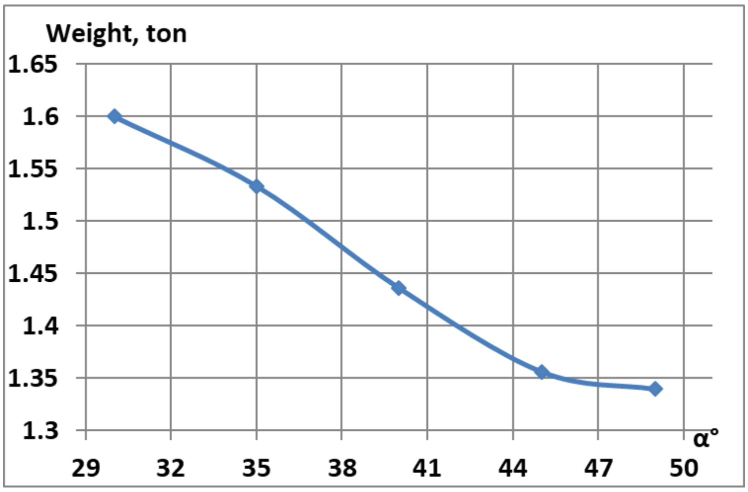

Figure 17. Staircase weight (B1) depending on the slope.

The data show that the staircase weight varies slightly in terms of the weight of the entire structure (less than 1 %) depending on the slope. Thus, the staircase weight cannot be a determining factor. Therefore, the staircase slope recommendations derived from the rigidity analysis and SSS of the tank will be accepted as final in the current study.

4. Conclusions

The study represents additional recommendations for the design solution and the creation of finite element models of vertical cylindrical tanks with a diameter of up to 50 m and a capacity of up to 30 thousand m^3. Considering the results of determining the effect of spiral staircases on the strength and rigidity of tanks, the conclusions of the paper are as follows:

- full-scale design of a spiral staircase significantly refines the stress-strain state of the tank as a whole;
- the most preferable option is staircase number 1 in accounting for increasing rigidity (the value of the belt critical stresses increases to 6 % compared to option number 2);
- the maximum increase in the rigidity of the shell is observed when the staircase slope to the horizon is in the range of 30...40°;
- the refined spreading of the wind layer around the staircase reduces the active pressure on the shell, which leads to a decrease in the acting stresses by up to 7 %;
- full-scale designing of staircases and refined wind load allows to increase critical belt stresses by up to 50 %;
- the weight of the spiral staircase is no more than 1 % of the weight of the entire tank structure and is not a determining factor;
- the stress concentration in the staircase fastening zones does not exceed 5 %.

The results represent the fact that spiral staircases significantly increase the rigidity of the tank shell. Moreover, spiral staircases do not have a significant negative effect on the strength of the VCT. Taking them into account allows expanding the list of methods for strengthening the tank shell s and determining the real reserves of structures. The lightweight and usage of spiral staircases make it possible to consider them as a promising method for increasing the rigidity of the VCT shells, both in new design and reconstruction.

References

1. Chen, C., Reniers, G. Chemical industry in China: The current status, safety problems, and pathways for future sustainable development. Safety Science. 2020. 128. Pp. 104741. DOI: 10.1016/j.ssci.2020.104741
2. Zakaev, D., Nikolaichuk, L., Filatova, I. Problems of Oil Refining Industry Development in Russia. International Journal of Engineering Research and Technology. 2020. 13 (2). Pp. 267–270.
3. BP Statistical Review of World Energy 2019 | 68th edition. [Online]. System requirements: AdobeAcrobatReader. URL: https://www.bp.com/content/dam/bp/business-sites/en/global/corporate/pdfs/energy-economics/statistical-review/bp-stats-review-2019-full-report.pdf
4. Zhang, Z., He, M., Zhang, Y., Wang, Y. Geopolitical risk trends and crude oil price predictability. Energy. 2022. 258. 124824. DOI: 10.1016/j.energy.2022.124824
5. Chang, J.I., Lin, C.-C. A study of storage tank accidents. Journal of Loss Prevention in the Process Industries. 2006. 19(1). Pp. 51–59. DOI: 10.1016/j.jlp.2005.05.015
6. Godoy, L.A., Flores, F.G. Imperfection sensitivity to elastic buckling of wind loaded open cylindrical tanks. Structural Engineering and Mechanics. 2002. 13 (5). Pp. 1–9. DOI: 10.12989/sem.2002.13.5.533
7. Hanuhov, H.M., Alipov A.V. Normativno-tekhnicheskoe i organizacionnoe obespechenie bezopasnoj ekspluatacii rezervuarnyh konstrukcij [Regulatory, technical and organizational support for the operation of the storage tanks]. Himicheskoe i neftegazovoe mashinostroenie. 2011. 10. Pp. 1–40.
8. Pichugin, S.F., Klochko, L.A. Accidents Analysis of Steel Vertical Tanks. Proceedings of the 2nd International Conference on Building Innovations, ICBI 2019. Baku. 2020. Pp. 193–204. DOI: 10.1007/978-3-030-42939-3_21
9. Filippov, V.V., Prokhorov, V.A., Argunov, S.V., Buslayeva, I.I. Tekhnicheskoye sostoyaniye rezervuarov dlya khraneniya nefteproduktov obyedineniya «Yakutnefteprodukt» [Technical condition of tanks for storage of oil products of the association "Yakutsknefteprodukt"]. Izvestiya vuzov. Stroitelstvo. 1993. 7–8. Pp. 13–16.
10. Zhao, Y., Liu, Q., Cai, S., Dong, S. Internal Wind Pressures and Buckling Behavior of Large Cylindrical Floating-Roof Tanks Under Various Liquid Levels. Journal of Pressure Vessel Technology. 2020. 142 (5). DOI: 10.1115/1.4046982
11. Mushchanov, V.P., Bachurin, O.M., Krysko, O.A. Latest approach of tank strengthening. Vestnik Donbasskoy natsionalnoy akademii stroitelstva i arkhitektury. 2010. 86 (6). Pp. 145–150.
12. Dyachenko, L.Yu., Kravchunovskaya, T.S., Dyachenko, O.S. Proyektirovaniye ratsionalnykh parametrov bandazhnykh poyasov pri usilenii stenki stalnykh tsilindricheskikh rezervuarov i rekomendatsii po opredeleniyu stoimosti ikh usileniya metodom bandazhirovaniya [Designing rational parameters of shroud belts when strengthening the walls of steel cylindrical tanks and recommendations for determining the cost of their strengthening by the shrouding method]. Vestnik PDASA. 2009. 12 (141). URL: https://cyberleninka.ru/article/n/proektirovanie-ratsionalnyh-parametrov-bandazhnyh-poyasov-pri-usilenii-stenki-stalnyh-tsilindricheskih-rezervuarov-i-rekomendatsii-po (date of application: 1.09.2022).

13. Plevkov, V.S., Plyaskin, A.S., Bunkov, Ye.V., Ustinov, A.M. Raschet vertikalnogo stalnogo rezervuara usilennogo uglekompozitnym bandazhom v programmnom komplekse ANSYS [Design of a vertical steel tank reinforced with a carbon-composite bandage using ANSYS software]. Bezopasnost stroitelnogo fonda Rossii. Problemy i resheniya : Materialy Mezhdunarodnykh akademicheskikh chteniy. 2020. Pp. 87–94.
14. Mushchanov, V., Tsepliaev, M. Rational design solutions of ensuring the walls of tanks stability to the action of transverse loads. IOP Conference Series: Materials Science and Engineering. 2020. 896 (1). DOI: 10.1088/1757-899X/896/1/012024
15. Mushchanov, V., Tsepliaev, M. Ensuring the stability of the walls of the tanks based on the rational arrangement of the stiffening rings. Constr. Unique Build. Struct. 2018. Pp. 58–73. DOI: 10.18720/CUBS.72.4
16. Uematsu, Y., Yamaguchi, T., Yasunaga, J. Effects of wind girders on the buckling of open-topped storage tanks under quasi-static wind loading. Thin-Walled Structures. 2018. 124. Pp. 1–12. DOI: 10.1016/j.tws.2017.11.044
17. Zeybek, Ö., Topkaya, C., Rotter, J.M. Strength and stiffness requirements for intermediate ring stiffeners on discretely supported cylindrical shells. Thin-Walled Structures. 2015. 96. Pp. 64–74. DOI: 10.1016/j.tws.2015.08.004
18. Lemák, D., Studnička, J. Influence of Ring Stiffeners on a Steel Cylindrical Shell. Acta Polytechnica. 2005. 45(1). 674. DOI: 10.14311/674.
19. Bu, F., Qian, C. A rational design approach of intermediate wind girders on large storage tanks. Thin-Walled Structures. 2015. 92. Pp. 76–81. DOI: 10.1016/j.tws.2015.02.024
20. Teng, J.G., Rotter J.M. Buckling of Thin Metal Shells. London, Spon Press, 2004. ISBN: 0-203-34223-2.
21. Jahangiri, M., Fakhrabadi, M.H., Jahangiri, M. Computational Buckling Analysis of Wind Loaded Cylindrical Storage Tanks. Majlesi Journal of Energy Management. 2012. 4 (1). Pp. 22–31.
22. Sun, T., Azzuni, E., Guzey, S. Stability of Open-Topped Storage Tanks With Top Stiffener and One Intermediate Stiffener Subject to Wind Loading. Journal of Pressure Vessel Technology. 2018. 140(1). 011204. DOI: 10.1115/1.4038723
23. Shokrzadeh, A.R., Mansuri, F., Asadi, M., Sohrabi, M.R. Comparative analysis on buckling behavior of steel cylindrical tanks by consideration of more realistic numerical models. World Congress on Civil, Structural, and Environmental Engineering. 2020. Pp. 159-1–159-8. DOI: 10.11159/icsect20.159
24. Hussien, M.A., Hagag, S.Y.A., Maged, A., Korashy, M.M. Stability of Petroleum Storage Tanks considering the effect of Helical Stair Beams. International Journal of Research in Engineering and Management. 2020. 4 (1). Pp. 24–35. [Online]. System requirements: AdobeAcrobatReader. URL: http://www.crdeepjournal.org/wp-content/uploads/2020/08/Vol-4-1-3-IJREM-compressed.pdf (date of application: 1.09.2022).
25. Mochida, A., Tominaga, Y., Murakami, S., Yoshie, R., Ishihara, T., Ooka, R. Comparison of various k-ε models and DSM applied to flow around a high-rise building – report on AIJ cooperative project for CFD prediction of wind environment. Wind and Structures. 2002. 5 (2_3_4). Pp. 227–244. DOI: 10.12989/was.2002.5.2_3_4.227
26. Tominaga, Y., Mochida, A., Harimoto, K., Kataoka, H., Yoshie, R. Development of CFD method for predicting wind environment around a high-rise building : Part 3 : The cross comparison of results for wind environment around building complex in actual urban area using different CFD codes(Environmental Engineering). AIJ Journal of Technology and Design. 2004. 10 (19). Pp. 181–184. DOI: 10.3130/aijt.10.181
27. Shirasawa, T., Tominaga, Y., Yoshie, R., Mochida, A., Yoshino, H., Kataoka, H., Nozu, T. Development of CFD method for predicting wind environment around a high-rise building : Part 2 : The cross comparison of CFD results using various k-ε models for the flowfield around a building model with 4:4:1 shape (Environmental Engineering). AIJ Journal of Technology and Design. 2003. 9 (18). Pp. 169–174. DOI: 10.3130/aijt.9.169_2
28. Tsepliaev, M.N. Modeling of real loading diagrams of wind pressure on cylindrical tank using SCAD software. Metal Constructions. 2016. 22 (4). Pp. 169–174. [Online]. System requirements: AdobeAcrobatReader. URL: http://donnasa.org/publish_house/journals/mk/2016-4/02_tcepliaev.pdf (date of application: 1.10.2022).
29. Azzuni, E., Guzey, S. Stability of aboveground storage tanks subjected to wind loading. Analysis and Design of Plated Structures. Elsevier, 2022. Pp. 479–495. DOI: 10.1016/B978-0-12-823570-6.00006-9
30. Mushchanov, V., Tsepliaev, M. Refinement of the tanks wall stress-strain state when using 3D modeling of stiffening rings. International scientific-practical conference “Architecture and art: from theory to practice.” 2018. Pp. 76–88.

Information about authors:

Maxim Tcepliaev, *PhD in Technical Sciences*
ORCID: https://orcid.org/0000-0002-1729-4127
E-mail: m.n.cepliaev@donnasa.ru

Vladimir Mushchanov, *Doctor of Technical Sciences*
E-mail: mvf@donnasa.ru

Anna Zubenko, *PhD in Technical Sciences*
E-mail: a.v.zubenko@donnasa.ru

Alexander Mushchanov, *PhD in Technical Sciences*
E-mail: a.v.mushchanov@donnasa.ru

Anatoly Orzhehovsky, *PhD in Technical Sciences*
E-mail: a.n.orzhehovskiy@donnasa.ru

Received 06.10.2022. Approved after reviewing 17.01.2023. Accepted 01.02.2023.

Magazine of Civil Engineering. 2023. 119(3). Article No. 11907

Magazine of Civil Engineering

ISSN 2712-8172

journal homepage: http://engstroy.spbstu.ru/

Research article

UDC 691.11

DOI: 10.34910/MCE.119.7

Strength properties of raw wood after a wildfire

***A.L. Lukina*[1], *M.L. Lisyatnikov*[1], *M.L. Lukin*[1], *N. Vatin*[2], *S.R. Roshchina*[1]**

[1] *Vladimir State University named after Alexander and Nikolay Stoletovs, Vladimir, Russia*

[2] *Peter the Great St. Petersburg Polytechnic University. St. Petersburg, Russia*

vatin@mail.ru

Keywords: wood, wildfire, strength, weakened wood, residual resource, resource-saving

Abstract. Using fire-damaged wood is one of the efficient and resource-saving approaches to forest conservation. The object of the study is raw wood exposed to fire. The aim of the study is to analyze the mechanical properties of fire-damaged pinewood, the height of the trunk, and determine the possibility of its use as a structural material. Tests were carried out for static bending, compression along the fibers, and tension along the fibers. We performed the tests on samples taken from the lower, middle, and upper parts of the fired wood and compared them with wood that was not exposed to fire. It was established that during a ground and medium fire, the strength properties of wood are most reduced in the apical part of the trunk by 41.80 % compared to wood undamaged by fire. The smallest decrease in strength occurred in the lower part of the tree. It was determined that with sufficiently small damage to wood by fire, i.e., a decrease in the cross-sectional area to 15 %, it can be partially used as a structural material.

Funding: The study was supported by a grant from the Russian Science Foundation No. 22-29-01579. https://rscf.ru/project/22-29-01579/

Citation: Lukina, A.L., Lisyatnikov, M.L., Lukin, M.L., Vatin, N., Roshchina, S.R. Strength properties of raw wood after a wildfire. Magazine of Civil Engineering. 2023. 119(3). Article no. 11907. DOI: 10.34910/MCE.119.7

1. Introduction

Wood is characterized by the presence of various defects (knots, shrinkage cracks, oblique, etc.). Therefore, at the stage of designing wooden structures, there are increased requirements for knowledge of the strength characteristics of wood, features of load resistance [1–5]. Using wooden structures is inseparably associated with trends in energy and resource-saving of wood, increasing the strength and rigidity of elements while reducing their assembly weight and increasing operational reliability [6, 7].

Thus, in works [8–10], a method was proposed and scientifically substantiated to restore destructed wooden structures by impregnating them with a polymer composition. In [11] authors propose a method for estimating the residual resource of wooden structures by changing their geometric parameters. A general formula is given for calculating the service life of wooden structures. The authors of [12] studied samples of wood building materials (plywood, oriented strand board, and chipboard) in laboratory conditions because of exposure to heat flow from a natural flame. Experimentally confirmed that particle size plays a significant role in the ignition of the building structure. The works also describe and substantiated the issues of resource-saving of wood and the reduction of material consumption for building structures [13, 14].

Forest fires cause great damage to the state of natural forest ecosystems around the world. Many countries are facing this scourge. For example, in December 2010, in Israel (near Haifa), 5000 hectares of forest were engulfed in fire. The fire lasted over three days and was extinguished with the help of 24 countries [15]. A forest fire in the state of California (USA) covered 45000 hectares; in October 2017, 44000 hectares of forest burned down in Portugal because of fire [15]. Turkey's forest fires in 2021 brought significant damage to the economy [16].

Over three million hectares of forests in Siberia (Russia) covered by fire in 2019 clearly show what danger fires in the forest pose to the life and health of people and what damage they cause to property and wildlife [17–20]. Almost two-thirds of Russia's territory is covered with forest. According to the Federal Forestry Agency of the Russian Federation, the total area of forest fund lands is 1 billion 146 million hectares. From 9000 to 35000 forest fires are registered annually in Russia, covering areas from 0.5 to 3.5 million hectares [21]. Over 8.7 million hectares of natural territory burned down in 2021 in Yakutia, Russia [22].

Now there is a shortage of coniferous wood [23, 24]. The maximum use of natural resources should be increased through the wider use of wood with reduced technical characteristics. Thus, one of the main issues of forest research is the question of the technical quality of fire-damaged wood and the possibility of using it as a structural material.

In the works [25–27], studies of the residual mechanical properties of wood after a fire were carried out: static bending, estimation of Young's modulus, impact strength coefficient. The question of the strength properties of damaged wood under typical stress states, such as tension and compression along the fibers, has remained unexplored.

Using wood exposed to fire is one of the effective and resource-saving approaches to conserving forests. Works [28–31] show that partially charred wood keeps sufficiently high physical properties, making it possible to use it as a structural material. However, the amount of results obtained, including international studies, is insufficient to form a clear legal framework governing the use of raw wood exposed to fire in building structures [32–34]. Therefore, the research direction related to studying the physical and mechanical properties of raw wood exposed to fire is an urgent task. The research aimed to analyze the mechanical properties of fire-damaged pinewood, the height of the trunk, and determine the possibility of its use as a structural material.

2. Materials and Methods

Wood exposed to fire (high temperatures) is of considerable scientific interest. We are talking about wood, which is partially charred, and the rest has a visually healthy appearance (Fig. 1). The question arises: what are its residual strength properties? Whether such wood can be used as a structural material. To study the suitability of wood exposed to fire for use as a structural material, it is planned to analyze the mechanical properties of wood by comparing its characteristics with reference samples, i.e. unaffected by fire. As a "reference" wood was taken the 2nd grade pine (Pinus sylvestris), not exposed to fire, growing in the same area (Namsky Appany, Namsky Edeytsy, and Namtsy-1 Khomustakh).

Wooden building structures are mainly made of coniferous species (pine, spruce, larch), so we will limit ourselves to considering the residual strength of pine samples. For testing, samples were taken from wood (pine) exposed to fire. Forest growth areas are the Namsky Appany, Namsky Edeytsy, and Namtsy-1 Khomustakh (Yakutia, Russia). The type of intended purpose of the forest is operational. The type of fire is grassroots, stable, and medium. Samples were taken from trees in which the area of damage by fire along the trunk section was 10–15 % (Fig. 1). According to the nature of fire damage to trees and analysis of data from forest fire reports, we can conclude that the temperature of the fire was approximately 400 °C.

We selected from the bottom, middle and top parts. Samples were made from each cut along the radius: in the center, by 0.5 radii (middle), and on the periphery. Trees for testing (models) were selected as follows. Model trees are cut into ridges. The charred part of the tree was removed. The ridge is sawn into boards, and the boards into bars (blanks), and samples are made from the blanks (Fig. 1b).

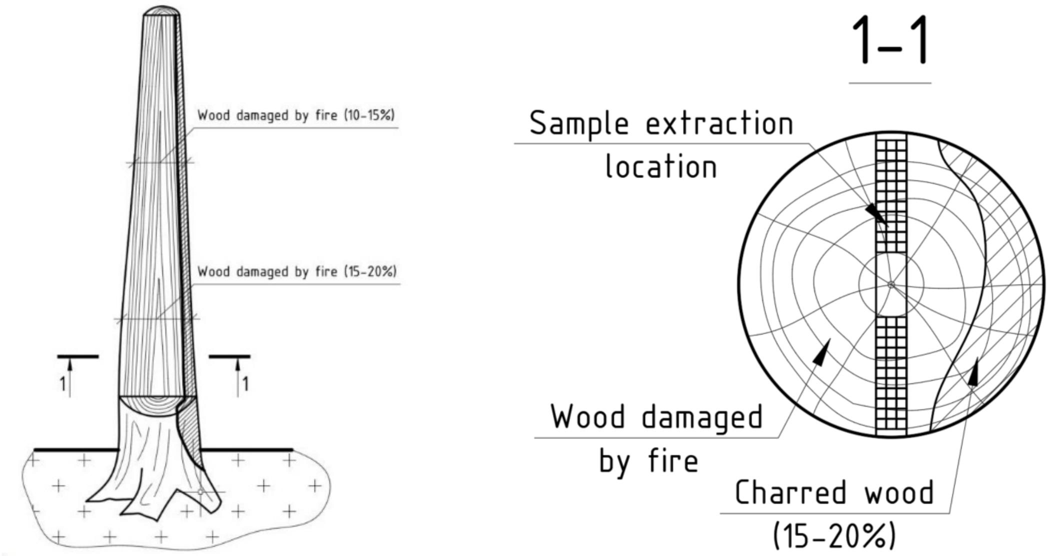

(a) **(b)**

Figure 1. Growing tree exposed to fire: (a) general view; (b) section.

To characterize the properties of wood as a homogeneous material, without defects, samples of a small section are selected for testing in order to avoid the influence of the curvature of the annual layers. At the same time, the samples must include a sufficient number of anatomical elements characteristic of the tested breed (at least 4 or 5 annual layers). Therefore, tests are carried out on samples with a cross section of 20×20 mm. The dimensions of the samples were determined with a sliding caliper with a measurement error of no more than 0.1 mm. The selection of units for testing was carried out according to the "Wood. General requirements for physical and mechanical tests". The least stressed places in the wooden beams are located in the middle part of the section (closer to the neutral axis), since the normal stresses in these areas have minimum values.

Sampling from the general population was carried out in one stage using systematic sampling. The minimum number of samples to be tested (nmin) was determined by the formula:

$$n_{\min} = \frac{V^2 \cdot t_\gamma^2}{P_\gamma^2}, \tag{1}$$

where, V is coefficient of variation of wood properties, %. The coefficient of variation was taken for testing: compression along the fibers – 13 % stretching along the fibers 20 %, for static bending – 15 %; γ is required confidence level; t_γ is quantile of Student's distribution; P_γ is relative accuracy of determining the sample mean with a confidence level.

The relative accuracy of determining the sample mean was taken as 5 % at a confidence level of 0.95. In case of partial replacement or damage of samples, the number of samples was increased by 20 % relative to the calculated number in each type of test.

The wood was stored at natural humidity after sampling. Before mechanical testing, the moisture content of the samples was adjusted to 12 %. The studies were carried out according to the methods described below.

The studies were carried out on a REM-100-A-1 testing machine (Russia, Tomsk, Rusenergo LLC). The universal testing machine REM-100-A-1 is designed for mechanical testing in tension, compression, and bending of specimens and products made of materials whose breaking load does not exceed 100 kN. Mechanical testing of samples on the machine is carried out by deforming the sample to failure with controlled movement of the traverse.

Multichannel measuring complex TDS-530 was used to register relative deformations with a high degree of accuracy. The complex performs simultaneous hardware-synchronized reception, digitization, processing of signals through all measuring channels and transmission of measured values via digital interfaces during single and multiple measurements in real time. The use of the complex makes it possible to register edge deformations of materials through the use of strain gauges with a base of 20 mm. The latter are glued to the previously cleaned and prepared surface of wooden elements using an adhesive composition based on cyanoacrylate. The deformations measurement accuracy was 0.001 mm.

2.1. Determination of the tensile strength of wood weakened by fire during static bending

The samples were made in the form of a rectangular prism (bar) with a cross-section of 20×20 mm and a length along the fibers of 300 mm. The sample was loaded uniformly at a constant loading rate (Fig. 2a,b). The sample is placed in the machine so that the bending force is directed tangentially to the annual layers (tangential bending) and loaded according to the scheme shown in Fig. 2c.

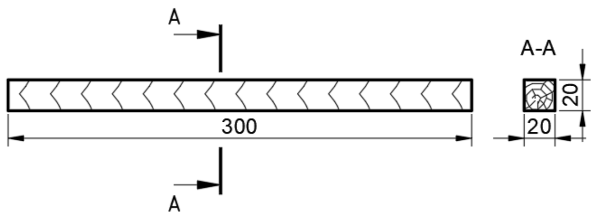

(a)

(b)

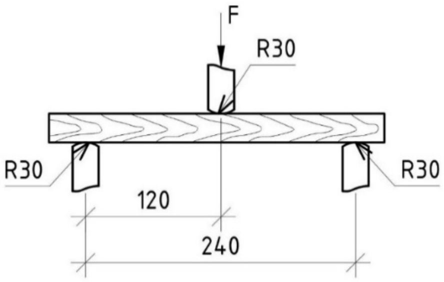

(c)

Figure 2. Testing wood weakened by fire for static bending: (a) the shape of the test piece, mm; (b) sample testing; (c) sample loading scheme.

The sample was loaded evenly at a speed of 4 mm/min for the loading head of the testing machine. The destruction occurred 1.5 min after the start of loading. Five series (repetitions) of tests were carried out. The number of tested samples was taken equal to 36. In all cases, the specified number of tested specimens refers to one series of tests for each type (compression, tension, shearing and bending). Each series of tests included specimens from different parts by trunk height (butt, middle and top) and tree growing region (3 regions).

2.2. Determination of the tensile strength of wood weakened by fire in compression along the fibers

The samples were made in the form of a rectangular prism with a base of 20×20 mm and a length along the fibers of 30 mm (Fig. 3). The sample was loaded uniformly at a constant loading rate.

The loading occurred evenly at a speed of movement of the loading head of the testing machine of 4 mm/min. The destruction of the sample occurred 1 min after the start of loading. Five series (repetitions) of tests were carried out. The number of tested samples was taken equal to 29.

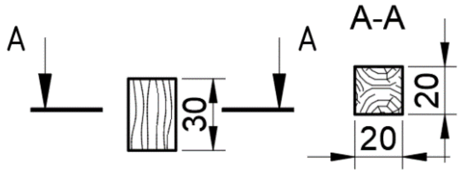

(a)

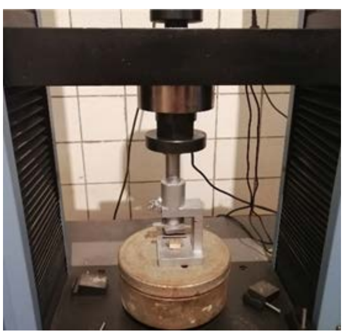

(b)

Figure 3. Testing wood weakened by fire for compression along the fibers: (a) the shape of the test specimen, mm; (b) sample testing.

The strength of the rod in compression and the loss of stability depends on the area and shape of its section, the length l and the type of fastening of its ends, which is taken into account by the stability coefficient φ. In relative short elements, the length of which does not exceed seven times the height of the section, they work in compression without loss of stability. Therefore, in the calculations, when determining the compressive stresses σ, the stability coefficient was not introduced.

2.3. Determination of the tensile strength of wood weakened by fire in compression along the fibers

Sample blanks were gouged out. The samples were made according to the shape shown in Fig. 4.

The sample was placed in the grips so that the part of each head adjacent to the rounding remained free for 20–25 mm. The tensile load coincided with the longitudinal geometric axis of the sample.

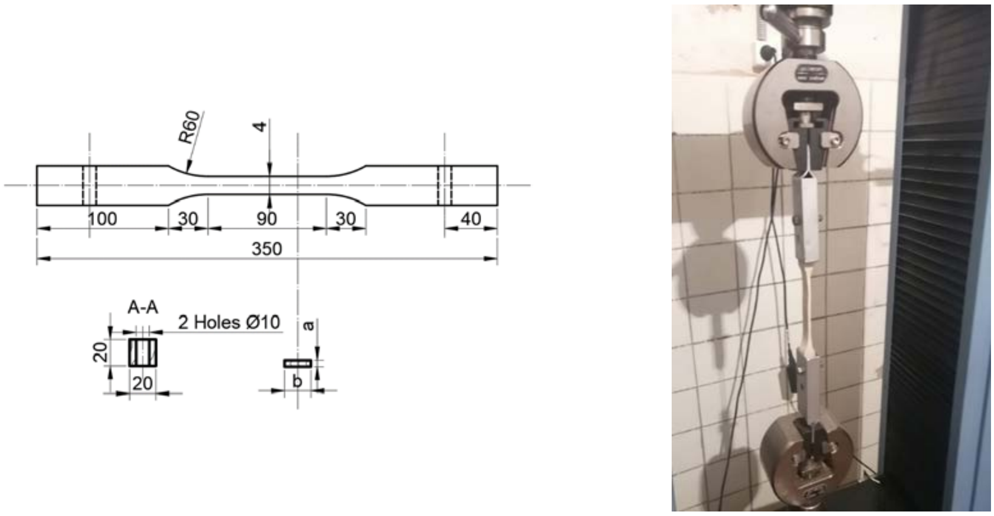

(a) **(b)**

Figure 4. Tensile testing of wood weakened by fire along the fibers: (a) the shape of the test specimen, mm; (b) sample testing.

Loading occurred evenly at a speed of movement of the loading head of the testing machine of 10 mm/min. The destruction of the sample occurred on average 98 seconds after the start of loading. Five series (repetitions) of tests were carried out. The number of tested samples was taken equal to 33.

The strength of wood is related to its density. Therefore, density indicators were determined for the studied parts of the tree. The essence of the method is to determine the mass and volume of the sample at the appropriate moisture content of the wood and calculate the density indicators. The results of laboratory tests are presented in Table 1.

For an adequate analysis of mechanical tests, the rheological properties of wood should be taken into account. Currently, a complete rheological model of wood consists of the following components [35]:

- elastic deformation ε^{el};
- non-regenerating plastic deformation ε^{pl};
- deformation shrinkage or swelling deformation caused by a change in wood moisture ε^{ω};
- viscoelastic creep deformation ε^{ve};
- mechanical sorption deformation ε^{ms}.

As a result, the total relative strain tensor of the wood comprises five components [35]:

$$\varepsilon = \varepsilon^{el} + \varepsilon^{pl} + \varepsilon^{\omega} + \sum_{i=1}^{n} \varepsilon_i^{ve} + \sum_{j=1}^{m} \varepsilon_j^{ms}. \tag{2}$$

The proposed rheological model reflects the deformations that occur most fully under real deformation conditions.

3. Results and Discussion

The experimental data of wood samples weakened by fire were compared with reference samples. Pine samples from undamaged wood by fire were taken as samples undamaged by the fire. Based on the test results, statistical processing of experimental data was carried out. The accuracy rate P (%) was determined by the formula:

$$P = \pm \frac{m}{V} \cdot 100\%, \tag{3}$$

where m is the average error of the arithmetic mean; V is the coefficient of variation.

Fig. 5 shows the results of testing samples for the static bend.

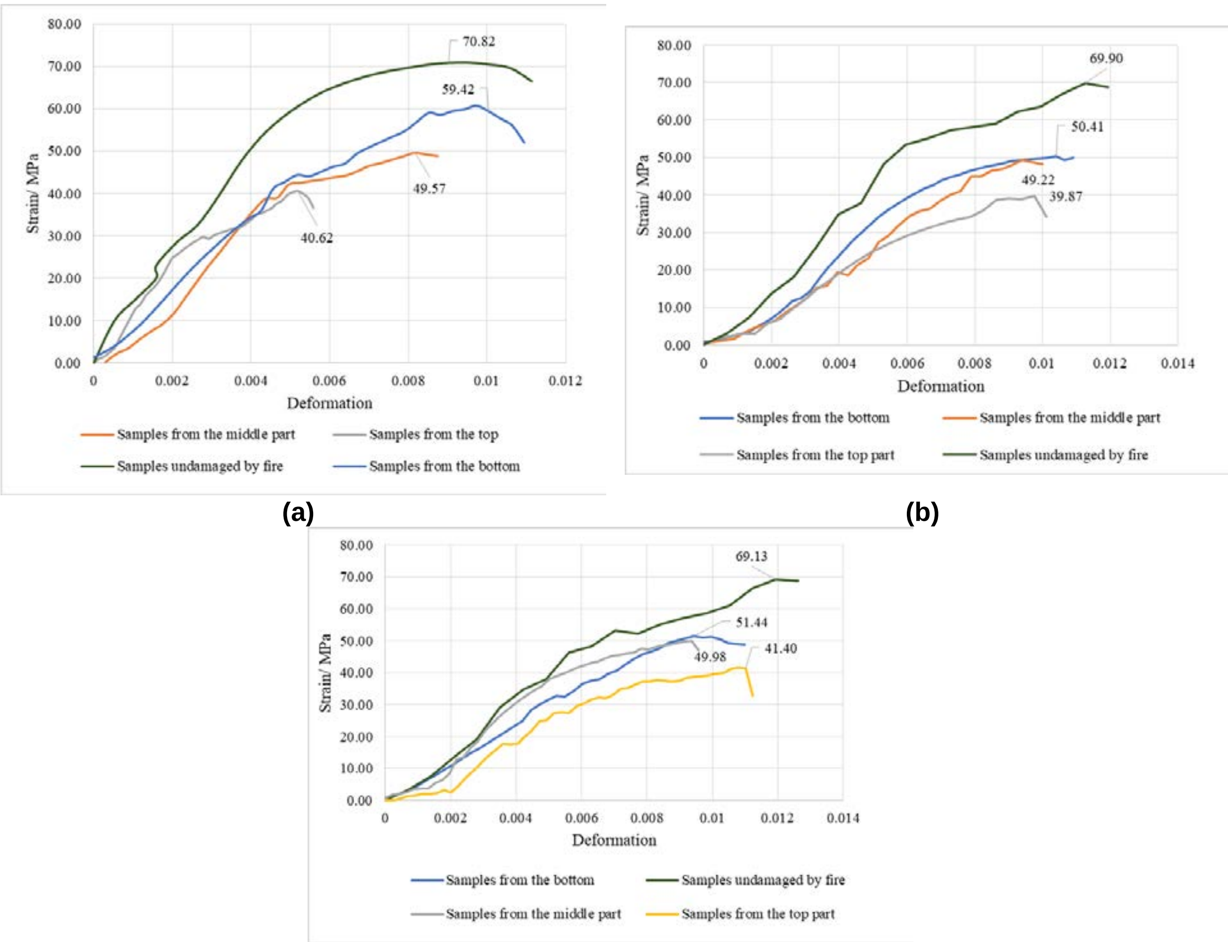

(a) (b)

(c)

Figure 5. The strength of pinewood weakened by fire for static bending in different parts of the trunk: (a) Namsky Appany; (b) Namtsy-1 Khomustakh; (c) Namsky Edeytsy (Yakutia, Russia).

Fig. 6 shows the results of testing samples for compression along the fibers.

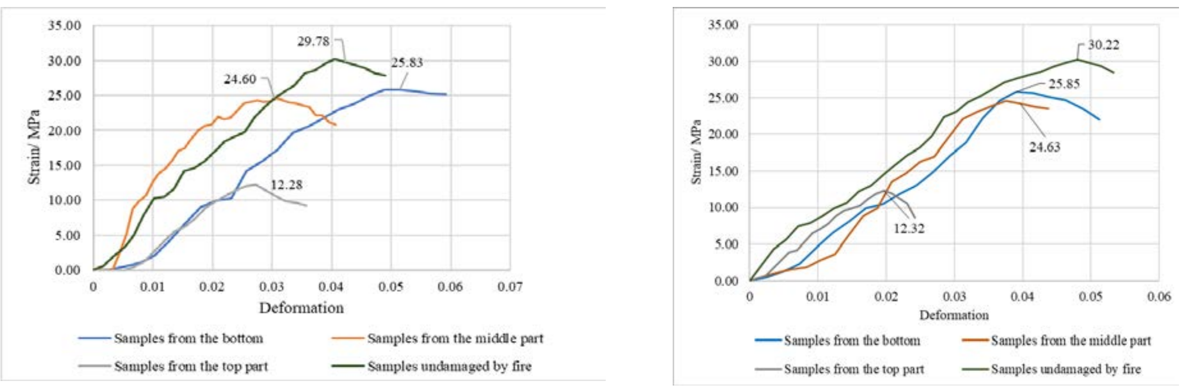

(a) (b)

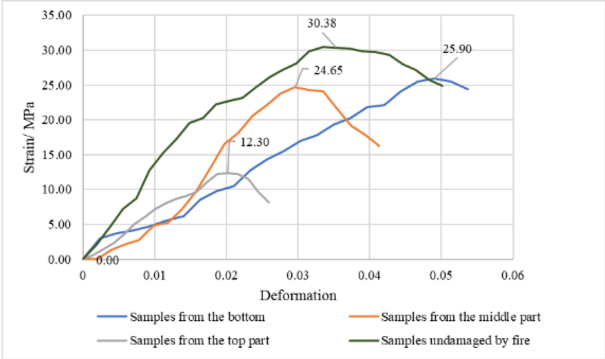

(c)

Figure 6. The strength of pinewood weakened by fire for compression along the fibers in different parts of the trunk: (a) Namsky Appany; (b) Namtsy-1 Khomustakh; (c) Namsky Edeytsy (Yakutia, Russia).

Fig. 7 shows the strength of pinewood weakened by fire in tension along the fibers in different parts of the trunk.

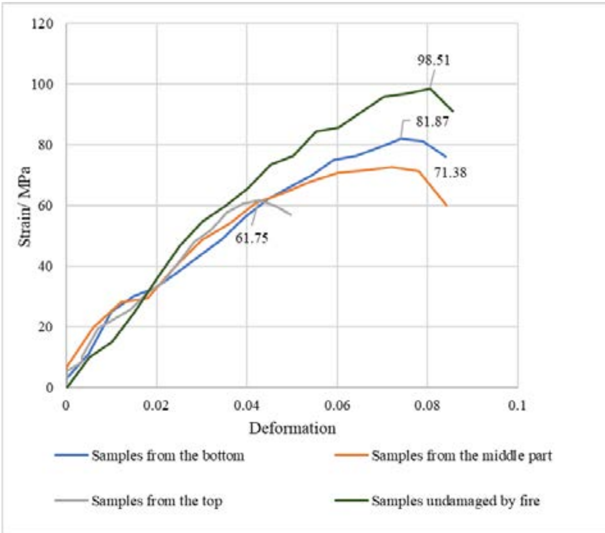

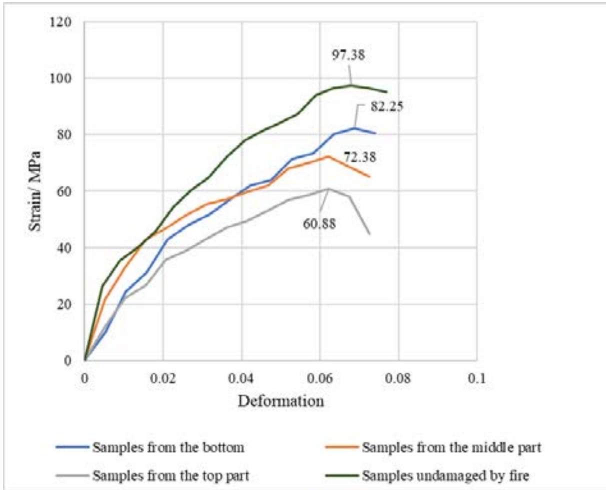

(a) (b)

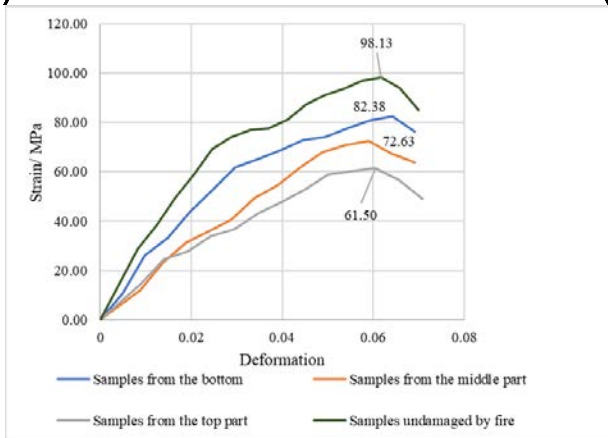

(c)

Figure 7. The strength of pinewood weakened by fire in tension along the fibers in different parts of the trunk: (a) Namsky Appany; (b) Namtsy-1 Khomustakh; (c) Namsky Edeytsy (Yakutia, Russia).

Experimental data allow us to consider all materials up to certain loading limits as elastic and obey Hooke's law [36, 37]. The simplest form of the law of deformation in time describes the flow of an ideally viscous fluid in which strain is proportional to the rate of deformation ε:

$$\sigma = \kappa \cdot \varepsilon, \tag{4}$$

where σ is the strain, κ κ is the coefficient of proportionality, ε is the deformation.

The coefficient of proportionality κ is called the coefficient of viscosity or the coefficient of internal resistance.

Hooke's law is preserved to a greater extent in the diagram when the wood is stretched along the fibers to destruction (see Fig. 7). Wood works in tension almost like an elastic material and has high strength. The destruction of the stretched elements occurred brittle, in the form of an almost instantaneous rupture of the least strong fibers along a sawtooth surface.

The fracture mechanics of the sample under compression along the fibers is shown in Fig. 6. Up to about half of the tensile strength, the growth of deformations occurs according to a close to linear law, i.e., strain growth is directly proportional to the applied load [38, 39]. Thus, that wood working in real conditions almost elastically. In the section of a compressed element, the compressive force acting along its axis gives rise to almost equal normal compressive stresses σ. As the load increases, the increase in deformations increasingly outstrips the growth of stresses, indicating the elastic-plastic nature of the wood deformation. The destruction of the samples occurred plastically, as a result of the loss of local stability of the walls of a number of wood fibers. Therefore, compressed elements work more reliably than stretched ones, and are destroyed only after obvious deformations. Analysis of the dependence "strain-deformation" (Fig. 6) illustrates that viscoelastic deformations appear during failure. Defects in natural wood less reduce the strength of the compressed elements, since they perceive part of the compressed elements.

Fig. 5-7 illustrate that in the study areas after the fire (Namskie Appany, Namtsy-1 Khomustakh, Namsky Edeytsy, Yakutia, Russia), one common pattern is observed, namely the largest decrease in mechanical characteristics in the top part of the tree. The limiting normal strains σ at which the specimens failed in all types of tests was determined by the failure load indicators.

Determining the limiting normal strains are convenient for a comparative assessment of the strength of various types of wood. The strength of wood under various types of stress states and with their various combinations (complex stress) must be known for a reasonable calculation of the elements of wooden structures.

Table 1 shows the averaged results of the tests. The tests show that the mechanical strength of wood decreases in different ways, depending on the type of load and the height of the trunk. The greatest decrease in strength for all types of tests is observed in samples taken from the upper part of the tree trunk. The smallest decrease in strength in all three tests was observed in samples taken from the bottom.

According to the test results, it can be seen that the ground fire was weak and did not fundamentally change the quality of the wood [40]. The properties of wood within the same trunk are not constant, and these changes are subject to the following generally accepted pattern: the best wood is in the bottom part of the trunk; as it rises along the trunk, strength decreases. The obtained data are consistent with the works [41, 42].

Table 1. Averaged results of the tests of wood samples.

Type of tests	$\frac{\textbf{Strain}, [\textbf{MPa}]}{\textbf{Accuracy index P}, \%}$			
	Bottom part	Medium part	Top part	Wood samples undamaged by fire
Static bend	$\frac{53.75}{\pm 0.36}$	$\frac{49.59}{\pm 0.33}$	$\frac{40.63}{\pm 0.32}$	$\frac{69.90}{\pm 0.38}$
Strength reduction, %	-23.10	-29.00	-41.80	-
Compression along the fibers	$\frac{25.86}{\pm 3.27}$	$\frac{24.63}{\pm 3.12}$	$\frac{12.13}{\pm 2.75}$	$\frac{30.13}{\pm 3.83}$
Strength reduction, %	-14.10	-18.20	-59.71	-
Stretch along the fibers	$\frac{82.17}{\pm 2.08}$	$\frac{72.13}{\pm 1.84}$	$\frac{61.34}{\pm 1.55}$	$\frac{98.01}{\pm 2.47}$
Strength reduction, %	-16.1	-26.40	-37.40	-
Wood density, kg/cm^3	476.61	427.46	439.55	495.65

Note. The numerator indicates the strain at the relevant tests; in the denominator – an indicator of accuracy (in percent) relative to wood samples undamaged by fire.

The decrease in the technical qualities of wood along the entire height of the trunk is explained by the destruction of wood, which occurred under the influence of high temperature. The structure of the wood changes, the water content in the wood decreases sharply, and its distribution along the tree trunk causes thermal destruction of the wood components [43]. Thus, high temperature during a fire has a devastating effect on the structure of wood. This type of destruction of cell walls can be explained by the fact that under the influence of high temperature free moisture boils off in the cavities of vessels, which in turn leads to an increase in excess pressure of the vapor-air mixture, which contributes to the destruction of cell walls in groups of vessels.

Wood with reduced technical qualities cannot be used for the load-bearing wooden structures in the shipbuilding and automotive industry and for wooden frames, roofs, and various supports. But it is suitable for the manufacture of non-load-bearing structures, rough finishes, the construction of temporary huts, sheds, etc., which, in conditions of an acute shortage of wood, solves many issues.

4. Conclusions

As a result of the study, the following conclusions can be drawn:

1. It has been established that the "strain-deformation" diagrams of tension, compression along the fibers and static bending of specimens exposed to fire are comparable to those of healthy wood specimens. A general characteristic trend is observed: the highest strength is shown for samples experiencing tensile forces. When stretched, the fracture was brittle. During compression, the samples were destroyed due to the loss of local stability. However, the compressed structural elements, as a rule, have a length much greater than the cross-sectional dimensions, and are not destroyed as small standard samples, but as a result of buckling, which occurs before the compressive stresses reach the tensile strength.

2. The destruction of samples during compression along the fibers had a viscous character of destruction; therefore, this wood can be used in compressible elements of wooden structures. Destruction is preceded by obvious signs in the form of significant deformations. Tensile specimens show higher strength, but fracture is brittle.

3. During the study, a decrease in strength was found in samples taken from the upper part of a tree trunk. Thus, with static bending relative to the wood samples undamaged by fire, the decrease is more than 20 %, with compression along the fibers, the decrease is 40 %, and with tension, the decrease is 30.61 %.

4. The smallest decrease in strength for all three types of tests was observed in samples taken from the buttom. Thus, with static bending relative to the wood sample undamaged by fire, the decrease is about 23 %, with compression along the fibers, the decrease is 15.0 %, and with tension, the decrease is 8.39 %.

5. It has been established that with sufficiently small damage to a tree by fire, i.e., reducing the cross-sectional area up to 15.0 %, its partial use as a structural material is possible.

References

1. Chernykh, A., Mironova, S., Mamedov, S. Ecological Peculiarities and Problems of Glued Timber Structures Reinforcement. Rocznik Ochrona Srodowiska 2020. 22. Pp. 203–213.
2. Wimmers, G. Wood: a construction material for tall buildings. Nature Reviews Materials. 2017. 2 (12). 17051. DOI: 10.1038/natrevmats.2017.51
3. Slósarz, S. Strengthening of the wooden structures. Budownictwo i Architektura. 2020. 18 (3). Pp. 017–028. DOI: 10.35784/bud-arch.561
4. Iwuoha, S.E., Seim, W., Onyekwelu, J.C. Mechanical Properties of Gmelina Arborea for Engineering Design. Construction and Building Materials. 2021. 288. 123123. DOI: 10.1016/j.conbuildmat.2021.123123
5. Lisyatnikov, M., Lukina, A., Chibrikin, D., Labudin, B. The Strength of Wood-Reinforced Polymer Composites in Tension at an Angle to the Fibers. Lecture Notes in Civil Engineering. 2022. 182. Pp. 523–533.
6. Lukina, A., Lisyatnikov, M., Martinov, V., Kunitskya, O., Chernykh, A., Roschina, S. Mechanical and Microstructural changes in post-fire raw wood. Architecture and Engineering. 2022. 7 (3). Pp. 44–52. DOI: 10.23968/2500-0055-2022-7-3-44-52
7. Shishov, I., Lukin, M.V., Sergeev, M.S. Roofing of an Industrial Building with Variable Height Rafters and Wooden Decking. Lecture Notes in Civil Engineering. 2022. 182. Pp. 463–473.
8. Goremikins, V., Serdjuks, D., Buka-Vaivade, K., Pakrastins, L., Vatin, N. Prediction of Behaviour of Prestressed Suspension Bridge with Timber Deck Panels. The Baltic Journal of Road and Bridge Engineering. 2017. 12 (4). Pp. 234–240. doi:10.3846/bjrbe.2017.29
9. Roschina, S.I., Lisyatnikov, M.S., Lukin, M.V., Popova, M.V. Technology of Strengthening the Supporting Zones of the Glued-Wood Beaming Structure with the Application of Nanomodified Prepregs. Materials Science Forum. 2018. 931 MSF. Pp. 226–231.
10. Lukina, A., Roshchina, S., Gribanov, A. Method for Restoring Destructed Wooden Structures with Polymer Composites. Lecture Notes in Civil Engineering. 2021. 150. Pp. 464–474.
11. Lukina, A., Roshchina, S., Lisyatnikov, M., Zdralovic, N., Popova, O. Technology for the Restoration of Wooden Beams by Surface Repair and Local Modification. Lecture Notes in Networks and Systems. 2022. 403. Pp. 1371–1379.

12. Korolkov, D., Gravit, M., Aleksandrovskiy, M. Estimation of the Residual Resource of Wooden Structures by Changing Geometric Parameters of the Cross-Section. E3S Web of Conferences. 2021. 244. 04010. DOI: 10.1051/e3sconf/202124404010
13. Kasymov, D.P., Agafontsev, M.V., Tarakanova, V.A., Loboda, E.L., Martynov, P.S., Orlov, K.E., Reyno, V.V. Effect of Wood Structure Geometry during Firebrand Generation in Laboratory Scale and Semi-Field Experiments. Journal of Physics: Conference Series. 2021. 1867 (1). 012020. DOI: 10.1088/1742-6596/1867/1/012020
14. Martin, F. The Hamptons at MetroWest, a Case Study of Structural Repairs to Rot-Damaged Wood Condominium Buildings. Proceedings of the 2014 Structures Congress. Boston, Massachusetts, USA, April 3-5, 2014. Pp. 1244–1254.
15. Roshchina, S., Lukin, M., Lisyatnikov, M. Compressed-Bent Reinforced Wooden Elements with Long-Term Load. Lecture Notes in Civil Engineering. 2020. 70. Pp. 81–91.
16. International Information Agency "Russia Today". [Online]. URL: https://ria.ru/20181113/1532686839.html (date of application: 16.04.2022).
17. Information agency Interfax. [Online]. URL: https://www.interfax.ru/world/781890 (date of application: 16.04.2022).
18. Antonović, A., Barčić, D., Španić, N., Medved, S., Stanešić, J., Podvorec, T., Lozančić, M., Štriga, S., Ištvanić, J. Chemical Composition of Fired Aleppo Pine (Pinus Halepensis Mill.) sapwood. Proceedings of 29th International Conference on Wood Science and Technology, ICWST 2018: Implementation of Wood Science in Woodworking Sector. Zagreb, 6-7 December 2018. Pp. 13–26.
19. Stoddard, M.T., Roccaforte, J.P., Meador, A.J.S., Huffman, D.W., Fulé, P.Z., Waltz, A.E.M., Covington, W.W. Ecological Restoration Guided by Historical Reference Conditions Can Increase Resilience to Climate Change of Southwestern U.S. Ponderosa Pine Forests. Forest Ecology and Management. 2021. 493. 119256. DOI: 10.1016/j.foreco.2021.119256
20. Dupuy, J., Fargeon, H., Martin-StPaul, N., Pimont, F., Ruffault, J., Guijarro, M., Hernando, C., Madrigal, J., Fernandes, P. Climate change impact on future wildfire danger and activity in southern Europe: a review. Annals of Forest Science. 2020. 77. 35. DOI: 10.1007/s13595-020-00933-5
21. Kantieva, E., Snegireva, S., Platonov, A. Formation of Density and Porosity of Pine Wood in a Tree Trunk. IOP Conference Series: Earth and Environmental Science. 2021. 875 (1). 012016. DOI: 10.1088/1755-1315/875/1/012016
22. Information agency TASS. [Online]. URL: https://tass.ru/info/6712527 (date of application: 16.03.2022).
23. Information agency REGNUM. [Online]. URL: https://regnum.ru/news/economy/3381471.html (date of application: 16.03.2022).
24. Dias, A., Carvalho, A., Silva, M.E., Lima-Brito, J., Gaspar, M.J., Alves, A., Rodrigues, J.C., Pereira, F., Morais, J., Lousada, J.L. Physical, chemical and mechanical wood properties of Pinus nigra growing in Portugal. Annals of Forest Science. 2020. 77. 72. https://doi.org/10.1007/s13595-020-00984-8
25. Woodfiber prices pressured upward in Eastern Canada, mostly a result of supply infrastructure issues. International Woodfiber Report. 2014. 20 (3). Pp. 4–6.
26. Kukay, B., Barr, P.J., Friel, L., Coster, D.C., Halling, M.W. Post-Fire Assessments, Methodology, and Equations for Directly Determining Wood’s Residual Flexural Properties. Forest Products Journal. 2008. 58. Pp. 40–46.
27. Júnior, G.B., Moreschi, J.C. Physical–mechanical properties and chemical composition of Pinus taeda mature wood following a forest fire. Bioresource Technology. 2003. 87 (3). Pp. 231–238.
28. Kaku, C., Hasemi, Y., Yasui, N., Yasukawa, M., Kamikawa, D., Suzuki, A., Kameyama, N., Ono, T., Koshihara, M., Nagao, H. and Hagiwara, I. Influence of fire exposure on the mechanical properties of wood-Exposure temperature dependence of Young's modulus and bending strength of Japanese Cedar and Zelcova under and after heating. World Conference on Timber Engineering: Renaissance of Timber Construction, WCTE 2014, 2014. 110957.
29. Oyedeji, O., Young, A., Fasina, O. Bending Properties of Loblolly Pine. Industrial Crops and Products. 2017. 109. Pp. 905–911. DOI: 10.1016/j.indcrop.2017.09.060
30. Östman, B.A-L. Fire performance of wood products and timber structures. International Wood Products Journal. 2017. 8 (2). Pp. 74–79. DOI: 10.1080/20426445.2017.1320851
31. 31. Brischke, C. Wood Protection and Preservation. Forests. 2020. 11 (5). 549. DOI: 10.3390/F11050549
32. Akpan, E.I., Wetzel, B., Friedrich, K. Eco-Friendly and Sustainable Processing of Wood-Based Materials. Green Chemistry. 2021. 23 (6). Pp. 2198–2232. DOI: 10.1039/d0gc04430j
33. Hurmekoski, E., Jonsson, R., Nord, T. Context, Drivers, and Future Potential for Wood-Frame Multi-Story Construction in Europe. Technological Forecasting and Social Change. 2015. 99. Pp. 181–196. DOI: 10.1016/j.techfore.2015.07.002
34. Beims, R.F., Arredondo, R., Sosa Carrero, D.J., Yuan, Z., Li, H., Shui, H., Zhang, Y., Leitch, M., Xu, C.C. Functionalized Wood as Bio-Based Advanced Materials: Properties, Applications, and Challenges. Renewable and Sustainable Energy Reviews. 2022. 157. 112074. DOI: 10.1016/j.rser.2022.112074
35. Lukin, M., Prusov, E., Roshchina, S., Karelina, M., Vatin, N. Multi-Span Composite Timber Beams with Rational Steel Reinforcements. Buildings. 2021. 11 (2). 46. DOI: 10.3390/buildings11020046
36. Hassani, M.M., Wittel, F.K., Hering, S., Herrmann, H.J. Rheological Model for Wood. Computer Methods in Applied Mechanics and Engineering. 2015. 283. Pp. 1032–1060. DOI: 10.1016/j.cma.2014.10.031
37. Keskisalo, M., Luukkonen, J., Virtanen, J. BIM – object harmonization for timber construction. Wood Material Science & Engineering. 17 (4). Pp. 274–282. DOI: 10.1080/17480272.2022.2051071
38. Sokolovskyy, Y., Storozhuk, O., Levkovych, M., Kroshnyy, I., Boretska, I., Kshyvetskyy, B. Mathematical Modeling and Experimental Studies of Acoustic Wave Propagation in Anisotropic Medium. Proceedings of IEEE 16th International Conference on the Experience of Designing and Application of CAD Systems, CADSM 2021. Lviv, Ukraine, 22–26 February, 2021. Pp. 19–23.
39. Makarov, A.V. Technical qualities of wood affected by various types of fire. Forestry journal. 2011. 4. Pp. 14–18.
40. Belchinskaya, L., Zhuzhukin, K.V., Ishchenko, T., Platonov, A. Impregnation of Wood with Waste Engine Oil to Increase Water- and Bio-Resistance. Forests. 2021. 12 (12). 1762. DOI: 10.3390/f12121762
41. Platonov, A.D., Kuryanova, T.K., Snegireva, S.N., Makarov, A.V. Change in the density of pinewood damaged by fire during long-term storage under various conditions. Forestry journal. 2014. 1. Pp. 133–135.
42. Snegireva, S.N., Platonov, A.D., Kantieva, E.V. Hardness of pine bottom wood damaged by various types of fire after long-term storage. Proceedings of the international scientific-practical conference Green economy: "IFOREST", Voronezh, Russia, September 29, 2021.

43. Kuryanova, T.K., Platonov, A.D., Ogurtsov, V.A., Turkina, Yu.O. Change in density of pine wood after fire damage. Forestry magazine. 2012. 3 (7). Pp. 7–11.

Information about authors:

Anastasiya Lukina, *PhD in Technical Sciences*
ORCID: https://orcid.org/0000-0001-6065-678X
E-mail: pismo33@yandex.ru

Mikhail Lisyatnikov, *PhD in Technical Sciences*
ORCID: https://orcid.org/0000-0002-5262-6609
E-mail: mlisyatnikov@mail.ru

Mikhail Lukin, *PhD in Technical Sciences*
ORCID: https://orcid.org/0000-0002-2033-3473
E-mail: lukin_mihail_22@mail.ru

Nikolai Vatin, *Doctor of Technical Sciences*
ORCID: https://orcid.org/0000-0002-1196-8004
E-mail: vatin@mail.ru

Svetlana Roshchina, *Doctor of Technical Sciences*
ORCID: https://orcid.org/0000-0003-0356-1383
E-mail: rsi3@mail.ru

Received 28.10.2022. Approved after reviewing 09.12.2022. Accepted 25.03.2023.

Magazine of Civil Engineering. 2023. 119(3). Article No. 11908

Magazine of Civil Engineering

journal homepage: http://engstroy.spbstu.ru/

ISSN
2712-8172

Research article
UDC 692.23, 699.86
DOI: 10.34910/MCE.119.8

Effect of external facing vapor permeability on humidification of facade materials

M.I. Nizovtsev ✉, ***A.N. Sterlygov***

Kutateladze Institute of Thermal Physics, Novosibirsk, Russia

✉ *nizovtsev@itp.nsc.ru*

Keywords: facade system, heat- insulation layer, external facing, vapor permeability resistance, heat and moisture transfer, calculation model

Abstract. In this paper, the influence of the vapor permeability resistance of insulated facades external facing on the moisture content was numerically studied. The calculations were carried out for the climatic conditions of regions with a continental climate with relatively cold winters and warm summers. The WUFI computer program was used to perform heat and humidity calculations. The calculations found that the moisture content of the insulation layer increases with a decrease in the vapor permeability of the external façade facing in the cold season. Thus, the calculations found that with an increase in the resistance to vapor permeability of the external facing Sd > 0.2 m, the average moisture content of mineral wool increases by more than 3 % in the winter period. To reduce the moisture content of insulation, a version of installing an interlayer vapor permeability retarder is proposed. According to calculations, the relationships between the vapor permeability resistances of the external facing and the interlayer retarder were established. The proposed approach using an interlayer retarder can be applied in the development of various designs of building facades with external insulation to protect the insulation layer from humidification during the cold season in regions with a continental climate.

Funding: Mega-grant from the Ministry of Science and Higher Education of the Russian Federation (agreement No. 075-15-2021-575).

Citation: Nizovtsev, M.I., Sterlygov, A.N. Effect of external facing vapor permeability on humidification of facade materials. Magazine of Civil Engineering. 2023. 119(3). Article no. 11908. DOI: 10.34910/MCE.119.8

1. Introduction

The facade systems of modern buildings are the multifunctional structures that ensure comfortable conditions for people living. In cold and temperate climatic regions, facade systems, which include layers of heat-insulating materials, are used. Currently, two main facade systems with external insulation are widely applied: Ventilated Facade Systems (VFS) [1] and External Thermal Insulation Composite Systems (ETICS) [2]. Both of these facade systems in the summer season protect the interior from overheating and reduce air conditioning costs [3], and in winter they provide a low level of heat loss [4].

The ETICS is a facade system consisting of prefabricated thermal insulation panels glued or mechanically fixed to the wall and an external plaster layer or external brick facing. The advantages of this facade system are its high thermal uniformity in comparison with other facade systems [2], relatively low cost, and usability when renewing previously constructed buildings [5]. Operation of ETICS revealed two main problems. The first is caused by low impact resistance [2]. The second relates to defacement due to biological growth. Biological growth is driven by high levels of surface moisture, which is the result of the combined action of four parameters: wetting by surface condensation, which occurs mainly at night with clear skies, wetting by wind-driven rainfall, drying processes, and properties of the outer layer [6, 7].

Ventilated facades appeared with the development of Double-Skin Facades (DSFs) systems at the beginning of the 20th century [8]. Initially, the DSF consisted of two layers of glass separated by an inter-glass air gap. According to the practice of using such facades, buildings with DSFs overheated in summer, so later they began to be constructed with natural or forced ventilation, and such facades became known as ventilated facades (VFs) [9–11]. Later, not only transparent VFs, but also opaque ones, which were called “opaque ventilated facades” (OVFs) began to be used in construction [12–15]. Opaque ventilated facades were initially used in northern Europe to protect buildings from rain, wind and temperature fluctuations [14, 16]. Conventional VFSs during operation proved to be more resistant to moisture as compared to ETICS [17], but inferior to them in terms of thermal uniformity [18]. To improve the heat-shielding characteristics of ventilated facades, as well as to increase the speed and quality of installation, a new facade system based on prefabricated panels with ventilated channels has been developed and put into production [19, 20]. Laboratory and full-scale experimental and computational studies of the heat and humidity parameters of panels with ventilated channels were carried out, and they confirmed their high performance characteristics [21, 22].

One of the functions of facade systems is protection of the outer wall materials from excessive moisture. A high moisture content leads to additional heat losses due to a decrease in the efficiency of heat-insulating materials [23–27], and the growth of mold and algae is observed on facade facings [27, 28]. The limited frost resistance of porous materials at high humidity can be the cause of their structural damage [29, 30].

A number of papers draw attention to significant energy losses in buildings associated with increased air permeability of building envelopes. According to the results of analysis of heat losses in buildings located in the northern part of Spain, air infiltration consumes from 10.5 % to 27.4 % of energy in winter [31]. Studies performed in Finland have shown that air leakages in single-family houses are responsible for wasting 15–30 % of heating energy [32]. As a result, in these and some other works, it is concluded that when renovating buildings, the air permeability of building envelopes should be significantly reduced. However, a change in air permeability and vapor permeability of envelopes cannot be considered without taking into account their influence on the moisture content of materials in their composition, otherwise reconstruction of buildings may adversely affect the condition of building envelopes, internal environment and people health [33–35].

Barrier layers are used to limit moisture accumulation in building envelope materials. Usually, in a warm and humid climate, when the flow of vaporous moisture is directed inwards from the facade outer surface, the barrier layer is installed on the outer side of the facade [36]. In regions with a long cold period, the main flow of vaporous moisture during the year is directed from the facade inner surface to the outer one, and it is recommended to place the barrier layer on the inner surface of the facade [22]. However, internal vapor barriers are very sensitive to various mechanical damages [37]. Such barriers are difficult to install when renovating previously constructed residential buildings, since it is usually carried out from the outside without resettlement of residents. They try not to use internal vapor barriers when renovating historical buildings [38]. In the scientific literature, the issue of a possible use of vapor barrier layers inside facade systems is still insufficiently covered, although, in some cases, this position of the barrier layers can provide certain advantages.

The facade of a modern building can be considered as a multilayer structure consisting of porous materials with different vapor permeability. With different outdoor climatic parameters, as well as certain temperature and humidity conditions inside the premises, there is a difference in the partial pressures of water vapor of the outdoor and indoor air, which in turn causes the movement of water vapor through the multilayer porous structure of the facade. When water vapor moves, depending on vapor permeability of the materials of the facade layers and their sorption properties, condensation and moisture accumulation can occur.

Vapor permeability of the external facade facing (the facade layer or several layers located outside the thermal insulation layer of the facade) plays an important role in the moisture transfer process in facade systems. Analyzing the influence of vapor permeability of the external facing on moisture accumulation in the facade materials, one can abstract from specific features and consider ETICS and OVS facades from a unified position, characterizing the external facade facing with certain resistance to vapor permeability. For ventilated facades, this resistance reflects the resistance of ventilated layers or channels and the resistance of their inlets and outlets, and for ETICS facades, this resistance is caused by the resistance to vapor permeability of the outer plaster layers or the outer layer of the brickwork.

This work is aimed at consideration of the influence of vapor permeability resistance of the external facade facing on the moisture content in its materials during the long-term cycle of building operation in a continental climate with cold winters and relatively warm summers. The possibility of using thin retarder layers inside the facade with different vapor permeability of the external facade facing to reduce the moisture content of the heat-insulating layer is also considered.

2. Methods

The influence of vapor permeability of the external facing on the moisture state of the building wall materials was analyzed using the outer wall construction, widespread in practice, shown in Fig. 1. The main structural layer of the outer wall is made of clay bricks with a thickness of 250 mm. From the side of the room, a layer of cement-sand plaster 20 mm thick is applied to the brickwork, and from the outside, the brickwork is insulated with a layer of mineral wool 160 mm thick. On the outer side of the mineral wool there is a facade facing with a given vapor permeability resistance. The external facade facing can be a plaster layer, or a layer of another material, or the outer layer of a ventilated facade or panels with ventilated channels [20].

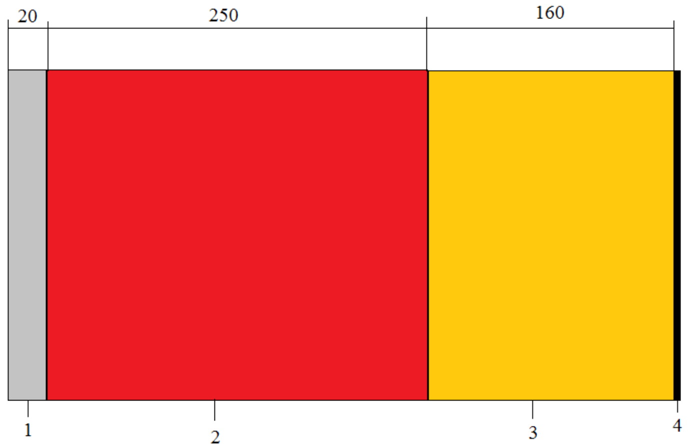

Figure1. The outer wall composition: 1 – cement-sand plaster, 2 – brickwork, 3 – mineral wool insulation, 4 – outer facing.

The WUFI computer program [39], developed and maintained by Franhofer-IBP (Germany), was used to perform heat and humidity calculations. In this program, the process of heat and moisture transfer in hygroscopic multilayer porous materials as applied to building structures is described by a system of two partial differential equations for each of the layers, which is solved by a finite volume procedure. Equation (1) describes a change in the enthalpy of a wet material over time, caused by thermal conductivity and thermal processes associated with evaporation and condensation of moisture. Equation (2) is the balance of moisture in a hygroscopic material, taking into account the movement of liquid and vaporous moisture.

$$\frac{dH}{d\vartheta}\frac{\partial\vartheta}{\partial t}=\nabla(\lambda\nabla\vartheta)+h_V\nabla(\delta_p\nabla(\varphi p_{sat}))+S_h \tag{1}$$

$$\frac{dw_V}{d\varphi}\frac{\partial\varphi}{\partial t}=\nabla(D_\varphi\nabla\varphi)+\delta_p\nabla(\varphi p_{sat}))+S_w \tag{2}$$

where H is enthalpy [J/m^3]; ϑ is temperature [K]; w_V is volumetric moisture [kg/m^3]; φ is relative humidity [-]; λ is coefficient of heat thermal conductivity [W/mK]; h_V is heat of water evaporation [J/kgK]; δ_p is water vapor diffusion coefficient [kg/msPa]; p_{sat} is water vapor saturation pressure [Pa]; D_φ is liquid transport coefficient [kgm/s]; S_h is additional heat source strength (W/m^3); S_w is additional moisture source strength (kg/sm^3)

Table 1 shows the properties of materials, and Fig. 2 and 3 show the moisture storage function and dependences of liquid transport coefficient, thermal conductivity on volumetric moisture content w_V, used in calculations (taken from the WUFI library).

Table 1. Material properties.

Material	Bulk density, kg/m^3	Porosity, m^3/m^3	Specific Heat Capacity (Dry), J/kgK	Thermal conductivity, (Dry), W/mK	Water Vapor Diffusion Resistance Factor
Brickwork	1900	0.24	850	0.6	10
Mineralwool	115	0.95	850	0.043	3.4
CementLime Plaster (Stuco)	1900	0.24	850	0.8	19

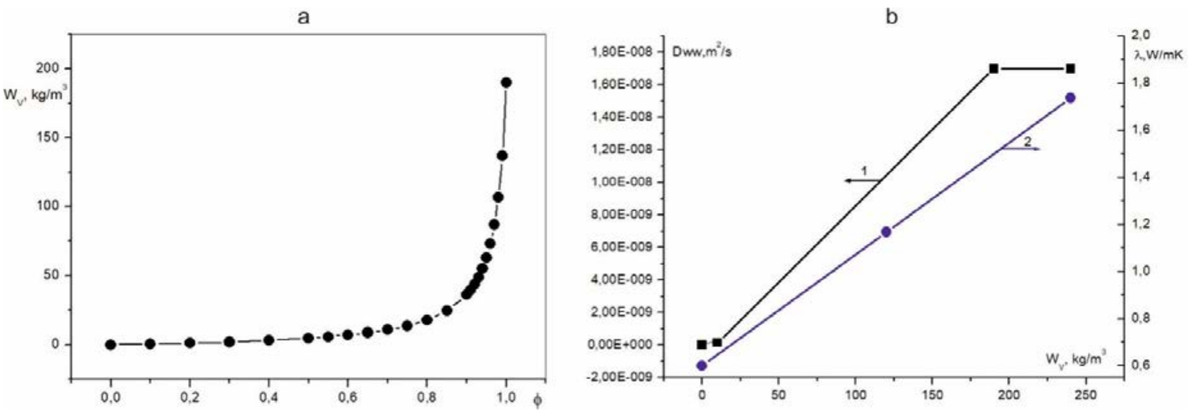

Figure2. Brickwork a) moisture storage function, b) 1 – liquid transport coefficient, 2 – thermal conductivity.

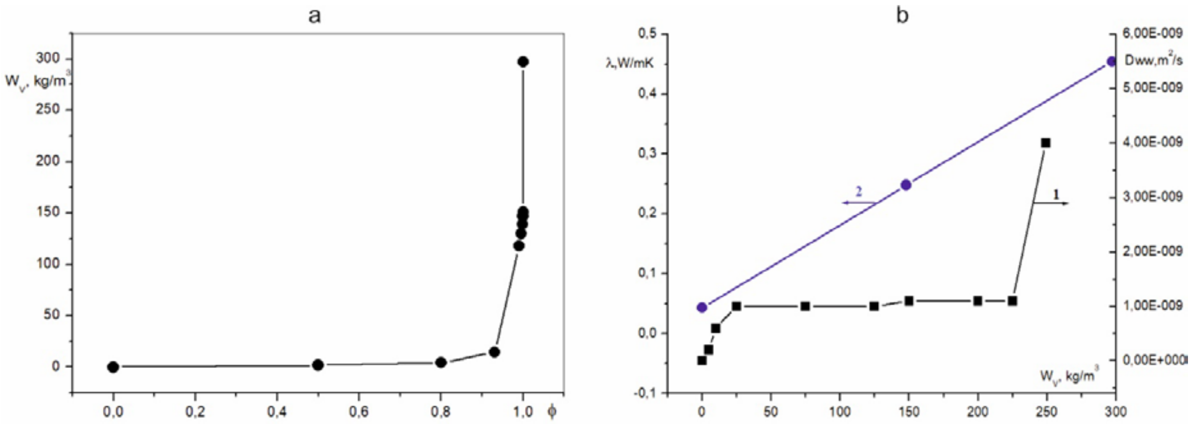

Figure3. Mineral wool a) moisture storage function, b) 1 – liquid transport coefficient, 2 – thermal conductivity.

The calculations were carried out for the climatic conditions of regions with a continental climate with relatively cold winters and warm summers. The city of Edmonton (Canada, 53.37ºN) was taken as a specific point. Calculations used hourly data of a typical year in Edmonton (Fig. 4, taken from the WUFI library). For indoor calculations, the air temperature was assumed to be 21 °C and its humidity was assumed to be 55 %. October 1 was taken as the start of calculations, while the moisture content of the brickwork and the plaster layer corresponded to the moisture content of the sorption isotherm at 80 % relative air humidity, and the moisture content of mineral wool corresponded to that at 55 % relative humidity, which is typical of the moisture content of materials at the end of building erection.

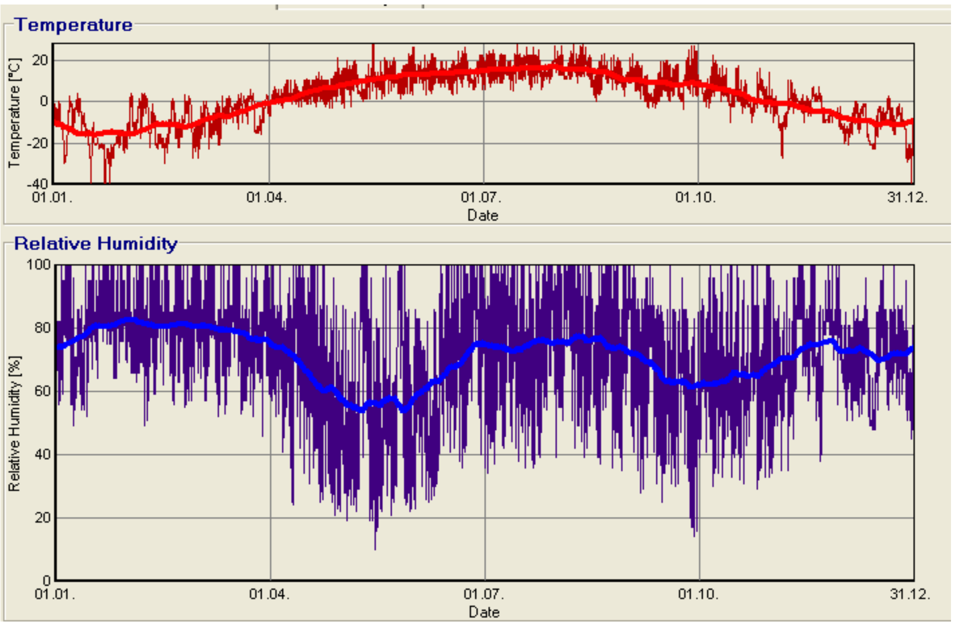

Figure 4. Temperature and relative air humidity in a standard year (Canada, Edmonton).

The computational grid was built with thickening towards the boundaries from the central zone of each material (Fig. 5).

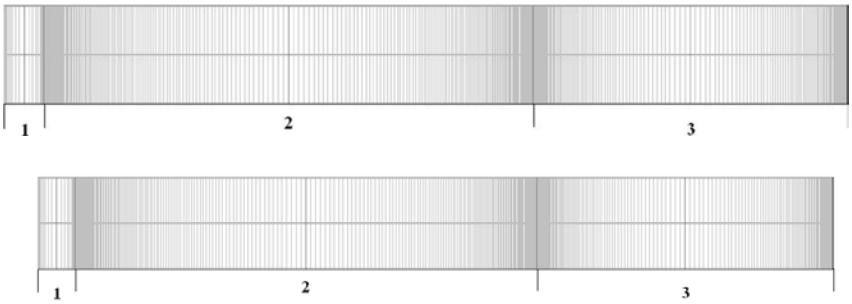

Figure 5. Computational grid 1 – plaster layer, 2 – brickwork, 3 – mineral wool.

To select the grid size, calculations at hourly intervals were carried out during the year to determine the average relative mass humidity w_i of a brickwork and mineral wool layer with the number of cells i = 128, 172, 258, and 386. As a result of determining abs$(w_{386} - w_i)/ w_{386}$ × 100 %, a grid with 258 cells was chosen for calculations, which, as compared to a grid with 386 cells, gave a deviation for brickwork of < 0.2 % (Fig. 6a), and for mineral wool, it was < 2 % (Fig. 6b).

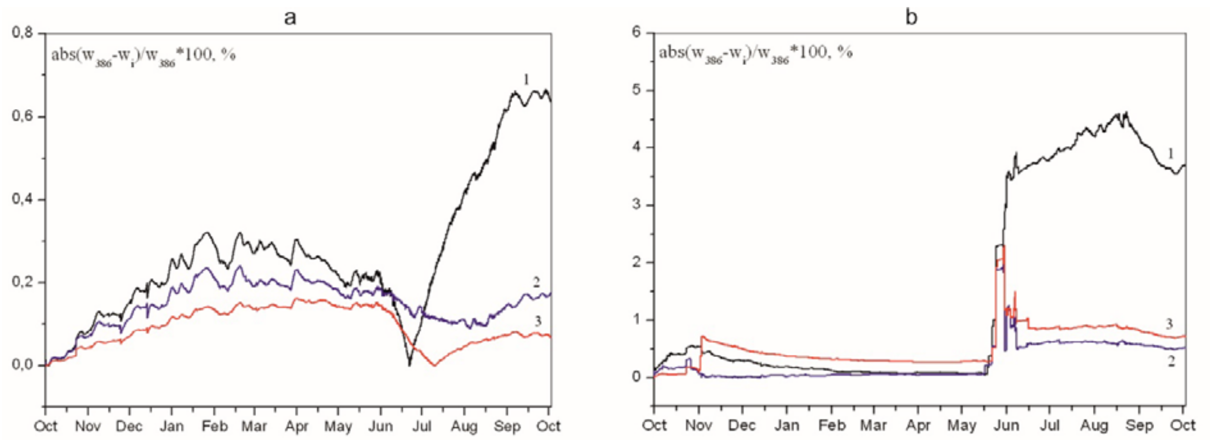

Figure 6. Comparison of average relative humidity for: a) brickwork,
b) mineral wool with a different number of grid cells: 1 – i = 128, 2 – 172, 3 – 258.

3. Results and Discussion

All calculation results presented in this section were performed during a 3-year period. At the initial stage, heat and humidity were calculated for the wall structure shown in Fig. 1, but without the external facing. Figure 7a shows calculation results on a change in the average mass moisture content in the mineral wool layer. According to calculation results, periodic annual fluctuations in humidity were observed with its increase to 3 % in late summer and early autumn: namely during this period of time there was high air humidity outside while the air temperature was still high (Fig. 4).

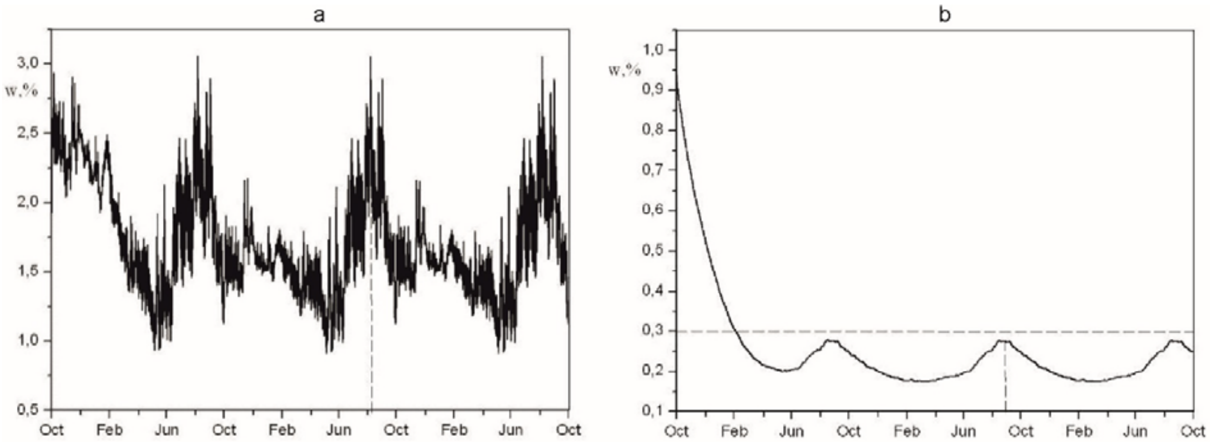

Figure 7. Relative mass humidity without external facing: a) mineral wool, b) brickwork.

The average mass moisture content in brickwork for the first six months after construction completion decreased rapidly, and then there were slight annual fluctuations with a maximum relative humidity of <0.3 % in September (Fig. 7b).

The results of calculating the density of the diffusion moisture flow at the boundary between brickwork and insulation for a wall structure without an outer coating are shown in Fig. 8. According to calculations for a 3-year period, a steady periodic annual change in the direction of the diffusion moisture flux was observed. In the summer period, the diffusion flow of moisture was directed towards the premises, and in the rest of the year, it was directed outside.

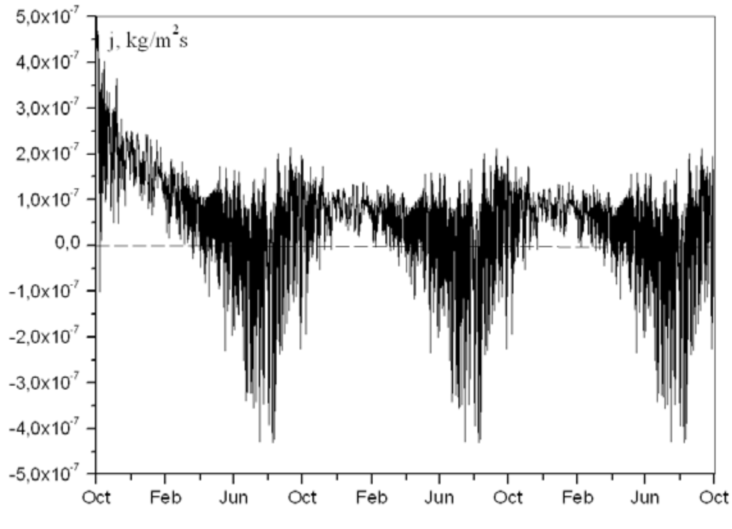

Figure 8. The density of diffusion moisture flow at the brickwork-insulation boundary.

The results of the average monthly density of the diffusion moisture flow for 3 years, which confirm this conclusion, are shown in Fig. 9 for clarity.

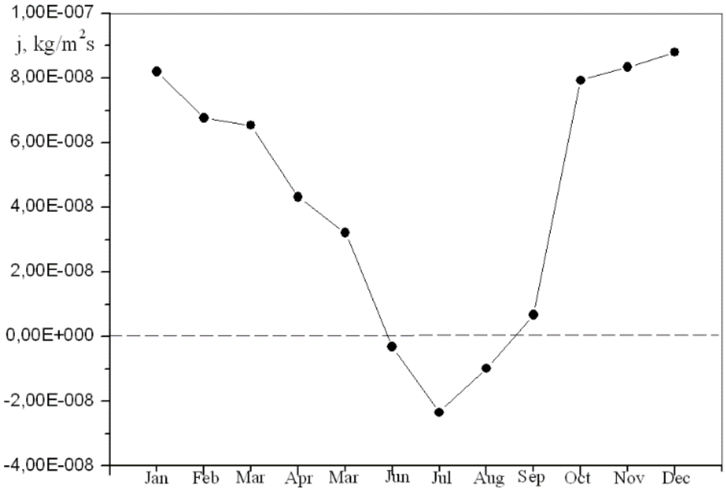

Figure 9. The average monthly density of the diffusion moisture flow at the brickwork-insulation boundary.

The inward direction of the diffusion moisture flow led to an increase in humidity in mineral wool and brickwork (Fig. 7). The magnitude and duration of the diffusion flow of moisture directed outside were large, but this did not lead to noticeable wetting of the mineral wool layer, since there was no external facing that would contribute to accumulation of moisture in the insulation.

Let us consider the results of calculations of the moisture state of the wall structure with an external facing on the outer surface with different vapor permeability resistance. The results of calculating a change in the average relative humidity of a mineral wool layer with vapor permeability of the external facing Sd = 0.2 m (which corresponds to vapor permeability of 10-mm layer of cement-sand plaster) are presented in Fig. 10a, b.

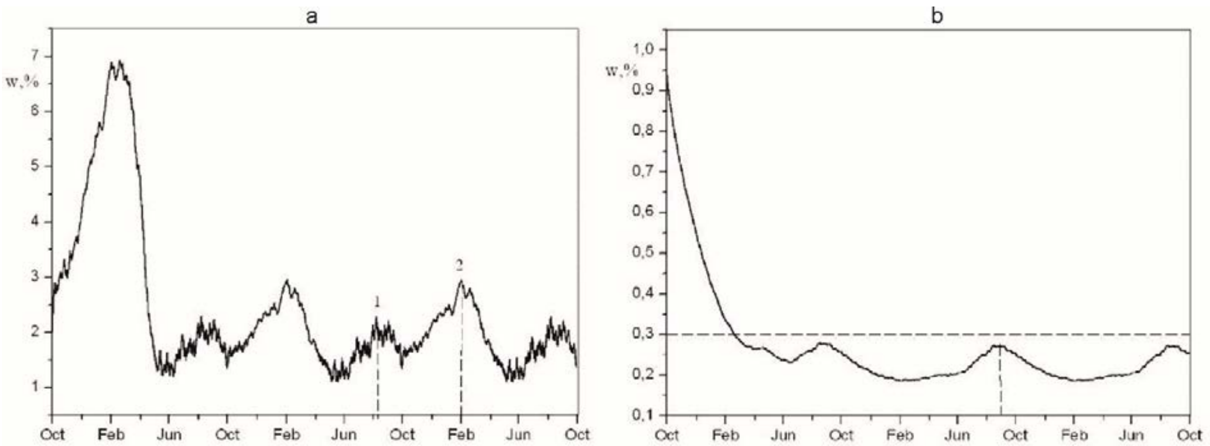

Figure10. Relative mass humidity at external facing resistance to vapor permeability Sd = 0.2 m: a) mineral wool, 1, 2 – annual humidity maxima; b) brickwork.

According to the calculation results, in the first year after construction completion, in February, there was a maximum increase in the average relative humidity of mineral wool up to 7 %, which is associated with the influence of vapor permeability resistance of the coating to the removal of moisture from the brickwork at its increased level in the initial period after construction completion. In subsequent years, the moisture level in mineral wool enters into cyclic annual fluctuations, but in contrast to the previously considered case (Fig. 7a), two humidity maxima are observed during the year. Maximum 1 is similar to the maximum in Fig. 7a in the warm period, but it is smaller in magnitude. Maximum 2 appears during the cold season, and its appearance is associated with the resistance to vapor permeation of the external facing.

The change in the average relative humidity of the brickwork with external facing resistance to vapor permeability Sd = 0.2 m (Fig. 10b) slightly differed from calculation results without coating (Fig. 7b). The conclusion about non-accumulation of moisture over the annual period in a brick facade with external insulation and facing resistance to vapor permeability Sd = 0.2 m is also confirmed by the results of calculations performed earlier for the climatic conditions of Holzkirchen (Germany) [40].

With a further increase in vapor permeability resistance of the external facing up to Sd = 0.5 m, a further increase in the maximum values of relative average humidity of the mineral wool layer in the cold season was observed (up to 10 % in the first year, and up to 5 % in the next two years; Fig. 11).

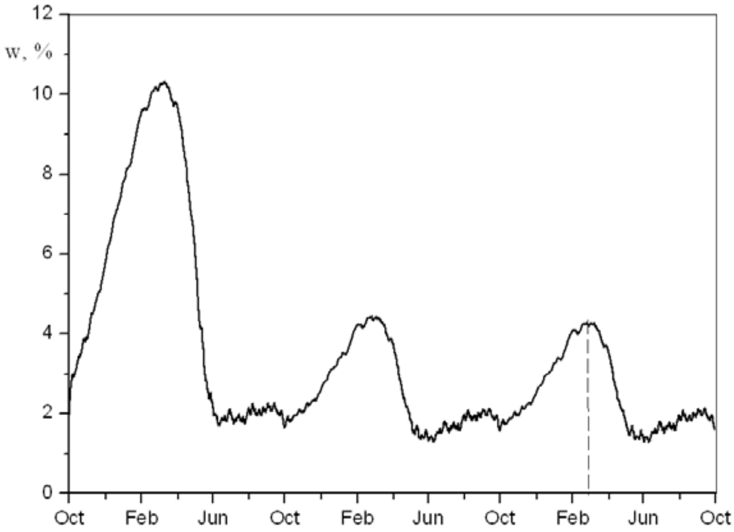

Figure 11. Average relative humidity of mineral wool at external facing resistance to vapor permeability Sd = 0.5 m.

It should be noted that humidity was not evenly distributed over the mineral wool layer, the moisture content of the outer half of the mineral wool layer (Fig. 12a) was significantly higher than that of the inner half of the layer (Fig. 12b), where the moisture content was less than 3 % and changed little over time throughout the year.

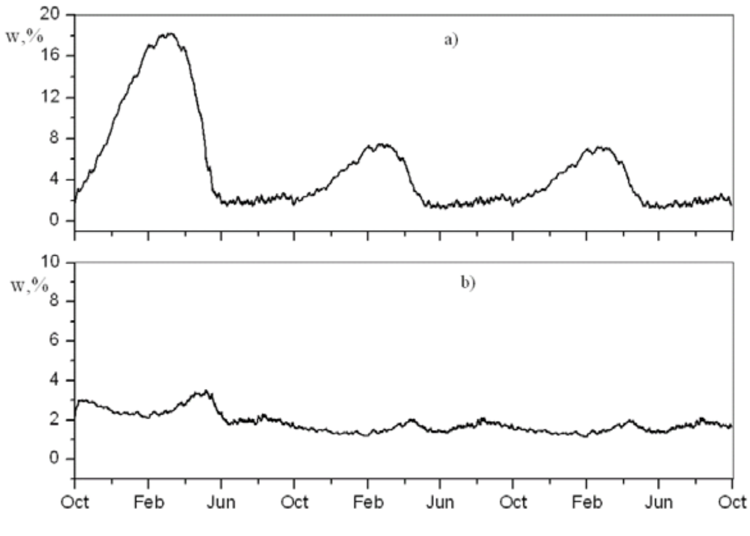

Figure12. Average relative humidity of mineral wool at external facing resistance to vapor permeability Sd = 0.5 m over the layers: a) outer half, b) inner half.

The results of calculating the changes in relative humidity of the brickwork with coating resistance to vapor permeability Sd = 0.5 m are shown in Fig. 13.

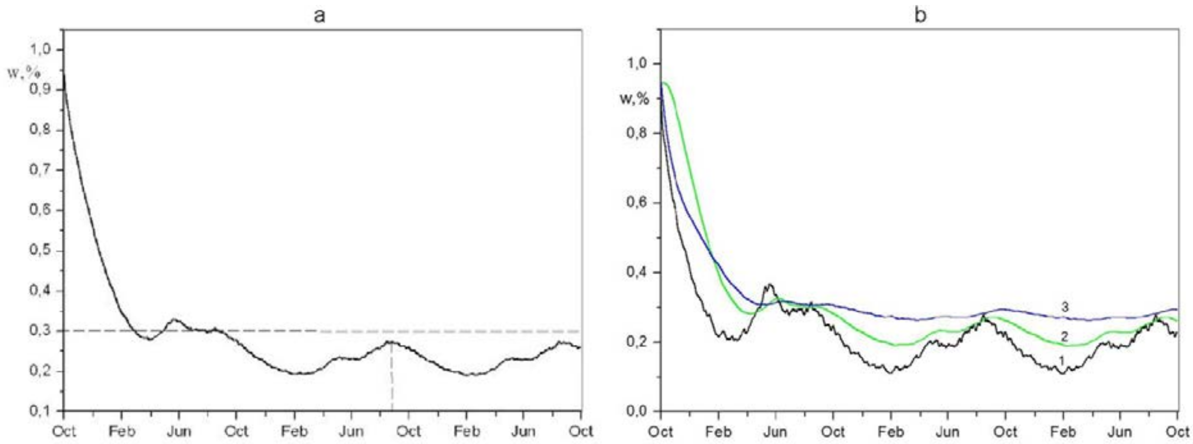

Figure13. Relative humidity of brickwork at external facing resistance to vapor permeability Sd = 0.5 m: a) average, b) 1 – outer layer, 2 – middle layer, 3 – inner layer.

The average humidity over the entire layer of brickwork in the summer of 1 year slightly exceeded 0.3 %; then it decreased and underwent annual fluctuations with an increase in humidity in the summer-autumn period (Fig. 13a). To analyze moisture distribution along the brickwork thickness, we conditionally divide it into 3 equal layers: outer, middle and inner ones. Fig. 13b shows the results of changing the relative humidity of the brickwork by layers. According to the results of calculations, the highest and most stable humidity, starting from year 2, was in the inner layer, and the lowest humidity, changing in the annual cycle, was observed in the outer layer (Fig. 8b).

Calculations were performed with a further increase in the resistance to vapor permeability of the external facing in the range Sd = 1 ÷ 20 m, as well as with an impermeable external facing (Fig. 14). As a result of calculations, it was found that with an increase in external facing resistance to vapor permeability, a consistent increase in the maximum average relative humidity of mineral wool in the cold season was observed, and for vapor-impermeable external facing it reached 16 % (Fig. 14a).

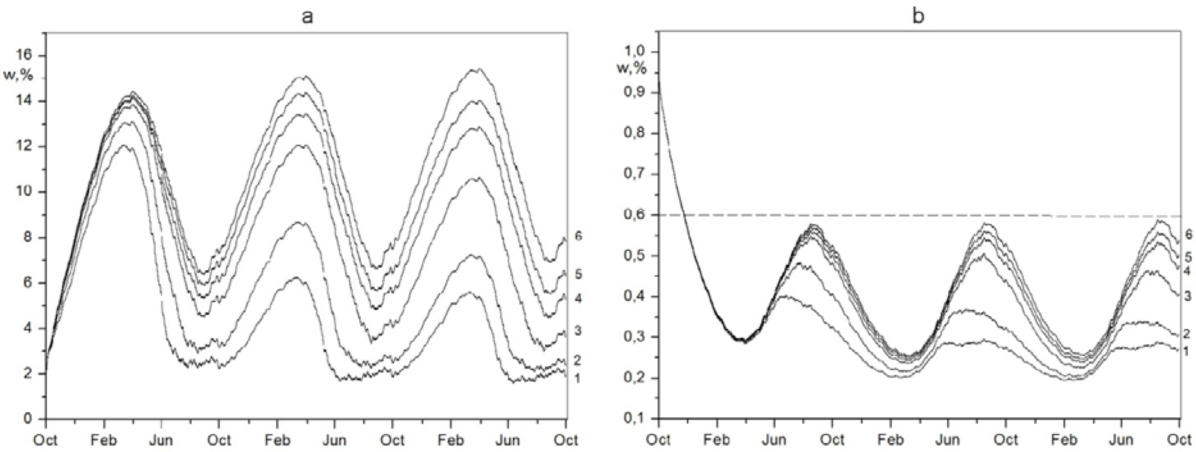

Figure14. Relative mass humidity: a) mineral wool, b) brickwork at different resistances of facing to vapor permeability: 1 – Sd = 1m, 2 – 2m, 3 – 5m, 4 – 10m, 5 – 20m, 6 – impermeable.

The average humidity of the brickwork increased during the summer-autumn period with an increase in external facing resistance to vapor permeability, while the maximum value obtained for the vapor-impermeable facing was about 0.6 % (Fig. 14b).

Thus, the calculations found that with an increase in the resistance to vapor permeability of the external facing Sd > 0.2 m, the average moisture content of mineral wool increases by more than 3 % in the winter period. To reduce the humidity of mineral wool, let us consider the option of installing an interlayer vapor permeability retarder (a thin layer with varying resistance to vapor permeability) between brickwork and mineral wool.

The results of calculations of average relative humidity of mineral wool (Fig. 15a) and brickwork (Fig. 15b) when installing an interlayer retarder with vapor permeability Sd = 1, 5, 10 and 20 m and vapor permeability of the external facing Sd = 1 m are shown in Fig. 15.

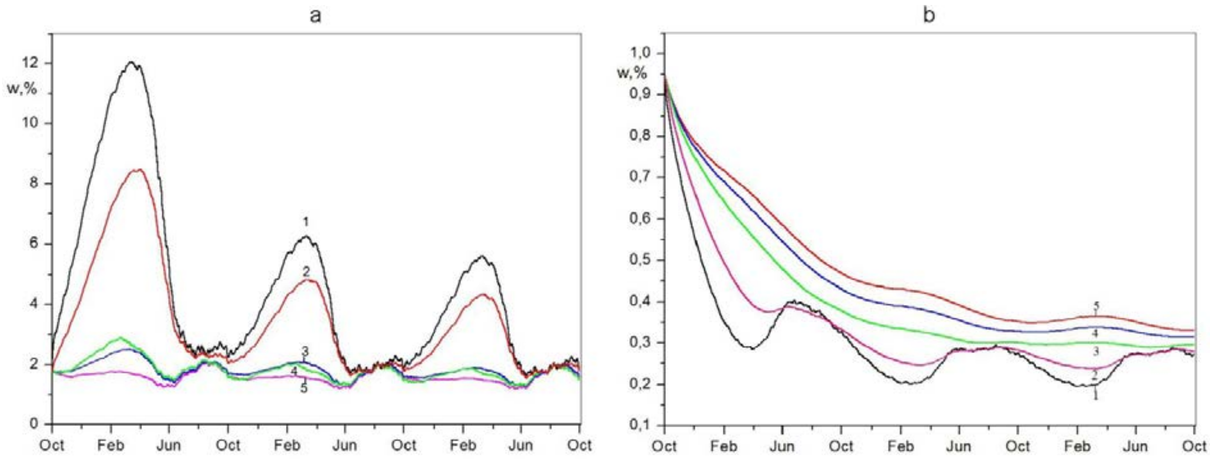

Figure15. A change in relative mass humidity of a) mineral wool and b) brickwork at facing resistance to vapor permeability Sd = 1 m and retarder resistance to vapor permeability: 1 – Sd = 0 m, 2 – 1 m, 3 – 5 m, 4 – 10 m, 5 – 20 m.

According to calculation results, with an increase in the resistance to vapor penetration of the interlayer retarder, a decrease in mineral wool humidity was observed in the winter-spring period, since the retarder provided additional resistance to the water vapor flow from the brickwork. With retarder resistance to vapor permeation Sd > 5, the maximum average humidity decreased below 3 %. It should be noted that when installing an interlayer retarder, a decrease in the moisture content of the mineral wool is accompanied by a slight increase in brickwork humidity (Fig. 15b), but this increase is insignificant and acceptable for brickwork. So, for an interlayer retarder with Sd = 5, the average moisture content of brickwork starting from the 2nd year after construction completion was less than 0.35 %.

The results of calculations of changes in humidity of mineral wool and brickwork with vapor permeability resistance of the external facing Sd = 10 m and when installing an interlayer retarder with vapor permeability resistance Sd = 1 ÷ 20 m are shown in Fig. 16.

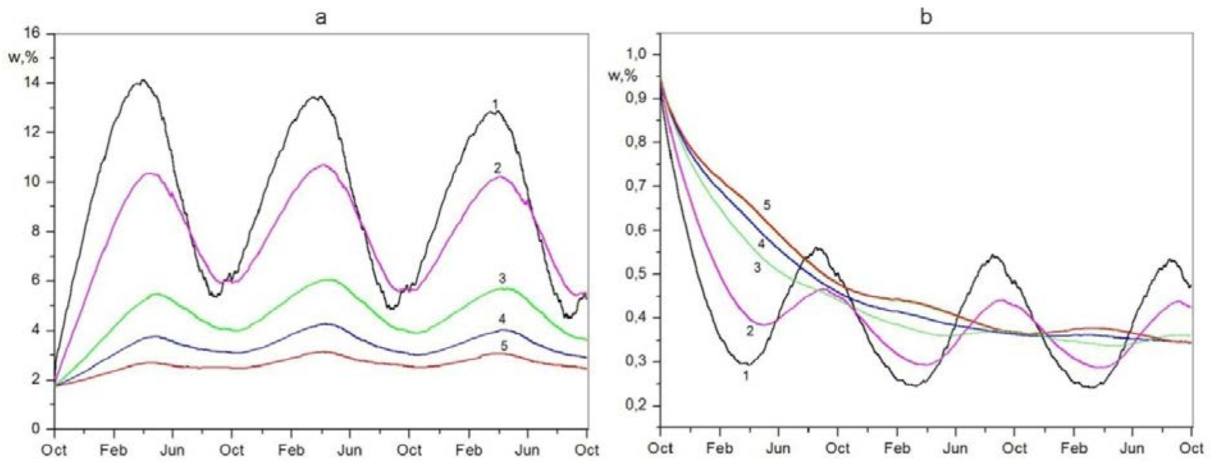

Figure16. A change in relative mass humidity of a) mineral wool and b) brickwork at facing resistance to vapor permeability Sd = 10 m and retarder resistance to vapor permeability: 1 – Sd = 0 m, 2 – 1 m, 3 – 5 m, 4 – 10 m, 5 – 20 m.

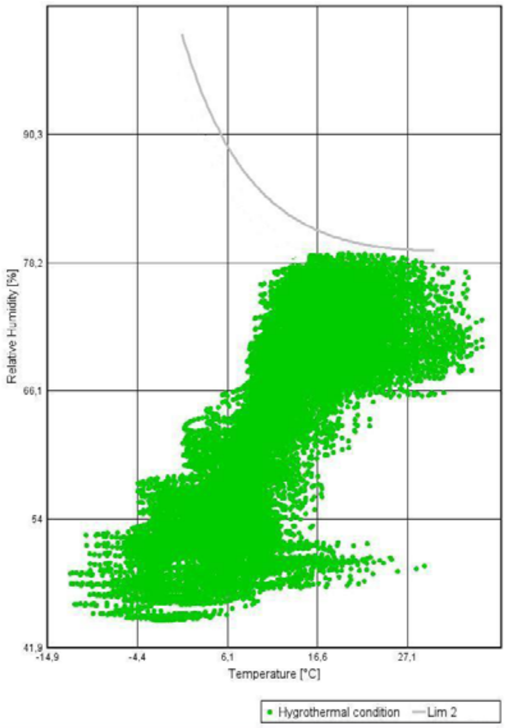

Figure17. Geothermal state of mineral wool with resistance to vapor permeability of the external facing and interlayer retarder Sd = 10 m.

It follows from the results presented in Fig. 17 that relative humidity in mineral wool did not exceed 80 % over a 3-year period and its geothermal state was characterized by points located below the limit line LIM 2, which provided its normal geothermal state.

It should be noted that new facade systems of buildings with high resistance to vapor permeability of the outer layers are beginning to be used in construction practice. As an example, we can cite facades using ballistic panels, in which the vapor permeability resistance can be Sd = 20 m ÷25 m [41]. For such facade systems, the possible moistening of facade materials due to the condensation of vaporous moisture is especially acute [42].

The result obtained on the advisability of using vapor retards on the inner surface of the thermal insulation of brick walls with external insulation is in good agreement with the results of experimental and computational studies concerning the use of vapor barriers and retards in wood frame wall structures [43–45]. In countries such as Canada, Norway and Sweden, it is obligatory to use a vapor barrier layer on the inner surface of the insulation in wooden frame walls.

4. Conclusions

To determine the effect of vapor permeability of the external facing on the moisture state of the outer wall materials during building operation in a continental climate, comprehensive heat and humidity calculations were carried out for a typical outer wall, consisting of an internal structural brick layer, an external mineral wool insulation layer and an external facing with different vapor permeability on the example of Edmonton. The numerical results allow to draw following conclusions:

1. It was found that with the resistance to vapor permeability of the external facing Sd ≤ 0.2 m, the average relative humidity in the mineral wool insulation layer is < 3 %, and in the brickwork, it is < 0.3 %, and special measures to prevent humidification of the outer wall materials are not required.

2. With an increase in the resistance to vapor permeability of the external facing Sd > 0.2 m, a consistent increase in the average moisture content of the mineral wool layer in the winter-spring period, and brickwork in the summer-autumn period, was observed. Thus, with vapor permeability resistance of the external facing Sd = 0.5 m, an increase in average relative humidity in mineral wool during the cold period was about 5 %; at that, the moisture in the layer was unevenly distributed: the outer layer was significantly more moistened as compared to the inner one. In the limiting case of an impermeable external facing, according to the results of calculations, the maximum increase in average relative humidity in the mineral wool layer was 16 %, and in the brickwork, it was 0.6 %.

3. To reduce mineral wool humidity with the resistance of external facing to vapor permeability Sd > 0.2 m, a case of location of a retarder (a thin layer with different vapor permeability) between the brickwork and the mineral wool layer was considered. As a result of calculations, it was found that installation of an interlayer retarder led to a decrease in the moisture content of mineral wool in the winter-spring period, while the greater the resistance to vapor penetration of the external facing, the higher the resistance of the interlayer retarder was required to reduce humidity. Based on the calculation results, the following relationships between the vapor permeability of the external facing and interlayer retarder can be recommended:

- Facing 0.2 m < Sd < 1 m – retarder Sd = 1 m;
- Facing 1 m < Sd < 5 m – retarder Sd = 5 m;
- Facing 5 m < Sd < 10 m – retarder Sd = 10 m.

4. The suggested approach using an interlayer retarder can be applied in the development of various designs of building facades with external insulation to protect the insulation layer from humidification during the cold season in regions with a continental climate.

References

1. Ibanez-Puy, M., Vidaurre-Arbizu, M., Sacristan-Fernandez, J.A., Martin-Gomez, C. Opaque ventilated facades: thermal and energy performance review. Renewable and Sustainable Energy Reviews. 2017. 79. Pp. 180–191. DOI: 10.1016/j.rser.2017.05.059
2. Barreira, E., de Freitas, V.P. External thermal insulation composite systems: critical parameters for surface hygrothermal behaviour. Advances in Materials Science and Engineering. 2014. 16. DOI: 10.1155/2014/650752
3. Shameri, M.A., Alghoul, M.A., Sopian, K., Fauzi, M., Zain, M., Elayeb, O. Perspectives of double skin facade systems in buildings and energy saving. Renewable Sustainable Energy Rev. 2011. 15. Pp. 1468–1475. DOI: 10.1016/j.rser.2010.10.016
4. Cristina Sanjuan, Maria Nuria Sánchez, Maria del Rosario Heras, Eduardo Blanco. Experimental analysis of natural convection in open joint ventilated façades with 2D PIV. Build Environ. 2011. 46. Pp. 2314–2325. DOI: 10.3390/en13010146
5. Becker, R. Patterned staining of rendered facades: hydrothermal analysis as a means for diagnosis. Journal of Thermal Envelope and Building Science. 2003. 26. Pp. 321–341. DOI: 10.1177/1097196303026004001
6. Barberousse, H., Ruot, B., Yepremian, C., and Boulon, G. An assessment of facade coatings against colonisation by aerial algae and cyanobacteria. Building and Environment. 2007. 42. Pp. 2555–2561. DOI: 10.1016/j.buildenv.2006.07.031
7. Barreira, E., Freitas, V. P. Experimental study of the hydrothermal behavior of external thermal insulation composite system (ETICS). Building and Environment. 2013. 63. Pp. 31–39. DOI:10.1016/j.buildenv.2013.02.001.
8. Aparicio-Fernández, C., Vivancos, J.-L., Ferrer-Gisbert, P., Royo-Pastor, R. Energy performance of a ventilated facade by simulation with experimental validation. Applied Thermal Engineering. 2014. 66. Pp. 563–570. DOI: 10.1016/j.applthermaleng.2014.02.041
9. Marinosci, C., Strachan, P.A., Semprini, G., Morini, G.L. Empirical validation and modelling of a naturally ventilated rainscreen façade building. Energy Build. 2011. 43. Pp. 853–863. DOI: 10.1016/j.enbuild.2010.12.005
10. Wang, Ya., Chen, Yo., Li, C. Airflow modeling based on zonal method for natural ventilated double skin façade with Venetian blinds. Energy and Buildings. 2019. 191. Pp. 211–223. DOI: 10.1016/j.enbuild.2019.03.025
11. Lin, Zh., Song, Ye., Chu, Yi. Summer performance of a naturally ventilated double-skin facade with adjustable glazed louvers for building energy retrofitting. Energy and Buildings. 2022. 267. 112163. DOI:10.1016/j.enbuild.2022.112163.
12. Giancola, E., Sanjuan, C., Blanco, E., Heras, M.R. Experimental assessment and modelling of the performance of an open joint ventilated facade during actual operating conditions in Mediterranean climate. Energy and Buildings. 2012. 54. Pp. 363–375. DOI: 10.1016/j.enbuild.2012.07.035
13. Peci Lopez, F., Jensen, R. L., Heiselberg, P., Ruiz de Adana Santiago, M. Experimental analysis and model validation of an opaque ventilated façade. Building and Environment. 2012. 56. Pp. 265–275. DOI: 10.1016/j.buildenv.2012.03.017
14. Davidovic, D, Piñon, J, Burnett, E.F.P., Srebric J. Analytical procedures for estimating airflow rates in ventilated, screened wall systems (VSWS). Build Environ. 2012. 47. Pp. 126–137. DOI: 10.1016/j.buildenv.2011.04.002
15. Maciel, A.C.F., Tereza Carvalho, M.T. Operational energy of opaque ventilated façades in Brazil. Journal of Building Engineering. 2019. 25. 100775. DOI: 10.1016/j.jobe.2019.100775
16. Falk, J, Sandin, K. Ventilated rainscreen cladding: a study of the ventilation drying process. Build Environ. 2013. 60. Pp. 173–184. DOI: 10.1016/j.buildenv.2012.11.015
17. Kvande, T., Bakken, N., Bergheim, E., Thue, J.V. Durability of ETICS with rendering in Norway–experimental and field investigations. Buildings. 2018. 8(7). 93. DOI: 10.3390/buildings8070093
18. Mashenkov, A.N., Cheburkanova, E.V. Determination of the coefficient of thermotechnical homogeneity of hinged facade systems with an air gap. Construction materials. 2007. 6. Pp. 10–12.
19. Nizovtsev, M.I., Bely, V.T., Sterlyagov, A.N. New facade system with ventilated channels for insulation of new and reconstructed buildings. Proceedings of the Scientific and Practical Conference "Energy and Resource Efficiency of Low-Rise Residential Buildings". Institute of Thermal Physics. S.S. Kutateladze SB RAS. 2013. Pp. 64–74.
20. Nizovtsev, M. I., Belyi, V. T., Sterlygov, A. N. The facade system with ventilated channels for thermal insulation of newly constructed and renovated buildings. Energy and Buildings. 2014. 75. Pp. 60–69. DOI: 10.1016/j.enbuild.2014.02.003
21. Nizovtsev, M. I., Letushko,V. N., Borodulin, V. Yu., Sterlyagov, A. N. Experimental studies of the thermo and humidity state of a new building facade insulation system based on panels with ventilated channels. Energy and Buildings. 2020. 206. 109607. DOI: 10.1016/j.enbuild.2019.109607
22. Borodulin, V.N., Nizovtsev, M.I. Modeling of the thermal and humidity state of the building facade insulation system based on panels with ventilated channels. Journal of Building Engineering. 2021. 40. 102391. DOI: 10.1016/j.jobe.2021.102391

23. Safin, I.Sh., Kupriyanov, V.N. Calculation-experimental study of moistening of building envelopes structures with vaporous moisture. Bulletin of the Volga Regional Branch of the Russian Academy of Architecture and Building Sciences. 2011. 14. Pp. 183–187.
24. Asphaug, S.K., Kvande, T., Time, B., Peuhkuri, R.H., Kalamees, T., Johansson, P., Berardi, U., Lohne, J. Moisture control strategies of habitable basements in cold climates. Build. Environ. 2020. 169. 106572. DOI: 10.1016/j.buildenv.2019.106572
25. Charisi, S., Thiis, T.K., Stefansson, P., Burud, I. Prediction model of microclimatic surface conditions on building façades. Building and Environment. 2018. 128. Pp. 46–54. DOI: 10.1016/j.buildenv.2017.11.017
26. Harriman, L.G., Grimes, C., Hart, K.Q., Hodgson, M., Thi, L.C.N., Offermann, F., Rose, W., Harriman, L.G., Zhang, J. Position Document on Limiting Indoor Mold and Dampness in Buildings. ASHRAE: AtlantaGA USA. 2021. 18. https://www.ashrae.org/file%20library/about/position%20documents/ashrae---limiting-indoor-mold-and-dampness-in-buildings.pdf.
27. Sedlbauer, K. Prediction of mould growth by hygrothermal calculation. J. Therm. Envelope Build. Sci. 2002. 25. Pp. 321–336. DOI: 10.1177/0075424202025004093
28. Feist, W.C. Outdoor wood weathering and protection. Adv. Chem. 1989. 225 (11). Pp. 263–298. DOI: 10.1021/ba-1990-0225.ch011
29. Thelandersson, S., Isaksson, T. Mould resistance design (MRD) model for evaluation of risk for microbial growth under varying climate conditions. Build. Environ. 2013. 65. Pp. 18–25. DOI: 10.1016/j.buildenv.2013.03.016
30. Safin I.Sh., Kupriyaov V.N. Raschetno-eksperimentalnoye issledovaniye uvlazhneniya ograzhdayushchikh konstruktsiy paroobraznoy vlagoy [Calculation and experimental study of moistening of building envelopes with vaporous moisture]. Vestnik Volzhskogo regionalnogo otdeleniya Akademii Arkhitektury i stroitelnykh nauk. 2011. 4. Pp. 183–187.
31. Meiss. A., Feijó-Muñoz, J. The energy impact of infiltration: A study on buildings located in north central Spain. Energy Effic. 2015. 8. Pp. 51–64. DOI: 10.1007/s12053-014-9270-x
32. Jokisalo, J.; Kurnitski, J.; Korpi, M., Kalamees, T., Vinha, J. Building leakage, infiltration and energy performance analyses for Finnish detached houses. Build. Environ. 2009. 44. Pp. 377–387. DOI: 10.1016/j.buildenv.2008.03.014
33. Recart, C., Dossick, C.S. Hygrothermal behavior of post-retrofit housing: A review of the impacts of the energy efficiency upgrade strategies. Energy and Buildings. 2022. 262. 112001. DOI: 10.1016/j.enbuild.2022.112001
34. Collins, M., Dempsey, S. Residential energy efficiency retrofits: potential unintended consequences. J. Environ. Plann. Manage. 2019. 62 (12). Pp. 2010–2025. DOI: 10.1080/09640568.2018.1509788
35. Ortiz, M., Itard, L., Bluyssen, P.M. Indoor environmental quality related risk factors with energy-efficient retrofitting of housing: A literature review. Energy and Buildings. 2020. 110102. DOI: 10.1016/j.enbuild.2020.110102
36. Bendouma, M., Colinart, T., Glouannec P., Noël, H. Laboratory study on hygrothermal behavior of three external thermal insulation systems. Energy and Buildings. 2020. 210. 109742. DOI:10.1016/j.enbuild.2019.109742.
37. Tomson, J., Vimmrova, A., Cerny, R. Long-term on-site assessment of hygrothermal performance of interior thermal insulation system without water vapour barrier. Energy Build. 2009. 41 (1). Pp. 51–55. DOI: 10.1016/j.enbuild.2008.07.007
38. Andreotti, M., Calzolari, M., Davoli, P., Pereira, L.D. Hygrothermal performance of an internally insulated masonry wall: Experimentations without a vapour barrier in a historic Italian Palazzo. Energy and Buildings. 2022. 260. 111896. DOI: 10.1016/j.enbuild.2022.111896
39. Kunzel, H.M. Simultaneous Heat and Moisture Transport in Building Components. Fraunhofer IRB Verlag. Suttgart. 1995.
40. Kunzel, H.M. Effect of interior and exterior insulation on the hygrothermal behaviour of exposed walls. Materials and Structures. 1998. 31. Rr. 99–103.
41. Borodinecs, A., Geikins, A., Barone, E., Jacnevs, V., Prozuments, A. Solution of bullet proof wooden frame construction panel with a built-in air duct. Buildings. 2022. 12. 30. DOI: 10.3390/buildings12010030
42. Borodinecs, A., Prozuments, A., Zemitis, J., Zajecs, D., & Bebre, G. Hydrothermal performance of the external wooded frame wall structure reinforced with ballistic panels. 2020. Paper presented at the E3S Web of Conferences. 172. 07005. DOI: 10.1051/e3sconf/202017207005
43. Geving, S., Holme, J. Vapour retarders in wood frame walls and their effect on the drying capability. Frontiers of Architectural Research. 2013. 2. 1. Pp. 42–49. DOI: 10.1016/j.foar.2012.12.003
44. Nik, V. Application of typical and extreme weather data sets in the hygrothermal simulation of building components for future climate – A case study for a wooden frame wall. Energy and Buildings. 2017. 154. Pp. 30–45. DOI: 10.1016/j.enbuild.2017.08.042
45. Straube, J., Smith, R., Finch, G. Spray Polyurethane Foam: The Need for Vapor Retarders in Above-Grade Residential Walls. Research Report – 0912. 2009. Building Energy Group, University of Waterloo. 49 P.

Information about authors:

Mikhail Nizovtsev, *Doctor of Technical Sciences*
ORCID: https://orcid.org/0000-0003-2372-6544
E-mail: nizovtsev@itp.nsc.ru

Alexei Sterlygov, *PhD in Technical Sciences*
E-mail: sterlyagov@itp.nsc.ru

Received 24.06.2022. Approved after reviewing 27.02.2023. Accepted 27.02.2023.

Magazine of Civil Engineering

ISSN 2712-8172

journal homepage: http://engstroy.spbstu.ru/

Research article

UDC 691.32:620.191.33

DOI: 10.34910/MCE.119.9

Strength and crack-resistance of concrete with fibre fillers and modifying nano-additives

V.A. Perfilov

Volgograd State Technical University, Volgograd, Russia

vladimirperfilov@mail.ru

Keywords: concrete construction, stress rates, strength of materials, fibre, nano-additives, crack resistance, methods of analysis, strength criteria

Abstract. The article dwells on a comprehensive method for determining concrete strength and crack-resistance in sample testing with varying loading rate. The method allows for receiving simultaneously kinetic parameters of the microstructure defects and length and rate of the main crack growth. The authors consider the impact of effective involved volume on the formation and growth of minor structural defects in cement gel with their eventual phased transition to larger defects. It facilitates increased stress concentration and the development of main cracks at the matrix-aggregate interface. Control over the development of the main crack allows for determining the time till destruction for concrete (longevity). The suggested method and the obtained formula helped applying a wide range of loading rates for determining the critical length of the main crack in concrete. The testing results were used to identify the coefficients of dynamic strengthening for the sample sets with and without an artificially created main crack. These coefficients were applied for calculating the main crack critical length. The article presents the results of experiments aimed at development of concrete compositions comprising fibre fillings and modifying additives including nano-additives followed by determination of their strength and crack-resistance as per the presented comprehensive method. The found values of efficient involving volume, activation energy characterise the microstructure parameters and critical length of the main crack in concrete. The resulting conclusion was that the main crack length in all of the developed concrete compositions exceeded the half of the section in the sample where it developed. Comprehensive assessment of concrete strength and crack-resistance and accumulation of experimental data improve the reliability of scientific research due to the emerging integrated approach to determining quantitative parameters of crack-resistance and longevity of the developed concrete compositions with forecasted properties.

Citation: Perfilov, V.A. Strength and crack-resistance of concrete with fibre fillers and modifying nano-additives. Magazine of Civil Engineering. 2023. 119(3). Article no. 11909. DOI: 10.34910/MCE.119.9

1. Introduction

Today strength.crack-resistance and longevity of solid bodies including high weight concrete are determined by means of fracture mechanics methods [1–5 and other]. These methods suggest that under mechanical load microfractures present in the solid body develop with further formation of an unbalanced main fracture that can break the sample with sound speed that results in the loss by the sample of its bearing capacity and its full destruction. Even most break-through technologies for preparation of different types and compositions of concrete do not produce a homogeneous dense structure having no micro-pores and micro-fractures that serve as stress points and under the impact of external loads result in the course of operation into reduction of strength and fracture-resistance of concrete. Similar studies have been performed by foreign researches for ceramics [6, 7], HW concrete [8–10] and cellular concrete [11–14]. Unfortunately, no universal method for a reliable determination of main fracture growth parameters in concrete has been found so far.

To describe the mechanism of solid bodies destruction it is necessary to take into account the micro-structure defects that include point (to the extent of atoms) dislocations, micro-pores and micro-fractures that are concentrated around concrete structure irregularities. Under mechanical load the concentration of point defects increases and they joint with larger dislocations. While applied load is small, movement of differently directed dislocations results in their annihilation, i.e. their mutual intertwinement, temporary slowdowning and stress relaxation. This does not produce micro-deformations in concrete. As externally applied load increases, there grow similarly directed dislocations that result in formation and development of larger structure defects in the form of micro-fractures. At that deformations develop in a thermally-activated mode that is addressed from the kinetic theory of strength perspective [15–18].Such approach was considered with respect to concrete by S.N. Leonovich and S.I. Karpenko [19].

It is understood that the behavior of solid bodies under increasing external load is based on the destruction of micro-pores that contribute to creation and further development of micro-fractures with their further transition to macro-level. The Russian Standard GOST 29167 recommended for determination of fracture-resistance properties of concrete based on the use of energy and force criterion of fracture mechanics has a number of shortfalls. In particular, the method for determination of the developing main fracture using capillary method during the process of receiving the full deformation diagram and fracturing of standard concrete samples is restricted by stage-wise stopping of the testing implied by technology. However, in concretes with heterogeneous micro- and macro-structure that includes different agents fractures continue growing when the testing is stopped that results in additional errors in the values of the main fracture length and width. Thus, there arises the necessity to develop a new method for measuring the length of the main fracture that is continuously growing with time. Moreover, testing during receiving full diagrams of concrete fracturing is impossible in the majority of process construction laboratories because of the high cost of equipment and technical complexity including processing of the obtained results.

Another known method is tensiometric identification of the dimensions and growth rate of the main fracture that implies fixation of its path during the process of stable fracturing or during dynamic testing with varying rate of concrete samples loading [20]. Such testing with the use of modern high capacity registration equipment allows determining fracturing energy, stress intensity coefficient and main fracture dimensions and growth rate simultaneously.

Integrated use of methods for determining dependences between fracture toughness, strength and, for example, rate of samples mechanical loading (stressing) is promising at the moment. In earlier studies conducted by S. Mindess [21], I. M. Grushko, A.I. Kazachuk, A.P. Vashchenko [22–24] et al. samples stressing rate varied from 10^{-3} to 10^{3} MPa/s. Impact stress was checked at rates 10^{4}–10^{5} MPa/s. Use of dynamic tests to determine strength, fracture resistance and longevity is an urgent task for different concrete types of compositions with expected properties.

In order to receive more information on mechanical properties of concrete it is necessary to consider the use of an integrated approach that allows for receiving fracture mechanics parameters, kinetics of micro-defects development, macro-fractures length and growth rate under the conditions of stable fracturing. The objective of the research is the development of a comprehensive method for determination of strength and fracture-resistance parameters (time till destruction) of known and newly created concrete compositions with pre-set physical and mechanical properties. The following tasks were implemented:

- develop a comprehensive method for determining strength and fracture-resistance of concretes that includes the methods of fracture mechanics, kinetic strength theory and samples testing with varying loading rate;
- based on the offered comprehensive method determine the values of activation energy U_0 and efficient involving volume γ in the samples of the developed concrete compositions modified with plasticising and nanocarbon additives to identify their impact on the amount of defects and micro-structure strength;
- determine parameters of critical length of the main fracture in the samples of the developed concrete compositions by means of testing by standard fracture mechanics methods and by means of testing with varying loading rates.

2. Methods

Based on the large quantity of accumulated theoretical and experimental data [25–28] it was determined that during operation concrete under the impact of external loads in samples demonstrate the development of elastic, quasi-elastic and plastic deformations. Their further growth depends on the accumulated structure defects and on their size that further on can result in the formation and development of micro- and macro-fractures of shearing and split types. Under small loads small-size, point (to the extent of one or several atoms) defects are formed in nano-structure. Such defects are thermally activated within approximately one atom. From the point of view of strength theory [15, 17, 18, 23] the development of micro-fractures depends on the change in activation energy U_0 and efficient involving volume γ ($\gamma = v \cdot n$, where v is involving volume, n is excessive stress coefficient) that is characterised by the development of deformations under the impact of one thermal activation.

The numerous studies performed by the author [25–27] have established the impact of loading (stress) rate of concrete samples on changing of kinetic characteristics of micro-structure and their significant impact on the obtained values of strength and fracture-resistance. The mechanism of impact of efficient involving volume on possible phase transition of point defects of one level into dislocations that results in the formation and development of the main fracture (fractures), changes in strength depending on the stress rate are shown in Fig. 1.

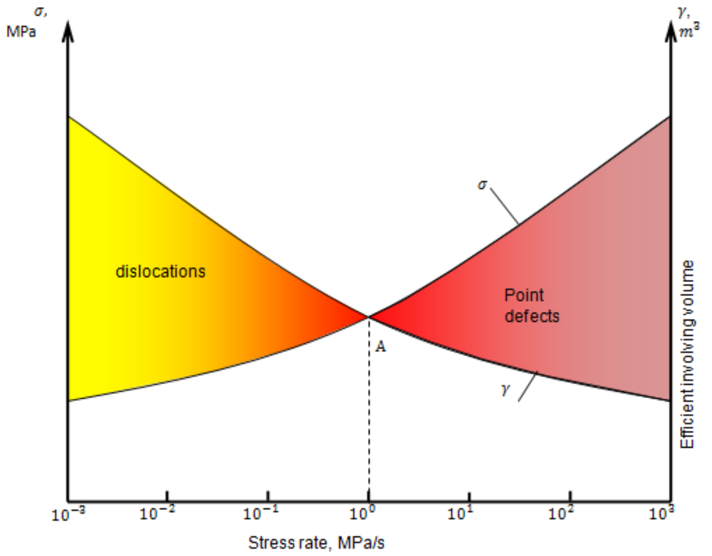

Figure 1. Scheme describing the influence of different defects on concrete strength at differing stress rates.

In order to determine time till destruction (longevity) of concrete, it is necessary to control the development of the main fracture in the process of its slow growth. The existing theories and few experiments have so far contradictory results and cannot be considered reliable.

Of the few papers there is one method for determination of the critical length of a macro-fracture for concrete [2] that includes static tensile in bending testing of several samples with an initiated main fracture and of the samples with the same composition and dimensions, but without an artificially initiated macro-fracture. The testing results were used to determine ultimate stresses and critical length of macro-fractures. This method [2] has certain deficiencies, the concrete samples strength in all tests was determined under standard loading with the same rate. At that the obtained values of the main fracture critical length is 10 times less than the dimensions of the tested samples that is not reliable. Accumulation and development of the theoretical and experimental databases allowed for developing the method for determining the main fracture critical size [25, 27] using different loading rates when testing samples. At that loading is performed in bending tension of samples with an artificially initiated fracture and similar samples without such fracture. The results of testing a set of samples with different rate allow for determining dynamic strengthening coefficients based on which critical length of the main fracture in concrete can be identified by the following formula:

$$l_{\kappa p} = h \cdot Y \cdot \frac{K'_{\partial.y.}}{K_{\partial.y.}}, \tag{1}$$

where l_{cr} is main fracture critical length, m; h are linear dimensions of the sample (its thickness or height), by which the fracture is developed, m; Y is function depending on the size of the sample and testing scheme); $K'_{d.s}$ is dynamic strengthening factor for the samples with an artificially induced fracture; $K_{d.s}$ is dynamic strengthening factor for the samples without an artificially induced fracture.

Use of different loading rates and determination of dynamic strengthening coefficients that are characterised by the relation of the concrete strength limit registered at the maximum rate to the sample strength obtained at the minimum (below standard) loading rate allowed for receiving periods of growth of the main fracture. The moment of the fracture development start is correlated with the minimum strength received at the lowest loading rate, and the moment of the sample full destruction is characterised by maximum strength registered at the highest loading rate.

The essence of the testing is as follows. According to the developed composition there are two sets of standard samples in the form of prisms for further in bending tensile testing. In one set the main fracture is initiated by means of applying a cut with a diamond tool or placing in advance a metal plate when preparing the sample. There was no artificially induced main fracture in the other set of the samples. The size of the induced fracture a shall exceed about twice and more the maximum size of the aggregates, and the ratio between the fracture length and the sample section height h shall make 0.2–0.4 [2]. The prepared samples after hardening were tested at a various rage of loading rates at the special unit ranging from 10^{-7} m/s to 10^{1} m/s. Such concrete loading rate range has been widely used for concrete testing by other researchers [21–24 and other]. The strength values obtained as a result of the tests were further used to determine dynamic strengthening coefficients in the sample sets with and without an artificially induced fracture for calculating the main fracture critical length by formula (1).

During the experiments we determined optimal compositions of the concrete mixtures and the method for their production with the view to increase strength and fracture-resistance parameters by means of using components that modify macro-, micro- and nano-structure of concrete.

For production of the concrete mix we used Portland cement brand PC M500 D0-N produced by ZAO Oskolcement, quartz sand from the Orlovsky sandpit with a fraction of 1.9-2.0. Coarse filler was granite crushed stone from the Bystrorechensky pit.

Micro-structure of concrete mixes were modified by plasticising agents and nanocarbon components. It is known that plasticising agents, when they completely dissolve in the mix water, improve the solution wettability, its fluidity, decrease water-cement ratio and create conditions for more even distribution of all mix components and for the formation of a dense micro-structure not participating in the processes of the cement stone microcrystal formation [29–34]. Introduction of firm nanocarbon hollow tubes facilitates directed formation of hydrosilicates crystals formation in the cement stone micro-structure. During cement gel structure hardening hydrosilicates adsorb on the internal and external surfaces of hollow nanocarbon tubes and form more strong crystallohydrates. The modified reinforced micro-structure formed after hardening has better physical and mechanical properties. The advantages of the use of nano admixtures for concrete are considered in detail in papers [35–37]. Superplasticising agent Poliplast SP-3 was used as modifier as per TS 5870-006-58042865-05 as well as carbon nano-tubes with a length of 4–45 mcm and a diameter of up to 35 nm.

Fibres were used to increase concrete strength and fracture-resistance at the micro- and macro-level; cement hydration nano-activated products adhesion occurred on their surfaces, too. Steel fibre MIxarm produced by Severstal-metiz was used as macro-filler, its specification is given in TS 1211-205-46854090-2005. The fibre structurally has cone-shaped anchors with the help of which up to 95 % of it is retained in concrete that facilitates blocking of the formation and development of micro- and macro-fractures in concrete.

Concrete mix production with account of the differences in the properties of its components was as follows. Appropriately selected and measured fibres, portland cement and quartz are mixed electromagnetically in a linear induction spinning device for 5 minutes. Under the influence of alternative electromagnetic field steel fibres, acting as ferromagnetic elements, facilitate better mixing, dispergation and increase specific surface of the obtained powdered dry mixture. Under the influence of magnetic field cement and quartz sand particles are adsorbed on the surface of steel fibres that increases the effectiveness of further reactions in water medium with other concrete mix components. Advantages of such devices with vortex layer and the impact of mechanochemical activation and ultrasonic dispergation have been considered in detail in papers [38–40].

At the same time water insoluble nanocarbon admixtures and superplasticising agent are mixed with water during 1–2 minutes in ultrasonic disperser with a frequency not less than 20 kHz. The obtained dry mix with fibres is further treated during 4–5 minutes in the standard concrete mixers adding coarse aggregate and mix water activated in the ultrasonic unit.

In order to compare the results we prepared a reference composition as per the conventional technology without using the linear induction spinning device and ultrasonic disperser. The quantity of fibre fillers and modifying admixtures in the reference samples complied with composition No. 1 (Table 1).

The compositions of the fibre fillers and modifying admixtures that significantly influence the physical and mechanical properties of concrete mixes are given in Table 1.

Table 1.Compositions of modifying admixtures and fibre filler.

Name	Content of the modifying admixtures components, % of the cement weight		
	1	2	3
Superplasticising agent Poliplast SP-3	0.5	0.55	0.6
Carbon nano-tubes with diameters 5–35 nm and lengths 4–45 mcm	0.005	0.0075	0.01
Steel fibre Mixarm with a diameter of 1 mm and a length of 54 mm, % of the mix volume	0.75	1.25	1.75

With the results of determining the main fracture critical length and rate of its growth the time till destruction (longevity) can be found by formula:

$$\tau = \frac{l_{cr.}}{V} = \frac{h \cdot Y \cdot K'_{\partial.y.} / K_{\partial.y.}}{V}, \tag{2}$$

where l_{cr} is critical length of the main fracture, m; V is fracture growth rate, m/s.

Thus, the offered samples testing method implying testing within a wide range of loading rates for determination of the main fracture critical length and growth rate as well as kinetic parameters of the concrete micro-structure corresponds to the known method of concrete fracture mechanics as per GOST 29167. The developed comprehensive method for determining strength and crack resistance parameters, followed by forecasting the time until concrete is erected, demonstrates high accuracy and reliability.

3. Results and Discussion

The quantitative confirmation of the offered scheme describing the influence of structural defects on changing strength was obtained in the course of special experiments implying testing of concrete samples with aggregates of various origins (Fig. 2 and Table 2). According to the obtained data when the rate of mechanical load grows, strength parameters in all samples increase. At stress rate equalling 1 MPa/s the strength vs. stress rate diagram showed a “change” to a sharper strength growth in all concrete samples with different aggregates (Fig. 2). Apparently, nearby this stress rate there is the area of possible transition of defects of one level (point defects, vacancies) to the other (dislocations) because of the increasing involving volume that corresponds to the conclusions of the kinetic strength theory.

Increasing of concrete strength parameters with growing stress rate takes place to a certain value that corresponds to the rate of stress relaxation. It has been experimentally determined that strength growth stops at stress rate approximately equalling 10^2 MPa/s. With further stress rate growth in some cases there was observed a slight reduction of strength values, which can be related to instantly occurring over stresses that result in an uncontrolled drastic growth of the main fracture (macro-fractures) and destruction of the sample. Such experiments with the same results were reflected in surveys [21–24, and other].

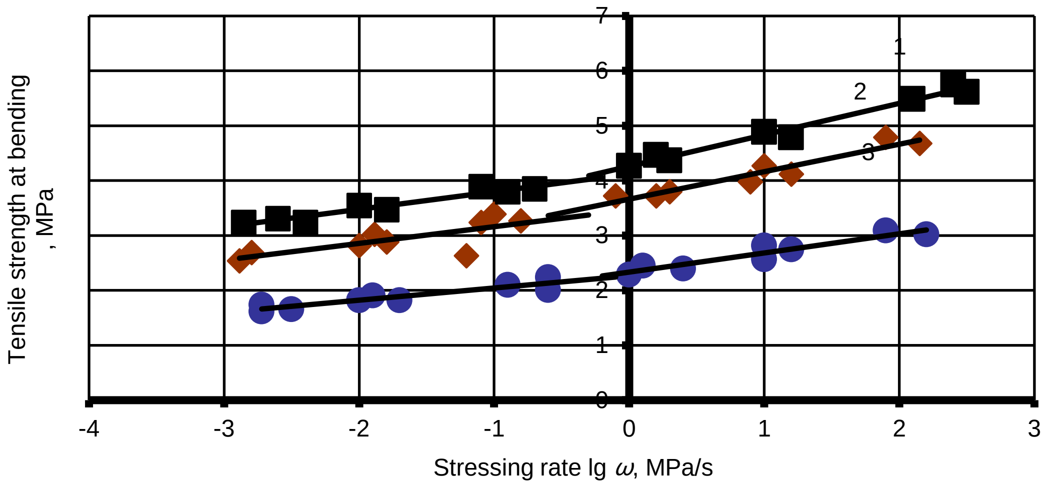

Figure 2. Changing of strength depending on stress rate logarithm for concrete with aggregate of: 1 – granite, 2 – limestone, 3 – keramzit.

Kinetic parameters of the structure defects, i.e. activation energy U_0 and efficient involving volume γ in concrete samples with different aggregates tested at differing stress rates were determined by formula [23]:

$$\sigma_p = \frac{KT}{\gamma}\ln\left[1+\frac{\tau_0}{KT}\exp\frac{U_0\omega\gamma}{KT}\right], \tag{3}$$

where σ_p is applied stress, MPa, K is Boltzmann's constant; T is absolute temperature, K; τ_0 is pre-exponential factor, 10^{-12} s; U_0 is activation energy, J; γ is efficient involving volume, m^3; ω is stress rate, MPa/s.

Quantitative values of kinetic parameters of the tested concrete samples with different aggregates given in Table 2 showed decrease in efficient involving volume γ at slight reduction of activation energy U_0 with stress rates exceeding 1 MPa/s (after the "change").

Table 2.Kinetic characteristics of concrete strength.

Type of aggregate	γ *10^{-26}, m^3		U_0*10^{-19}, (J)	
	"before the change"	"after the change"	"before the change"	"after the change"
Keramzit	4.19	2.65	1.3	1.11
Limestone	2.94	1.81	1.37	1.15
Granite	2.82	1.66	1.45	1.18

Consequently, when the stress rate of the samples grows, point defects of structure concentrate in some volume that does not promote a large-scale development of micro-fractures, and concrete strength grows.

The offered method showed that concrete samples testing with different stress rates demonstrate the kinetic process of the structure point defects transition into dislocations, micro- and macro-fractures both in the cement gel and nearby the matrix-aggregate structural irregularities. Thus, there is the possibility to refuse from direct registration of the main fracture dimensions and growth rate that reduces the process complexity and the reliability of the obtained results is high. The proof is that the offered method is related to fracture mechanics that determines the parameters of the main fracture development and to the kinetic parameters of the development of different defects of concrete micro-structure.

Based on the offered comprehensive method for determination of strength and fracture-resistance the authors have performed experiments with the aim to develop concrete compositions with fibre fillers and modifying additives. During testing there were used standard units as well as the units developed by the author aimed at determination of the quantity parameters of fracture formation and destruction of concrete.

Concrete samples with dimensions 100×100×400 mm were manufactured for testing with the view to determine strength parameters and kinetic characteristics when loaded at different rates. Testing with the scheme implying three-point bending was performed at the special unit with loading rates ranging from 10^{-7} m/s to 10 m/s.

Quantitative measurement of values of activation energy U_0 and efficient involving volume γ that allow for determining the influence of different micro-structure defects on the processes of fracturing was performed following the method [23, 25]. The results of the performed experiments are given in Table 3.

The analysis of the data presented in Table 3 showed that the offered concrete compositions with the Mixarm fibre filler, plasticising and nanocarbon additives and the methods of their preparation with the indicated component ratios bring to the increasing of compression strength and tensile strength in bending as compared to reference samples. It has been identified that maximum compression strength gain of 28.2 %, and bending tensile strength gain of almost 40 % was received in composition No. 2. At that all samples demonstrated reduction of kinetic parameters of the efficient involving volume compared to the reference samples. The developed compositions with the plasticising and nanocarbon additives have strong micro-structure that testifies to the prevailing development of point defects in small amount that does not lead to a large-scale fracturing. Use of fibres with cone-shaped anchors at the ends promoted slowing of the processes of formation and propagation of main fractures in concrete. With account of the obtained experimental data we have selected an optimal concrete composition with maximum strength characteristics and better kinetic parameters of fracturing (Table 2, composition 2). The developed fibre-concrete composition is recommended for use in reinforced concrete beams [41, 42].

Micrographs of the structure of fibre-concrete with the Mixarm fibre filler, superplasticising agent Poliplast SP-3 and nanocarbon additives that were made using "Altami LCD" stereomicroscope showed compaction and strengthening of the cement-sand matrix due to filling of the interparticle space with stringer steel fibres (Fig. 3).

a) 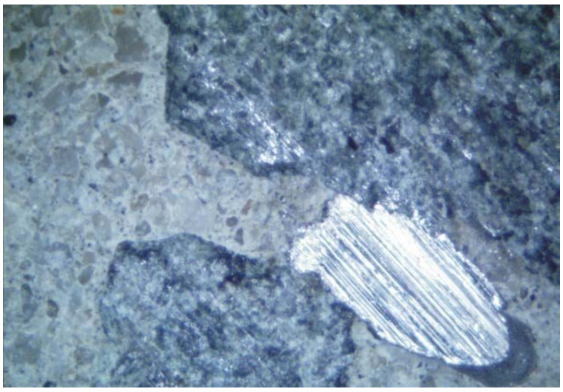 b) 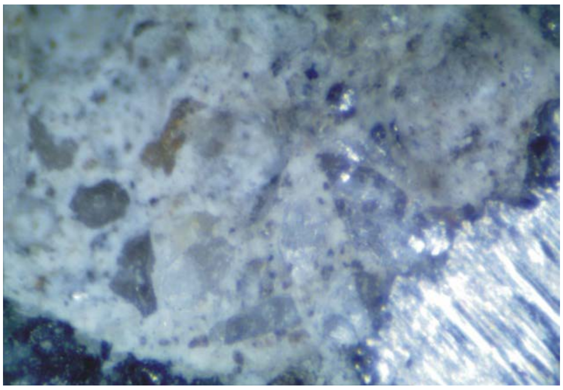

Figure 3. Micrographs of the structure of fibre-concrete with the Mixarm fibre filler and complex modifying additive that includes superplasticising agent Poliplast SP-3 and nanocarbon tubes: 1) 100 X, b) 200 X.

In order to determine the characteristics of macro-fracturing and destruction of the selected compositions (Table 2) the authors performed testing of the concrete samples by fracture mechanics methods with the receipt of full deformation diagrams and by the offered testing method with different loading rates and identification of dynamic strengthening coefficients. During the experiments with the receipt of the full destruction diagrams we used capillary (as per GOST 29167) and tensiometric [20] methods to measure the length of the developing main fracture.

For the tests we prepared a set of samples with dimensions 100×100×400 mm with an artificially induced fracture having a length of 40 mm made by a cutting tool. No artificial macro-fracture was made in the other set of concrete samples. The testing unit loading rates ranged from 10^{-7} m/s to 10 m/s. As a result we received esperimental daata and determined the quantitative values of the main fracture critical length in concrete by the standard fracture mechanics method $l_{cr.st.}$ and by the offered method $l_{cr.}$ finding dynamic strengthening coefficients [25] (Table 3).

Table 3.Concrete strength and fracture-resistance parameters.

No. of mix	R_b, MPa	R_{bf}, MPa	$\gamma \cdot 10^{-26}$, m³	$U_0 \cdot 10^{-19}$ J	$K_{d.s.}$	$K'_{d.s.}$	$l_{cr.st.}$, m	$l_{cr.}$, m
Reference sample	61.2	11.3	$\frac{2.81}{1.94}$	$\frac{2.43}{1.72}$	1.87	1.05	0.065	0.063
1	70.38	12.75	$\frac{2.68}{1.82}$	$\frac{2.51}{1.86}$	1.94	1.12	0.066	0.065
2	78.43	15.81	$\frac{2.47}{1.62}$	$\frac{2.87}{2.29}$	2.0	1.21	0.069	0.068
3	74.25	13.62	$\frac{2.58}{1.73}$	$\frac{2.68}{1.99}$	1.9	1.13	0.067	0.067

Comments. R_b is strength limit of concrete at compression received with standard loading rate; R_{bf} is strength limit of concrete at bending received with standard loading rate; γ is efficient involving volume, above the line are values of γ "before the change", under the line – "after the change". U_0 is activation energy, above the line are values of U_0 "before the change", under the line – "after the change".

It has been determined that an increased sensitivity to the formation and growth of the main fracture is characteristic of the concrete having a significant difference in strength limits of the samples with an artificially induced fracture and without such fracture, and, consequently, the smaller ratio $\left(\frac{K'_{d.s.}}{K_{d.s.}}\right)$. At that the main fracture critical length has minimum values. And vice versa, the smaller the difference in the strength values of the samples with and without a fracture is, the higher fracture-resistance of the concrete is and the larger the macro-fracture critical length is.

It has been established that the obtained size of the main fracture in all concrete samples has values more the half of the section of the sample in which it developed that demonstrates a significant deviation from the known results of other researchers [2]. The development of the formed main fracture in the developed concrete compositions with modifying additives and steel fibres is accompanied by constant overcoming of the coarse aggregate in the contacts with the cement-sand matrix and highly firm fibre that reinforces the macro-structure of concrete. As a result the growth slows down and the value of the macro-fracture critical length determined as per GOST 29167 and the offered method grows (Table 3). However, the developed method for determination of the main fracture critical size in concrete is more accurate and reliable as compared with the fracture mechanics method because the macro-fracture growth was controlled constantly, but not stage-wise. Based on the performed research and determination of the main fracture critical length and growth rate under the impact of external mechanical load the time till full destruction (longevity) of the concrete samples was determined by formula (2). The offered comprehensive method for determination of fracture-resistance parameters can be applied in practice, including for the structures manufactured of fibre-concrete.

4. Conclusions

1. A comprehensive method of an uninterrupted testing of concrete samples at different loading rates has been developed. It allows for simultaneous determination of the micro-structure defects growth kinetics and fracture mechanics parameters related to determination of the main fracture critical length and growth rate as well as forecasting of the time till destruction (longevity) under the impact of mechanical load.

2. The developed concrete compositions with fibre fillers, plasticising and nanocarbon additives and their preparation method in the course of testing with different loading rates have demonstrated a reduction of the efficient involving volume γ that testifies to the micro-structure increased strength by means of formation of a small amount of defects that does not result in a large-scale formation of micro-fractures. The optimal composition of concrete has been selected that has the maximum compression strength gain of 28 % and tensile strength gain of 40 % compared with the reference composition.

3. Based on the offered method the characteristics of formation of macro-fractures have been determined for the developed concrete compositions with fibre fillers and modifying additives prepared using a linear induction spinning device and an ultrasonic disperser. It has been determined that in all samples the values of the main fracture maximum critical length determined by capillary method of standard fracture mechanics and by the offered method implying the use the samples dynamic strengthening coefficients in a wide range of loading rates varied from 63 to 68 mm with the height of the section where the macro-fracture was developing equalling 100 mm. The time of the main fracture growth and its length is related to the strength of the micro- and nano-structure of the developed concrete compositions with modifying additives and to the use of non-standard fibres with cone-shaped anchors that slow down the macro-fractures propagation.

Thus, the use of the offered comprehensive method for determining concrete strength and fracture-resistance parameters demonstrated the required accuracy and requires less effort that expands the scope of application and accumulation of experimental data and improves their reliability. This article has a more methodical orientation for subsequent wide practical use in the development of new and well-known concrete compositions with specified physical and mechanical properties and service life.

References

1. Cherepanov, G.P., Ershov, P.V. Mekhanika razrusheniya [Fracture mechanics]. Moscow, 1977. 222 p.
2. Certificate of Authorship No. 819618 Method for identification of materials crack resistance. Trapeznikov, L.P., Pashchenko, V.I., Pak, A.P. published on 7.4.1981.
3. Piradov, K.A., Guzeev, E.A. Podkhod k otsenke natriazhenno-deformirovannogo sostoiania zhelezobetonnykh ele-mentov cherez parametry mekhaniki razrushenia [Approach to assessment of strain and stress state of reinforced concrete elements through the fracture mechanics parameters]. Concrete and reinforced concrete. 1994. 5. Pp. 19–23.
4. Leonovich, S.N. Treshchinostoykost I dolgovechnost betonnykh i zhelezobetonnykh elemetov v terminal silovykh i energeticheskikh kriteriev mekhaniki razrusheniya [Crack resistance and longevity of concrete and reinforced concrete elements in terms of force and energy criteria of fracture mechanics]. Minsk, 1999. 266 p.
5. Kolchunov, V.I., Demianov, A.I. Neordinarnaia zadacha o raskrytii treshchin v zhelezobetone [An unconventional challenge related to fracture opening in reinforced concrete]. Magazine of Civil Engineering. 2009. 4 (88). Pp. 60–69. DOI: 10.18720/MCE.88.6
6. Evans, A.G., Wiederhorn, S.H. Ceramic materials testing is an analitic basic for predicting fracture. International Journal of fracture. 1974. 10. Pp. 377–392.
7. Evans, A.G., Langdon, T.J. Konstruktsionnaya keramika [Structural Ceramics]. Moscow, 1980. 256 p.

8. Mindess S., Nadeau J. Effect of notch width on K1 for mortar and concrete. Cement and Concrete Research. 1976. 6(4). Pp. 529–534.
9. Strange, P.C., Bryant, A.H. The role of aggregate in the fracture of concrete. Journal of Materials Science. 1979. 14. Pp. 1863–1868.
10. Bazant, Z.P., Planas, J. Fracture and size effect in concrete and other quasibrittle materials. USA, 1998. XXII. 616 p.
11. Minghao, T., Peiwei, G., Limin, W., Yilang, T. Study on Mechanical and Crack Resistance of Expanded Fiber Rein-forced Concrete. IOP Conference Series: Materials Science and Engineering. Vol. 774. 4th International Conference on Material Science and Technology 22-23 January 2020. China, 2020. DOI: 10.1088/1757-899X/774/1/012083
12. Limin, W., Peiwei, G., Minghao, T., Yilang, T., Jianjun, Zh. Investigation on axial compressive stress-strain relation-ship of expanded fiber reinforced concrete. IOP Conference Series: Materials Science and Engineering. 768. Materials Application and Civil Engineering. 3rd International Symposium on Application of Materials Science and Energy Materials. SAMSE 2019. 30-31 December 2019. China, 2021. DOI: 10.1088/1757-899X/768/3/032026.
13. Wei, L., Zuo, W., Pan, H., Lyu, K., Zhang, W., She, W. Rational design of lightweight cementitious composites with reinforced mechanical property and thermal insulation: Particle packing, hot pressing method, and microstructural mechanisms. Composites Part B: Engineering. 2021. 226. DOI: 10.1016/j.compositesb.2021.109333
14. Inozemtcev, A. Case Studies of High-strength Lightweight Concrete Using Expanded Siliceous Aggregate. IOP Conference Series: Materials Science and Engineering. 2020. 840. DOI: 10.1088/1757-899X/840/1/012017.
15. Regel, V.R., Slutsker, A.I., Tomashevskiy, E.E. Kineticheskaya priroda prochnosti tverdykh tel [Kinetic nature of strength of solid bodies]. Moscow, 1974. 535 p.
16. Cheremskoy, P.G., Slezov, V.V., Betekhtin, V.I. Pory v tverdom tele [Pores in solid bodies]. Moscow, 1990. 376 p.
17. Vakulenko, A.A., Kukushkin, S.A. Kinetika fazovykh perekhodov v tverdykh telakh pod nagruzkoi [Kinetics of phase transitions in solid bodies under load] FTT. 2000. 42(1). Pp. 172–173.
18. Vakulenko, A.A., Kukushkin, S.A., Shapurko, A.V. Kinetika poroobrazovania pri plasticheskoi deformatsii kristallov so strukturoi 43(2). Pp. 261–264.
19. Leonovich, S.N., Karpenko, S.I. Osnovy fiziki tverdogo tela [Solid body physics]. Minsk. 2002. 270 p.
20. Invention patent No. 2200943. Method for identification of materials crack resistance. Perfilov, V.A., Mityaev, S.P. Reg. on 20.03.2003.
21. Mindness, S., Nadean, J. Effect of loading rate of the flexural strength of cement u mortar. The American Ceramic Society Bulletin. 1977. 56. Pp.429–430.
22. Grushko, I.M., Ilin, A.G., Rashevsky, S.T. Prochnost betona na rastyazhenie [Concrete tensile strength]. Kharkov, 1973. 156 p.
23. Kazachuk, A.I., Solntseva, I.Yu., Stepanoc, V.A., Shleizman, V.V. Rol storosti nagruzhenia v razrushenii khrupkikh tel [Role of loading rate in the destruction of brittle bodies]. FTT. 1983. 25(7). Pp. 1945–1952.
24. Vashchenko, A.P. Eksperimentalnie metody i mekhanicheskie svoistva konstruktsionnikh materialov pri deformatsiI (102…105 s^{-1}) i temperaturakh 77…773 K [Experimental methods and mechanical properties of construction materials at high-rate deformation (102…105 s^{-1}) and temperatures 77…773 K]. Strength Challenges. 2002. 3. Pp. 55–61.
25. Oreshkin, D.V., Perfilov, V.A., Pervushin, G.N. Kompleksnaya otsenka treshcinnostoikoski tsementnykh materialov: monografia [Complex assessment of crack resistance of cement materials: Thesis]. Moscow. 2012. 207 p.
26. Perfilov, V.A., Oreshkin, D.V., Zemlyanushnov, D.Y. Concrete strength and crack resistance control. Procedia Engi-neering 2. 2nd International Conference on Industrial Engineering. ICIE 2016. Pp. 1474–1478. DOI: 10.1016/proeng. 2016.07.085
27. Perfilov, V.A. Effects of various factors on concrete strength and crack-resistance. Journal of Physics: Conference Series, Vol. 1967. International Scientific Practical Conference Materials science, shape-generating technologies and equipment 2021. ICMSSTE 2021. 17-20 May 2021. Yalta, Russian Federation. 2021. 9 p. DOI: 10.1088/1742-6596/1967/1/012056
28. Shevchenko, V.I. Primenenie metodov mekhaniki razrushenia dlia otsenki treshchinostoikosti i dolgovechnosti betona [Application of fracture mechanics methods to assessment of crack resistance and logevity of concrete]. Volgograd, 1988. 104 p.
29. Ponmohan, K.B., Suchithra, S. Crack resistant concrete using municipal solid waste incineration ash and low cost natural fibres. International Journal of Scientific and Technology Research. 2020. 9. Pp. 6782–6786.
30. Ngo, V.T., Lam, T.K.K., Do, T.M.D., Nguen, Ch.Ch. Povyshennaia plastichnost nanobetona so stalnimi voloknami [Increased plasticity of nano-concrete with steel fibres]. Magazine of Civil Engineering. 2020. 93(1). Pp. 27–34. DOI: 10.18720/MCE.93.3
31. Aslani, F., Wang, L., Zheng, M. The effect of carbon nanofibers on fresh and mechanical properties of lightweight engineered cementitious composite using hollow glass microspheres. Journal of Composite Materials. 2019. 53(17). Pp. 2447–2464. DOI: 10.1177/0021998319827078
32. Golaszewski, J., Cygan, G., Golaszewska, M. Development and Optimization of High Early Strength Concrete Mix Design. IOP Conference Series: Materials Science and Engineering. 2019. 471(1124). DOI: 10.1088/1757-899X/471/11/112026
33. Solovyov, V., Sokolova, Yu. Fine-grained concrete with organomineral additive. MATEC Web of Conferences. 2016. 86. DOI: 10.1051/matecconf/20168604045
34. Pyataev, Eu., Semenov, V., Tregubova, E., Kirushok, D. Fine-grained concrete modified with a multifunctional additive. IOP Conference Series: Materials Science and Engineering. 2020. 869. DOI: 10.1088/1757-899X/869/3/032050
35. Pukharenko, Yu.V. Sovremennoe sostoianie i perspektivy primenenia fulleroidnikh nanostruktur v tsementnykh kompozitsiiakh [Modern state and future of the use of fulleroid nanostructures in cement mixes]. Siberian Industrialman. 2008. 3. Pp. 30–31.
36. Smolikov, A.A. Beton armirovannii nanovoloknami [Concrete reinforced with nano fibers]. Concrete and reinforced concrete. 2009. 4. Pp. 8–9.
37. Falikman, V.R. Nanomateriali i nanotekhnologii v sovremennikh betonakh [Nanomaterials and nanotechnologies in modern concrete]. Industrial and civil construction. 2013. 1. Pp. 31–34.
38. Ibragimov, R.A., Korolev, E.V., Kayumov, R.A., Deverdeev, T.R., Leksin, V.V., Sprintze, A. Effektivnost aktivatsii min-eralnikh viazhushchikh v apparatakh vikhrevogo sloia [Efficiency of activation of mineral binders in vortex layer units]. Magazine of Civil Engineering. 2018. 82(6). Pp. 191–198. DOI: 10.18720/MCE.82.17
39. Samchenko, S., Zorin, D. Electricity costs for grinding of cement with expanding additives. International Journal of Engineering and Technology (UAE). 2018. 7(2). Pp. 274–276.

40. Tkach, E., Semenov, V., Shumilina, Yu. Optimization of the composition and technological processes of dispersed cement systems with high performance properties. IOP Conference Series: Materials Science and Engineering. 2021. 1030. DOI: 10.1088/1757-899X/1030/1/012024
41. Travush, V.I., Konin, D.V., Krylov, A.S. Prochnost zhelezobetonnikh balok iz visokoprochnykh betonov I fibrobetonov [Strength of reinforced concrete beams of highly strong concretes and fibre-reinforced concretes]. Magazine of Civil Engineering. 2018. 77(1). Pp. 90–100. DOI: 10.18720/MCE.77.8
42. Belostosky, A.M., Karpenko, N. I., Akimov, P. A., Sidorov, V. N., Karpenko, S.N., Petrov, A.N., Kaytukov, T. B., Khari-tonov, V. A. About development of numerical methods of analysis of spatial plate-shell reinforced concrete structures with allowance for non-linearities. IOP Conference Series: Materials Science and Engineering. 2018. 456. DOI: 10.1088/1757-899X/456/1/012103

Information about author:

Vladimir Perfilov, *Doctor of Technical Sciences*
ORCID: https://orcid.org/0000-0001-9196-7572
E-mail: vladimirperfilov@mail.ru

Received 10.11.2021. Approved after reviewing 23.03.2023. Accepted 29.03.2023.